675

ANL-7675
RETURN TO ANL (IDAHO) LIBRARY.

Argonne National Laboratory

CHEMICAL ENGINEERING DIVISION

ANNUAL REPORT 1969

The facilities of Argonne National Laboratory are owned by the United States Government. Under the terms of a contract (W-31-109-Eng-38) between the U. S. Atomic Energy Commission, Argonne Universities Association and The University of Chicago, the University employs the staff and operates the Laboratory in accordance with policies and programs formulated, approved and reviewed by the Association.

MEMBERS OF ARGONNE UNIVERSITIES ASSOCIATION

The University of Arizona
Carnegie-Mellon University
Case Western Reserve University
The University of Chicago
University of Cincinnati
Illinois Institute of Technology
University of Illinois
Indiana University
Iowa State University
The University of Iowa
Kansas State University
The University of Kansas
Loyola University
Marquette University
Michigan State University
The University of Michigan
University of Minnesota
University of Missouri
Northwestern University
University of Notre Dame
The Ohio State University
Ohio University
The Pennsylvania State University
Purdue University
Saint Louis University
Southern Illinois University
University of Texas
Washington University
Wayne State University
The University of Wisconsin

LEGAL NOTICE

This report was prepared as an account of Government sponsored work. Neither the United States, nor the Commission, nor any person acting on behalf of the Commission:

A. Makes any warranty or representation, expressed or implied, with respect to the accuracy, completeness, or usefulness of the information contained in this report, or that the use of any information, apparatus, method, or process disclosed in this report may not infringe privately owned rights; or

B. Assumes any liabilities with respect to the use of, or for damages resulting from the use of any information, apparatus, method, or process disclosed in this report.

As used in the above, "person acting on behalf of the Commission" includes any employee or contractor of the Commission, or employee of such contractor, to the extent that such employee or contractor of the Commission, or employee of such contractor prepares, disseminates, or provides access to, any information pursuant to his employment or contract with the Commission, or his employment with such contractor.

Printed in the United States of America
Available from
Clearinghouse for Federal Scientific and Technical Information
National Bureau of Standards, U. S. Department of Commerce
Springfield, Virginia 22151
Price: Printed Copy $3.00; Microfiche $0.65

ANL-7675
General

ARGONNE NATIONAL LABORATORY
9700 South Cass Avenue
Argonne, Illinois 60439

CHEMICAL ENGINEERING DIVISION ANNUAL REPORT—1969

R. C. Vogel, Division Director
L. Burris, Associate Division Director
A. D. Tevebaugh, Associate Division Director
D. S. Webster, Associate Division Director
E. R. Proud, Assistant Division Director
J. Royal

April 1970

Preceding Annual Report:
ANL-7575 January–December 1968

TABLE OF CONTENTS

SUMMARY 1
I. FUEL CYCLE TECHNOLOGY 19
A. Liquid Metal-Molten Salt Technology 19
1. Salt-Transport Process for LMFBR Fuels 19
2. Liquid Metal Decladding of LMFBR Fuels 20
3. Pyrochemical Purification of Plutonium-238 24
4. Engineering Development 25
5. Laboratory Investigations 35
B. Fluidization and Volatility Processing 44
1. Laboratory Investigations 44
2. Engineering-Scale Investigations 52
3. Basic Mechanisms of Fluidization 57
C. Preparation of Fuel Materials 57
1. Oxidation of Uranium to UO_2 in a Fluidized Bed 57
2. Conversion of FBR Oxide Fuel to Carbide Fuel 60
II. SODIUM TECHNOLOGY 62
A. Chemical Developments 63
1. Sodium Chemistry 63
2. Sodium Analytical Development 68
B. Engineering Developments 70
1. Monitoring of Sodium Purity 70
2. Fission Product Behavior and Control 72
3. Nature and Control of Sodium Aerosol Formation 73
III. MATERIALS CHEMISTRY AND THERMODYNAMICS 74
A. High-Temperature Thermodynamic Studies 74
1. Volatilization Studies of Plutonium Oxide Compounds by Mass Spectrometry 74
2. Phase Diagram of the Ternary Oxide System U-Pu-O 77
3. Phase Diagram of the U-Pu-O System Containing Nonradioactive Fission Products 79
4. Total Effusion of Pu-O and U-Pu-O Systems 80
5. Oxygen Gradients, Total Vapor Pressures, and Oxygen Potentials in Reactor Fuels 81
6. Volatilization Studies of Plutonium Carbide Compounds by Mass Spectrometry 81
7. Transpiration Studies of the Uranium-Carbon System 84
B. Reactor Safety and Physical Property Studies 86
1. Enthalpies and Heat Capacities by Drop Calorimetry 87
2. Other Physical Property Studies 89
3. Segregation in Ceramic Fuels: Fuel Migration Studies 92
C. Calorimetry 93
1. Thermochemistry of Uranium Compounds 93
2. Thermochemistry of Plutonium Compounds 94
3. Thermochemistry of Hydrogen Fluoride 95
4. Chemical Bonding in NSF_3, NSF, and NS 97
5. Enthalpy of Formation of Molybdenum Disulfide 98
6. Miscellaneous Fluorine Bomb Calorimetric Studies 98
7. Thermochemistry of Aqueous Xenon Trioxide 99
8. Enthalpies of Formation of $KBrO_4$(c) and $KBrO_3$(c) and the Thermodynamic Properties of the Perbromate and Bromate Ions 99
9. Enthalpy of Formation of Disodium Acetylide 100
IV. ANALYTICAL AND REACTOR CHEMISTRY 101
A. Chemistry of Irradiated Fast Reactor Fuels and Materials 101
1. Chemical Studies of Irradiated Ceramic Fuels 101
2. Electron Microprobe Analysis of Irradiated Fuels 102
3. Feasibility Study of Fuel-Failure Detection: Sodium-Soluble Tags 108
B. Xenon Tagging of Fuel Elements in EBR-II 110
1. Preparation of Tag Mixtures 111
2. Addition of a Tag to a Fuel Element 112
3. Possible Detrimental Effects of Xenon Tagging 113
4. Identification of a Released Xenon Tag 114

C. Fast-Reactor Cross-Section Measurements 115
1. Spectrum-Averaged Measurements 115
2. Low-Mass, Fast-Neutron Fission Yields 119
D. Determination of Burnup of Fast Reactor Fuels 119
1. X-Ray Spectrometric Determination of Rare Earth Fission Products 120
2. Development of a New Method for the Determination of Fast Fission Yields 122
V. CHEMISTRY OF LIQUID METALS AND MOLTEN SALTS 124
A. Liquid Metal Studies 125
1. Thermodynamics 125
2. Transport Properties: Electronic Conductivity of Selenium- and Sulfur-Containing Cathode Alloys 134
3. Ultrasonic Measurements in Liquid Metallic Solutions 136
B. Molten Salt Studies 137
1. Thermodynamics: Phase Diagrams of Lithium Halide-Containing Systems 137
2. Structure Investigations by Spectroscopic Methods 138
C. Energy Conversion Studies 141
1. Lithium/Chalcogen Cells 141
2. Immobilization of Molten-Salt Electrolytes 147
3. Materials Stability 149
D. Battery Development 151
1. High-Specific-Energy Lithium/Selenium Batteries for Implantation 151
2. High-Specific-Power Lithium/Selenium Cells for Vehicle Propulsion 153
3. Lithium/Sulfur Cells for Vehicle Propulsion 158
4. Performance Comparison 163
VI. FLUIDIZED-BED COMBUSTION OF FOSSIL FUELS 165
A. Laboratory-Scale Investigations 165
B. Bench-Scale Experimentation 166

Chemical Engineering Division Annual Report—1969

ABSTRACT

The research and development programs of Argonne's Chemical Engineering Division consisted of the following: (1) Pyrochemical processes employing salt-transport separations for the recovery and purification of LMFBR fuel were investigated during the first half of 1969. During the second half of 1969, research was redirected to the liquid metal decladding of LMFBR fuels as an alternative head-end step for aqueous processing. (2) The work on fluid-bed fluoride volatility processing culminated in a conceptual design and evaluation study which indicated that fluoride volatility methods are technically feasible for the purification and recovery of LMFBR fuels. (3) The program in sodium technology was expanded during the second half of 1969. Work in sodium technology included the study of mechanisms of carbon transport in sodium-steel systems, the establishment of a center for sodium analytical chemistry, and work on the development, evaluation, and improvement of purification devices and on-line monitors for impurities in sodium. (4) Work on the thermodynamics and physical properties of candidate FBR fuels at high temperatures was continued. (5) Calorimetric studies were made of substances of interest in nuclear technology. (6) Studies were made of the chemical behavior of irradiated FBR fuels. This program was directed mainly toward uranium-plutonium oxide fuels, with emphasis on fuel-cladding interactions and fission product migration and interaction. (7) A method for the detection of fuel failure in EBR-II was developed in cooperation with the EBR-II project. This method depends on the use of mixtures of xenon isotopes as tags for the identification of a failed fuel element. (8) Studies of the chemistry and thermodynamics of liquid metals, alloys, and molten salts were continued. The work included studies of the thermodynamic behavior of various systems as expressed by liquid-solid phase diagrams, liquid-phase activity coefficients, vapor-liquid equilibria, and solubilities of various gases and solids in liquids. (9) Studies of electrochemical energy conversion by means of cells with liquid metal electrodes and fused-salt electrolytes have led to the development of cells which promise many uses as energy storage devices. (10) Studies were continued on the development of methods for determining the burnup of FBR fuels. (11) Measurements of nuclear cross sections of FBR fuel, cladding, and structural materials were continued. (12) Work was carried out on the preparation of ceramic FBR fuel materials. (13) Studies were made to provide physical-property data for use in evaluating the safety of various prospective FBR materials. (14) Fluidized-bed combustion of coal was studied as a means of reducing the emission of pollutants into the air.

SUMMARY

I. Fuel Cycle Technology (pages 19 to 61)

Liquid Metal-Molten Salt Technology

Technological and economic features of pyrochemical processes that make them attractive for the processing of fast breeder reactor fuels include (1) an ability to handle short-cooled, high-burnup fuels, which results in decreased out-of-reactor fuel inventory, (2) the simplification or elimination of chemical conversions, (3) less shielded processing space because of small process volumes and compact equipment, and (4) the direct production of solid radioactive wastes.

Pyrochemical processes employing salt-transport separations have been under investigation. In separations of this type, solute plutonium or uranium is transported from one liquid alloy (donor) to another liquid alloy (acceptor) by cycling a molten chloride salt between the two alloys and mixing the salt with

each alloy in turn. Most of the process chemistry for a salt transport process has been investigated and is well understood, and much of the basic engineering information is also available. In mid-1969, however, development work on the salt transport process was terminated because of a decision by the AEC to limit funding to the development of aqueous processes. At the present time, a reduced effort is continuing on the development of a liquid metal decladding procedure proposed as the head-end step for the aqueous processing of fast breeder reactor fuels.

Liquid metal decladding of LMFBR fuel

Conceptual design studies on zinc decladding of stainless steel-clad LMFBR fuels. To evaluate decladding with molten metal as a scheme for the head-end processing of liquid metal fast breeder reactor (LMFBR) fuels, a conceptual design study has been initiated for decladding stainless steel-clad UO_2-20 wt % PuO_2 fuel with zinc in a 5 metric tons/day plant. The study considers the steps between unloading fuel assemblies from sodium-filled shipping casks and feeding the oxide fuel to an aqueous dissolution or other interfacing step. The fuel assemblies are loaded into baskets in a decladding vessel and immersed in molten zinc, which dissolves the stainless steel. The fuel is unaffected and is removed in the baskets for transfer to the main plant.

Material and heat balances have been made. Also, preliminary cell equipment layouts have been completed. A major objective of the study is to identify key problems to be solved in a R&D program. A preliminary criticality analysis of the decladding operation has been made that will aid in setting vessel design criteria.

Glovebox facility. A shift in the pyrochemistry program, from development of a complete fuel process to the development of a liquid metal head-end step for aqueous processing of oxide fuel, has changed the requirements for the glovebox facility originally planned for engineering-scale demonstration experiments. The portion of the facility planned to be used for the head-end steps of the salt transport process are virtually complete except for slight modifications needed for the present program. Work on the balance of the facility has been terminated. In the initial experiments performed in the facility, simulated fuel elements containing about 5 kg of UO_2 will be declad in zinc. The use of baskets for retaining declad fuel and the behavior of sodium and fission products during decladding will be studied. A design for a full-scale decladding vessel will be developed and materials of construction tested.

Cladding dissolution. The dissolution of type 304 stainless steel in zinc at 800°C has been found attractive as a decladding concept, but other cladding materials and metal solvents have also been considered. Experiments were performed in vessels with identical geometry and with gentle agitation to compare the dissolution rates of types 304 and 316 stainless steel and Zircaloy-2 in zinc at 800°C with the dissolution rate of type 304 stainless steel in Sb-18 at. % Cu at 900°C. (Copper-antimony alloy was studied as a backup decladding solvent.) The measured rates are 2, 4, 20, and >20 mils/min, respectively. In another test, the dissolution rate in zinc at 800°C for a type 304 stainless steel sample that had been irradiated in EBR-II was about twice the rate for similar unirradiated specimens. All of these systems exhibit an adequate dissolution rate for fuel cladding.

Additional experiments were performed to estimate the capacity of zinc for stainless steel. The cosolubilities of chromium and iron in zinc were found to be 5.8 and 1.0 wt %, respectively, at 800°C. This indicates that less than 8 wt % stainless steel can be dissolved completely in zinc at 800°C. It has been found, however, that after zinc is saturated with chromium and iron, it continues to attack stainless steel, producing a fine dispersion of suspended solids. This attack continues until the zinc contains in solution and suspension at least 15 wt % stainless steel (the highest level studied).

An investigation was made of the evaporation of residual zinc from oxide fuel (following zinc decladding and transfer of the bulk of the zinc and stainless steel out of the decladding vessel). A satisfactory condenser and transfer tube were designed. The zinc was evaporated from below a 1-in. layer of salt,* through the transfer tube in the upper portion of the decladding vessel, to a separate condenser. Agitation during evaporation proved beneficial, reducing "bumping" and the resultant salt-phase entrainment. To decrease undesired condensation within the decladder, an argon stream was passed from a port at the top of the furnace (above the heat shields) and through the condenser. In the first experiment, removal of 100% of the zinc from the fuel was demonstrated; 85% of the zinc was collected in the condenser, and the balance of the zinc was condensed on the heat shields and at the top of the decladding vessel. Condensation could be reduced further by appropriate relocation of the inlet nozzle for the argon and modification of the heat shield design. No further work on this evaporation step is planned unless a definite need for the step becomes apparent.

* Salt reduces zinc vaporization during decladding, consolidates fuel fines, and improves heat transfer after the zinc has been removed.

Pyrochemical purification of plutonium-238

Pyrochemical processing techniques were investigated as a means of recovering and purifying plutonium-238 in various types of materials. Two laboratory-scale runs were performed to demonstrate the recovery of metallic plutonium-238 by the reduction of $^{238}PuO_2$ in liquid Zn-Mg or Zn-Ca, followed by vacuum distillation of the solvent metals. Most of the light elements that result in undesirable (α,n) reactions were separated from plutonium-238 by this procedure.

Two experiments were performed with $^{239}PuO_2$ microspheres (a stand-in for $^{238}PuO_2$) by procedures similar to those described above except that after plutonium was reduced into a reduction-donor alloy it was oxidized into a salt phase and transported to an acceptor alloy where it was again reduced and subsequently purified by retorting. Good recovery of plutonium and good separation from light elements were achieved in both laboratory-scale experiments.

Two runs to recover high-purity plutonium metal from $^{239}PuO_2$-molybdenum cermet fuel utilized a salt transport scheme similar to that used in processing $^{239}PuO_2$ except that the plutonium oxide was converted to the chloride by $CuCl_2$ in the salt system prior to transfer of the plutonium to an acceptor alloy. Disintegration of the cermets was effected in both runs, but the ^{239}Pu metal product contained excessive concentrations of copper.

Work on this project was discontinued June 30, 1969.

Engineering development

Agitator-pump mixer-settler investigations. An agitator-pump mixer-settler for separation of fission products from plutonium by liquid metal-molten salt extraction has been developed. A specific design was selected, and the mixing and pumping characteristics determined, first with water and organic liquids in plastic mixer-settler models and then in a stainless steel single-stage mixer-settler with the liquid Mg-Cu and $MgCl_2$-NaCl-KCl-MgF_2 system proposed for the plutonium purification step of the salt transport process. The single-stage mixer-settler has a mixing chamber volume of about 1 liter and is designed to operate at flow rates (i.e., pumping rates) for metal plus salt in the range of 1 to 3 liters/min. The flow-rate range may be changed by changing the inlet orifices in the agitator-pump and in the liquid-metal metering cup. An extraction experiment was performed in which cerium (a stand-in for plutonium) was transferred from Mg-Cu to $MgCl_2$-NaCl-KCl-MgF_2 at 675°C. The stage efficiency in this run was greater than 99%.

Development of a large-scale mixer-settler. A pump loop has been operated to test a mixer-settler design proposed for a large-capacity salt transport process, e.g., a uranium purification process. The equipment was fabricated of type 304 stainless steel and included two 18-liter mixer-settlers. In operation, salt was circulated through the mixer-settlers at pumping rates up to about 4 liters/min. Data were taken for the extraction of uranium from a Cd-2.2 at. % Mg alloy into $MgCl_2$-30 mol % NaCl-20 mol % KCl salt in one mixer-settler and for the extraction of this uranium out of the salt and into a Cd-45 at. % Mg alloy in a second mixer-settler. The metal phases were "captive" in each extractor. Mass-transfer coefficients were of the order of 100 kg U/(min) (wt fraction U in salt phase) and varied with agitation intensity, which was also measured. The entrainment of metal from one mixer-settler to the other averaged 2×10^{-5} g of alloy per gram of salt circulated.

Development of liquid level probe. Earlier designs of mutual inductance coils(for measurement of liquid metal levels) were used with containment wells fabricated of austenitic stainless steels, graphite, or ceramic materials. A newly designed mutual inductance coil is usable in a tantalum containment well having a 30-mil wall.

Materials testing. Tungsten specimens were brazed with an alloy of Ni-20 wt % Cr-10 wt % Si-3 wt % Fe. Slight undercutting of the joints was noted when they were exposed up to 144 hr to Zn/$CaCl_2$-CaF_2 at 800°C, but when the brazed joints were given an 8-hr diffusion treatment at 1370°C prior to exposure to that system for similar durations, no undercutting was detected.

Refractory metals and Fe-Cr alloys were also tested. Results indicate that they are useful for containing Mg-Cu/chloride salt systems—refractory metals because of good corrosion resistance and the Fe-Cr alloys (which have fair corrosion resistance) because of lower cost and better fabricability. Some embrittlement of tantalum and niobium materials by reaction with hydrogen liberated from salt at 400°C and 700°C was observed.

An investigation was made of the stability of plutonium solutions in contact with various materials of construction and in the presence of atmospheric and reagent impurities. It was concluded that tungsten, tantalum, and Mo-30 wt % W are compatible with Mg-Cu-Ca-Pu solutions and that any impurities in the standard magnesium, copper, and calcium reagents used in the salt transport process do not react with plutonium to an extent that results in detectable plutonium losses. The introduction of oven-dried $CaCl_2$ and CaF_2 to a melt of Mg-Cu-Ca-Pu led to the loss of

about 3% of the plutonium from the solutions. The specific mechanism of plutonium removal from solution has not been identified, and procedures for salt purification or pretreatment are being evaluated.

Laboratory investigations

Chemical studies in support of the development of a head-end process and other processes related to the salt transport method for recovery of spent FBR fuel include the following: (1) studies of the mechanism of the dissolution of stainless steel in molten zinc, (2) measurements of the solubility of zirconium in liquid Cu-Mg-Ca alloys, (3) determination of the phase diagram for the Cu-Ca-Mg system, (4) computation of the activity coefficient of neptunium in liquid magnesium, (5) study of the mechanism of the reduction of UO_2 by magnesium or calcium dissolved in their chlorides, (6) study of the reaction of PuO_2 with molten $MgCl_2$, (7) determination of the solubility of calcium in liquid $CaCl_2$, and (8) study of the radiolysis of solid $MgCl_2$-NaCl-KCl salt mixture.

Liquid metal systems. The dissolution of type 304 stainless steel in liquid zinc was studied by metallographic, electron microprobe, X-ray, and thermal analysis techniques. These studies suggest that the dissolution proceeds by the penetration of liquid zinc into the grains of the stainless steel and the preferential diffusion of nickel from the steel into the liquid zinc. Eventually, the stainless steel gamma phase becomes sufficiently depleted in nickel to transform into alpha iron. These alpha iron grains are dispersed in the liquid zinc.

The solubility of zirconium in a liquid 60 at. % Mg-40 at. % Cu alloy was found to vary from 0.09 at. % at 558°C to 2.9 at. % at 852°C. The equilibrium solid phase is a zirconium-copper intermetallic phase having the approximate composition $ZrCu_2$. The addition of calcium to the magnesium-copper alloy markedly decreases the zirconium content of the liquid phase. At about 850°C the zirconium solubility decreases from 2.9 at. % to 0.02 at. % as the calcium content increases from zero to 35 at. %.

The phase fields and approximate liquidus curves were determined for the Cu-Mg-Ca ternary system by means of metallographic, electron microprobe, X-ray diffraction, and thermal analysis techniques. The phase previously reported as Ca_4Cu was shown to be Ca_2Cu, and a new phase CaCu was found.

The activity coefficient of neptunium in dilute liquid magnesium solution was computed to be 23.3 at 650°C and 16.0 at 700°C. The solubility of neptunium in liquid magnesium is estimated to be 4.4 at. % at 650°C.

Molten salt systems. The reduction of UO_2 by magnesium or calcium dissolved in their chloride salts has been studied by a ceramographic technique. The rate of reduction was found to be directly proportional to the concentration of the reductant in the molten salt. The dependence of the reduction rate on temperature was small, which indicates that a transport-controlled reaction occurs. The products of the reduction reaction form concentric layers around partially reduced UO_2 pellets.

The dissolution of PuO_2 in molten $MgCl_2$ salts has been shown to involve the reaction

$$PuO_2 + MgCl_2 \rightarrow PuOCl + MgO + \tfrac{1}{2}\, Cl_2$$

The solubility of calcium in molten $CaCl_2$ in equilibrium with liquid Ca-Cu alloys has been measured as a function of the calcium content of the alloy and the temperature. The dissolution of calcium in $CaCl_2$ probably occurs by the reaction

$$Ca + CaCl_2 = 2\ CaCl$$

since this equation best fits the data, indicating that the calcium content of the $CaCl_2$ is proportional to the square root of the calcium activity in the liquid alloy.

Radiolysis of $MgCl_2$-NaCl-KCl. A solid salt consisting of $MgCl_2$-30 mol % NaCl-20 mol % KCl was irradiated for a total of 236 hr with a ^{60}Co gamma source at a dose rate of 3.6×10^{20} eV g^{-1} hr^{-1} at 28 and 58°C and a dose rate of 1.3×10^{20} eV g^{-1} hr^{-1} at 150°C. No gaseous chlorine was liberated from the salt. At a given temperature, the free chlorine and metal concentrations in the salt were found to increase linearly with absorbed dose. The highest yield for the radiolytic decomposition was observed at 150°C.

Fluidization and Volatility Processing

Research and development work was continued on fluoride volatility processes for the recovery of uranium and plutonium from fast breeder reactor fuels. In fluoride volatility processing, a fluorinating agent is reacted with fuel materials in fluidized-bed systems to produce the volatile hexafluorides of uranium and plutonium, which are separable from the nonvolatile fission product compounds. In the investigations reported here, emphasis was placed on the separation of uranium from plutonium in the fluorination step of a fluoride volatility process and the separation of plutonium from volatile fission product compounds.

The results of a conceptual design and evaluation study indicate that fluoride volatility methods have a good potential for LMFBR fuels. However, owing to a decision by the AEC to emphasize the development of aqueous reprocessing methods for this application, the program on fluoride volatility process development is being terminated.

Laboratory investigations

Fluorination of UO_2-PuO_2-fission product pellets. A 2-in. dia fluid-bed reactor was used to study the fluorination of uranium and plutonium from simulated liquid metal fast breeder reactor (LMFBR) fuels containing nonradioactive fission product oxides. In these studies, the UO_2-20 wt % PuO_2 fuel was usually first oxidized to U_3O_8-PuO_2 fines with oxygen. Uranium was then fluorinated to the volatile hexafluoride with dilute fluorine, and plutonium was subsequently fluorinated to the volatile hexafluoride with concentrated fluorine. Fast breeder reactor fuels were simulated by using a solid solution UO_2-20.0 wt % PuO_2 powder combined with a mixture of nonradioactive oxides of fission product elements representative of LMFBR core fuel with a burnup of 100,000 MWd/metric ton.

A fractional factorial series of five experiments was performed to determine how the plutonium content of the final fluidized bed was affected by oxidation of the fuel, by the time-temperature sequence in the plutonium fluorination step (4 hr at 400°C and 4 hr at 550°C or 4 hr at 500°C and 4 hr at 550°C), and by the rate of increase in fluorine concentration (high or low) during the first hour of the plutonium fluorination step. For this series of experiments, neptunium was also added to the initial fluidized bed as NpO_2 powder.

Plutonium concentration in the final fluidized-bed samples ranged from 0.09 to 0.21 wt %; these results corresponded to 0.9 to 2.2% of the plutonium charged. The statistical evaluation of the results indicated that the plutonium content of the final bed can be reduced by using an oxidation step, by increasing the fluorine concentration quickly at the start of the plutonium fluorination step, and by using 400°C rather than 500°C as the initial temperature in the plutonium fluorination step. Two replicate experiments demonstrated that operating conditions can be chosen that will reduce residual plutonium in the final fluidized bed to 1% or less of the plutonium charged.

The highest rates for plutonium fluorination were observed at the start of the plutonium fluorination period. The average rate of production for PuF_6 at 400°C was 2.2 lb/(hr)(ft^2) with the reactor operating at an average of 53% of equilibrium for the reaction, $PuF_4(s) + F_2(g) \rightleftarrows PuF_6(g)$. At 500°C the average rate was 2.4 lb PuF_6/(hr)(ft^2) at only 28% of equilibrium. An apparent activation energy of 8.6 kcal/mol was calculated from reaction rate data as a function of temperature for this series of experiments and a series of experiments reported in the preceding annual report (ANL-7575).

In the uranium fluorination step using dilute fluorine, NaF product traps were used to collect UF_6 product. High U/Pu ratios of 5280 and 3700 (indicating good separation of uranium from plutonium) were obtained in runs in which the traps were taken off-stream as soon as fluorine was detected in the reactor off-gas. When excess fluorine was present in the off-gas, indicating that most of the uranium had been fluorinated, plutonium was also fluorinated from the fluid-bed reactor. These results show that an initial separation of uranium from plutonium could be obtained by a suitable choice of operating conditions. About 1.7% of the uranium charged was fluorinated with the plutonium during the plutonium fluorination step. Most of the molybdenum appeared to be fluorinated during the uranium fluorination step, while ruthenium and neptunium were fluorinated during both fluorination steps.

The final fluidized beds contained about 1 to 2% of the neptunium charged, 5 to 18% of the ruthenium charged, and $\leq$0.1% of the uranium charged. Calculations indicate that conversion of Al_2O_3 to AlF_3 during 10 to 20 hr of fluorination ranged from 6.9 to 10.3%.

Fission product chemistry. Chemical and thermogravimetric investigations indicated that oxyfluorination reactions of fission products are of a complex nature and that for some fission product elements, volatile oxides and oxyfluorides form, as well as volatile binary fluorides. In addition, catalytic effects seem to be of importance—for example, the formation of RuO_4 appears to be catalyzed by F_2. The following are proposed for the reaction of RuO_2 with 10:1 oxygen-fluorine mixtures:

$$1.\ (a + b)\ RuO_2 + (O_2\text{-}F_2) \begin{cases} \nearrow aRuF_5 \\ \searrow bRuO_4 \end{cases}$$

$$2.\ bRuO_4 \rightarrow bRuO_2 + O_2$$

$$3.\ bRuO_2 + (O_2\text{-}F_2) \begin{cases} \nearrow cRuF_5 \\ \searrow (b - c)RuO_4 \end{cases}$$

in which RuO_4 is a recurring intermediate and a, b, and c are numbers of molecules.

Decontamination of plutonium hexafluoride. Bench-scale studies were carried out to test the proposed separation of ruthenium from plutonium by preferential condensation of ruthenium fluoride at −10°C. If the ruthenium product produced by fluorination of irradiated nuclear fuel is RuF_5 only, adequate separation of ruthenium from PuF_6 at −10°C is predicted because of the large difference in vapor pressures of the pure materials at this temperature.

Mixtures of PuF_4 and ruthenium metal were fluorinated, and the resulting gaseous mixture was passed through a cold trap at −10°C and then through a cold trap at −78°C. The quantities of ruthenium penetrating the −10°C trap were small fractions of the total ruthenium, but nevertheless were several orders of magnitude greater than the quantities that would have penetrated if the solid species in the trap had been RuF_5 only. Comparison of the quantities of ruthenium in the exit gas from the −78°C cold trap with the theoretical quantities for various ruthenium species (calculated from vapor pressures) indicated that the small, more volatile fraction may be RuO_4.

The removal of PuF_6 from process gas streams by reaction with LiF has been proposed. The reaction is also of interest because of its potential for the separation of PuF_6 from volatile fission products such as ruthenium fluoride. The products of this reaction are the solid complexes $LiPuF_5$ and Li_4PuF_8. Since the subsequent recovery of plutonium from these complexes is important to the economics of plutonium processing, the effects of temperature, partial pressure of fluorine, and partial pressure of PuF_6 on the rates of fluorination of these complexes have been studied. The rates of fluorination of both $LiPuF_5$ and Li_4PuF_8 with fluorine to produce volatile PuF_6 were found to be represented by the equation $FW_0 = kt$, where F is the fraction of PuF_4 reacted in time t, k is the rate constant, and W_0 is the initial weight of PuF_4 in the complex. The dependence of rate constants on temperature over the range 350 to 450°C yielded activation energies of 12 kcal/mol for the fluorination of $LiPuF_5$ and 10 kcal/mol for the fluorination of Li_4PuF_8, both with fluorine at 1 atm. The dependence of the rate constants on the partial pressure of fluorine was found to be essentially of first order in the range 0.3 to 1 atm. The results of the reactions of the complex solids with PuF_6-fluorine mixtures indicated a justification for ignoring the back reaction in the treatment of the rates of reaction of the complexes with pure fluorine. From the reaction rates obtained by reaction of PuF_6-fluorine mixtures with Li_4PuF_8 at 400°C, the equilibrium constant p_{F_2}/p_{PuF_6} for the reaction $Li_4PuF_8 + F_2 \leftrightarrows PuF_6 + 4\ LiF$ was calculated to be between 1.3×10^3 and 1×10^3.

Ultraviolet-activated synthesis of PuF_6. Plutonium hexafluoride was produced at room temperature by ultraviolet irradiation (3125 Å) of the system: solid PuF_4-gaseous fluorine (300 Torr). The apparent yield was 4×10^{-3} molecules per quantum.

Engineering-scale investigations

Conceptual fluoride volatility process for fast-reactor fuels. A conceptual design study of a large fluoride volatility plant (with a capacity for handling one metric ton of actinides per day) for processing fast breeder reactor fuels was completed. Such a facility would service power plants with a total capacity of about 15,000 MW(e). The reference fuel is stainless steel-clad UO_2-PuO_2.

The reference process, though not optimized, has a high potential for handling short-cooled fuel, as well as considerable flexibility in processing fuel materials with a wide range of concentrations of fissile material. The study concludes that a substantial body of basic and technological information is available that supports this application of fluoride volatility processing to LMFBR fuels. Key problems are outlined that represent the basis for a research and development program.

The technique of developing reference process and plant designs without initially considering optimization and economics appears to be a valuable technique for assessing the potential of processes for nuclear fuels and other chemicals.

Continuous-feed, two-stage, slab fluidized-bed reactor. Testing of fluid-bed systems was continued in support of the fluoride volatility concept study (Section I.B.2.a of this report). The fluorination steps in the conceptual process are to be performed continuously in 4-in.-thick, slab-shaped, fluidized-bed reactors, which are designed to meet heat transfer and criticality requirements. Since no information was available on the design and operation of reactors with this thickness, an exploratory study was initiated.

Initial work was done with a column having a 4-in.-square cross section. A technique was developed for achieving continuous downward solids flow through the orifice that admits the fluidizing gas, thereby avoiding the use of downcomer pipes. Single-stage and two-stage columns were tested, each stage having an inverted-pyramid-shaped gas inlet section. With the appropriate combination of gas-inlet orifice size (0.5-, 0.75-, and 1-in. dia) and gas velocity, solids flow rates through the reactor of 10 to 9000 lb/(hr) (ft^2) were achieved. With a variable-position plug inserted above the orifice, control over solids flow rate was improved.

A two-stage, slab-shaped, fluidized-bed column of 4-in. by 24-in. cross section and having six gas-inlet sections was mocked up of Lucite and tested qualitatively—i.e., solids flow and the quality of fluidization were observed. Countercurrent flow of solids through the gas orifices could not be stabilized, indicating the need for some improvement in design.

A two-stage column of 4-in. by 24-in. cross section was fabricated, which incorporated (1) a weir section for overflow of solids from the upper stage to the stage below and (2) flat drilled-plate gas distributors. Re-

sults for this design indicate that slab shapes should prove satisfactory for fluid-bed reactors.

Pulsed-bed studies. Studies were continued on the pulsed-bed approach to fluidization. Pulsed beds are obtained by controlled, intermittent upflow of gas through a bed of solid particles, causing the bed to expand; the bed contracts during the period when the gas flow is shut off. A unique characteristic of pulsed beds is that good particle motion exists below the minimum fluidization velocity. Heat-transfer rates from an internal surface to a pulsed bed were determined under a series of pulsing conditions. Data were obtained using four sizes of glass beads, ranging from 73 μm to 580 μm (average diameter). For operation with large sizes of particles and heavier particles, heat-transfer rates are higher in pulsed beds than in conventional fluidized beds. A model for the heat-transfer mechanism in gas-solid particle systems has been proposed, which can be used to estimate heat-transfer coefficients in pulsed beds.

Dense-phase transport of granular solids. Dense-phase transport of granular solids through pipelines is a technique that may have application in nuclear fuel cycles. The results of recent exploratory studies indicate that solids typical of those contemplated for use in fluoride volatility processes can be transported by this technique. A mocked-up system consisting of a 20-liter pressurized solids feed vessel, a ⅜-in.-ID, 55-ft-long polyethylene transport line, a solids collection vessel, and gas-flow instrumentation was used to investigate the characteristics of this transport technique. Solids flow rates of 127 to 694 g/min for nominally 48 to 100 mesh alumina were achieved with motivating air pressures of 40 to 60 psig in the solids feed vessel. The solids-to-gas ratios for this method of transport are much higher than for conventional pneumatic transport of solids.

Alpha facility maintenance and cleanout. Useful information on the durability of gloves has been obtained during operation of the engineering-scale alpha facility. Deterioration of seamless, milled-neoprene gloves occurred, mainly in the form of cracking at folds and creases after relatively long periods when the gloves were not used. Polymer-coated neoprene gloves were superior to uncoated neoprene gloves in this regard and showed resistance to deterioration from room illumination and ozone attack. Little damage to gloves due to abrasion or wear was evident, even at locations in the box where fairly heavy mechanical work had been performed. Recommendations are that gloves be left fully extended when not in use, and that, as a minimum, gloves be inspected annually.

Cleanup and decontamination of the engineering-scale alpha facility is planned for FY 1970 as part of the phasing-out of the fluoride volatility program in the Chemical Engineering Division. The large and small gloveboxes were cleared of equipment, and decontamination work is in progress. The gloveboxes will be left in a clean, safe standby condition.

Basic mechanisms of fluidization

Fluidized-bed heat transfer. As a first step in investigating the complex mechanism of heat transfer in a fluidized bed, the rate of heat transfer to the bed as a function of fluidized-particle residence time at a heater surface was considered. Two aspects of this problem were studied: (1) the case of infinite particle residence time (the bed at minimum fluidization with little or no particle motion) and (2) the case of finite particle residence time (the bed fluidized with particles in motion).

A model was proposed which describes heat transfer from a heater to a bed of particles for gas flow through the bed equal to that required for minimum fluidization. It was assumed in this model that all of the heat is removed by the flowing gas. Predicted heat-transfer coefficients for both cylindrical and flat heaters were in good agreement with experimentally determined heat-transfer coefficients.

Two other models were proposed for unsteady-state heat transfer from a wall to particles moving within a fluidized bed. One model was based on a bed of spheres in orthorhombic array, and a second, simplified model approximated a bed of spheres by a series of alternating slabs to represent the gas and solid phases of a fluidized bed.

Numerical analyses showed good agreement between models. Good agreement between theory and experiment was also obtained.

Preparation of Fuel Materials

Oxidation of uranium to UO_2 in a fluidized bed. Stoichiometric UO_2 of low carbon content was prepared in a fluidized-bed reactor by oxidation of uranium at 750 to 825°C with CO_2 in helium or nitrogen diluent. Prior to oxidation, the bulk uranium (~300 g per run) was hydrided to produce a fine powder and then partially nitrided. The carbon content of the UO_2 product of one run was less than 100 ppm, which is within current specifications. In runs in which the nitriding step was omitted, the products contained up to 1.5 wt % carbon as a result of carbon deposition during the rapid initial reaction of uranium metal with CO_2.

Conversion of FBR oxide fuel to carbide fuel. Studies of the use of a plasma torch for the conversion of FBR oxide fuel to carbide fuel have been initiated.

The current work is devoted to the conversion of uranium oxide to uranium monocarbide, but the process is expected to be applicable to the production of (U-Pu)C in equipment installed in an alpha-tight enclosure. The present objective is to determine the operating conditions required to produce high yields of reactor-grade uranium monocarbide in order to assess the feasibility of a continuous production process using a plasma-torch reactor.

A 25-kW, inductively heated plasma-torch reactor has been installed. Preliminary experiments were conducted with uranium dioxide-graphite agglomerates (~100 mesh particles). The agglomerated particles (containing 8.7 wt % C) were fed into the plasma flame at 0.6 to 0.9 kg/hr. The operating conditions were those that had earlier been established to be the optimum for spheroidizing crushed alumina. The carbon content of the UC product from these experiments ranged from 5.0 to 6.5 wt %, whereas the carbon content of UC is 4.8 wt %. However, the oxygen content of the product was near that in the feed, indicating that the hot particles emanating from the plasma torch had reacted with atmospheric oxygen in the reaction chamber. Equipment modifications are under way whereby an atmosphere of argon can be maintained in the reaction chamber and oxygen excluded.

II. Sodium Technology (pages 62 to 73)

Beginning with FY 1970, the ANL program in sodium technology was expanded. The major objectives of this program are to (1) provide base sodium technology support to EBR-II and other ANL-operated national test facilities, (2) demonstrate selected processes and equipment, with EBR-II being used as a test facility for the advanced equipment and procedures that are being developed for subsequent LMFBRs, and (3) advance sodium technology in selected fundamental areas of sodium chemistry and materials compatibility. The ANL program includes work in the following areas: sodium chemistry, sampling and analysis of sodium, sodium purification and monitoring of sodium purity, fission product behavior and control, behavior and monitoring of cover gases, and materials compatibility. Most of the materials compatibility work is carried out in the Materials Science Division and is not reported here.

Sodium Chemistry

Decarburization of iron-carbon alloys and ferritic steels in sodium is believed to involve the formation of disodium acetylide (Na_2C_2). As part of a program to test this concept, the acetylide content of sodium equilibrated with an Fe-0.11 wt % C alloy was determined at 400 and 650°C. Significant loss of carbon from the alloy and significant amounts of acetylide in the equilibrated sodium were found at both temperatures. Moreover, the levels of acetylide were invariant with time, suggesting that an equilibrium or steady-state concentration was established.

The stability of Na_2C_2 in sodium is being determined. High-temperature X-ray powder diffraction patterns have shown that acetylide undergoes a transition from tetragonal to cubic structure at 275°C, and that the cubic modification is stable to at least 450°C.

The solubility of helium in sodium was measured as a function of temperature and pressure. Between 350 and 550°C, the solubility, in terms of the Ostwald coefficient λ (volume of helium dissolved per unit volume of sodium), can be represented by the equation $\log \lambda = 0.511 - 3070\ T^{-1}$, where T is in degrees Kelvin. The heat of solution calculated from this equation is 13.0 ± 0.4 kcal/mol. Helium solubility was shown to obey Henry's law at 500°C over the pressure range 2 to 9 atm; a Henry's law constant of 1.56×10^{-7} atm^{-1} was obtained.

To elucidate the role of surface diffusivity in mass transfer in sodium systems, samples of α-iron were heated in liquid sodium at 800°C for different lengths of time, after which the surfaces were examined by interference microscopy. Well-developed grain-boundary grooves were observed. Preliminary analysis of the groove profiles and their growth rates has shown that surface diffusion is an important mechanism in the corrosion of α-iron by liquid sodium, and that surface diffusion proceeds more rapidly in a liquid sodium environment than in vacuum.

A study to establish the morphology of sodium oxide crystallites and the kinetics of their growth in sodium has been started.

Sodium Analytical Development

A center for sodium analytical chemistry, with the responsibility for coordinating analytical developments in the national LMFBR Sodium Technology Program, has been organized in the Chemical Engineering Division. This responsibility includes assessing the analytical needs of the various laboratories and organizations in the national program, and then satisfying these needs with certified standard analytical procedures. Certification of standard methods is expected to involve either evaluation and improvement of existing analytical methods or development of new ones.

Prior to the formation of the center, the analytical effort was mainly concerned with the use of the Sodium Analytical Loop (SAL) to evaluate and calibrate on-line instruments for sodium analysis. It was found that a dip-sampling technique was superior to line-sampling, and that oxygen analyses of dip samples gave reliable results. Two United Nuclear Corporation (UNC) oxygen meters were calibrated on the SAL and subsequently sent to EBR-II for use. The SAL, originally located in the Reactor Engineering Division, was shut down, moved, and rebuilt in the Chemical Engineering Division, where it is once again in operation.

Sodium Engineering

Work has been initiated on the development, testing, evaluation, and improvement of on-line monitors for impurities in sodium. The on-line monitoring work includes the prooftesting of meters for oxygen, carbon, and hydrogen activities in sodium. The United Nuclear Corporation (UNC) electrolytic cell for oxygen and the UNC diffusion meter for carbon are both under test. The most reliable models of these meters that are developed will be installed in the Radioactive Sodium Chemistry Loop (RSCL) being constructed for the primary sodium system at EBR-II. A hydrogen diffusion meter is being developed to determine hydrogen activity in sodium, particularly in connection with the detection of water leaks into sodium in LMFBR steam generators. The meter will employ a nickel diffusion membrane in the sodium and a mass spectrometric detector on the vacuum side of the membrane.

The technical problems in LMFBR plant operation that result from the release of fission product activity from the fuel elements into the sodium coolant are being defined. Preliminary results of this continuing calculational study indicate the importance of investigating the behavior of short-lived fission products.

A study of the nature and control of aerosol formation in sodium is being undertaken. In the initial experiments, sodium aerosols will be formed, visually observed, sampled, and analyzed to determine aerosol-mass concentration.

III. Materials Chemistry and Thermodynamics (pages 74 to 100)

High-Temperature Thermodynamic Studies

The mass-spectrometric Knudsen effusion study of the plutonium, plutonium monoxide, and plutonium dioxide partial pressures over two-phase Pu_2O_3-$PuO_{1.61}$ has been completed. The three gases are assumed to result from the reactions

$$7.33\ Pu_2O_3(s) = 13.66\ PuO_{1.61}(s) + Pu(g)$$
$$2.77\ Pu_2O_3(s) = 4.54\ PuO_{1.61}(s) + PuO(g)$$
$$4.54\ PuO_{1.61}(s) = 1.77\ Pu_2O_3(s) + PuO_2(g)$$

with heats of reaction of 110.0, 118.4, and 132.0 kcal/mol, respectively. Measurements of the partial pressures of the vapor species over $U_{0.8}Pu_{0.2}O_{2-x}$ have been initiated.

The metal-rich boundary of the U-Pu-O fluorite phase has been established from 1868 to 2168°C for a uranium-plutonium mixed oxide containing 19.8 at. % plutonium. Measurements at other plutonium concentrations and at the oxygen-rich boundary are in progress.

Vapor transport experiments are being carried out to establish the conditions required for fission product iodine attack on stainless steel cladding of nuclear fuel. The oxygen activity in the fuel determines the extent to which fission product cesium reacts with the fuel, thus freeing iodine from CsI.

The ultrahigh-vacuum Knudsen effusion system has been modified to accept a quadrupole mass spectrometer. Measurements are in progress to establish relative ion cross sections of uranium and uranium oxide molecules. Plutonium compounds will be studied after completion of the present investigations.

The new high-temperature transpiration equipment is being tested by measuring O_2 and UO_3 pressures over UO_{2+x} and U_4O_9-U_3O_8 prior to studies of the Pu-O and U-Pu-O systems.

The pressures of plutonium gas over the two-phase regions Pu_2C_3-C, Pu_2C_3-PuC_2, and PuC_2-C have been measured mass-spectrometrically. Heats of reaction of 97.6, 118.7, and 88.3 kcal/mol, respectively, were established for the reactions

$$\tfrac{1}{2}\ Pu_2C_3(s) = \tfrac{3}{2}\ C(s) + Pu(g)$$
$$2\ Pu_2C_3(s) = 3\ PuC_2(s) + Pu(g)$$
$$PuC_2(s) = 2\ C(s) + Pu(g)$$

Carbon activities over the U-C system have been measured over C/U ratios of 0.98 to 1.85 at temperatures from 1882 to 2282°C. These data, when combined with literature values for uranium activities, yield heats of formation at 298°K of -22.6 ± 0.5 and -23.7 ± 1.0 kcal/mol for $UC_{1.00}$ and $UC_{1.85}$, respectively.

Reactor Safety and Physical Property Studies

Three calorimetric systems for the measurement of high-temperature enthalpy increments by the method

of mixtures are in operation. These systems complement each other; one uses resistance heating for temperatures to 1600°K, a second uses electron beam heating for temperatures to 2500°K, and the third uses induction heating for temperatures to 3600°K.

Enthalpy data from the first two calorimetric systems are reported for UB_2, Na_3Bi, UO_2, and Al_2O_3 (N.B.S. standard sapphire) in the temperature range 600 to 1500°K. The enthalpy of fusion of Na_3Bi has been determined also.

The induction-heated calorimetric system was used to measure the enthalpy of uranium dioxide to 3475°K. Values were determined for the heat of fusion and the heat capacity of molten uranium dioxide. At present, the equipment is being modified for use with $(U,Pu)O_2$.

A program has been initiated to provide high-temperature vapor pressure data for reactor fuels in order to reduce the extent to which presently available data must be extrapolated in reactor safety calculations. A high-temperature transpiration apparatus has been built and tested with apparent success in determining the vapor pressure of stoichiometric urania at 2600°K. The full range of the program calls for measurements extending to temperatures beyond the melting point of UO_2.

Studies have been initiated to obtain spectroscopic properties of gaseous oxides of uranium from which thermodynamic properties at high temperatures may be calculated. The purpose of the research is to provide data needed by the reactor safety program to predict vapor pressures within fuel pins under reactor accident situations. By employing the technique of matrix-isolation infrared spectroscopy, one is able to obtain high-resolution spectra of species that are present in measurable concentration in the gas phase only at very high temperatures. Future studies will also include visible and ultraviolet spectroscopic investigations of these species so that information about thermodynamically important low-lying electronic states can be obtained.

A calculational scheme has been devised to determine the contributions of fission product and fuel components to the internal pressure of a fuel pin, under both normal operating and hypothetical accident conditions. Although sufficient thermodynamic data exist to carry out simplified calculations for fuel pin temperatures up to 2500°K, very few data are available for the higher temperatures (4000–8000°K) of interest to reactor safety analysts. Because these data cannot be obtained directly by experimental means, studies are being undertaken to find a suitable theoretical basis on which to extrapolate existing low-temperature data.

Work has begun to measure the speed of sound in liquid sodium, liquid uranium dioxide, and other molten materials of importance to reactor safety. Electronic equipment and a suitable furnace for these measurements have been acquired. At present some cell and furnace modifications are in progress.

Studies of migration of plutonium in a thermal gradient (~1000°C/cm) for metal oxide fuels were continued. Previous experiments utilizing slightly hyperstoichiometric (O/M = 2.01) mixed oxide gave indications of enhancement of plutonium concentration at the hotter end of the specimens; similar experiments employing hypostoichiometric materials (O/M = 1.97) showed no significant plutonium concentration changes. Plutonium migration studies were also initiated using $(U_{0.85}Pu_{0.15})C$ pellets.

Calorimetry

Calorimetric measurements of the low-temperature thermal properties from 1 to 350°K, enthalpy of formation at 298°K, and high-temperature enthalpy increments from 600 to 1500°K of uranium diboride have been completed in a cooperative effort with other ANL scientists. In other studies on uranium compounds, work has been started on the determination of the enthalpy of formation of $US_{1.9}$ (tetrag.).

In a continuing program to provide accurate thermochemical data for plutonium compounds, the standard enthalpy of formation of plutonium monocarbide has been determined to be $\Delta Hf^{\circ}_{298}(PuC_{0.878\pm0.001},c) = -11.53 \pm 0.64$ kcal mol^{-1}. If a sample now being prepared at Los Alamos Scientific Laboratory turns out to be suitable, measurements will also be carried out on Pu_2C_3.

As part of an effort that has been going on for some years to clear up the uncertainties in the thermochemistry of hydrogen fluoride, (1) the enthalpy of formation of liquid hydrogen fluoride was determined by direct combination of the elements in a calorimeter, and (2) the enthalpy of solution of liquid hydrogen fluoride in water was measured in the dilution range $HF \cdot 2OOH_2O$ to $HF \cdot 5551H_2O$.

Measurements of the energy of combustion of $N{\equiv}SF_3$ in fluorine yielded $\Delta HF^{o}(NSF_3)$; the latter result, combined with mass spectrometric appearance potential data, gave the enthalpy of formation of $N{\equiv}SF$ and the $N{\equiv}S$ bond strength in both NSF_3 and NSF. Values were also deduced for $\Delta Hf^{\circ}_{0}(NS)$ and $\Delta Hf^{\circ}_{0}(NS^{+})$. A Hartree-Fock-Roothaan *ab initio* calculation for NS yielded an ionization potential, based on Koopmans' theorem, within 3% of the experimental value.

Several years ago, an oxygen bomb calorimetric study of the energy of combustion of MoS_2 was car-

ried out at this laboratory. However, because the chemical processes in the bomb were difficult to define, a reliable result could not be obtained. A determination of $\Delta Hf^o(MoS_2)$ by combustion in fluorine has now been completed.

Miscellaneous fluorine bomb calorimetric studies are reported for SiC(hex.), SiC(cubic), PF_3(gas), IF_5(l), IF_7(gas), B_2O_3(c), and B_2O_3(amorph.). The last two compounds were also studied by solution calorimetry in aqueous media.

The solution calorimeter was also used to study (1) the reaction between aqueous XeO_3 and aqueous HI and (2) the reaction between crystalline I_2 and aqueous HI. These studies resulted in a precise value for $\Delta Hf^o(XeO_3,\text{aqueous})$.

The recent discovery in the Chemistry Division of preparative methods for perbromates leads logically to a study of their stability relative to the bromates. The enthalpies of decomposition of $KBrO_4$ and $KBrO_3$ to KBr and O_2 were measured in a bomb calorimeter. Those measurements yielded values for $\Delta Hf^o(KBrO_4)$ and $\Delta Hf^o(KBrO_3)$. The compounds were also studied in the solution calorimeter to obtain enthalpies of formation of the aqueous perbromate and bromate ions.

In connection with the sodium-cooled reactor program, methods for the determination of the enthalpy of formation of Na_2C_2 are being explored. Na_2C_2 is of interest because it has been postulated that it is the species responsible for carbon transport in liquid sodium systems.

IV. Analytical and Reactor Chemistry (pages 101 to 123)

Chemistry of Irradiated Fuels and Materials

The program to study the chemical behavior of irradiated fast reactor fuels has continued. Shakedown tests of a helium-atmosphere cave facility in the Chemistry Division have been completed. The moisture and oxygen levels of the helium atmosphere (0.5 and 5 ppm, respectively) are lower than design specifications.

An analytical technique combining laser-beam sampling and spark-source mass spectrometery was found to have limited applicability to the study of the microstructure of irradiated fuels. Work was recently initiated on the development of a method for microsampling and analysis of fission product gases retained in irradiated ceramic fuels.

Electron microprobe studies have continued, with principal emphasis being placed on the study of fuel-cladding interactions. Examination of a UO_2-20 wt % PuO_2 fuel pin irradiated in EBR-II to 3.7 at. % burnup showed that (1) an interaction had occurred between the fuel and the type 304 stainless steel cladding, (2) fission product iodine was present at the fuel-cladding interface, and (3) iron from the cladding had been transported into the fuel matrix. A postulated mechanism for this reaction is discussed. Examination of a UC-20 wt % PuC fuel pin irradiated in EBR-II to 6.9 at. % burnup showed that an interaction had also occurred between the carbide fuel and the type 304 stainless steel cladding, but to a lesser extent than in the UO_2-PuO_2 fuel. In the carbide fuel, nickel from the cladding had been transported into the carbide matrix. Possible mechanisms for the nickel transport are presented.

In the program to develop methods for identifying the position of fuel failure in EBR-II by means of sodium-soluble tags, two tagging methods have been devised. In one method, each fuel element in a subassembly would be tagged with the same mixture of ^{121}Sb and ^{197}Au; the weight ratios would be varied to produce multiple tags. In the event of fuel failure, the tags would be released to the primary sodium coolant. The sodium would be assayed gamma spectrometrically for the tag activation products ^{122}Sb (2.8 days) and ^{198}Au (2.7 days), and the ratio of these activities would identify the faulty subassembly. The second method, which utilizes mixtures of ^{197}Au and ^{198}Pt, would operate on the same general principles, and tag identification would be made on the basis of the ratio $^{198}Au/^{199}Au$. The ^{199}Au (3.15 days) is produced by beta decay of the platinum activation product ^{199}Pt.

Insufficient funding has required the termination of the sodium-soluble tagging program; however, these proposed methods may find application in future fast reactors.

Xenon Tagging of Fuel Elements in EBR-II

A xenon-tag method for the identification of failed fuel elements is being used in EBR-II with experimental fuel elements. Each fuel element in a subassembly is tagged with 1 ml of a mixture of xenon isotopes which is unique for that subassembly. In the event of cladding failure, mass-spectrometric analysis of the reactor cover gas will permit rapid identification of the affected subassembly and its location in the reactor. This rapid identification should enhance the EBR-II plant factor.

Eighteen tag mixtures have been prepared by blending light-isotope-enriched xenon with natural xenon. Twenty-three additional tag mixtures can be made by blending available enriched mixtures and by adding

natural xenon to some of the blends. A larger number of tag mixtures can be prepared by blending available xenon mixtures with pure ^{128}Xe; a contract has been awarded for preparation of ^{128}Xe by thermal irradiation of ^{127}I. Three methods of adding a tag to a fuel element have been developed and used.

The effect of a xenon tag upon the thermal conductance of the fuel-to-cladding gap is being examined further; an instrumented subassembly has been prepared which will allow a study of the conductance to be made over a range of power levels in EBR-II.

A cover-gas sampling system has been developed and a mass spectrometer procured for identification of a released tag. The spectrometer incorporates a dual collector system and three sample inlet modes to permit rapid tag identification for a variety of sample conditions.

Fast-Reactor Cross-Section Measurements

Measurements of cross sections for materials of interest to the fast breeder reactor program are continuing. Principal effort is being devoted to determining cross sections in the broad neutron energy spectrum of EBR-II. Irradiations of various materials (monitors) such as stainless steel, scandium, and gold, have provided activation-rate data necessary to calculate the neutron flux in EBR-II as a function of radial position. These flux values have been used, along with appropriate activation rate data, to determine spectrum-averaged cross sections for other reactions in EBR-II.

A discussion is presented of the feasibility of using the ratio of the reaction rates of the $^{54}Fe(n,p)^{54}Mn$ and $^{54}Fe(n,\gamma)^{55}Fe$ reactions as an indicator of neutron spectral shape (spectral index). Such an index would be extremely valuable in correlating spectrum-averaged cross sections obtained in different reactor positions or in different reactors.

Capture-to-fission ratios (alpha) for samples of ^{233}U and ^{239}Pu irradiated in EBR-II are presented as a function of radial position in EBR-II. The status of the experimental program to measure the fast-fission yields of low-mass particles (tritium, hydrogen, helium) is also described.

Determination of Burnup of Fast Reactor Fuels

A method is under development for the measurement of burnup in fast reactor fuels by X-ray spectrometric assay of the four principal rare earth fission products: lanthanum, cerium, praseodymium, and neodymium. The procedure consists of the following steps: (1) terbium is added as an internal standard, (2) the rare earth fission products and terbium are separated from interferences by anion exchange, and (3) the separated rare earths are electroplated on a metal plate and assayed by X-ray spectrometry by means of line-intensity ratios (rare earth-to-terbium internal standard).

The procedure was tested in two experiments. In the first, a standard mixture of rare earths was taken through the entire procedure. In the second, the rare earth mixture was spiked with uranium and the other major fission product elements (to simulate a 1 at. % burnup sample). These tests revealed no major difficulties in the procedure, although minor refinements are needed to achieve the desired accuracy of $\pm 1\%$. The analysis of a sample of highly irradiated UO_2 ($\sim$6.5 at. % burnup) was in good agreement with analyses of the same sample by several other methods.

A new method is being developed for determining the number of fissions that have occurred in fast reactor fuel. This method is expected to provide a means for determining fast fission yields more easily than existing methods and with comparable accuracy. Two irradiations are required: one of about 2-hr duration and one of about 3-month duration. The short (calibration) irradiation establishes a factor relating the number of fissions to the activity of a particular fission product (e.g., ^{144}Ce). The number of fissions in the long irradiation is then established from the ^{144}Ce activity and the previously determined factor. An evaluation of this approach, which was made in work supporting an experiment of the Reactor Physics Division, has demonstrated its feasibility.

V. Chemistry of Liquid Metals and Molten Salts (pages 124 to 164)

An important area of scientific and technological interest is that devoted to the chemistry and thermodynamics of liquid metals, alloys, and molten salts. The continuing programs in this area include studies of the thermodynamic behavior of various systems as expressed by liquid-solid phase diagrams, liquid-phase activity coefficients, vapor-liquid equilibria, and solubilities of various gases and solids in liquids. Recently, greater interest has developed in transport properties, especially those relating to the transport of both charged and uncharged species in molten phases. Continuing investigations of the structure of liquid metals and molten salts have been made primarily by ultrasonic methods and Raman spectroscopy. The studies of electrochemical energy conversion by means of cells with liquid metal electrodes and molten-salt electrolytes have led to the development of cells which show promise for energy storage. New programs in the areas

of cell scale-up and battery design, construction, and evaluation have been initiated as a result of funding from various government departments.

Liquid Metals Studies

The studies on the sodium-bismuth system have continued with the extension of the quasi-ideal solution theory to the calculation of the liquid-solid phase diagram. Good agreement between calculated and observed phase boundaries was obtained when a value of 11.1 kcal/mol was used for the heat of fusion of Na_3Bi. However, when the recently measured value of ~7 kcal/mol is used in the calculations, the Na_3Bi phase boundaries lie well below the experimentally determined boundaries. This disagreement between theory and experiment is being investigated further.

The experimental studies of the vapor-liquid equilibria in the lithium-tin system have been completed, and a vapor-liquid temperature-composition diagram for a pressure of 0.7 Torr has been constructed. This diagram shows that excellent separation of lithium from lithium-tin alloys can be achieved at a pressure of 0.7 Torr, a conclusion of importance in the design of thermally regenerative galvanic cells.

The thermodynamics of the lithium-selenium system is being investigated by emf, thermal analysis and other techniques. The emf measurements have yielded values for the activity coefficient of lithium in selenium as a function of concentration and temperature, and approximate locations for liquid-liquid and liquid-solid phase boundaries. These results, coupled with those from thermal analysis and microscopic examination of quenched samples, have permitted the construction of a partial phase diagram for the lithium-selenium system showing the presence of the very stable compound Li_2Se and a large liquid-liquid immiscibility region. Initial investigations of the phase diagram of the lithium-sulfur system indicate that it is likely to be similar to the lithium-selenium phase diagram.

The solubilities of Se, Li_2Se, and Li_2S in molten lithium halide mixtures were measured over a range of temperatures. The solubilities of Se and Li_2S are in the range from 0.02 to 0.2 mol % at 350 to 550°C, whereas the solubility of Li_2Se is 2 to 6 mol % at 500 to 700°C. In general, addition of LiI to the fused-salt phase caused an increase in the heat of solution values observed.

A model for predicting gas solubilities in liquid metals has been prepared. The model successfully accounts for the molar excess Gibbs free energies of solution of noble gases (He, Ar, Kr) dissolved in sodium at 400°C.

The principle of corresponding states, which provides a relationship between the surface tension of a liquid at absolute zero (γ_0), the critical molar volume (V_c), and the critical temperature (T_c), was demonstrated not to be in accord with available critical data for mercury or the alkali metals. A new empirical equation of the form $\gamma_0(V_c - B)^{2/3} = AT_c$, where A = 1.67 erg/(°K) (mol$^{2/3}$) and B = 31 cm^3/mol, was developed which does relate γ_0, V_c, and T_c for these metals. This relationship was used to estimate T_c and V_c for a variety of other liquid metals.

The electronic conductivities of liquid semiconductors such as selenium and sulfur are being investigated. Our measurements indicate that Group V and VII dopants (such as phosphorus and iodine) increase the conductivity of selenium and sulfur more than Group VI dopants (such as tellurium). These studies are expected to aid in the formulation of a theory of liquid semiconductors.

The absorption of sound (135 MHz) in liquid gallium was measured between 100 and 500°C. The absorption was anomalous in the same regions where the density, viscosity, and surface tension exhibit discontinuities.

Molten Salt Studies

In the area of molten salts, the studies of thermodynamics have been concerned primarily with phase diagrams of systems containing lithium halides. The binary systems LiI-KI and LiI-RbI have been studied by thermal analysis methods; the experimental results agree well with theoretical predictions. The melting point of the LiI-RbI eutectic was found to be 252°C; this electrolyte should, therefore, be useful for low-temperature electrochemical studies. A minimum melting point of 184°C was found in the system LiCl-LiBr-LiI-KI-CsI; this is the lowest temperature that has been reported for a molten alkali halide mixture.

Structural studies of fused salts and other molten systems have been carried out by laser-Raman spectrophotometry. The spectra of P_4S_3 and P_4S_{10} (as solids and liquids) indicate that their structures are based upon P_4 tetrahedra, with single sulfur atoms located between phosphorus atoms (P_4S_{10} and P_4S_3), and terminally on the corners of the P_4 tetrahedra (P_4S_{10} only). The terminal sulfur atoms tend to become dissociated from the P_4 cage in the liquid phase. The Raman spectra of molten MgI_2-KI mixtures supplement similar studies reported earlier (ANL-7575) for the corresponding bromide and chloride systems, and support the conclusion that the ion MgX_4^{-2} (where X is Cl, Br, or I) exists in significant concentrations (>10 mol %) in these melts. The Raman spectra of molten carbonates are reported for the first time. The structure and behavior of the carbonate ion was found to be very

similar to that of the nitrate ion, with respect to the influence of the alkali metal cation environment on the molecular vibrations of the anion.

Energy Conversion Studies

The investigations of new liquid-metal, fused-salt electrochemical cells for energy storage and conversion have continued. New sulfur- and phosphorus-containing cathodes have been investigated, including pure sulfur, P_4S_{10}, and P_4S_3. These cells have proved capable of delivering power densities of 7.5 W/cm^2 for short periods of time and energy densities of at least 0.3 W-hr/cm^2 over longer periods of time. The operating temperature of the lithium/selenium cell has been reduced below 300°C, without loss of power density, by using mixed-cation electrolytes (such as LiCl-LiI-KI) and by adding some tellurium to the selenium to improve the electronic conductivity of the cathode material. Lithium/selenium cells with paste electrolytes have been shown to be capable of delivering 2.7 W/cm^2 for short periods of time and storing over 0.3 W-hr/cm^2; the latter value corresponds to greater than 80% utilization of the cathode material.

The immobilization of at least one of the liquid phases in the electrochemical cells is important in the evolution of cells that will be insensitive to motion. In this connection, pastes formed from a mixture of molten-salt electrolytes and high-specific-area ceramic fillers have been developed. The inorganic syntheses and reactions of a number of double oxides including $LiAlO_2$, Li_5AlO_4, and $LiAl_5O_8$ for use as fillers have been studied. The properties of paste electrolytes prepared using these fillers are being investigated in an attempt to maximize the strength and minimize the resistivity of the paste.

Materials stability and corrosion studies are continuing in a program to identify suitable materials of construction for experiments involving highly corrosive alkali metals, chalcogens, and alkali halides.

Battery Development

New programs have been initiated for the scale-up of electrochemical cells and the development and evaluation of secondary batteries. These programs are sponsored by the National Heart and Lung Institute, the U. S. Army, and the National Air Pollution Control Administration (NAPCA).

The ultimate goal of the National Heart and Lung Institute program is the development of an implantable 10-W, 120-W-hr battery weighing 1 kg or less for artificial heart application. Lithium-selenium cells are currently being scaled up to 7.5-cm dia for evaluation of various designs. Design calculations based on the results of experiments with 2.5-cm dia laboratory cells indicate that it should be possible to develop a thermally insulated, implantable battery having the desired electrical capabilities and weighing less than 1 kg.

The battery program for the U. S. Army (Ft. Belvoir, Va.) has as its ultimate goal the development of high-specific-power, multikilowatt, lithium/selenium secondary batteries to provide acceleration and hill-climbing power for electrically driven Army vehicles. The present, shorter-term objective is to develop sealed 7.5-cm dia cells with paste electrolytes capable of 1 to 3 W/cm^2 at peak power and with lifetimes of 1000 to 2000 hr and 1000 to 2000 charge-discharge cycles. Energy densities in excess of 0.3 W-hr/cm^2 and peak power densities of 2 W/cm^2 have been demonstrated.

The work sponsored by NAPCA includes laboratory studies aimed toward the development of economical secondary batteries for pollution-free vehicle propulsion. The laboratory work has centered around the study of small-scale lithium/sulfur cells (0.7 to 4 cm^2 electrodes) and the achievement of high power densities (>5 W/cm^2 with liquid electrolytes) and high capacity densities (>0.3 A-hr/cm^2 with liquid electrolytes). The development of suitable cell designs for mobile applications and efficient current collection and mass transport in the cathode are the most prominent problem areas.

VI. Fluidized-Bed Combustion of Fossil Fuels (pages 165 to 167)

The combustion of coal in a fluidized bed to which particulate limestone is added is being studied as a means of reducing emission of the sulfur dioxide released during combustion. Results of a literature survey and supporting investigations conducted on a variety of proposed additives indicated limestones to be the most favorable for SO_2 reaction. An empirical model was developed to relate laboratory-obtained kinetic data on the reaction rates of limestone and SO_2 to the fluidized-bed operating parameters of bed height, superficial gas velocity, and additive particle size. The model predicts that the reduction in emission of SO_2 would be enhanced by decreasing the additive particle size and superficial gas velocity and by increasing the bed height.

Bench-scale experiments in a 6-in. dia fluidized-bed combustor are being performed to investigate the emission of SO_2 under conditions applicable to conceptual designs of both utility-sized power-generating stations and industrial steam boilers. The major results of the

experiments performed thus far, which were all conducted at a combustion temperature of 1600°F and a superficial gas velocity of 3 ft/sec, are as follows:

1) The emission of SO_2 in the flue gas was reduced to 29 to 87% of the SO_2 concentration without additive, depending on the type, particle size, and quantity of limestone added.
2) The most favorable result thus far (87% reduction in the emission of SO_2) was obtained when a calcitic limestone (designated BCR-1359) of 25-μm average particle size was added at 2.2 times the stoichiometric requirement.
3) For any particular type of limestone additive, greater SO_2 removal was generally noted for fine-particle-sized material than for coarse particle size.
4) The maximum degree of CaO utilization achieved during the experiments was 38%.
5) Partially reacted additive that accumulated in the fluidized bed contributed little to the overall reaction with SO_2; apparently, CaO particles react with SO_2 to a negligible extent after about 30% of the CaO is converted to $CaSO_4$.
6) The combustion efficiencies in two experiments were 96.7 and 97.1% (expressed as the percentage of carbon completely burned).
7) Solids elutriation rates determined during periods of no additive feeding indicate that virtually all of the ash associated with the coal used in these experiments was elutriated. The average particle size of elutriated solids was about 90 μm during periods of no additive feeding and decreased to about 60 μm during an experiment in which 25-μm additive was being added to the fluidized bed. Analysis of solids elutriated during an experiment that employed a 25-μm particle-size additive indicated that the fines residence time in the fluidized bed was sufficient for about 80% of the additive to be calcined before it was elutriated.
8) Bench-scale experiments conducted at 1600°F with argon substituted for nitrogen established that the source of NO_x compounds in the flue gas is nitrogen compounds contained in coal.
9) A reduction of 30–40% in nitric oxide emission was noted when limestone additive (BCR-1359) was introduced into the fluidized-bed combustor. The reduction (concomitant with the reduction in SO_2 concentration) could be due to catalysis or other enhancement of reactions to form NO_2, or decompose NO, or react NO with CaO or $CaSO_4$.

ARGONNE NATIONAL LABORATORY

Chemical Engineering Division Annual Report

U of C-AUA-USAEC

1969

ANNUAL REPORT

ANNUAL REPORT

I

Fuel Cycle Technology[1]

(*D. S. Webster, J. W. Simmons*)

A. LIQUID METAL-MOLTEN SALT TECHNOLOGY (*R. K. Steunenberg*)

Compact pyrochemical processes employ high-temperature, nonaqueous solutions for separations of actinide metals from fission products and other impurities. Liquid metals and molten salt systems are used as the process solvents. The liquid metals are usually binary alloys of magnesium with copper, zinc, or cadmium. The salts most frequently consist of $MgCl_2$ in combination with alkali or alkaline earth chlorides.

Certain technological and economic features of pyrochemical processes make them attractive for the processing of fast breeder reactor fuels. These features include (1) an ability to handle short-cooled, high-burnup fuels, which results in decreased out-of-reactor fuel inventory, (2) the simplification or elimination of chemical conversions, (3) the need for less shielded processing space because of small process volumes and compact equipment, and (4) the direct production of solid radioactive wastes.

The objectives of a pyrochemical process for fast breeder reactor fuels are to remove fission products from the spent fuel, to extract bred plutonium from the blanket, to enrich the core fuel with plutonium, and to repair irradiation damage. These objectives require that the cladding material, uranium, plutonium, and fission products be separated.

Pyrochemical processes employing salt-transport separations have been under investigation. In separations of this type, solute plutonium or uranium is transported from one liquid alloy (donor) to another liquid alloy (acceptor) by cycling a molten chloride salt between the two alloys and mixing the salt with each alloy in turn. Pyrochemical processes employing salt-transport separations show promise of high decontamination of actinides from fission products, together with high plutonium and uranium recoveries.

Pyrochemical processing techniques have also been under investigation for the recovery and purification of plutonium-238 from recycled scrap material generated in the preparation of isotopic power sources. The objective of this investigation is to remove (1) light elements that cause neutron emission through (α,n) reactions and (2) other impurities that appear in the recycle streams.

[1] A summary of this section is given on pages 1 to 8.

1. Salt-Transport Process for LMFBR Fuels (*R. K. Steunenberg*)

The salt transport process, which has been under development for the recovery of LMFBR fuels, is described in detail in the preceding annual report (ANL-7575, p. 28). Briefly, this process consists of the following operations: Stainless steel cladding is removed from the oxide fuel by dissolution of the cladding in liquid zinc. The separated oxide fuel is then reduced to metal by a Cu-Mg-Ca alloy with the aid of a $CaCl_2$-CaF_2 flux, and the volatile fission products from the decladding and reduction steps are collected in the argon cover gas. The subsequent separations of plutonium and uranium from fission products are effected in a series of liquid metal-molten salt extraction steps. After purification, metallic plutonium and uranium are recovered from product solutions by vacuum distillation of the solvent metal (Zn-Mg). The actinide metals are powdered by hydriding, then reconverted to the oxides by treatment with CO_2 in a fluidized-bed reactor.

Most of the process chemistry has been investigated and is well understood. Much of the required basic engineering information is also available, and work was started on facilities for a bench-scale engineering demonstration of the process. In mid-1969, however, development work on the entire salt transport process was terminated because of an AEC decision to concentrate on aqueous processes. At the present time a reduced effort is continuing on the development of the liquid metal decladding procedure as an alternative to a shear-leach step proposed as the head-end step for the aqueous processing of fast breeder reactor fuels.

2. Liquid Metal Decladding of LMFBR Fuels (*R. D. Pierce*)

a. Conceptual Design Studies on Zinc Decladding of Stainless Steel-Clad LMFBR Fuels (*N. M. Levitz, W. J. Walsh, G. J. Vogel, T. R. Johnson*)

A conceptual design study of a plant for decladding 5 metric tons/day of stainless steel-clad LMFBR fuel assemblies in molten metal was initiated. This head-end facility is assumed to be coupled to a large, central aqueous reprocessing plant, although the concept is also applicable to smaller plants and to separate head-end plants. Objectives are to achieve process simplicity, to minimize the number of mechanical handling steps, and to minimize the required shielded area and number of process vessels.

Decladding with molten metal is an alternative to mechanical decladding schemes,[2] which require sodium removal, disassembly of the fuel assembly, and shearing operations. An advantage of a molten metal decladding step is that the fuel oxide does not react with the decladding chemicals and, once separated, can be fed either to an aqueous dissolution step or to another interfacing step. An additional advantage is that no special treatment is required for fuel pins that are sodium-logged as a result of cladding failure or for pins on which sodium adheres externally.

An Atomics International stainless steel-clad UO_2-20 wt % PuO_2 fuel element[3] has been selected as a reference. Special attention must be given to the high plutonium content of this fuel, its high heat load, and its high gaseous fission product content. Other design bases for this study are similar to those selected for a recent fluoride volatility plant design concept study.[4]

The present study considers the fuel from the time it arrives at the reprocessing plant in sodium-filled shipping casks until it is charged to the step following decladding. Zinc, which dissolves stainless steel at practical rates, has been selected as the decladding agent in preference to another candidate decladding solvent, antimony-copper, since zinc is capable of adequate stainless steel loadings at moderate temperatures, is considerably cheaper than antimony-copper, and appears to give less of a containment problem.

The tentative operational scheme for the metal decladding operations, which will be performed in an inert-gas process cell, includes the following steps:

1) Transport of fuel assemblies from a sodium-filled shipping cask to a cutting station or to the decladding vessel. The fuel assemblies are transported in turret-like fixtures; during steps 3 to 5 these turrets are attached to the top of the decladding vessel.

2) Sawing of excess hardware from the inactive end of fuel assemblies for disposal as waste; alternatively, this step may be bypassed and the hardware dissolved with the cladding in the decladding vessel. The latter alternative might require larger vessels and a larger inventory of zinc.

3) Loading of fuel assemblies into perforated, removable refractory metal baskets in the decladding vessel. The present design provides five loading stations to which turrets may be attached. In this concept, two decladding vessels are employed on a 48-hr alternating cycle consisting of 24 hr to complete four successive dissolutions (approximately 50–60 fuel assemblies per day) and 24 hr for cleanout.

4) Partial stainless steel dissolution in molten zinc to release fission product gases.

5) Completion of the dissolution of cladding in mildly agitated zinc solution.

6) Fuel removal from the decladding vessel in baskets for subsequent charging of the fuel to the main processing plant.

Evaluation and analysis of this decladding concept will establish priorities for required R&D work. For example, still to be determined is the extent of fuel fragmentation during decladding; this will be a factor in the design of both the process and the equipment.

Graphite and tungsten are under initial consideration as materials of construction for containment of the molten metal systems. A tentative design of the decladding vessel designates graphite as the basic ma-

[2] C. D. Watson et al, "Head-End Processing of Spent LMFBR Fuel," in *Proceedings of 16th Conference on Remote Systems Technology*, pp. 19–38 (1969).

[3] H. Dieckamp, L. H. Roddis, Jr., "The GPU/AI Demonstration Plant," *Nucl. News* **11**(7), 41 (1968).

[4] N. M. Levitz et al, "A Conceptual Design Study of a Fluoride Volatility Plant for Reprocessing LMFBR Fuels," USAEC report ANL-7568 (1969).

terial of construction since graphite is more readily fabricated and far less expensive than tungsten. Nominal dimensions of the vessel for the present scale of operation are an 8-ft length, 8-ft height, and 2-ft width. Vessel size was selected on the basis of achieving a 15 wt % loading of stainless steel in zinc.

The fuel assemblies will be charged vertically, from the top, into the refractory metal baskets. A function of the baskets is to separate batches of fuel from each other for criticality safety; each basket accommodates three fuel assemblies.

Coarse fuel material will be readily contained in the baskets. Fines that migrate through the basket to the zinc phase will be recovered after each day's operations by a technique demonstrated with UO_2 fines (ANL-7575, pp. 29–31), namely, contacting of the molten zinc with a layer of molten salt above the metal, which effects transfer of the fuel to the salt phase. The layer of molten salt over the zinc in the decladding vessel may also serve other purposes, e.g., suppression of zinc vaporization and trapping of some fission product iodine. Total retention of the iodine and other fission product gases is a basic goal of this concept study. Iodine and other volatile fission products that penetrate the salt layer will be removed from the closed decladding vessel in a purge-gas stream.

After decladding is completed, the baskets will be used for conveying the fuel to the next processing station (e.g., the voloxidizer[2] described by ORNL).

The salt will be removed from the decladding vessel and kept in a storage vessel during cleanup of the decladding vessel, then recycled. Processing of the salt will be required only when the fuel concentration in the salt becomes high; the fuel loading limit for the salt needs to be established. Disposal of the zinc-stainless steel solution will be by casting into rods for storage as waste after monitoring to verify that it does not contain actinides.

Material and heat balances around the decladding vessel have been prepared, along with preliminary cell layouts, which show that an inert-gas process cell, approximately cube-shaped and 30 ft on a side, would be adequate. The cell includes a floor-port fuel unloading station; a saw for trimming excess hardware from the fuel assemblies; two decladding vessels; turret storage racks; salt storage tanks; scales, hoists, and manipulators; and a number of auxiliary components.

A criticality evaluation resulted in the selection of a decladder design using mass control rather than geometry control. The evaluation was based on the following assumptions:

1) A single basket will contain the fuel from three fuel assemblies and will be critically safe even if double-batching occurs.

2) Simultaneous rupturing of two baskets, with the contents accumulating around a third basket in a "compact" geometry, is sufficiently unlikely that on the basis of the "double contingency" principle, safety is maintained.

3) Basket design will prevent excessive transfer of fuel fines out of the basket; regular inspection and some special instrumentation will help detect any accumulation of fuel in the decladding vessel.

4) Gross deterioration of the graphite vessel to form fine particulate graphite (moderator) in the zinc phase will not occur.

5) Full graphite reflection.

Computer calculations based on transport and diffusion theory indicate that the minimum critical mass of unmoderated UO_2-20% PuO_2 with graphite reflection is about 300 kg or ~30 liters.

A very brief, exploratory examination of a continuous decladding concept has been made. Continuous operation of a single decladding vessel, instead of alternating operation of two vessels, is one advantage of the continuous concept which merits further study.

b. Glovebox Facility (*G. J. Bernstein, D. E. Grosvenor, T. R. Johnson, W. E. Miller, I. O. Winsch, T. F. Cannon, N. P. Quattropani, J. J. Stockbar*)

The Plutonium Salt Transport Facility (described in ANL-7575, pp. 34–35) was in the process of being built to provide equipment capable of demonstrating all of the steps in a complete pyrochemical process flowsheet when emphasis of the pyrochemical program was shifted from a complete pyrochemical process to a liquid metal head-end step for aqueous processing of oxide fuel. The portion of the facility that will provide experimental apparatus for the study of pyrochemical decladding and head-end operations is being completed without major changes (work on the two gloveboxes that have solids-handling equipment and 12-in. dia furnace wells connected by transfer lines is nearly done, but there are no plans to complete the glovebox that would have contained metal-salt contactors and a retort).

Plutonium will not be used in the initial liquid metal decladding studies planned for the facility. These experiments will be directed toward the investigation of a process that involves the dissolution of stainless steel cladding (containing fuel pellets) in liquid zinc at 800°C, collection of fuel pellets in a basket (made of tungsten mesh), and introduction of the fuel into an aqueous process via an oxidation step. In the first series of experiments with simulated fuel assemblies, the stainless steel dissolution rate in zinc will be determined as a function of dissolved stainless steel content and agitation intensity. In the next series of experi-

TABLE I-1. RELATIVE RATES OF CLADDING DISSOLUTION (MILD AGITATION)

Cladding	Solvent	Temperature (°C)	Dissolution Rate (mils/min)
304 SS	Zinc	800	~2
316 SS	Zinc	800	~4
Zircaloy-2	Zinc	800	~20[a]
304 SS	Sb-18 at. % Cu	900	>20

[a] After an 8-min induction period.

ments, a simulated assembly will be surrounded by tungsten screens of various mesh sizes and designs to investigate (1) the effect of the different screens on the dissolution rate, (2) the ability of the screens to retain broken fuel pellets, and (3) the composition of the material retained in the basket when the basket is lifted out of the zinc. Other topics for investigation include (1) materials of construction for a full-scale decladding vessel, (2) behavior of sodium and certain fission products in this step, (3) proportion of volatile fission products released and trapped, and (4) alternative pyrochemical head-end processes.

c. Cladding Dissolution (*W. J. Walsh, J. J. Stockbar, T. F. Cannon, L. Anderson*[5])

Experimental studies of the removal of stainless steel cladding from oxide fuels have continued. Previous work (ANL-7575, pp. 29–31) demonstrated the feasibility of decladding large stainless steel fuel assemblies using liquid zinc at 800°C. The dissolutions were shown to be rapid and complete. Satisfactory separation of the fuel from the zinc-stainless steel solution with negligible losses of fuel was demonstrated. Recently, work has been concentrated on (1) the rate of zinc decladding for various candidate cladding materials and degrees of agitation, (2) the maximum loading of stainless steel in liquid zinc, and (3) the rate of decladding with a Sb-Cu solvent metal.

A series of three experiments was conducted to determine the relative rates of dissolution in liquid zinc of ⅜-in. thick, 1½-in. dia discs of Zircaloy-2 and types 304 and 316 stainless steel. In each test, a 4½-in. dia baffled tungsten crucible was charged with 3.67 kg of zinc and 100 g of salt (to retard zinc vaporization). The system was brought to a steady-state temperature of 800°C, and a disc (attached rigidly to the bottom of a 2-in. dia agitator and encased in tantalum except for a ¾-in. dia circular area of the bottom surface that was in direct contact with the zinc) was lowered into the melt. The tantalum enclosures served to prevent the changing configuration of the dissolving specimen from

[5] Co-op student from Illinois Institute of Technology.

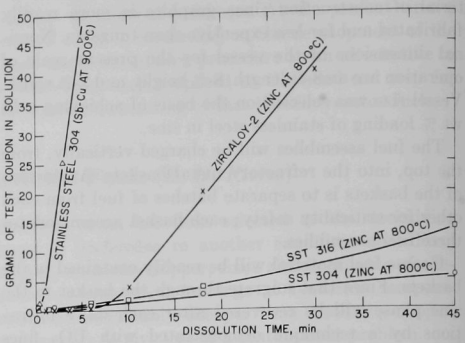

308-2147

FIG. I-1. Dissolution of Cladding Materials by Liquid Zn and Sb-Cu.

altering the mixing characteristics and also to provide a fixed, known surface area in the early stages of dissolution. The agitator was rotated at 350 rpm to ensure homogeneity of the liquid metal for sampling. Samples of the liquid metal solution were taken during dissolution. After about one hour of contact, the agitator-test coupon assembly was removed from the melt for inspection and analysis.

Another experiment was performed in which a type 304 stainless steel coupon was dissolved in Sb-18 at. % Cu at 900°C; other experimental conditions were identical to those described above. Copper-antimony alloy, recommended by Payrissat and Wurm,[6] is currently being studied as a backup decladding solvent.

The results of these four tests are given in Fig. I-1. The slowest dissolution was observed for type 304 stainless steel in zinc. Since this system had previously been demonstrated on an engineering scale to possess a satisfactory decladding rate (ANL-7575, pp. 29–31), it is clear that the other three systems tested would also have practical decladding rates. The initial rates of dissolution are given in Table I-1.

An experiment was conducted to test the effect of irradiation on the rate of dissolution of stainless steel in zinc. A type 304 stainless steel rod, 0.14 in. in dia by 2.6 in. long, was used. This rod had been irradiated in EBR-II from August 29, 1965, to January 22, 1966, at a flux of 4.9×10^{13} neutrons/(cm^2) (sec) (MW) with an average neutron energy of ~400 keV. This irradiation would correspond to a burnup of ~2.2 at. % if LMFBR core fuel were exposed to this flux. The irradiated rod was dissolved, along with several nonirra-

[6] M. Payrissat, J. G. Wurm, "Decladding of UO_2-PuO_2/Stainless Steel Fast Reactor Fuels by Liquid Metals," EAES Symposium, Mol, Belgium, 1968.

diated type 304 stainless steel rods of identical geometry, to allow comparison of the dissolution rates of irradiated and nonirradiated alloys.

In this experiment, an alumina crucible (5.6 in. in dia by 12 in. high) was charged with 10 kg of zinc and heated to 800°C in a furnace located in a walk-in hood. The irradiated rod was charged into the zinc melt, together with five nonirradiated rods. The solution was agitated mildly (150–300 rpm) to homogenize the liquid metal solution and allow representative samples to be taken. Eleven filtered samples of the zinc-stainless steel solution were taken at sampling times ranging from 4 to 252 min after introduction of the rods. The samples were analyzed for irradiated steel by measuring the radioactivity of the solution (the original 4-g rod yielded a 25-R beta-gamma contact dose rate, with the principal activity due to ^{54}Mn). The samples were also analyzed for total iron concentration by wet chemistry, and the dissolution rate for unirradiated stainless steel was obtained by subtraction.

The results of this experiment are given in Fig. I-2. The dissolution rate for irradiated steel rod was about twice the rate for unirradiated rods; the irradiated rods were completely dissolved in about 30 min. This result suggests that irradiation enhances the kinetics of stainless steel dissolution in zinc.

Based on an analysis of the binary phase diagrams of Zn-Fe, Zn-Cr, and Zn-Ni, it was estimated that the zinc would become saturated with chromium and iron at a loading of about 7–10 wt % stainless steel. A series of four experiments was made to investigate the maximum loading of stainless steel in zinc at 800–850°C and to study the effects of loading on the dissolution rate. These experiments involved heating 4.8 kg of zinc and 0.1 kg of salt to a steady-state temperature in the range 800–850°C and introducing into the melt type 304 stainless steel rods (⅜-in. dia by 1 in.) equivalent to 15 wt % loading. The systems were agitated mildly to promote homogenization of the zinc-stainless steel solution, and filtered samples were taken sequentially to monitor the rate and extent of dissolution. In all four experiments, the iron and chromium concentrations of the filtered samples of the liquid metal phase rose rapidly to about 5.8 wt % and 1.0 wt %, respectively, and remained essentially constant thereafter. About half of the stainless steel charged in each experiment was in solution in the zinc; however, examination of the frozen ingots at the end of the experiments showed that the rods had completely disintegrated. Sections of the ingots were metallographically examined and found to contain suspensions of finely divided grains of α-iron containing zinc and chromium in solid solution.

The experiments led to the following conclusions: (1) the maximum "solubility" of stainless steel in zinc

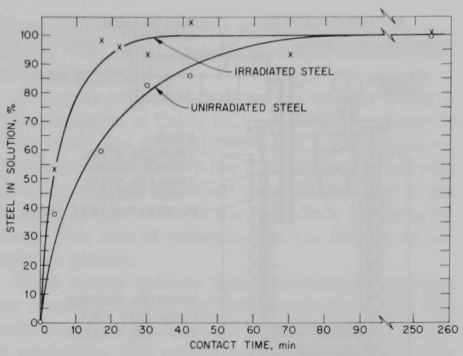

308-2148

FIG. I-2. Zinc Dissolution Kinetics of Irradiated and Unirradiated Type 304 Stainless Steel Rods.

is less than 8 wt %; (2) rapid disintegration of stainless steel continues after the zinc is saturated with chromium and iron; (3) loadings of 15 wt % (including the suspended solids) are readily achieved, and the resulting mixtures appear to be quite fluid with no evidence of settling of solids; and (4) effective separation of the zinc slurry from an oxide fuel bed appears to be feasible. Consequently, loadings of at least 15 wt % stainless steel may be possible when decladding with zinc.

The rate of disintegration of stainless steel may decrease sharply when the zinc becomes saturated with nickel (corresponding to an estimated stainless steel loading of 65–70 wt %). Additional studies are planned to define the optimum decladding techniques and the maximum stainless steel loading.

K. M. Myles of this Laboratory has investigated the mechanisms of formation of the solid suspensions (discussed in Section I.A.5 of this report).

d. Zinc Evaporation (*I. O. Winsch, T. F. Cannon*)

After transfer of the bulk of the zinc supernatant solution at the conclusion of a zinc decladding step in the salt-transport process (ANL-7550, p. 8), a heel of zinc remains with the oxide fuel pellets in the decladding vessel. To develop equipment and techniques for removing this zinc heel prior to a subsequent process operation, seven experiments were completed in which the zinc was evaporated and the distillate was collected in a horizontal graphite-lined condenser. In these experiments, a tungsten crucible in the stainless steel well of a 20-kW resistance furnace was used, as shown in the schematic in Fig. I-3. A typical charge consisted of 4 kg of zinc, 0.5 kg of UO_2 pellets, and 4 kg of $CaCl_2$-20 mol % CaF_2 (1-in. thick layer). The zinc was evaporated at 700–750°C; the initial pressure of

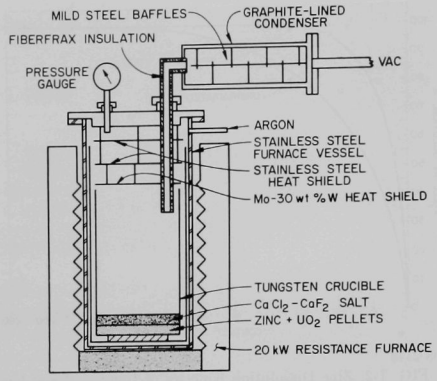

308-2149

FIG. I-3. Zinc Condenser Assembly.

125 Torr was slowly reduced to less than 1 Torr as evaporation progressed to completion. The distillate entered the condenser from one end and flowed horizontally, impinging and condensing on vertical baffles staggered along the length of the condenser.

In the initial experiments, a number of difficulties were encountered: metal condensed on the heat shields, the condenser inlet plugged, and the salt-metal mixture "bumped" during evaporation. The position of the inlet to the condenser was changed to that shown in Fig. I-3, and insulation of the transfer tube leading from the furnace to the condenser was improved. The inside diameter of the transfer tube was reduced from 1¾ in. to ⅝ in. to increase the vapor velocity through the inlet, and a continuous purge of argon at 5 cfh was maintained through the furnace and condenser. These changes eliminated plugging and reduced condensation on the furnace heat shields.

Mixing of the metal-salt mixture at about 300 rpm during evaporation prevented "bumping" and the resultant entrainment of salt in the vapor stream. The final design of the baffles in the condenser provided a relatively even distribution of the condensate in the condenser and prevented buildup of condensate near the inlet to the condenser.

In the final experiment, 100% of the zinc was removed from the fuel by evaporation and 85% was collected in the condenser. Seven percent of the zinc condensed on the top section of the stainless steel secondary vessel, and 8% condensed on the heat shields. With further refinement of the design, this type of condenser could be used successfully in a full-scale decladding operation. However, no further work is planned on the evaporation step.

3. Pyrochemical Purification of Plutonium-238 (*P. A. Nelson, J. Fischer, J. F. Lenc, J. R. Haley, J. D. Schilb*)

Pyrochemical processing techniques were investigated as a means of recovering and purifying plutonium-238 in plutonium scrap material. The facility described in ANL-7550, pp. 20–22, was used for work with plutonium-238.

The procedure used in two initial laboratory-scale experiments with ^{238}Pu consisted of suspending impure $^{238}PuO_2$ powder or microspheres in a molten chloride salt and reducing the plutonium to metal by mixing the salt with liquid Zn-Mg or Zn-Ca alloys. The salt and metal phases were separated, and then a metallic plutonium-238 product was recovered by vacuum distillation of the solvent metals. This process was effective in removing the light-element impurities that contribute undesirable neutron emission from (α,n) reactions in impure plutonium-238. In one experiment, the neutron count of the product was 2930 n/(sec) (g ^{238}Pu) [i.e., 2360 n/(sec) (g Pu)] as compared with a neutron count of 42,500 n/(sec) (g ^{238}Pu) for the starting material (10 g of $^{238}PuO_2$). The initial and final neutron counts in the other experiment were 89,300 and 3980 n/(sec) (g ^{238}Pu). In the experiment in which Zn-Mg was used as the reduction alloy, 10.08 g of the 10.8 g of plutonium charged was recovered in the residue from vacuum distillation.

A total of seven experiments (two of which were reported in ANL-7575, pp. 40–43, and are not reported here) has been performed with materials containing plutonium-239 (a stand-in for plutonium-238). The materials were $^{239}PuO_2$ microspheres, $^{239}PuO_2$-molybdenum cermets, and $^{239}PuO_2$-ZrO_2 solid solutions.

In one experiment (PR-4) utilizing 10 g of $^{239}PuO_2$ microspheres, the procedure was (1) reduction of $^{239}PuO_2$ with a Mg-30 wt % Cd reduction-donor alloy in contact with a $MgCl_2$-42 wt % $CaCl_2$ salt system, (2) transport of the plutonium away from impurities that remain in the reduction-donor alloy by cycling the salt between the reduction-donor alloy and a Zn-25 wt % Mg acceptor alloy having a high plutonium affinity, and (3) recovery of ^{239}Pu metal product by retorting the acceptor alloy. Of the 8.82 g of plutonium charged in Run PR-4, 7.827 g was transferred to the acceptor alloy. Of 6.58 g plutonium retorted in this run, 6.05 g was recovered in the product. The light ele-

ments and uranium were successfully removed in this run, in which high-purity zinc (nominally 99.9999 wt % Zn) and magnesium (nominally 99.995 wt % Mg) were used for the acceptor alloy.

Another experiment with $^{239}PuO_2$ microspheres (in which stainless steel also was charged) utilized the following procedure: (1) reduction with Zn-Ca in contact with a $CaCl_2$-KCl salt system, (2) addition of $ZnCl_2$ to oxidize the ^{239}Pu and excess calcium in the reduction alloy to $^{239}PuCl_3$ and $CaCl_2$ in the salt phase, (3) transfer of the $^{239}PuCl_3$-bearing salt phase to a Zn-Ca acceptor alloy and reduction of the $^{239}PuCl_3$ in the salt to ^{239}Pu metal in the acceptor alloy, and (4) recovery of the purified ^{239}Pu metal by retorting the acceptor alloy. Spark-source mass spectrographic analysis of the ^{239}Pu metal product indicated that the plutonium had been separated from the bulk of the iron and nickel but not from chromium. There had been no removal of uranium impurity, indicating that processes requiring high uranium removals should use magnesium rather than calcium as the reducing agent.

Two runs to evaluate the recovery of high-purity plutonium metal from PuO_2-molybdenum cermet used the following steps: (1) dissolution of $^{239}PuO_2$-molybdenum cermet in a chloride salt system containing $CuCl_2$ as a chlorinating agent, (2) reduction of the molybdenum and copper compounds in the salt by contacting the salt with a zinc metal phase, (3) transfer of the ^{239}Pu-bearing salt phase away from the Zn-Mo-Cu metal phase to a Zn-Mg or a Zn-Ca phase, (4) reduction of the ^{239}Pu compounds to metal in the Zn-Mg or Zn-Ca phase, and (5) recovery of the ^{239}Pu product by retorting the Zn-Mg or Zn-Ca metal phase. Disintegration of the cermet was achieved in both runs, but the ^{239}Pu metal products contained excessive concentrations of copper.

A run was performed to determine whether $^{238}PuO_2$-ZrO_2 suspended in $CaCl_2$-KCl salt could be reduced to ^{238}Pu metal and zirconium metal in a Mg-Cd-Ca reduction alloy at 725°C. After 3.75 hr of reduction with agitation, samples of the salt were analyzed and it was determined that 1.60% of the PuO_2-ZrO_2 had been reduced. This rate of reduction was too low for an acceptable process.

These results indicate that pyrochemical processes are generally feasible for these applications but that techniques have not been sufficiently developed for use in production. The results do, however, indicate that certain pyrochemical procedures may have immediate production applications. These include (1) reduction of $^{238}PuO_2$ scrap material to produce a metal alloy for subsequent aqueous processing, (2) reduction of relatively pure $^{238}PuO_2$ to remove light-element impurities and simultaneously produce plutonium-238 metal, and (3) disintegration of $^{238}PuO_2$-Mo compacts in a $CuCl_2$-containing molten salt for aqueous processing.

This project was discontinued June 30, 1969. Comprehensive reports have been prepared describing the experimental portion of this work[7] and the facility in which the experiments with plutonium-238 were conducted.[8]

[7] P. A. Nelson, J. Fischer, J. F. Lenc, J. R. Haley, J. D. Schilb, "Pyrochemical Processing of Fuel Materials and Scrap Containing Plutonium-238," ANL report to be published.

[8] J. Fischer, "Glovebox Facility for Pyrochemical Research and Development Work with Plutonium-238," ANL-7568 (1969); see also ANL-7575, pp. 40–41.

4. Engineering Development (*R. D. Pierce*)

a. Agitator-Pump Mixer-Settler Investigations (*G. J. Bernstein, J. B. Knighton, G. N. Vargo*)

The proposed design and mode of operation of a seven-stage mixer-settler for the separation of fission products from plutonium by molten salt-liquid metal extraction was described in ANL-7575, pp. 31–33. The mixer-settler is a box type having side-by-side stages in the form of boxes.

During the past year, investigations of mixing and flow characteristics[9] culminated in the design of an agitator-pump and mixing chamber for one stage of a mixer-settler for such extractions. In a run, some of the phases flow continuously between stages; other phases (captive phases) are moved batchwise between runs. Figure I-4 shows a captive-metal stage of the conceptual multistage mixer-settler. This design provides a 1-liter mixing chamber and a 7.0-cm dia agitator that produces a high degree of agitation while reducing the bypassing of solutions to an acceptably low level.

In normal operation with a two-phase system, both phases enter the zone above the mixing chamber and flow downward. A horizontal baffle and sleeve above the mixing chamber prevent entrainment of gas in the fluids if the liquid level is kept at least 3 cm above the baffle. (Gas entrainment decreases the effective mixing power at any mixing speed and depresses the normal rise in mixing power that accompanies increasing mix-

[9] R. D. Pierce, W. E. Miller, J. B. Knighton, G. J. Bernstein, "Multistage Contactors for Liquid Metal-Salt Extraction," *Nuclear Metallurgy*, Vol. 15, *Reprocessing of Nuclear Fuels*, CONF-690801, pp. 511–533 (1969).

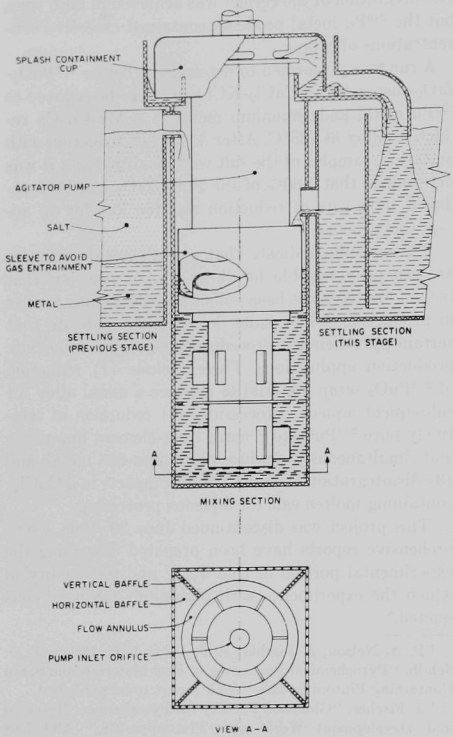

308-2150

FIG. I-4. Arrangement of Mixing and Settling Chambers (captive-metal stage).

ing speed.) In the mixing chamber, the two phases are mixed by blades attached to the pump rotor.

A fixed horizontal baffle that has an 8.9-cm dia opening is located at about mid-elevation of the mixing chamber. A horizontal disk, 7.6-cm OD, is mounted on the agitator-pump at the same elevation. Thus the chamber is divided into two mixing zones with a 0.65-cm annular connection. This configuration, by decreasing top-to-bottom mixing and approaching the performance of two total backmix[10] stages operating in series, reduces the amount of material that might otherwise bypass the mixing region. In the two zones of the mixing chamber, the phases are vigorously agitated and eventually enter the bottom of the pump through the inlet orifice. The mixed phases are pumped up into the collecting chamber and then flow into the settling chamber. The inverted cup surrounding the pump outlet eliminates spraying of metal from the pump discharge ports and thereby controls magnesium evaporation in the high-temperature Mg-Cu system.

In the settling chamber, the fluids separate. The light (salt) phase flows out through an overflow spout, and the heavy (metal) phase flows under a baffle and through an overflow spout. Flow is either back to the mixing chamber (as is the case for the metal phase in Fig. I-4) or to the mixing chamber of a following stage (as is the case for the salt phase in Fig. I-4).

During development of the present design, a number of tests were performed in a mockup mixing assembly consisting of a stainless steel agitator-pump (built for use in the high-temperature furnace) and a plastic chamber. Observation of two-phase mixing using water and organic phases showed that good dispersion could be achieved. However, it was desired to have a quantitative measure of mixing power input in order to compare the degree of mixing with other known systems.

Mixing power and pumping rate tests using water as a single phase also were conducted. Mixing power was determined with a dynamometer that measures drive-motor torque. Pumping rates were measured for different lifts, pump-inlet-orifice sizes, and rotational speeds. The pumping rate decreases with the increased lift that results from reduced holdup (i.e., from a lower liquid level) in the mixing section. This holdup-flow relationship tends to stabilize operation of a multistage system. The mixing power is proportional to the cube of rotational speed. Pumping does not begin until a minimum speed is reached, and the maximum pumping rate is limited by the size of the pump-inlet orifice.

Since the pumping rate and mixing power delivered to the mixing chamber are both dependent upon agitator-pump speed, it would be desirable to have a mixing chamber and pump design in which mixing power increases more rapidly with agitator-pump speed than does pumping rate. Under such conditions, the reduced residence time that results from increased throughput at higher agitator-pump speeds would be offset by increased mixing intensity. Figure I-5 shows the relationship between mixing power and pumping rate at various agitator-pump speeds for three different sizes of pump-inlet orifice. Over the range of probable operating speeds (600–800 rpm), overall mixing intensity increases with increasing agitator-pump speed and with decreasing pump-inlet orifice size.

It would be desirable that the multistage mixer-settler operate under continuous flow conditions with a

[10] A total backmix stage is one in which the composition of all the material in the stage is uniform at any instant so that the material leaving the stage has the same composition as the material in the stage.

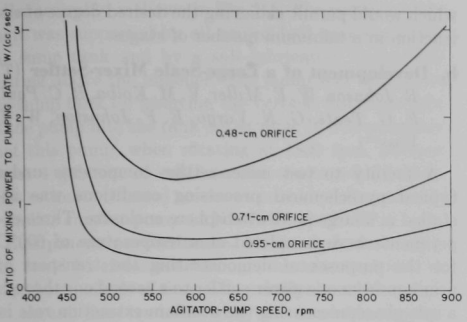

308-2151

FIG. I-5. Mixing Power-to-Pumping Rate Ratio for Agitator-Pump as a Function of Agitator-Pump Speed and Size of Pump-Inlet Orifice (pump lift = 16 cm).

mean residence time of one minute or less. In a total-backmix stage, the residence time of any infinitesimal unit of material varies from zero to infinity. When very high (~99%) stage efficiency is desired, the mean residence time is far less significant than is the fraction of material exposed for short times. Therefore, as described above, the mixing chamber was designed to minimize the quantity of material leaving the chamber after only a short residence time. In the salt-metal systems of interest, the rates of extraction are known to be rapid, but have not been precisely defined.

A series of tests were conducted in a mockup mixing assembly to determine the residence-time distribution in the mixing chamber. The tests were conducted at various mixing speeds (400–1000 rpm) in a nonflow system with the pump-inlet orifice closed. The tests were designed to measure the rate of approach to equilibrium composition at the bottom of the mixing chamber after a small quantity of acid was injected just below the top horizontal baffle. A pair of platinum electrodes adjacent to the injection point signaled the start of injection, and a pair of electrodes at the bottom of the mixing chamber (close to the closed pump orifice) sensed the rise in solution conductivity at that point. From the data it was possible to calculate the stage efficiency achievable for any given mean residence time and reaction rate.[9] It has been reported[11] that in experiments involving batch extraction of cerium from Cd-Zn-Mg into $MgCl_2$-Nacl-KCl at 600°C, ~95% of equilibrium was reached in 4 min. The measured power input in the experiments was almost a factor of 100 times lower than the expected power input in the mixing chamber of the mixer-settler. Accordingly, it was anticipated that 90% of equilibrium could be reached in a few seconds. Based upon a reaction rate in which 90% of equilibrium would be achieved in 4 sec, it was calculated that 99.8% stage efficiency would be achieved in the reference stage design operating at a flow rate that provides a 1-min mean residence time.

A high-temperature, single-stage mixer-settler was fabricated of type 304 stainless steel for operation with Mg-Cu alloy and $MgCl_2$-NaCl-KCl-MgF_2 salt at 675°C. A view of the equipment is shown in Fig. I-6. The components were designed to give experimental flexibility and to fit into an existing furnace. The mixing chamber and agitator-pump (located at the center of the lower section) have the same configuration as that shown in Fig. I-4. The settling chamber surrounds the mixing chamber. In the lower foreground is the metering cup, which is used to measure the flow rate of the metal phase. An orifice (0.64-cm dia) is located in the bottom of the cup; an induction probe located in a vertical tube passing through the cup indicates the level of metal in the cup; precalibration allows flow rate to be determined from the metal level in the cup. At the lower left is the flow diverter, which can direct the flow from the collecting chamber into either the

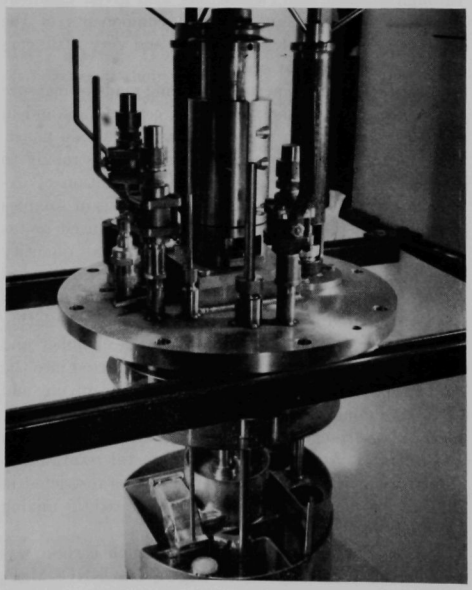

308-2098

FIG. I-6. High-Temperature Single-Stage Mixer-Settler.

[11] T. R. Johnson, R. D. Pierce, W. J. Walsh, "Recent Developments in the Technology of Molten Metal Salt Extractions," presented at AIChE Regional Symposium, University of Toledo, April 1966.

settling chamber or the metering cup. When both phases flow into the settling chamber, the salt overflows through a port back into the mixing chamber, and the metal flows through an underflow weir into the metering cup. The flow from the collecting chamber is diverted to the metering cup only when metal alone is being pumped since the discharge from the metering cup flows into a large metal reservoir that provides metal feed to the mixing chamber. The corresponding salt reservoir is located in the settling chamber. Separate displacement (or trim) tanks in the metal and salt reservoirs can be seen in the back and right-hand sides of the bottom section. These tanks are raised and lowered by means of the drive screws at the rear of the upper section. These tanks are manipulated to adjust the quantity of each phase in the mixing chamber and thereby vary the total volume of mixture as well as the ratio of the two phases.

Three sample ports are also shown in the top section of the mixer-settler. These ports permit sampling of (1) the metal in the metering cup and the underflow weir and (2) the salt in the settling chamber. At the center of the upper section is the spindle and its drive-shaft bearing. The spindle is a commercial unit and has given excellent performance for more than one thousand hours of operation. The 1-in. dia shaft passes through a shaft seal, which has also given excellent service. The pump and internal components of the furnace have shown high integrity and very little corrosion during the test operations.

A series of extraction runs are being made to measure stage efficiency for the transfer of cerium (a stand-in for plutonium) from a metal phase to a salt phase. Cerium was selected because it distributes strongly to the salt phase, allowing precise determination of extraction out of the metal phase by analysis of samples of the metal phase. Cerium-141 tracer is used to facilitate analyses. Prior to extraction, a small quantity of Cu-Mg-Ce-^{141}Ce is added to the Cu-Mg metal phase. This material is added to the metering cup and then distributed into the metal reservoir by circulating the metal overnight through the mixing chamber and metering cup. In a run, the cerium is extracted into the salt by passing both phases through the mixing and settling chambers. A spiral-shaped partition in the metal-phase reservoir makes a long, narrow passage in the reservoir. As a result, depleted metal returning to the reservoir through the metering cup is restricted in diluting the metal which has not yet entered the mixing chamber.

One run has been completed in which cerium was transferred from Mg-Cu to $MgCl_2$-NaCl-KCl-MgF_2 at 675°C in the stainless steel mixer-settler. A high stage efficiency (greater than 99%) was demonstrated, which would permit achieving the desired degree of extraction in a minimum number of stages.

b. Development of a Large-Scale Mixer-Settler (*T. R. Johnson, W. E. Miller, V. M. Kolba, R. C. Paul, F. G. Teats, G. N. Vargo, E. F. Johnston, W. J. Voss*[12])

A facility to test mixer-settler components under typical pyrochemical processing conditions was installed in a large inert-atmosphere enclosure. Three experiments were completed at a temperature of 600°C for the purposes of demonstrating the transport of uranium from one mixer-settler to a second one through a salt phase, measuring the uranium extraction rate in the mixer-settlers, and determining the rate of entrainment of the metal phase in the flowing salt phase. The equipment (installed in an inert-gas enclosure) and the initial run are described in ANL-7425, pp. 38–39, and in ANL-7575, pp. 37–39.

The equipment was fabricated of type 304 stainless steel and was resistance heated. A fraction of the liquid salt ($MgCl_2$-30 mol % NaCl-20 mol % KCl) pumped into a constant-head tank flowed by gravity through two mixer-settlers, a weigh tank, and then back into a sump tank for recycle. The flow rate of this stream was controlled by the liquid head and with a valve in the constant-head tank. The remainder of the liquid salt in the constant-head tank flowed into a standpipe and directly back into the sump tank.

At the start of each run, the first mixer-settler (mixer-settler 1) contained a Cd-2.2 at. % Mg alloy and uranium. Only part of the uranium could be dissolved in this liquid alloy; thus most of the uranium in this unit was present as a solid. Uranium was extracted from this "donor" alloy into the flowing salt and then was extracted from the salt in mixer-settler 2 by a magnesium-rich cadmium alloy (the "acceptor" alloy). Since magnesium is exchanged for uranium when uranium is extracted, the magnesium concentration increased in the donor alloy and decreased in the acceptor alloy as transport of uranium progressed. Consequently, the transport rate of uranium from the first mixer-settler to the second decreased during a run.

The salt flowed into the central, conical-shaped region of a mixer-settler (Fig. I-7) where it was mixed with the liquid metal alloy. The salt then flowed under the cone and baffle assembly and into the quiescent region outside the cone where metal droplets separated from the salt by gravity. The salt left the mixer-settler tank through a standpipe that maintained a constant salt level in the tank.

The salt was circulated by a centrifugal pump in the sump tank. The general arrangement of the pump im-

[12] Central Shops, Argonne National Laboratory.

peller assembly is shown in Fig. I-8. The vertical pump shaft was supported by oil-cooled ball bearings above the sump tank and by a salt-lubricated, hydrostatic bearing above the impeller. The pump was coupled to the sump tank by inserting the vertical discharge tube of the pump into the tank outlet pipe. It was estimated that this pump, when rotating at 1800 rpm, pumped about 4 gal/min of salt into the constant-head tank. This estimate is based on the measured performance of a similar smaller pump (ANL-7325, pp. 35–37).

Equipment performance. In the shakedown runs, salt could be circulated through the mixer-settlers for only short periods of time. The principal problems were (1) the salt lines tended to plug with insoluble magnesium oxide, (2) the graphite sleeve bearings for the agitators in the mixer-settlers galled and seized the shafts, and (3) the salt-lubricated bearing on the pump rubbed and galled the impeller shaft.

Plugging of lines was eliminated by minimizing exposure of the liquid salt and metal to the enclosure atmosphere (which contained small amounts of oxygen and water vapor). It was not practical to seal the process vessels completely from the enclosure atmosphere since the gas pressure in the vessels had to be maintained essentially at the pressure of the enclosure. The performance of the agitator bearings was improved considerably by replacing the graphite bearings with ones made of polyimide filled with silver or tungsten disulfide.

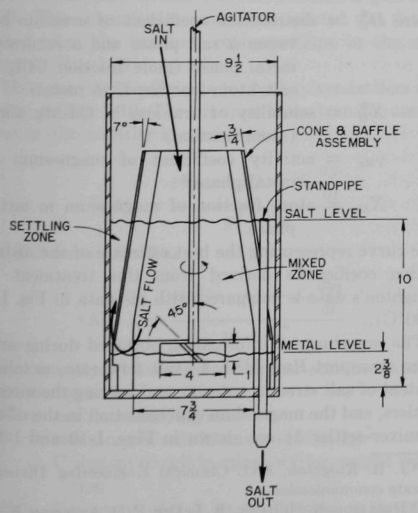

308-2152

FIG. I-7. Mixer-Settler (dimensions in inches).

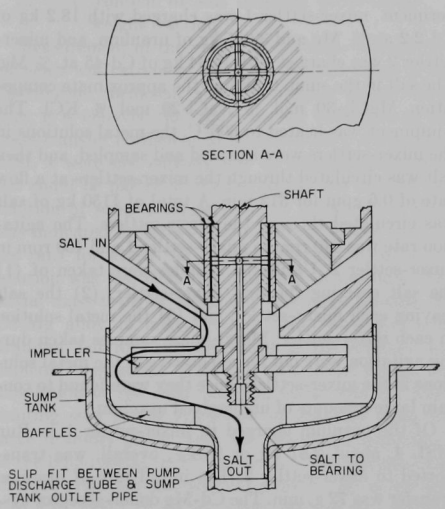

308-2153

FIG. I-8. Salt Pump–Impeller Assembly.

Installation of a newly designed salt-lubricated bearing in the centrifugal pump (Fig. I-8) ended operating difficulties. In this new type of bearing, salt forms a flowing film separating the rotating shaft and the stationary bearing. The design of the shaft and bearing should prevent their touching. If the shaft moves off-center, a force develops to push the shaft back to the center. Although this force is small (the estimated force developed at 1600 rpm for this bearing is about 2 lb),[13] it is as effective in maintaining the position of the shaft as a much larger force applied to the top of the shaft, because the force is applied at the unsupported end. The chambers in the bearing help to develop the centering force by increasing axial flow and decreasing tangential flow. The present pump bearing is made of graphite, which is not expected to be the final choice as material of construction for this application because the graphite may react with solutes to form carbides. A hard material will be selected that will minimize the likelihood of galling of the shaft if the rotating shaft and bearing touch occasionally. A bearing made of a cermet (type 304 stainless steel-52 wt % TiC) was fabricated and installed in a spare pump.

In general, the equipment operated well during subsequent runs, indicating that the earlier problems had been solved.

Run MSL 4—uranium transfer. To start this ex-

[13] E. E. Bisson, W. J. Anderson, "Advanced Bearing Technology," NASA-SP-38 (1965).

periment, mixer-settler 1 was charged with 18.2 kg of Cd-2.2 at. % Mg and 3.055 kg of uranium, and mixer-settler 2 was charged with 12.34 kg of Cd-45 at. % Mg. The salt in the sump tank had the approximate composition $MgCl_2$-30 mol % NaCl-20 mol % KCl. The equipment was heated to 600°C, the metal solutions in the mixer-settlers were agitated and sampled, and then salt was circulated through the mixer-settlers at a flow rate of 0.6 gpm for 312 min. A total of 1150 kg of salt was circulated through the mixer-settlers. The agitation rate was 640 rpm in mixer-settler 1 and 460 rpm in mixer-settler 2. Unfiltered samples were taken of (1) the salt entering the first mixer-settler, (2) the salt leaving each mixer-settler, and (3) the metal solution in each mixer-settler. Metal-phase samples taken during agitation were not representative of the metal solutions in the mixer-settlers since they were found to contain large amounts of undissolved uranium.

Of the uranium charged to mixer-settler 1 in Run MSL 4, about 2.81 kg or 93.4%, overall, was transported to mixer-settler 2. The initial rate of uranium transfer was 72 g/min. The Cd-Mg donor-acceptor system was selected for this experiment because a salt-transport process could be demonstrated in a stainless steel apparatus with this alloy system and not because this alloy is an efficient system for the transport of uranium. Much higher rates (g material transported/g salt circulated) for the transport of uranium or plutonium can be achieved by using Cu-Mg donor alloys.

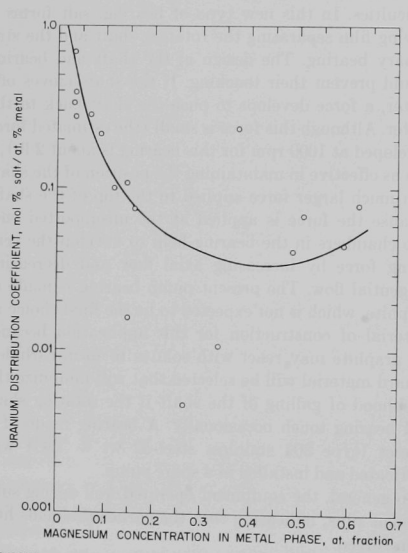

308-2154

FIG. I-9. Uranium Distribution Coefficient Between $MgCl_2$-30 mol % NaCl-20 mol % KCl and Cd-Mg Alloys at 600°C (data from investigations of J. Knighton, 1964 through 1967).

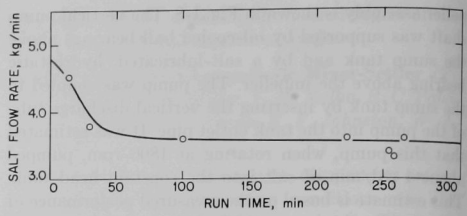

308-2155

FIG. I-10. Salt Flow Rate through Mixer-Settlers During MSL 4.

To calculate mass-transfer coefficients, K_sA, from the experimental data, the equilibrium distribution of uranium between the salt and metal phases must be known accurately. Uranium distribution measurements made by J. Knighton[14] were evaluated by means of a thermodynamic analysis. From the equilibrium constant for the reaction

$$U_{(metal)} + 3/2MgCl_{2(salt)} \rightleftarrows UCl_{3(salt)} + 3/2Mg_{(metal)}$$

it can be shown that at constant temperature

$$D_U^* \propto \frac{1}{(X_U^*)(\gamma_{Mg})^{3/2}(X_{Mg})^{3/2}}$$

where D_U^* = distribution coefficient of uranium between a salt phase and a saturated metal phase (mole fraction UCl_3 in salt/atom fraction U in metal)

X_U^* = solubility of uranium in Cd-Mg alloy (atom fraction)

γ_{Mg} = activity coefficient of magnesium in metal phase[15]

X_{Mg} = atom fraction of magnesium in metal phase.

The curve representing the best estimate of the distribution coefficients derived from this treatment of Knighton's data is compared with his data in Fig. I-9 (600°C).

The experimental information obtained during uranium transport Run MSL 4 (salt flow rate, uranium content of salt streams entering and leaving the mixer-settlers, and the magnesium concentration in the metal in mixer-settler 1) are shown in Figs. I-10 and I-11.

[14] J. B. Knighton, ANL Chemical Engineering Division, private communication.

[15] Data from R. Hultgren, R. L. Orr, P. D. Anderson, K. K. Kelley, *Selected Values of Thermodynamic Properties of Metals and Alloys*, John Wiley, New York (1963).

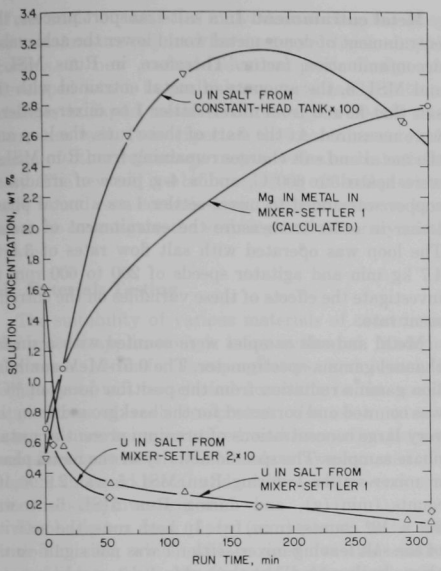

308-2156

FIG. I-11. Solution Compositions During Mixer-Settler Run MSL 4 (note scale factors).

The curve in Fig. I-11 that represents the magnesium concentration was calculated from the uranium transported from mixer-settler 1 to mixer-settler 2 (see Fig. I-12). The amount of uranium transported was determined from the uranium concentrations in the salt streams (Fig. I-11).

Mass-transfer coefficients for both mixer-settlers are shown in Fig. I-12. The uranium mass-transfer coefficient in mixer-settler 1 is defined as

$$(K_sA)_1 = \frac{s(y_1 - y_p) + S_1 \dfrac{dy_1}{dt}}{y_1^* - y_1}$$

and in mixer-settler 2 as

$$(K_sA)_2 = \frac{s(y_1 - y_2) + S_2 \dfrac{dy_2}{dt}}{y_2 - y_2^*}$$

where subscripts 1 and 2 refer to mixer-settlers 1 and 2, respectively, and

s = salt flow rate, kg/min

S = inventory of salt in mixer-settler, kg

y = U content of salt in mixer-settler, weight fraction

y^* = U content of salt in equilibrium with saturated metal phase, weight fraction

y_p = U content of salt entering mixer-settler, 1, weight fraction

Measurement of the values of the mass-transfer coefficients was extremely sensitive to small errors in the distribution coefficient and to sampling errors. However, it is believed that the observed variations in the mass-transfer coefficient in mixer-settler 1 during Run MSL 4 were not entirely due to experimental errors but could be partly attributed to the low rate of dissolution of solid uranium into the metal phase. This was indicated by metal-phase samples (taken early in the run) for which the uranium content of the metal solution was less than the solubility of uranium. The initial mass-transfer coefficient was large because the Cd-Mg alloy in mixer-settler 1 was saturated with uranium, but its value decreased as the solution was depleted of uranium. After this brief initial period, the dissolution of the solid uranium metal was the rate-limiting step in the extraction of uranium since the large uranium pieces were not suspended completely in the liquid metal by the agitation. (The uranium was charged originally as rods that were $^5/_{32}$ in. in dia and 2 to 3 in. long.) In 70 min about 50% of the uranium had been removed, after which the mass-transfer coefficient increased to values greater than 200 kg/(min)(wt fraction U in the salt phase). This increase is attributed to the ability of the agitator to suspend more completely the smaller uranium pieces. When more than 75% of the uranium had been transferred, the value of the interfacial mass-transfer coefficient decreased, probably because the dissolution rate be-

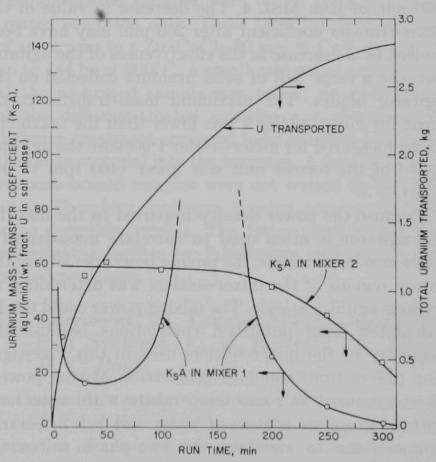

308-2157

FIG. I-12. Uranium Transfer During Run MSL 4.

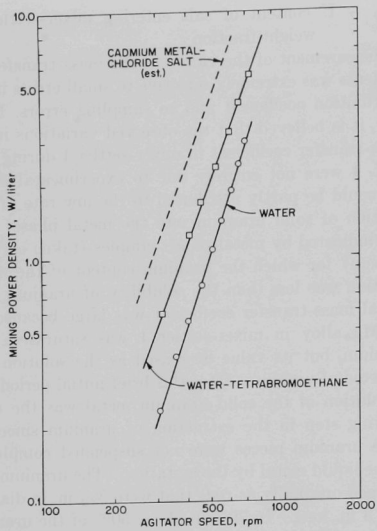

308-2158

FIG. I-13. Mixing Power Density in Mixed Region of Mixer-Settlers in Salt Transport Loop.

came limited by the decreased surface area of the remaining uranium rods.

The mass-transfer coefficient in mixer-settler 2 was relatively constant at an average value of about 55 kg U/(min) (wt fraction U in salt phase) during the first 200 min of Run MSL 4. The decrease in value of the mass-transfer coefficient after 200 min may have been caused by a decrease in the effectiveness of the agitator because a large ball of solid uranium collected on the agitator blades. The maximum mass-transfer coefficient for mixer-settler 2 was lower than the maximum value measured for mixer-settler 1 because the agitator speed of the former unit was lower (460 rpm vs 640 rpm).

Because the power density imparted to the fluid by the agitator is often used to correlate mass-transfer rates in stirred vessels, the mixing power density in the mixed regions of the mixer-settlers was determined at various agitator speeds. The mixing power could not be calculated from published correlations because the geometry of the mixer-settlers used in this investigation differs from standard geometries. Mixing powers were measured at room temperature with water and with a two-phase system of water and 1,1,2,2-tetrabromoethane to simulate the two-phase salt-metal system. The measured data and the estimated power for the salt-metal system are shown in Fig. I-13.

Metal entrainment. In a salt-transport process, the entrainment of donor metal would lower the achievable decontamination factor. Therefore, in Runs MSL 5 and MSL 6, the amounts of metal entrained with the salt that flowed from mixer-settler 1 to mixer-settler 2 were measured. At the start of these runs, the loop and the metal and salt charges remaining from Run MSL 4 were heated to 600°C, and a 4-g piece of irradiated copper was added to mixer-settler 1 as a metal phase tracer in order to measure the entrainment of metal. The loop was operated with salt flow rates of 3.1 to 4.7 kg/min and agitator speeds of 200 to 600 rpm to investigate the effects of these variables on the entrainment rate.

Metal and salt samples were counted with a single-channel gamma spectrometer. The 0.51-MeV annihilation gamma radiation from the positron decay of ^{64}Cu was counted and corrected for the background from the very large concentrations of uranium present in metal-phase samples. The specific activity of the metal phase in mixer-settler 1 during Run MSL 5 was 2.9×10^4 counts/(min)(g), and during Run MSL 6 it was 8.5×10^4 counts/(min)(g). In both runs, the activity of the salt leaving mixer-settler 1 was not significantly above background, but there was a detectable increase in the activity of the metal phase in mixer-settler 2. The average amount of metal entrained in both runs was 0.02 g of Cd per kg of salt circulated. The entrainment rate apparently increased with increasing agitator speed, but because of the very low counting rates, the trend was only barely significant. If the uranium-transport run, MSL 4, had been a process step to separate uranium from a fission product element (such as zirconium) that does not distribute significantly to the salt phase, the estimated decontamination factor for the product uranium (calculated from the measured entrainment rate) would have been 750. With a more efficient salt-transport system, less salt would be circulated to transport the same amount of uranium; this would result in a higher decontamination factor.

After Run MSL 6, the loop was shut down and partly disassembled for inspection.

c. Liquid Level Probe Development (*F. G. Teats, T. R. Johnson*)

A device has been needed in pyrochemical studies to measure the depth of liquid metals in process vessels. A probe based on a mutual inductance coil was developed and has been described.[16] This probe, however, could be used only in containment wells made of 300-series stainless steels, graphite, or ceramic materials.

[16] T. R. Johnson, F. G. Teats, R. D. Pierce, "An Induction Probe for Measuring Levels in Liquid Metals," *Nucl. Appl.* 4(1), 47 (1968).

Wells made of tungsten, molybdenum-tungsten alloys or tantalum are required for most pyrochemical applications. A new mutual-induction probe design was developed which in preliminary tests easily detected changes in liquid metal level through a 30-mil thick tantalum well. It is expected that containment wells made of other refractory metals will also be satisfactory. The new coil is a bifilar winding of 8-mil platinum wire wound on a ceramic form. Further tests are being made to investigate the stability and accuracy of the device.

d. Materials Testing

The suitability of various materials of construction for process applications is being evaluated. Materials for vessels, transfer lines, agitators, and associated components will be selected according to the specific application of each component. Corrosion rates of materials are being measured, and interaction between container materials and the solute uranium and plutonium in liquid metal and molten salt process solutions is being investigated.

Emphasis has been placed on materials to be used with (1) zinc, which will be used for fuel element decladding, and (2) Mg-Cu and Zn-Mg alloys, which are used as donor and acceptor alloys in salt-transport separations.

(1) Corrosion by Zinc/Halide Salt, Zinc-Copper/Halide Salt, and Zinc-Magnesium/Halide Salt Systems (*V. M. Kolba, L. F. Dorsey, R. C. Paul*)

Tungsten-coated graphite crucible. Testing of a 5¾-in. dia graphite crucible that has a 30-mil vapor-deposited tungsten coating (described in ANL-7575, p. 37) was continued. The crucible was temperature-cycled and then tested for containment of a molten salt. After these tests proved to be successful, the crucible was exposed to the metals and salts proposed for the decladding, reduction, and acceptor steps of the salt-transport loop. The liquid solutions were poured from the crucible at the conclusion of each experiment. No uranium or plutonium was contained in these solutions.

The conditions for testing tungsten-coated graphite crucibles are listed in Table I-2. All materials were contained successfully, and no cracking or spallation of the tungsten coating was observed. However, small amounts of tungsten (100–200 ppm) and carbon (~50 ppm) were found in the metal and salt phases after the run. This method of coating graphite appears to offer promise for fabricating the head-end processing vessel and the acceptor alloy vessel, if equipment for coating large vessels becomes available.

TABLE I-2. Test Conditions for Tungsten-Coated Graphite Crucible

Run Time (hr)	Temp. (°C)	Metal	Salt	
55	650–850	—	$MgCl_2$-30 mol % NaCl-20 mol % KCl	Temperature-cycled three times
48	800	Zn	$CaCl_2$-20 mol % CaF_2	
98	800	Mg-44 at. % Cu	$CaCl_2$-20 mol % CaF_2	
96	750	Zn-29 at. % Mg	$MgCl_2$-30 mol % NaCl-20 mol % KCl	

Brazing of tungsten. Brazing is a potential method of assembling tungsten components. To prevent exposure of brazed material to corrosive environments, brazing should be followed by a diffusion treatment to reduce the braze metal concentration at the braze interface. Two methods of brazing rolled tungsten sheet (produced by powder metallurgy techniques) with Coast Metals 60 braze alloy (Ni-20 wt % Cr-10 wt % Si-3 wt % Fe) were tested.

One set of specimens was brazed in a dry (−51°C dewpoint) hydrogen atmosphere at 1100°C, followed by an 8-hr diffusion treatment at 1350°C. A second set was brazed in a vacuum (5×10^{-4} Torr) at 1200°C, followed by an 8-hr diffusion treatment at 1370°C. Specimens from the hydrogen-brazed set were tested in both the as-brazed and diffusion-treated conditions; vacuum-brazed samples were tested in the diffusion-treated condition only. These tests involved exposure of specimens to a Zn/$CaCl_2$-20 mol % CaF_2 system for up to 144 hr at 800°C. A small amount of undercutting of the as-brazed sample was noted; no undercutting of the diffusion-treated samples was observed. The diffusion treatment appeared to be effective in diffusing the braze material into the tungsten. A few areas in the vacuum-brazed samples were not wetted by the braze alloy. Therefore, hydrogen brazing appears to be the more desirable process. The latter process should be investigated further by fabricating and testing small prototype vessels.

(2) Corrosion in Copper-Magnesium/Halide Salt Systems (*V. M. Kolba, L. F. Dorsey, R. C. Paul*)

Corrosion testing. Corrosion tests were conducted to aid in the selection of a material for use in the construction of mixer-settler components. Previous testing (ANL-7375, p. 33; ANL-7425, p. 35; ANL-7575, p. 35) indicated that Fe-Cr alloys and refractory metals

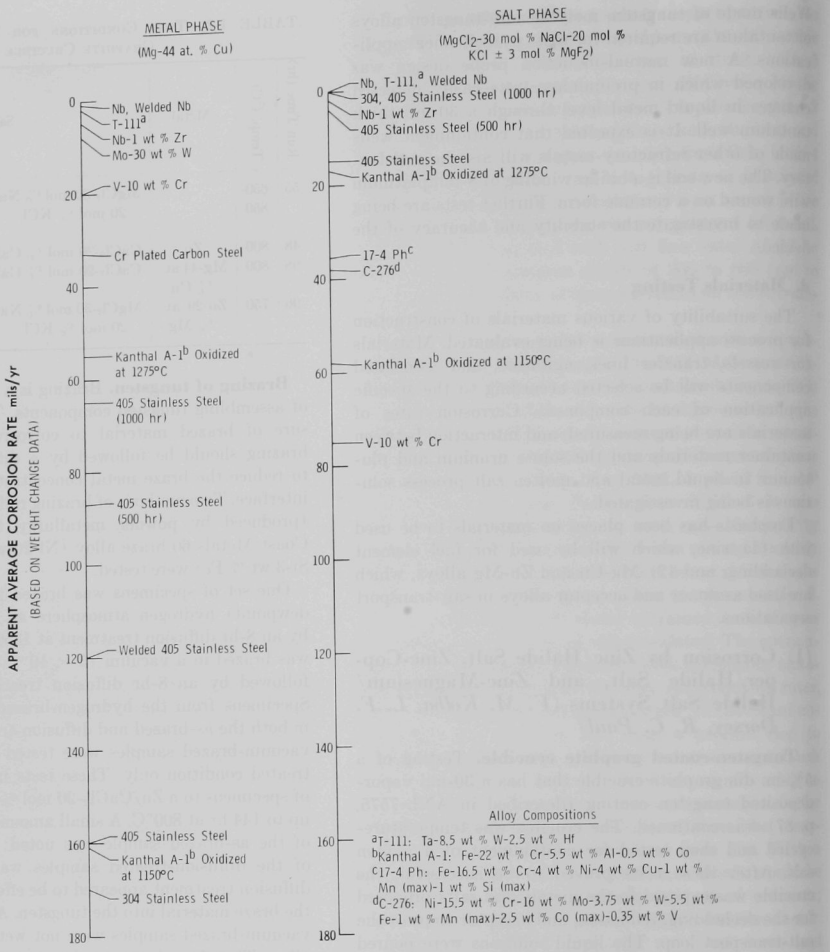

308-2097

FIG. I-14. Corrosion Test Data for Proposed Materials of Construction for Mixer-Settlers (700°C; exposures of at least 190 hr).

possess attractive properties. The former have lower costs and better fabricability, while the latter have better corrosion resistance. The following materials were tested[17] as agitator blades at ~700°C for periods up to 1000 hr in Mg-44 at. % Cu/ternary or quaternary chloride systems: niobium, Nb-1 wt % Zr, T-111 (Ta-8.5 wt % W-2 wt % Hf), Kanthal A-1 (Fe-22 wt % Cr-5.5 wt % Al-0.5 wt % Co), type 304 stainless steel, type 405 stainless steel, 17-4 Ph (Fe-16 wt % Cr-4 wt % Ni-4 wt % Cu-1 wt % Si-1 wt % Mn-0.07 wt % C), titanium (Ti-55A), and V-10 wt % Cr and welded specimens of niobium, type 405 stainless steel, Mo-30 wt % W, Hastelloy B-282 (Ni-28 wt % Mo-5 wt % Fe-2 wt % V-0.6 wt % Cr-0.6 wt % Mn-0.35 wt % Si-0.02 wt % C), and Haynes C-276 (Ni-16 wt %

[17] M. L. Kyle, R. D. Pierce, V. M. Kolba, "Containment of Materials for Pyrochemical Processes," Nuclear Metallurgy, Vol. 15, *Reprocessing of Nuclear Fuels*, P. Chiotti, Ed., USAEC CONF-690801 (1969).

Mo-15.5 wt % Cr-5.5 wt % Fe-3.8 wt % W-2.5 wt % Co-1 wt % Mn-0.35 wt % V). Corrosion rates observed for exposures of at least 190 hr at 700°C in the metal and salt phases are shown in Fig. I-14.

The refractory metals all have low corrosion rates and are probably desirable materials for long-term operation. Embrittlement was noted (as in earlier work) in blades of Nb-1 wt % Zr, niobium, and to a less extent in the T-111 alloy exposed to the salt phase. No accelerated corrosion in the weld zone of the welded niobium specimens was observed. Electron beam welds in Mo-30 wt % W were brittle, and cracks in the weld and weld zone tended to propagate during environmental testing.

The Fe-Cr alloys, type 405 stainless steel, and Kanthal A-1 (oxidized) showed significant corrosion rates but could possibly be used for short-term expendable components. No adverse corrosion effects were noted at the weld or weld zone of the type 405 stainless steel; however, the hardness of these regions was reduced by exposure. The behavior of any tentatively selected materials must be further evaluated with respect to the effect of uranium and plutonium in the liquid solutions.

Embrittlement in salt. The embrittlement of niobium, tantalum, and their alloys when exposed to salt was investigated. Hardness and bend tests were used to evaluate the degree of embrittlement of the alloys after exposure times ranging from 0.5 to 195 hr at temperatures of 650 to 700°C.

Embrittlement of Nb-1 wt % Zr alloy was found after as little as a 1-hr exposure at 700°C, and the maximum effect was evident after only about 2.5 hr. Impurities in the argon, salt, or equipment were suspected. Testing eliminated the argon as a major contributor (Table I-3). Analyses of the gas in the region above the salt at 400°C and after 1 hr at 700°C (Table I-3) indicated that impurities in the salt were the major contributors to the embrittlement.

The formation of niobium hydride or tantalum hydride appears to be the major factor contributing to embrittlement. The hydrogen is probably from residual moisture or OH^- in the purified salt or, to a lesser degree, from adsorbed moisture on the equipment. Methods of reducing the quantity of moisture in the salt prior to use are being evaluated. Further study of salt purification methods is needed.

TABLE I-3. IMPURITIES IN FURNACE ATMOSPHERE

Impurity	Concn. (ppm) in Argon Supply	Concn. in Furnace Atmosphere	
		400°C	700°C
O_2	~25	Interference of H_2 masked the O_2	
N_2	~10	~75 ppm	~60 ppm
H_2	50–100	1.0 ± 0.1%	5.3 ± 0.5%
CH_4	<50	~300 ppm	~1000 ppm
Cl_2	—	<50 ppm	<50 ppm

(3) Solution Stability Studies (*W. J. Walsh, I. O. Winsch, T. F. Cannon*)

An experimental program was initiated to study the stability of plutonium solutions in contact with various materials of construction and in the presence of the impurities in standard grades of reagents and inert cover gas. The purpose of the study was to identify the conditions that could cause plutonium losses from solution and to determine the preventive action required. High-precision liquid-metal sampling and plutonium analytical techniques were employed to allow detection and measurement of slight plutonium losses.

Two runs with Mg-42 at. % Cu solutions containing plutonium (no salt present) were conducted at 800°C, each run having a duration of several days. Tungsten, tantalum, and Mo-30 wt % W metal surfaces were allowed to contact the metal solutions, and calcium was added to the solutions. In both runs, ~100% material balances for plutonium were achieved, and no losses of plutonium from solution were detected. It was concluded that tungsten, tantalum, and Mo-30 wt % W are compatible with Mg-Cu-Ca-Pu solutions and that the use of standard grades of copper, magnesium, and calcium reagents does not result in detectable plutonium losses. At the conclusion of one run, two additions of oven-dried $CaCl_2$-CaF_2 salt were made; duplicate samples of the liquid metal and salt were taken before and after each addition. Introduction of the salt resulted in removal from the metal and salt solutions of about 3% of the plutonium in each run, probably by reaction with impurities in the salt. It was concluded that a salt pretreatment or purification will be required. Possible procedures for $CaCl_2$-CaF_2 purification are being evaluated.

5. Laboratory Investigations (*I. Johnson*)

The objectives of the laboratory-scale investigations are to provide basic chemical data of importance to pyrochemical processing and to originate and evaluate new process concepts. During the period covered by this report, the major effort has been devoted to the further development of a pyrochemical process for fast breeder reactor fuels that employs a salt-transport separation. Salt-transport separations are based on the

selective transfer of a solute from one liquid alloy to another by the circulation of a molten salt between the two alloys. Chemical studies in support of the process development include (1) studies of the mechanism of the dissolution of stainless steel in molten zinc, (2) measurements of the solubility of zirconium in liquid Cu-Mg-Ca alloys, (3) determination of the phase diagram for the Cu-Ca-Mg system, (4) computation of the activity coefficient of neptunium in liquid magnesium, (5) study of the mechanism of UO_2 reduction by magnesium or calcium dissolved in their chlorides, (6) study of the reaction of PuO_2 with molten $MgCl_2$, (7) determination of the solubility of calcium in liquid $CaCl_2$, and (8) study of the radiolysis of a solid $MgCl_2$-NaCl-KCl salt mixture.

a. Liquid Metal Systems

Solubility and phase relations involving liquid metal systems are of importance in the development of liquid metal decladding methods, oxide reduction alloys, separation schemes based on solubility differences, and the evaluation of corrosion data. The reaction of stainless steel with liquid zinc has been studied to obtain the basic chemical data needed for the development of a liquid zinc decladding method. The solubility of zirconium in liquid Cu-Mg-Ca alloys was determined so that the behavior of fission product zirconium in the Pu-U separation step of the salt-transport process can be more accurately predicted. The phase fields and the approximate liquidus temperatures were determined for the ternary Cu-Mg-Ca alloy system used in the oxide reduction step of the salt-transport process. The activity coefficient of neptunium in liquid magnesium was computed and constituted additional thermodynamic data useful for the systematic development of processes for the separation of actinide metals.

(1) Dissolution of Stainless Steel in Liquid Zinc (*K. M. Myles, R. Yonco*)

In preliminary experiments, the dissolution-disintegration of type 304 stainless steel cladding by liquid zinc was studied to obtain data needed for the development of a liquid zinc decladding method. Known quantities of zinc shot and stainless steel bar stock were heated in quartz tubes. After heating for various times and temperatures, the alloys were cooled to room temperature. The nature of the dissolution-disintegration process was deduced by metallographic, electron microprobe, X-ray, and thermal analysis techniques.

The interrelationship between the phase diagram and the process can be seen in the photomicrograph of a partially dissolved stainless steel bar (Fig. I-15). Adjacent to the unattacked steel in the upper right of the micrograph is a wide region of iron-zinc alloy in which the grain sizes increase with distance from the steel. The grain diameters vary from less than 0.04 mm to 0.1 mm. No relationship is apparent between the size of these grains and the size of the grains in the unreacted stainless steel. A large crack runs through this region toward the stainless steel. At the lower end of the crack, the grains are of fairly uniform size, but become more thinly dispersed close to the edge of the quartz tube.

To provide a framework for explanation of the experimental results, a tentative phase diagram of the Fe-Ni-Zn system was constructed based on published information for the Ni-Zn and Ni-Fe systems and on the postulates that chromium can be considered as if it

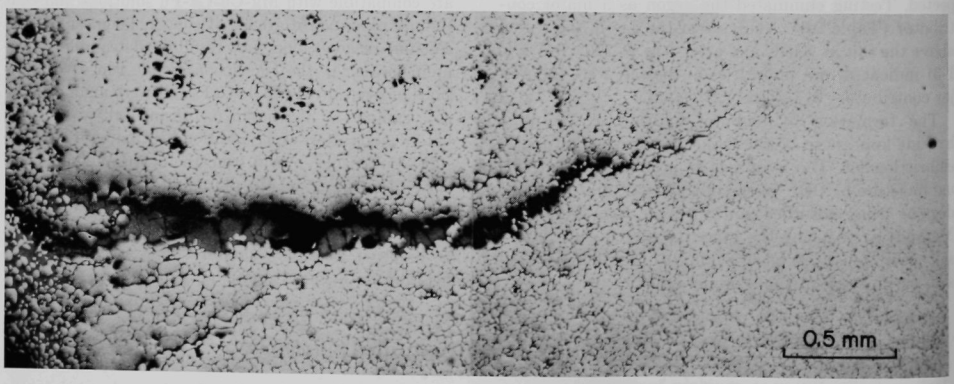

308-2223

FIG. I-15. Type 304 Stainless Steel Bar after Being Partially Dissolved by Liquid Zinc (original magnification of photomicrograph, × 50).

were iron and that the minor elements are in solid solution. The significant features of the diagram are the single-phase regions, gamma and delta, that extend across the ternary from the Fe-Zn binary to the Ni-Zn binary and the phase regions that contain the Ni-Zn beta phase and extend over to alpha iron. The occurrence of any of these intermediate phases during the dissolution-disintegration process, a condition that is quite likely at the proposed reaction temperature of 800°C, would impede reaction by forming a barrier to diffusion.

The evidence indicates that dissolution-disintegration begins with penetration of liquid zinc into the grains of stainless steel and with the preferential diffusion of nickel from stainless steel into zinc. Iron and chromium also enter the zinc, but at rates lower than that for nickel. As the surface of the stainless steel is depleted of nickel, the structure of the austenitic gamma phase transforms into the ferritic alpha phase. The first-formed alpha grains are relatively large because of their growth at the expense of small grains. The influx of zinc solution into the boundaries of the alpha grains alters the volume of the transformed region, and cracks appear as a result of the volume increase. When dissolution-disintegration at ~800°C is complete, the alpha iron grains are dispersed in the zinc and contain 11 wt % zinc.

Although the presence of the beta phase has not been conclusively shown by X-ray diffraction, photomicrographs reveal a phase surrounding the alpha grains that is presumably the beta phase. The beta phase might cause the alpha grains to agglomerate as large clinker-like particles at high stainless steel loadings in liquid zinc.

At least two additional phases, namely, gamma and delta FeNi-Zn, are formed as the zinc solution is cooled to room temperature. Since a large increase in volume, about 20%, accompanies formation of the delta phase, crucibles may fracture if the cooling rate is not controlled. Thermal analysis data indicate that the delta phase forms below 655°C.

(2) Solubility of Zirconium in Liquid Copper-Magnesium-Calcium Alloys (*I. Johnson, R. M. Yonco*)

In a pyrochemical process (salt-transport process) for the recovery and purification of spent fuel from fast breeder reactors, the fuel oxide, after decladding, is reduced to the metallic form by use of a liquid Cu-Ca-Mg alloy. The less electropositive fission product metals, if present as oxides in the fuel, are also expected to be reduced to the metallic form. At completion of reduction, the plutonium is completely in solution in the liquid alloy and most of the uranium is present as a metallic precipitate. A study was performed to obtain the solubility data needed to predict the behavior of fission product zirconium in this step of the process.

A saturated solution of zirconium in a liquid copper-magnesium alloy was prepared by heating and stirring (500 rpm) 101.9 g of zirconium, 401.9 g of copper, and 201.0 g of magnesium at 850°C for about 24 hr in a tantalum crucible. A filtered sample of the liquid was found to contain 5.95 wt % Zr-29.6 wt % Mg-59.6 wt % Cu, indicating that not all of the zirconium had dissolved. This was confirmed at the end of the experiment when several pieces of unreacted zirconium rod (weight ~55 g) were found in the ingot. The magnesium-to-copper weight ratio of the solution (0.497, compared with the ratio of 0.500 for the charge) indicates that about 1.4 g of magnesium was lost from the melt (by vaporization or oxidation) during the long holding period at 850°C. With the alloy at a specified temperature, the alloy was stirred for 2 hr and then allowed to settle for 20 min. A filtered sample of the liquid phase was taken. This procedure was repeated to obtain samples of the liquid phase at about 550, 630, 700, 770, and 850°C. The temperature sequence was arranged so that equilibrium was approached from both lower and higher temperatures. Next, the system was cooled to room temperature, the furnace tube opened (in a dry-helium-atmosphere glovebox), and calcium metal was added. Magnesium, which had collected on the cooler parts of the furnace tube, was returned to the melt. The melt was reheated and sampled at each of the temperatures listed above. Incremental additions of calcium were made to obtain a series of solutions containing between 1 and 34 wt % calcium. The samples were assayed for zirconium. Selected samples were also assayed for calcium, magnesium, and copper. The results are given in Table I-4.

An examination of the data obtained in the Series A solution (which contained no calcium) shows that the magnesium-to-copper atom ratio increases from about 1.3 at 850°C to 1.5 at 558°C. Thus, as the zirconium content of the liquid phase decreases with decreasing temperature, the relative amount of magnesium dissolved increases. The compositional changes observed as the temperature is lowered are consistent with precipitation of a zirconium-copper intermetallic compound of the approximate formula $ZrCu_2$.

The addition of calcium suppresses the solubility of zirconium. The magnesium-to-copper ratio is found to increase with decreasing temperature for those series in which calcium is present, suggesting that a zirconium-copper intermetallic compound precipitates as the temperature is lowered. For systems in which calcium is present, the formula of the precipitated phase is not well defined, ranging between $ZrCu_{0.6}$ and

$ZrCu_{2.2}$. In view of the large uncertainty of these estimates, it is not possible to specify the solubility equilibria in detail. The lower solubility of zirconium at higher calcium concentrations is probably due to an increase in the activity coefficient of zirconium with increasing calcium concentration.

(3) Phase Diagram for the Ternary System Copper-Magnesium-Calcium (*K. M. Myles, P. Mack*)

Interest in the Cu-Mg-Ca alloy system stems from the proposed use of a Cu_{42}-Mg_{58} eutectic alloy that contains various amounts of calcium to reduce chemically UO_2-PuO_2 to metal, separating uranium and plutonium from spent nuclear reactor fuel mixtures. No systematic attempt to study the phase relations of the ternary system was previously undertaken, although a large amount of information is available about the binary diagrams. Accordingly, a phase diagram for the Cu-Mg-Ca system has been derived from metallographic, X-ray diffraction, electron microprobe, and thermal analysis data.

TABLE I-4. SOLUBILITY OF ZIRCONIUM IN COPPER-MAGNESIUM-CALCIUM ALLOYS

Series	Temp (°C)	Zr (at. %)	Ca (at. %)	Mg (at. %)	Cu (at. %)
A	558	0.0931	—	60.1	39.8
	627	0.190	—	58.2	41.6
	700	(0.486)[a]	—	[b]	[b]
	771	1.041	—	58.5	40.5
	851	2.72	—	54.8	42.5
	852	2.93	—	54.9	42.2
B	549	(0.0569)	(1.2)[c]	[b]	[b]
	625	0.149	1.07	59.5	39.3
	698	(0.360)	(1.2)	[b]	[b]
	771	0.822	1.34	58.1	39.7
	846	(2.36)	(1.2)	[b]	[b]
C	550	(0.041)	(3.9)	[b]	[b]
	623	(0.103)	(3.9)	[b]	[b]
	699	0.286	3.34	57.1	39.3
	774	0.558	4.55	55.6	39.3
	849	(1.34)	(3.9)	[b]	[b]
D	549	(0.0425)	(7.8)	[b]	[b]
	620	(0.0612)	(7.8)	[b]	[b]
	696	(0.147)	(7.8)	[b]	[b]
	773	0.398	7.07	55.4	37.2
	851	0.675	8.58	52.8	37.9
E	550	0.00764	19.7	47.7	32.5
	773	0.0771	20.2	45.9	33.8
	851	(0.138)	(19.9)	[b]	[b]
F	549	(0.000913)	(35.4)	[b]	[b]
	849	0.0242	35.4	38.4	26.2

[a] Values in parentheses were computed from the zirconium content (wt %) and average atomic weight of Cu-Mg-Ca alloy.
[b] Analyses not made for magnesium and copper.
[c] Average calcium content of series.

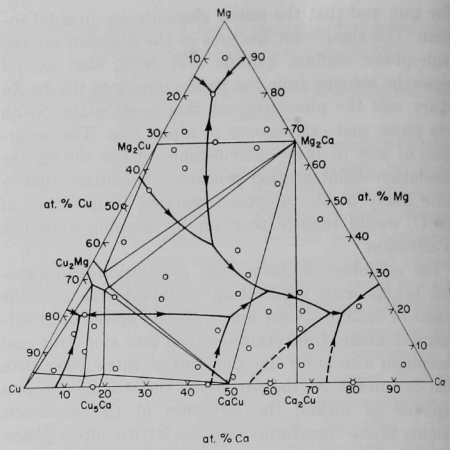

308-2059

FIG. I-16. The 350°C Isothermal Section and the Liquidus Valleys of the Cu-Mg-Ca Phase Diagram.

The phase diagram is shown in Fig. I-16; the observed phases and reactions, as well as the methods by which they were observed, are listed in Table I-5. In the figure are superimposed the liquidus valleys and an isotherm that delineates the equilibrium phase regions at 350°C. Whereas the isotherm is considered to be fairly accurate, the placement of the liquidus curves must be considered approximate to within ±3 at. %. The temperature dependence of the liquidus curves is not known, but it is apparent that the temperature decreases continuously across the diagram from the Cu-Mg binary toward the ternary eutectic near pure calcium.

Two quasi-binary sections exist in the diagram: one between Mg_2Cu and Mg_2Ca and the other between Cu_2Mg and Cu_5Ca (the Cu_2Mg-Cu_5Ca section is not strictly a quasi-binary due to the partial solid solubility of the terminal compounds). Three examples of a Class I four-phase equilibrium (ternary eutectics) are found:

$$L \rightleftarrows Mg + Mg_2Cu + Mg_2Ca \ (430°C)$$

$$L \rightleftarrows Cu + Cu_2Mg + Cu_5Ca \ (700°C)$$

$$L \rightleftarrows Ca + Mg_2Ca + Ca_2Cu \ (350°C)$$

TABLE I-5. COMPOSITIONS AND PHASES OF Cu-Mg-Ca ALLOYS

Composition (at. %)			Observed Phases[a]
Cu	Mg	Ca	
90.0	5.0	5.0	Cu(d p), Cu + Cu_5Ca(d p), Cu + Cu_5Ca + Cu_2Mg (d)
83.0	0.0	17.0	Cu_5Ca(d p)
79.8	15.2	5.0	Cu(d p), Cu + Cu_2Ca(d p), Cu + Cu_5Ca + Cu_2Mg(d)
79.9	10.1	10.0	Cu_5Ca(d p), Cu_5Ca + Cu_2Mg(d), Cu_5Ca + Cu_2Mg + Cu(d)
74.9	20.0	5.1	Cu_2Mg + Cu_5Ca(d p), Cu_2Mg + Cu_5Ca + Cu(d)
74.0	17.0	9.0	Cu_5Ca(d p), Cu_5Ca + Cu_2Mg(d p)
75.0	5.1	19.9	Cu_5Ca(d p), Cu_5Ca + Cu_2Mg(d), Cu_2Mg + CaCu
65.0	25.0	10.0	Cu_2Mg(d p), Cu_2Mg + Cu_5Ca(d), Cu_2Mg + CaCu
55.0	40.0	5.0	Cu_2Mg(d p), Cu_2Mg + Mg_2Cu(d)
54.0	24.0	22.0	Cu_2Mg(d p), Cu_2Mg + CaCu, CaCu + Mg_2Ca
54.9	5.1	40.0	Cu_5Ca(d p), Cu_5Ca + CaCu(d p), CaCu + Cu_2Mg(d p)
54.9	0.0	45.1	Cu_5Ca(d), Cu_5Ca + CaCu(d)
50.1	49.9	0.0	Cu_2Mg(d p), Cu_2Mg + Mg_2Cu(d p)
49.9	30.0	20.1	Cu_2Mg(d p), Cu_2Mg + Mg_2Ca(d p), Mg_2Ca + CaCu
48.0	2.0	50.0	CaCu(d), CaCu + Mg_2Ca, Mg_2Ca + Ca_2Cu
45.0	15.0	40.0	Cu_5Ca(p), Cu_5Ca + CaCu(d p), CaCu + Cu_2Mg(d p), CaCu + Mg_2Ca(d)
41.4	54.6	4.0	Cu_2Mg + Mg_2Cu(d p), Cu_2Mg + Mg_2Ca(d)
40.1	10.2	49.7	CaCu(d p), CaCu + Mg_2Ca(d p), Mg_2Ca + Ca_2Cu(p)
40.0	0.0	60.0	Ca_2Cu(p), CaCu(d p)
34.9	24.9	40.2	Cu_2Mg(d p), Cu_2Mg + CaCu(d p), CaCu + Mg_2Ca(d)
34.9	5.3	59.8	Ca_2Cu(p), Ca_2Cu + CaCu(d p), Ca_2Cu + Mg_2Ca
29.6	65.5	4.9	Mg_2Cu(d p), Mg_2Cu + Mg_2Ca(d), Mg_2Ca + Cu_2Mg(d)
30.0	60.0	10.0	Mg_2Cu(d), Mg_2Cu + Mg_2Ca(d), Mg_2Ca + Cu_2Mg(d)
29.0	37.0	34.0	Mg_2Ca(d p), Mg_2Ca + Cu_2Mg(d p), Mg_2Ca + CaCu(d)
30.0	30.0	40.0	Mg_2Ca(d p), Mg_2Ca + Cu_2Mg(d p), Mg_2Ca + CaCu(d p)
30.2	19.9	49.9	CaCu(d p), CaCu + Mg_2Ca(d p), Mg_2Ca + Ca_2Cu(p)
30.0	5.0	65.0	Ca_2Cu(d), Ca_2Cu + CaCu, Ca_2Cu + Mg_2Ca, Ca_2Cu + Mg_2Ca + Ca
25.0	70.1	4.9	Mg_2Cu(d p), Mg_2Cu + Mg_2Ca(d p), Mg_2Cu + Mg_2Ca + Mg(d)
25.0	14.8	60.2	CaCu(p), CaCu + Mg_2Ca(p), Mg_2Ca + Ca_2Cu(p)
25.1	10.1	64.8	Ca_2Cu(p), Ca_2Cu + CaCu(d), Ca_2Cu + Mg_2Ca
22.1	20.0	57.9	CaCu(d p), CaCu + Mg_2Ca(d p), Mg_2Ca + Ca_2Cu(p)
19.0	67.0	14.0	Mg_2Ca(d p), Mg_2Ca + Mg_2Cu(d)
19.9	25.2	54.9	Mg_2Ca(d p), Mg_2Ca + CaCu(d p), Mg_2Ca + Ca_2Cu(p)
20.0	0.0	80.0	Ca(d p), Ca + Ca_2Cu(p)
13.0	80.0	7.0	specimen not examined
10.0	65.0	25.0	Mg_2Ca(d p), Mg_2Ca + Mg_2Cu(d)
10.0	55.0	35.0	Mg_2Ca(d p), Mg_2Ca + Cu_2Mg(d p), Mg_2Ca + CaCu(d p)
8.1	20.9	71.0	Ca(p), Ca + Ca_2Cu(p), Ca + Ca_2Cu + Mg_2Ca
5.0	90.1	4.9	Mg(d p), Mg + Mg_2Ca(d p), Mg + Mg_2Ca + Mg_2Cu(d)
5.0	70.0	25.0	Mg_2Ca(d p), Mg_2Ca + Mg_2Cu(d p), Mg_2Ca + Mg_2Cu + Mg(d)
4.8	45.1	50.1	Mg_2Ca(d p), Mg_2Ca + Ca(p), Mg_2Ca + Ca + Ca_2Cu(p)
5.0	5.0	90.0	Ca(d p), Ca + Ca_2Cu, Ca + Ca_2Cu + Mg_2Ca

[a] Metallographic techniques identified all of the listed phases and reactions; the observations were supported by X-ray diffraction (d) and electron microprobe (p) methods.

Four Class II type four-phase equilibria are found:

$$L + Mg_2Cu \rightleftarrows Cu_2Mg + Mg_2Ca$$

$$L + Cu_5Ca \rightleftarrows Cu_2Mg + CaCu$$

$$L + Cu_2Mg \rightleftarrows CaCu + Mg_2Ca$$

$$L + CaCu \rightleftarrows Ca_2Cu + Mg_2Ca$$

The temperatures of these latter reactions were not determined. No Class III four-phase invariant reactions (ternary peritectics) were observed.

The binary systems were not investigated *per se;* however, the results of this study necessitate revision of the tentative Ca-Cu binary diagram given by Hansen and Anderko.[18] A phase with the highly speculative stoichiometry of Ca_4Cu was previously reported.[19] The present microprobe results indicate that the actual stoichiometry is approximately Ca_2Cu. In addition, a

[18] M. Hansen, K. Anderko, "Constitution of Binary Alloys," pp. 395, 401, and 594, McGraw-Hill, New York (1958).

[19] N. Baar, *Z. Anorg. Chem.* **70**, 377 (1911).

TABLE I-6. DIFFRACTION DATA OF THE INTERMEDIATE PHASES CaCu AND Ca_2Cu (CuKα RADIATION)

CaCu		Ca_2Cu	
d(Å)	I	d(Å)	I
5.49	50	7.24	90
4.49	20	5.63	70
3.86	50	3.155	30
2.858	90	3.112	40
2.735	80	2.985	60
2.305	100	2.811	100
2.128	90	2.623	40
1.939	40	2.586	50
1.869	40	2.469	20
1.682	80	2.333	80
1.465	50		
1.434	40		
1.336	40		
1.305	70		
1.261	80		
1.234	30		
1.210	50		

new phase has been discovered that has the stoichiometry CaCu. The existence of a compound of this composition was previously assumed by Nowotny.[20] This choice of stoichiometry is strengthened by the occurrence of the compound CaZn, which exhibits a similar powder pattern to CaCu.[21] The *d*-spacings and relative intensities of the major lines associated with Ca_2Cu and with CaCu are given in Table I-6. Both Ca_2Cu and CaCu are line compounds that melt congruently. Although the temperatures of the reactions in the CaCu binary were not determined, they may well be related to those given in Hansen and Anderko. Unfortunately, difficulties in preparing oxide-free and nitride-free melts precluded a careful investigation of the very calcium-rich alloys.

The diagram shows that at 800°C (the proposed operating temperature for the pyrochemical process), roughly 80 at. % Ca can be added to the Cu-Mg eutectic alloy, and it will still remain completely liquid.

(4) Activity Coefficient of Neptunium in Liquid Magnesium (*I. Johnson*)

The activity coefficient of neptunium in liquid magnesium has been computed from experimental data (see ANL-7425, p. 27) on the distribution of neptunium between a liquid $MgCl_2$-NaCl-KCl salt mixture and various liquid Cd-Mg alloys. The distribution of neptunium between the molten ternary salt mixture and the liquid cadmium-magnesium alloy may be represented by the equilibrium

$$NpCl_3(\text{salt}) + \tfrac{3}{2}Mg(\text{alloy}) \rightleftarrows Np(\text{alloy}) + \tfrac{3}{2}MgCl_2(\text{salt}) \quad (1)$$

The equilibrium constant relation may be used to derive the equation (see ANL-7125, p. 146 and ref. 22)

$$\ln \gamma_{Np} = \ln D + \tfrac{3}{2} \ln X_{Mg} + \tfrac{3}{2} \ln \gamma_{Mg} + \ln K_s \quad (2)$$

where γ_{Np} = activity coefficient of Np in liquid alloy
$D = X_{NpCl_3}/X_{Np}$ (distribution coefficient)
X_{NpCl_3} = mole fraction $NpCl_3$ in the molten salt
X_{Np} = atom fraction Np in the liquid alloy
X_{Mg} = atom fraction Mg in the liquid alloy
γ_{Mg} = activity coefficient of Mg in the liquid alloy
$K_s = K_a\, \gamma_{NpCl_3}/a_{MgCl_2}^{3/2}$
K_a = thermodynamic (activity) equilibria constant for reaction 1
γ_{NpCl_3} = activity coefficient of $NpCl_3$ in the molten salt
a_{MgCl_2} = activity of $MgCl_2$ in the molten salt

The procedure used to compute the activity coefficient of neptunium in liquid magnesium utilizing Eq. 2 has been reported.[22] Briefly, limiting values of the quantity $\ln D + \tfrac{3}{2} \ln X_{Mg}$ are determined as $X_{Mg} \to 0$ and $X_{Mg} \to 1$, and these limiting values are then used to compute the activity coefficient using the equation

$$\ln \gamma_{Np(Mg)} = [\ln D + \tfrac{3}{2} \ln X_{Mg}]_{X_{Mg}\to 1} - [\ln D + \tfrac{3}{2} \ln X_{Mg}]_{X_{Mg}\to 0} - \tfrac{3}{2} \ln \overset{0}{\gamma}_{Mg(Cd)} + \ln \gamma_{Np(Cd)} \quad (3)$$

where $\gamma_{Np(Mg)}$ and $\gamma_{Np(Cd)}$ are the activity coefficients of neptunium in dilute solutions of magnesium and cadmium and $\overset{0}{\gamma}_{Mg(Cd)}$ is the activity coefficient of magnesium in an infinitely dilute solution of liquid cadmium.

The limiting values of $\ln D + \tfrac{3}{2} \ln X_{Mg}$ were determined by a graphical procedure (Fig. I-17). Values of $\overset{0}{\gamma}_{Mg(Cd)}$ were obtained from Hultgren's compilation,[23] and values of $\gamma_{Np(Cd)}$ were computed from high-temperature galvanic cell data on the Np-Cd system (see ANL-7575, p. 27). Numerical details of the computation are given in Table I-7.

No other data on the activity coefficient of neptunium in liquid magnesium have been reported. The large positive deviations from ideal behavior discovered in the present study suggest that the neptunium-mag-

[20] H. Nowotny, *Z. Metallk.* **34**, 247 (1942).

[21] A. F. Messing, M. D. Adams, R. K. Steunenberg, *Transactions Quarterly* **56**, 345 (1963).

[22] I. Johnson, J. B. Knighton, R. K. Steunenberg, *Trans. TMS-AIME* **236**, 1242 (1966).

[23] R. Hultgren, R. L. Orr, K. K. Kelley, *Supplement to Selected Values of Thermodynamic Properties of Metals and Alloys, Cadmium-Magnesium System*, Univ. of California, Berkeley, Calif. (1966).

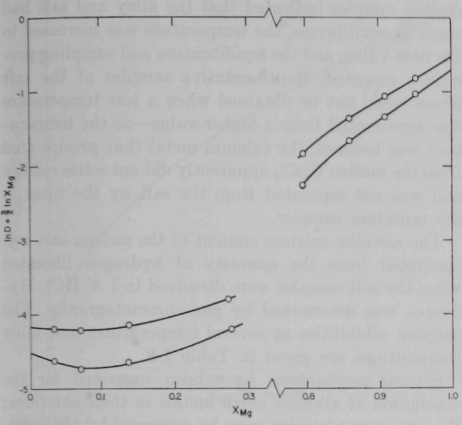

308-2060

FIG. I-17. Dependence of $\ln D + \frac{3}{2} \ln X_{Mg}$ on X_{Mg} for the Distribution of Neptunium Between 50 mol % $MgCl_2$-30 mol % NaCl-20 mol % KCl and Cadmium-Magnesium Alloys.

nesium system should exhibit a liquid-liquid miscibility gap. Another reason for expecting a miscibility gap in the neptunium-magnesium system is the existence of miscibility gaps in both the uranium-magnesium and plutonium-magnesium systems.

The composition of the two liquid phases for the neptunium-magnesium system was estimated on the assumption that the concentration dependence of the activity coefficient of neptunium is similar to that of plutonium.[24] At 650°C the neptunium content of the magnesium-rich phase is estimated to be 4.4 at. % (31 wt %) while the neptunium-rich phase would contain only 0.02 wt % magnesium. Thus, the mutual solubilities of liquid neptunium and magnesium are expected to be smaller than those observed in the plutonium-magnesium system, but much larger than those reported for the uranium-magnesium system.[25]

b. Molten Salt Systems

The major separation processes of the pyrochemical process for FBR fuels involve the use of molten salts as reaction media. A study has been made of the role of the salt phase in the reduction of UO_2. The reaction of PuO_2 with molten $MgCl_2$ has been studied, and the solubility of calcium in molten $CaCl_2$ has been measured.

[24] W. Knoch, J. B. Knighton, R. K. Steunenberg, *Symposium on Reprocessing of Nuclear Fuels*, P. Chiotti, Ed., USAEC CONF-690801, pp. 535–546 (1969).

[25] P. Chiotti, H. E. Shoemaker, *Ind. Eng. Chem.* **50**, 137–140 (1958).

(1) Reduction of UO_2 by Magnesium or Calcium Dissolved in Molten Chlorides (*R. A. Sharma, I. Johnson*)

A paper, "Study of the Reduction of UO_2 by Magnesium or Calcium Dissolved in Molten Chlorides" by Ram A. Sharma and Irving Johnson, has been published [*Metallurgical Transactions* **1**, 291–297 (1970)]. The abstract of this paper is as follows:

> The reduction of solid UO_2 to uranium by magnesium or calcium dissolved in their molten chlorides has been studied. The rate of reduction per unit area of UO_2 surface, at constant temperature and concentration of reductant in the molten chloride, was found to increase with time to a constant value. The rate of reduction per unit area was observed to be proportional to the concentration of reductant in the molten salt. The small increase observed in the reaction rate over the temperature range 750–850°C suggests that the reduction is controlled by transport of the reductant to the reaction site.
>
> Solidified salt, containing UO_2 pellets which had been partially reduced, was sectioned, polished, and examined microscopically. The products of the reduction reaction form concentric layers around the UO_2 pellets. Layers of metallic uranium and oxide containing small amounts of dispersed salt alternated with layers of salt containing small amounts of metallic uranium and oxide. The layers were ruptured, presumably because the volume of the products (uranium and oxide) is greater than the volume of the UO_2. Therefore, an impervious layer did not form on the oxide surface to inhibit the reduction reaction.

(2) Reaction of PuO_2 with Molten $MgCl_2$ (*D. A. Wenz, I. Johnson*)

In a study of the solubility of oxides in molten salts (ANL-7375, p. 30), it was found that PuO_2 is much

TABLE I-7. Computation of the Activity Coefficient of Neptunium Dissolved in Liquid Magnesium from Distribution Data

	Temp	
	650°C	700°C
$[\ln D + \frac{3}{2} \ln X_{Mg}]_{X_{Mg}\to 0}$	−4.525	−4.170
$[\ln D + \frac{3}{2} \ln X_{Mg}]_{X_{Mg}\to 1}$	−0.700	−0.525
$\frac{3}{2} \ln \gamma^0_{Mg(Cd)}$ (Ref. 25)	−3.271	−3.064
$\ln \gamma_{Np(Cd)}$ (ANL-7575, p. 27)	−3.946	−3.934
$\ln \gamma_{Np(Mg)}$	3.150	2.775
$\gamma_{Np(Mg)}$	23.3	16.0

TABLE I-8. SOLUBILITY OF CALCIUM IN LIQUID $CaCl_2$ IN EQUILIBRIUM WITH LIQUID Ca-Cu ALLOYS

Calcium (atom fraction) in Ca-Cu Alloy	Mol % Calcium in $CaCl_2$			
	800°C	850°C	900°C	925°C
0.30	0.263	0.335		0.473
0.43	0.576	0.624	0.668	0.69
0.55	0.820	1.078		1.647
0.63	1.66	1.926		2.33
0.70	1.737	2.061		2.435
0.76	1.796	2.322		2.801
1.00	2.142	2.748	3.257	3.466
	(2.45 at 830°C)			(3.598 at 940°C)

more soluble than UO_2 in molten salts that contain $MgCl_2$. A more detailed study, described in a brief communication,[26] showed that the reaction describing PuO_2 dissolution in molten $MgCl_2$ salts may be written

$$PuO_2 + MgCl_2 \rightarrow PuOCl + MgO + \tfrac{1}{2}Cl_2$$

The reaction is very slow and incomplete when performed in fused silica equipment, but is rapid in tantalum equipment. Tantalum reacts with the evolved chlorine and therefore provides more thermodynamic driving force for the reaction. It was also shown that lead or zinc provide a chloride sink.

(3) Solubility of Calcium Metal in Molten $CaCl_2$ (*R. A. Sharma*)

The reduction of UO_2 under the conditions employed in the pyrochemical process has been shown to occur by a mechanism that involves the transport of the reductant metal (calcium) from the reductant alloy (Cu-Mg-Ca) through the reductant salt ($CaCl_2$-CaF_2) to the surface of the UO_2 pellet. Thus, the rate of reduction may be expected to depend upon the solubility of calcium in the molten salt. The calcium content of liquid $CaCl_2$ in equilibrium with liquid Ca-Cu alloys has been measured as a function of the calcium concentration in the alloy and the temperature.

The experimental procedure has been described in connection with a study of the solubility of magnesium in molten $MgCl_2$.[27] Briefly, a liquid Ca-Cu alloy of known composition and molten anhydrous $CaCl_2$ were held in a tantalum crucible at a desired temperature (800, 850, 900, or 925°C) until equilibrium was established. Filtered samples of the salt were taken using tantalum samplers. When the calcium content of successive samples indicated that the alloy and salt had come to equilibrium, the temperature was increased to the next value, and the equilibration and sampling procedure repeated. Representative samples of the salt phase could not be obtained when a test temperature was approached from a higher value—as the temperature was lowered, the calcium metal that precipitated from the molten $CaCl_2$ apparently did not settle readily and was not separated from the salt by the filter in the tantalum sampler.

The metallic calcium content of the molten salt was computed from the quantity of hydrogen liberated when the salt samples were dissolved in 1 *N* HCl. Hydrogen was determined by gas chromatography. The calcium solubilities at several temperatures and alloy compositions are given in Table I-8.

Several mechanisms have been suggested for the dissolution of alkaline earth metals in their chlorides; the two more plausible may be expressed by the equations

$$Ca + CaCl_2 = 2CaCl \quad (1)$$

$$Ca + CaCl_2 = Ca_2Cl_2 \quad (2)$$

i.e., the formation of a subchloride (CaCl) or the diatomic cation (Ca_2^{++}). In the present case, since a calcium-copper alloy was used, the dependence of the metallic calcium content of the $CaCl_2$ on the calcium activity in the alloy may be used to determine which of the two equations best fits the data. If dissolution is by Reaction 1, the solubility of calcium in the salt is proportional to the square root of the calcium activity in the alloy

$$x_{Ca(CaCl_2)} = (K_1\, a_{CaCl_2})^{1/2} a_{Ca}^{1/2} \quad (3)$$

The solubility is directly proportional to the calcium activity in the alloy if dissolution is by the second reaction

$$x_{Ca(CaCl_2)} = K_2\, a_{CaCl_2} a_{Ca} \quad (4)$$

where K_1 and K_2 are the thermodynamic equilibrium constants for Reactions 1 and 2, respectively; a_{CaCl_2} is the activity of $CaCl_2$ in the molten salt (approximately unity); and a_{Ca} is the activity of calcium in the molten alloy. A plot of the solubility of calcium in $CaCl_2$ *vs.* the activity of calcium in the alloy at 925°C is shown in Fig. I-18. The values of the activity of calcium in the Ca-Cu alloys were estimated from the values of the activity of calcium in Ca-Zn alloys since no experimental data for the Ca-Cu system have been reported. It is seen that the data are in agreement with Eq. 3. Thus the dissolution of calcium in $CaCl_2$ probably occurs by the first reaction.

[26] D. A. Wenz, I. Johnson, *Inorg. Nucl. Chem. Lett.* **4**, 735 (1968).

[27] M. Krumpelt, J. Fischer, I. Johnson, *J. Phys. Chem.* **72**, 506 (1968).

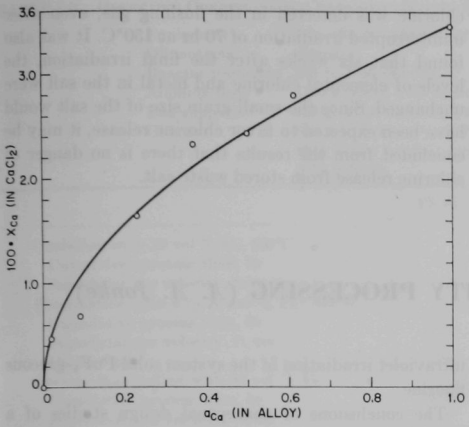

308-2159

FIG. I-18. Calcium Content of Liquid $CaCl_2$ in Equilibrium with Ca-Cu Alloys at 925°C.

c. Radiolysis of $MgCl_2$-NaCl-KCl (*M. Krumpelt, J. Heiberger*)

Ionic salts are known to be considerably more radiation resistant than covalently bonded substances. This higher radiation resistance was one reason for the development of pyrochemical fuel reprocessing schemes. In the salt-transport process (ANL-7575, p. 29), the solvent salts would not only be exposed to intense irradiation during the reprocessing operation, but would, after solidification, also serve as a storage medium for fission products. The integrated absorbed dose from fission products could reach very high levels in

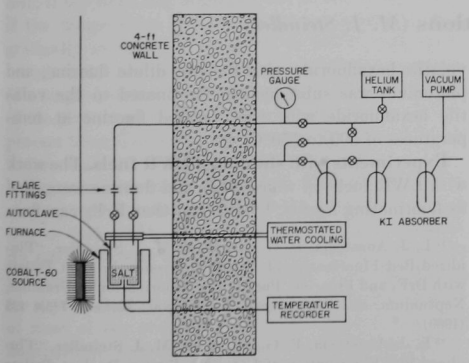

308-2160

FIG. I-19. Radiolysis Apparatus.

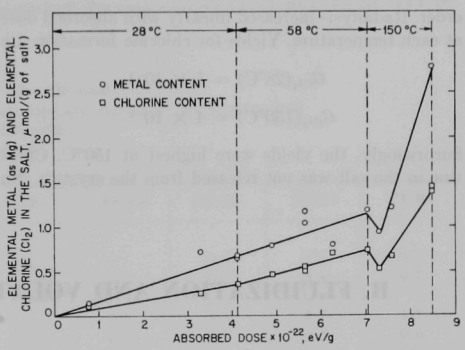

308-2161

FIG. I-20. Metal and Chlorine Content in Irradiated $MgCl_2$-NaCl-KCl.

the stored waste salt, and it was of interest to investigate whether a release of chlorine could result from the high exposure.

A salt waste stream ($MgCl_2$-30 mol % NaCl-20 mol % KCl-3 mol % MgF_2) that contains the rare earth fission products is estimated to absorb 10^{21} eV g^{-1} hr^{-1} of beta and gamma energy during the early storage period. To evaluate the effects of high radiation fluxes, a $MgCl_2$-30 mol % NaCl-20 mol % KCl salt was irradiated in the cobalt-60 cave of Argonne's Chemistry Division for a total of 236 hr. The apparatus, schematically shown in Fig. I-19, was fabricated of nickel and nickel alloys that were chlorinated prior to the experiment. The Inconel autoclave had a Conflat[28] flange and a copper gasket. About 100 g of purified salt, with a particle size ranging from 0.25 to 0.59 mm, was irradiated in turn at 28, 58, and 150°C. The dose rate was 3.6×10^{20} eV g^{-1} hr^{-1} for the 28 and 58°C irradiations and 1.3×10^{20} for the 150°C irradiation. The apparatus was occasionally flushed with helium, which was passed through KI absorbers to trap any released chlorine. The salt was periodically sampled and analyzed for metal and elemental chlorine. The hydrolysis apparatus used for metal analysis has been described.[29] Chlorine was determined by dissolving a sample in a 4% KI solution and titrating the liberated iodine with thiosulfate.

Metal and chlorine concentrations in the salt samples, plotted against absorbed dose, are given in Fig. I-20. Chlorine and metal concentrations are of the same

[28] W. R. Wheeler, *Trans. Tenth American Vacuum Society Symp.*, p. 163, Macmillan Corp., New York (1963).

[29] M. Krumpelt, J. Fischer, I. Johnson, *J. Phys. Chem.* **72**, 506 (1968).

order. Radiolysis increased linearly with absorbed dose at each temperature. Yields for chlorine formation are

$$G_{Cl_2}(28°C) = 5 \times 10^{-4}$$

$$G_{Cl_2}(150°C) = 4 \times 10^{-3}$$

Surprisingly, the yields were highest at 150°C. Chlorine in the salt was not released from the crystals. No chlorine was detected in the flushing gas, even after uninterrupted irradiation of 70 hr at 150°C. It was also found that six weeks after the final irradiation, the levels of elemental chlorine and metal in the salt were unchanged. Since the small grain size of the salt would have been expected to favor chlorine release, it may be concluded from the results that there is no danger of chlorine release from stored waste salt.

B. FLUIDIZATION AND VOLATILITY PROCESSING (*A. A. Jonke*)

Fluidization and fluoride volatility studies conducted in the Chemical Engineering Division have made significant contributions to the technology of nuclear fuel cycles. The basis for the fluoride volatility processing method is the reaction of fluorinating agents with fuel materials in fluid-bed systems to produce the volatile hexafluorides of uranium and plutonium, which are separable from nonvolatile fission product compounds. Since volatile fluorides of certain fission product elements accompany UF_6 and PuF_6, additional separation procedures are necessary to produce purified products.

Laboratory investigations during the report period concerned (1) a method for the separation of uranium from plutonium in the fluorination step of the fluoride volatility process for oxidic FBR fuel, (2) the identification of ruthenium fluoride species in product streams from an oxyfluorination step, (3) the sorption of ruthenium fluorides in cold traps, (4) the reaction of PuF_6 with LiF, and (5) the synthesis of PuF_6 by ultraviolet irradiation of the system solid PuF_4-gaseous fluorine.

The conclusions of conceptual design studies of a large fluoride volatility plant for processing FBR fuels are reported, as are the results of supporting studies on pulsed beds; a continuous-feed, two-stage slab fluid-bed reactor; dense-phase transport of granular solids; and heat transfer from a heated surface to a fluidized bed.

The results of the conceptual design and evaluation study indicate that fluoride volatility methods have good potential for application to LMFBR fuels. However, owing to a decision by the AEC to emphasize the development of aqueous reprocessing methods for this application, the program on fluoride volatility process development is being terminated. Work will continue on the application of fluidization technology to other portions of the fast breeder reactor fuel cycle.

1. Laboratory Investigations (*M. J. Steindler*)

a. Fluorination of UO_2-PuO_2-Fission Product Pellets in a 2-in. Dia Fluid-Bed Reactor (*L. J. Anastasia, D. Raue, M. Haas, R. V. Kinzler*)

A 2-in. dia fluid-bed reactor[30] was used to study the fluorination of uranium and plutonium from simulated discharged reactor fuels containing nonradioactive fission products corresponding to burnups of 10,000 MWd/metric ton for LWR fuels and 100,000 MWd/metric ton for FBR fuels. In these studies, the UO_2-PuO_2 fuel was usually first oxidized to U_3O_8-PuO_2 fines with oxygen. Uranium was then fluorinated to the volatile hexafluoride with BrF_5 or dilute fluorine, and plutonium was subsequently fluorinated to the volatile hexafluoride with concentrated fluorine at temperatures of 300 to 550°C.

Experiments with simulated LWR fuels. The work with LWR fuels, in which BrF_5 and fluorine were used as fluorinating agents,[31-33] showed that BrF_5 can fluo-

[30] L. Anastasia, P. Alfredson, M. Steindler, G. Redding, J. Riha, M. Haas, "Laboratory Investigations in Support of Fluid-Bed Fluoride Volatility Processes. Part XVI. The Fluorination of UO_2-PuO_2-Fission-product Oxide Pellets with Fluorine in a 2-inch-diameter Fluid-Bed Reactor," ANL-7372 (1967).

[31] L. J. Anastasia, P. G. Alfredson, M. J. Steindler, "Fluidized-Bed Fluorination of UO_2-PuO_2-Fission Product Pellets with BrF_5 and Fluorine. Part I. The Fluorination of Uranium, Neptunium, and Plutonium," *Nucl. Appl. Technol.* **7**(5), 425 (1969).

[32] L. J. Anastasia, P. G. Alfredson, M. J. Steindler, "Fluidized-Bed Fluorination of UO_2-PuO_2-Fission Product Pellets with BrF_5 and Fluorine. Part II. Process Considerations," *Nucl. Appl. Technol.* **7**(5), 433 (1969).

[33] M. J. Steindler, L. J. Anastasia, L. E. Trevorrow, A. A. Chilenskas, "Laboratory Development of the Fluoride Vola-

TABLE I-9. OPERATING CONDITIONS FOR EXPERIMENTS WITH SIMULATED FAST BREEDER REACTOR FUELS, RUNS FF-B1 TO FF-B6

Equipment:	2-in. dia fluid-bed reactor
Diluent gas:	nitrogen
Reactor pressure:	880 to 1330 mm Hg
Alumina bed:	1100 g Alcoa T-61 alumina, −40 +170 mesh
Bed support:	150 g ¼-in. to 8-mesh alumina chips and one 0.5-in. dia alumina ball
Charge:	650 g UO_2-20 wt % PuO_2 (−325 mesh)
	69 g fission product oxide mixture
	0.75 g NpO_2

	FF-B1	FF-B2	FF-B3	FF-B4	FF-B5	FF-B6
Oxidation with 20 vol % O_2, 450°C						
Cumulative process time, hr	—	—	—	0–4	0–4	0–4
Superficial gas velocity, ft/sec[a]	—	—	—	0.8	0.8	0.7
Fluorination with 8 to 20 vol % F_2,[b] 350°C						
Cumulative process time, hr	0–3	0–3	0–3	4–7	4–7	4–7
Superficial gas velocity, ft/sec	0.7	0.7	0.6	0.7	0.7	0.6
Diluent gas	N_2	N_2	[c]	O_2	O_2	O_2
Recycle-fluorination with 90 vol % F_2						
Cumulative process time, hr	3–11	3–11	3–11	7–15	7–15	7–15
Superficial gas velocity, ft/sec	0.6	0.4	0.4	0.4	0.4	0.4
Cumulative time (hr) at 400°C		3–7			7–11	7–11
500°C	3–7		3–7	7–11		
550°C	7–11	7–11	7–11	11–15	11–15	11–15

[a] Calculated for operating temperature and pressure.
[b] 8 vol % F_2 for the first 0.5 hr, 20 vol % F_2 thereafter.
[c] 20 vol % F_2, 20 vol % O_2, and 60 vol % N_2 used for this fluorination step.

rinate more than 99% of the uranium at high rates under controlled conditions and with an acceptable utilization of BrF_5. The BrF_5 fluorination provides a preliminary separation of uranium from plutonium, and then plutonium is recovered in a subsequent fluorination step with concentrated fluorine. Volatile NpF_6 forms in both fluorination steps, and the neptunium distributes about equally between the UF_6 and PuF_6 products. Fluorination conditions with BrF_5 and fluorine affect the residual plutonium concentrations in the bed; if the BrF_5 step is carried out at 250 to 350°C and if the temperature in the subsequent fluorine step is gradually increased from 300°C to 550°C, then residual plutonium in the fluidized bed following processing of a single batch of fuel is routinely held to 3% or less of the plutonium charged. Reuse of the alumina bed to process three batches of fuel reduces the plutonium loss to less than 1% of the plutonium charged.

Experiments with simulated FBR fuels. Initial scoping experiments simulating the processing of fast reactor fuels (UO_2-20 wt % PuO_2) by fluoride volatility methods consisted of a fractional factorial series of five experiments (ANL-7575, p. 49). Each experiment consisted of an oxidation step, followed by fluorination of most of the uranium with dilute fluorine and then fluorination (recycle-fluorination) of the plutonium with 90 vol % fluorine. In these tests the effects on plutonium in the final fluidized bed were determined for two levels of fuel-to-alumina ratio (0.3 and 0.6), two fluorination temperatures with 10 vol % F_2 (350 and 450°C), and two recycle-fluorination sequences (10 and 20 hr). Results indicated that the fraction of plutonium remaining in the final bed is increased by (1) using a fuel-to-alumina ratio of 0.6 rather than 0.3, (2) fluorinating with dilute fluorine at 450°C rather than at 350°C, and (3) using a 10-hr recycle-fluorination sequence rather than a 20-hr sequence.

A second set of statistically designed fluorination experiments, Runs FF-B1 to FF-B6, was completed for two conditions of each of the following variables: (1) oxidation of the UO_2-20 wt % PuO_2 fuel (yes or no), (2) recycle-fluorination sequence (4 hr at 400°C and 4 hr at 550°C, or 4 hr at 500°C and 4 hr at 550°C), and (3) a slow or rapid increase in fluorine concentration during the first hour of recycle-fluorination. The fluorination steps consisted of (1) fluorination of the oxidized fuel or alternatively the as-charged fuel with 8 to 20 vol % F_2 at 350°C to remove uranium and (2) the recycle-fluorination step with 90 vol % F_2 to remove plutonium. The charge for each experiment was 650 g of 20 wt % PuO_2-UO_2 powder, 1100 g of −40 +170 mesh alumina, 69 g of nonradioactive fission product oxides simulating a burnup of 100,000 MWd/metric ton, and 0.75 g NpO_2. The operating conditions for these experiments are summarized in Table I-9, and the experimental design and results are given in Table I-10. In Run FF-B3 (with no oxidation step), the fuel

tility Process for Oxidic Nuclear Fuels," Symposium on Reprocessing of Nuclear Fuels, Ames, Iowa, 1969, USAEC report CONF-690801.

TABLE I-10. EXPERIMENTAL DESIGN AND RESULTS FOR FLUORIDE VOLATILITY PROCESSING OF SIMULATED FAST REACTOR FUELS

Fuel/Al_2O_3: 0.6
Initial fluorination: 8–20 vol % F_2 at 350°C for 3 hr

Variables:
Oxidation Step[a]
+: Yes, 20 vol % O_2, 4 hr, 450°C
−: No oxidation step
Initial Temperature of Recycle-Fluorination
+: 4 hr at 500°C and 4 hr at 550°C
−: 4 hr at 400°C and 4 hr at 550°C
Fluorine Buildup for Recycle-Fluorination
+: Increase to 90 vol % as quickly as possible (~35 min)
−: Increase to 90 vol % in 1 hr

Run	Variables			Wt % Pu in Final Bed Samples		Percent of Pu Charge in Final Bed[b]	
	Oxidation	Initial Fluorination Temperature	Fluorine Buildup	Fluidized Sample	Riffled Sample	Fluidized Sample	Riffled Sample
FF-B1	−	+	+	0.19	0.21	1.9	2.2
FF-B2	−	−	−	0.16	0.16	1.6	1.6
FF-B3[c]	−	+	−	(0.10)[c]	(0.18)[c]	(1.0)[c]	(1.8)[c]
FF-B4	+	+	−	0.20	0.20	2.1	2.0
FF-B5	+	−	+	0.09	0.18	0.9	1.8
FF-B6	Repeat of FF-B5			0.10	0.11	1.0	1.1

[a] When an oxidation step was used, the uranium was first fluorinated with 8–20 vol % F_2 in oxygen (Runs FF-B4, -B5, and -B6); in two of the runs in which oxidation was omitted (FF-B1 and FF-B2), the diluent gas for the uranium fluorination step was nitrogen.

[b] Based on wt % Pu in sample. Bed was assumed to contain 1100 g Al_2O_3 and 87 g fission product fluorides.

Uranium was fluorinated with 20 vol % F_2, 20 vol % O_2 and 60 vol % N_2; a bed cake developed, and this run was omitted from the statistical evaluation.

was initially fluorinated with 20 vol % F_2, 20 vol % O_2, and 60 vol % N_2 to remove uranium. Two agglomerates (46 and 195 g) were recovered from the reactor after Run FF-B3; therefore, this run was omitted from the statistical evaluation of the experiments. In the subsequent experiments, FF-B4 to FF-B6, an oxidation step was used before fluorination of the bulk of the uranium; fluorination was with 8 to 20 vol % F_2 in oxygen. Oxygen rather than nitrogen was used as diluent in the uranium fluorination step of these experiments to simulate the proposed flowsheet for fast reactor fuels (ANL-7575, p. 70).

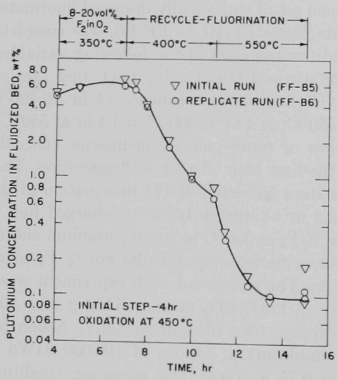

308-2162

FIG. I-21. Plutonium in Fluidized Bed in Replicate Experiments Following Oxidation for 4 hr at 450°C.

Results and discussion. The results listed in Table I-10 were obtained from two samples of the final fluidized bed; one sample was obtained while the bed was fluidized in the reactor, and the other was a riffled sample of the final bed after it had been dumped from the reactor. The statistical results indicate that the plutonium content of the final bed can be reduced by using an oxidation step, by increasing the fluorine concentration quickly at the start of the recycle-fluorination step, and by using 400°C rather than 500°C as the initial recycle-fluorination temperature.

The two replicate experiments, Runs FF-B5 and FF-B6, demonstrated that operating conditions can be chosen that will reduce residual plutonium in the fluidized bed to 1% or less of the charge; plutonium concentrations in the fluidized bed throughout these two experiments were in excellent agreement, as shown in Fig I-21.

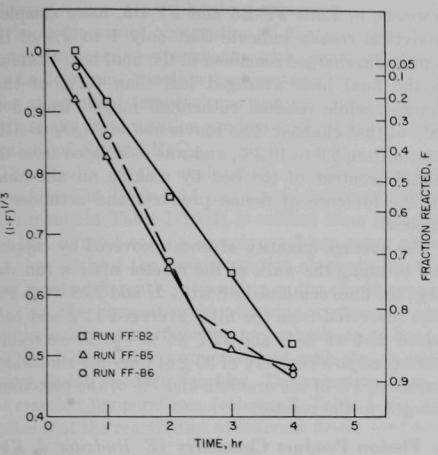

308-1866

FIG. I-22. Plutonium Fluorination from Fluidized Bed at 400°C.

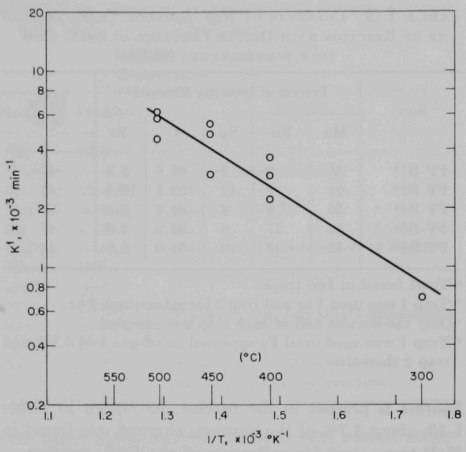

308-1867

FIG. I-23. Effect of Temperature on Plutonium Fluorination Rate Constants During Initial Recycle-Fluorination Period.

The highest rates for plutonium fluorination were observed during the initial period of recycle-fluorination. The reaction appears to follow the diminishing-sphere model during this period, as shown by the curves in Fig. I-22 for Runs FF-B2, -B5, and -B6. Rate constants calculated for the reaction for the current experiments and for previous experiments (ANL-7575, p. 54) are shown in Fig. I-23 as a function of temperature. The slope of the least-squares fit for these data gives an apparent activation energy of 8.6 kcal/mol for the fluorination of PuF_4 with fluorine, which is in good agreement with literature values[34-36] of 8.7 to 15.5 kcal/mol for the temperature range 170 to 500°C.

As shown in Table I-11, the production rates for PuF_6 are not materially lowered when recycle-fluorination is started at the lower temperature. The average rate of production for PuF_6 at 400°C was 2.2 lb/(hr)(ft²) with the reactor operated at an average of 53% of equilibrium for the reaction $PuF_4(s) + F_2(g) \rightleftarrows PuF_6(g)$. At 500°C the average PuF_6 production rate was 2.4 lb PuF_6/(hr)(ft²) at only 28% of equilibrium.

Distribution of actinides and selected fission products. In the initial set of experiments, Runs FF-A1 to FF-A5 (ANL-7575, p. 53), separation of uranium from plutonium during the fluorination step with dilute fluorine was demonstrated. Similar results were obtained for the second set of experiments as determined from the uranium and plutonium in two NaF product-collection traps. The U/Pu ratio in the product traps was 43 to 81 (Table I-12), compared with a U/Pu ratio of 4 in the fuel charge. In the replicate experiments, FF-B5 and FF-B6, high U/Pu ratios in the first trap (5280 and 3700, respectively) were observed by switching product collection from the first to the second NaF trap when fluorine appeared in the off-gas, indicating that most of the uranium had been fluorinated. (In previous experiments, no fluorine was detected in the off-gas when the traps were switched after one hour of fluorination.) The U/Pu ratios in the second NaF trap were 8 and 5 for FF-B5 and FF-B6, respectively, indicating that more pluntonium fluorinates during the dilute fluorination step when excess

TABLE I-11. PRODUCTION RATES FOR PuF_6 DURING INITIAL RECYCLE-FLUORINATION PERIOD

Run	Temp. (°C)	PuF_6 Production [lb/(hr)(ft²)]	Reaction Equilibrium[a] (%)
FF-B1	500	2.3	23.1
FF-B2	400	2.0	46.5
FF-B4	500	2.5	33.7
FF-B5	400	2.4	61.1
FF-B6	400	2.2	52.5

[a] Based on the reaction temperature, the reaction $PuF_4(s) + F_2(g) \rightleftarrows PuF_6(g)$, and the fluorine flow rate.

[34] R. Gendre, "Preparation de L'Hexafluoride de Plutonium," CEA-2162 (1962).

[35] G. Vandenbussche, "Kinetic Study of the Fluorination by Fluorine of Some Compounds of Uranium and Plutonium," CEA-R-2859 (1964).

[36] "Chemical Engineering Division Summary Report—July, August, September, 1958," ANL-5924, p. 32.

TABLE I-12. CONTENTS OF NaF PRODUCT TRAPS AFTER 3 HR OF REACTION WITH DILUTE FLUORINE AT 350°C (NaF TRAP TEMPERATURE: 100°C)

Run	Percent of Quantity Charged[a]					U/Pu (g/g)
	Mo	Ru	Np	U	Pu	
FF-B1[b]	55	9	2	67.6	5.9	45
FF-B2[b]	92	2	12	108.9	10.1	43
FF-B4[b, c]	56	5	8	64.6	3.2	81
FF-B5[c, d]	36	17	9	69.9	5.9	47
FF-B6[c, d]	40	~17	20	64.0	5.8	44

[a] Total found in two traps.
[b] Trap 1 was used 1 hr and trap 2 for subsequent 2 hr.
[c] Only the bottom half of each trap was sampled.
[d] Trap 1 was used until F_2 appeared in off-gas (~1.5 hr) and trap 2 thereafter.

fluorine is present in the reactor. As shown in Table I-13, about 1.7% of the uranium charged was found in NaF traps used for collection of the PuF_6 product.

Tables I-12 and I-13 indicate that most of the molybdenum was fluorinated during the dilute fluorination step and that ruthenium and neptunium were fluorinated during both fluorination steps. The data for ruthenium should be interpreted in relation to the results of previous laboratory, hot-cave, and 2-in. dia fluidbed tests that showed some ruthenium passing through NaF traps at 100 and 400°C (e.g., see Table I-13 of this report; ANL-7375, p. 89; and ANL-7425, pp. 47 and 59).

The uranium, ruthenium, neptunium, and fluorine contents for the final fluidized beds are shown in Table I-14. The variables had no significant effect upon the uranium, neptunium, and ruthenium contents of the final beds. The neptunium content of the final beds was less than 5% of the neptunium charged in three runs; however, in Runs FF-B5 and FF-B6, more complete analytical results indicate that only 1 to 2% of the neptunium charged remained in the final bed. Uranium in the final beds averaged less than 0.1% of that charged, while residual ruthenium ranged from 5 to 18% of that charged. The conversion of Al_2O_3 to AlF_3 ranged from 6.9 to 10.3%, and was calculated from the fluoride content of the bed by making an allowance for the presence of fission products and actinides in the bed.

TABLE I-13. CONTENTS OF NaF PRODUCT TRAPS USED DURING RECYCLE-FLUORINATION STEP

Trap temperature: 100°C
Traps 1 and 2 used in series
Gas-inlet half of each trap sampled

Run	Percent of Quantity Charged									
	Trap 1					Trap 2				
	U	Pu	Mo	Ru	Np	U	Pu	Mo	Ru	Np
FF-B1	1.7	67.0	3	4	25	0.001	0.0006	<0.01	3	0.8
FF-B2	1.6	73.4	8	1	20	0.006	0.006	0.2	0.8	0.6
FF-B4	1.5	56.0	4	2	16	—	—	[a]	—	—
FF-B5	1.7	64.8	3	5	[b]	—	—	[a]	—	—
FF-B6	1.7	72.1	7	<4	24	—	—	[a]	—	—

[a] Not sampled.
[b] Not analyzed.

The average quantity of fines recovered by rapping and brushing the walls of the reactor after a run was 24 g; the fines contained 8.8 wt % U and 23.8 wt % Pu; fines recovered from the filter averaged 11 g and contained 25.4 wt % U and 22.7 wt % Pu. These results correspond to a recovery of 35 g of fines per run, which contained 1% of the uranium and 7% of the plutonium charged to the reactor.

b. Fission Product Chemistry (*E. Rudzitis, J. Kincinas, D. Steidl*)

A conceptual fluoride volatility process (ANL-7575, pp. 68–71) includes a step in which uranium is volatilized by the reaction of powdered fuel oxide with an oxygen-fluorine mixture at 350°C. The question was raised of how fission products behave in oxygen-fluorine mixtures, since oxidation may compete with fluorination. Of particular interest are the fluorides of the nominally volatile fission products: Nb, Mo, Tc, Ru, Sb, Te, I_2, and Xe and their stable oxides (which may form by interaction of the elements with the UO_2 matrix).

A critical survey of the literature and an evaluation of chemical and physical properties of the fluorides and oxyfluorides suggested that oxyfluorination at elevated temperatures would yield $MoOF_4$, $TcOF_4$, and IOF_5 in addition to the binary fluorides. If catalytically active Ni-NiF_2 is available, XeF_4, a relatively nonvolatile product, might form by combination of Xe with F_2.

Experimental work to determine the products formed when selected fission products (as the element or oxide) were reacted with 10:1 O_2-F_2 proceeded in the

TABLE I-14. COMPOSITION OF FINAL FLUIDIZED BED

Run	Uranium (% of charge)	Ruthenium (% of charge)	Neptunium (% of charge)	Fluorine (wt %)	Al_2O_3 Converted to AlF_3 (%)
FF-B1	0.10	13	<5	9.5	6.9
FF-B2	0.05	10	<5	12.2	10.3
FF-B4	0.04	5	<5	9.6	7.1
FF-B5	0.06	18	2	12.6	10.3
FF-B6	0.04	12	1	11.4	9.1

following stages: (1) exploratory experimentation with provision for visual observation of the products; (2) thermogravimetric experiments with powdered samples to determine reaction temperatures and reaction rates at specified temperatures and to examine intermediate and final reaction products; (3) special investigations of Ru and RuO_2.

The results of the exploratory investigations are summarized in Table I-15 and those of thermobalance experiments in Table I-16. It is evident from both tables that in most cases a complex reaction takes place and that each of the fission product elements (or oxides) reacts differently, depending on the specific character of the element-oxygen-fluorine system. If the product oxides or oxyfluorides are volatile (e.g., RuO_4, $MoOF_4$, IOF_5), they are volatilized with the volatile binary fission product fluorides. The variation in initial reaction temperatures (column 2, Table I-16) indicates that the reactivities of different fission products differ widely.

The investigation of ruthenium, which undergoes complex reactions, included the development of analytical techniques for elemental analysis of ruthenium fluorides. These techniques were used to analyze the products of oxyfluorination experiments in which RuO_2 was reacted with a 10:1 oxygen-fluorine mixture at 250°C and at 380°C. The fission products were collected in three weighable traps at 0, −80, and −183°C. Analysis of the trapped products for ruthenium and fluorine suggests the following mechanism in which RuO_4 is a recurring intermediate and *a*, *b*, and *c* are numbers of molecules:

$$1.\ (a+b)\,RuO_2 + (O_2\text{-}F_2) \begin{matrix} \nearrow aRuF_5 \\ \searrow bRuO_4 \end{matrix}$$

$$2.\ bRuO_4 \rightarrow bRuO_2 + O_2$$

$$3.\ bRuO_2 + (O_2\text{-}F_2) \begin{matrix} \nearrow cRuF_5 \\ \searrow (b-c)RuO_4 \end{matrix}$$

The formation of RuO_4 appears to be catalyzed by fluorine. The formation of an unstable, volatile intermediate, Sb_2O_5, from antimony may be another instance of a fluorine-catalyzed reaction. The Sb_2O_5 decomposes to Sb_2O_4, which was observed in the form of a fog inside the apparatus in thermobalance experiments.

c. Decontamination of Plutonium Hexafluoride (*J. G. Riha, L. E. Trevorrow*)

Separation by selective condensation. Recent experimental studies of the separation of volatile fission product fluorides from PuF_6 have centered on PuF_6-ruthenium fluoride mixtures, since past experience showed that separation of ruthenium fluoride contaminant might prove difficult. Early results caused attention to be focussed on the operation in which ruthenium fluoride and plutonium fluoride were to be separated by (1) preferential condensation of ruthenium fluoride at −10°C and (2) condensation of most of the PuF_6 in cold traps at −78°C. At −10°C, the vapor pressure of pure PuF_6 is 7.89 Torr, which is greater than the partial pressure of PuF_6 in the effluent gas stream of the fluorination operation. The vapor pressure of RuF_5 at −10°C is 2.6×10^{-6} Torr, suggesting that if all ruthenium is in the form of RuF_5, passage of the gases

TABLE I-15. Results of Exploratory Oxyfluorination Experiments

Reagent: 10:1 O_2-F_2
Temperature: ~350°C

Reactant	Product	Remarks
NB	NbF_5	
Nb_2O_5	—	No significant reaction
Mo	$MoOF_4$	
MoO_3	$MoOF_4$	Possibly MoO_2F_2
Ru	RuF_5	
RuO_2	RuO_4 (?)	Substantial decomposition to RuO_2
Sb	SbF_5	Fog formation (Sb_2O_4?)
Sb_2O_5	SbF_5	
Te	TeF_6	Transient low-volatility intermediate
TeO_2	TeF_6	
I_2	IOF_5	
Xe	XeF_4	Ni helices in reactor
Xe	—	Al_2O_3 in reactor; no reaction

TABLE I-16. Results of Thermobalance Experiments

Reagent: 10:1 O_2-F_2
Flow rate: ~100 cm³/min

Reactant[a]	Temp[b] (°C)	Reaction Rates[c] (mm³/min)		Products		Relative Proportion (%) of Recovered Product[d]
		315°C	355°C	Intermediate	Final	
Nb	270	4.01	3.24	$Nb(III)O_xF_y$	NbF_5	100
Mo	175	7.34	6.48	Mo_2O_5(?)	$MoOF_4$	78.5
					MoF_6	21.5
Ru	300	3.66	5.03	RuF_3	RuF_5	68.8
					RuO_4	31.2
Sb	70	4.14	3.55	Sb_2O_4 plus unidentified phase	Sb_2O_4	100
Te	25	—	—	None	TeF_6	100
RuO_2	300	—	7.12	None	RuF_5	44.5
					RuO_4	55.5

[a] 1.01 ± 0.01 g of 300–350 mesh powder reacted to approx. 20%.
[b] Initial reaction temperature.
[c] Temperatures were kept within ±5°C of the nominal temperatures except that RuO_2 was reacted at 380°C.
[d] Based on the weights of cold-trap contents and relative volatilities.

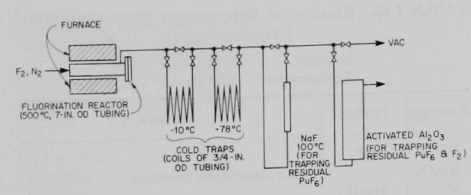

308-2163

FIG. I-24. Schematic Diagram of Apparatus for Bench-Scale Tests of Decontamination of Plutonium by a Series of Operations of the Fluoride Volatility Flowsheet.

formed by fluorination of ruthenium-plutonium mixtures through a trap at −10°C should result in condensation of nearly all of the ruthenium.

The behavior of plutonium-ruthenium mixtures was tested in seven bench-scale experiments using equipment diagrammed in Fig. I-24. The general procedure consisted of (1) fluorinating mixtures of 200–400 mg of PuF_4 and 15–20 mg of ruthenium metal (containing ^{106}Ru to permit radiochemical analysis) in a reactor at 500°C, (2) transporting the resulting gaseous mixture by gas flow through a train of vessels, each simulating a process vessel and a corresponding process operation, and (3) determining the final distribution of plutonium and ruthenium in the cold traps and gas stream.

Results presented in Table I-17 indicate that although the amounts of ruthenium penetrating the traps at −10°C are small fractions of the total ruthenium charged to the fluorination reactor, they are nevertheless several orders of magnitude greater than the theoretical quantities calculated from the known vapor pressure of RuF_5. This indicates that a ruthenium compound more volatile than RuF_5 was present.

The quantities of ruthenium penetrating the cold traps at −78°C are of special interest, since at this temperature, the vapor pressures of ruthenium species are sufficiently low that a small quantity of any species forms a solid phase in the trap. Comparison of the observed amounts of ruthenium transpiring through the trap with the theoretical amounts calculated from the vapor pressures of various ruthenium species (Table I-17) could, therefore, identify the solid species in the trap. The agreement of theoretical and observed moles of PuF_6 penetrating the −78°C trap had shown that the trap efficiently condenses PuF_6.

For five of the seven results in Table I-17, the observed quantities of ruthenium compound(s) transpired at −78°C have the same order of magnitude as the quantities calculated for RuO_4. If the RuO_4 is indeed formed, a source of the oxygen must be identified. The formation of very small quantities of RuO_4 might be explained by the presence of traces of moisture in the system or by the presence of an oxide film on the ruthenium metal powder.

The results of the experiments listed in Table I-17 can be summarized as follows: (1) In the reaction of fluorine at 500°C with ruthenium metal, ruthenium metal-alumina mixtures, or ruthenium metal-PuF_4 mixtures, a small fraction of the total ruthenium charged to the system formed a compound more volatile than RuF_5. (2) In five of the seven experiments, the observed quantities of ruthenium transpiring at −78°C had the same order of magnitude as the quantities calculated for RuO_4. (3) The volatility of ruthenium compounds produced by fluorination of ruthenium in the presence of PuF_4 or alumina does not differ consistently from the volatility of ruthenium compounds produced by fluorination of ruthenium alone.

Separation of PuF_6 by reaction with lithium fluoride. In the proposed volatility flowsheet for processing LMFBR fuels, beds of LiF are used to remove PuF_6 from process gas streams. The reaction of PuF_6 with LiF is also potentially useful for decontamination of PuF_6 from volatile fission products such as ruthenium fluoride. Results of previous experiments (ANL-7575, pp. 62–63) have indicated that at least two solid com-

TABLE I-17. Observed and Theoretical Quantities of Ruthenium Compounds in Exit Gases from −10°C and −78°C Cold Traps (fluorination temperature: 500°C)

Material Fluorinated	Initial Moles of Ru	Moles Transpired at −10°C		Moles Transpired at −78°C				
		Ru(obs)	RuF_5(th)	Ru(obs)	RuF_5(th)	RuF_6(th)	RuO_4(th)	$RuOF_4$(th)
Ru-PuF_4	17×10^{-5}	1.3×10^{-5}	3.7×10^{-9}	1.7×10^{-6}	6.8×10^{-16}	3.1×10^{-5}	1.1×10^{-7}	4.9×10^{-9}
Ru-PuF_4	15×10^{-5}	1.9×10^{-5}	3.2×10^{-9}	2.7×10^{-6}	6.3×10^{-16}	2.8×10^{-5}	0.98×10^{-7}	4.6×10^{-9}
Ru powder only	14×10^{-5}	2.4×10^{-6}	3.7×10^{-9}	1.5×10^{-7}	6.8×10^{-16}	3.1×10^{-5}	1.1×10^{-7}	4.9×10^{-9}
Ru-alumina	15×10^{-5}	3.8×10^{-7}	3.2×10^{-9}	2.0×10^{-7}	6.3×10^{-16}	2.8×10^{-5}	0.98×10^{-7}	4.6×10^{-9}
Ru-PuF_4	17×10^{-5}	2.0×10^{-6}	3.2×10^{-9}	4.8×10^{-7}	6.3×10^{-16}	2.8×10^{-5}	0.98×10^{-7}	4.6×10^{-9}
Ru powder only	14×10^{-5}	9.4×10^{-7}	3.2×10^{-9}	2.9×10^{-7}	6.3×10^{-16}	2.8×10^{-5}	0.98×10^{-7}	4.6×10^{-9}
Ru-PuF_4	16×10^{-5}	5.8×10^{-7}	3.2×10^{-9}	1.6×10^{-7}	6.3×10^{-16}	2.8×10^{-5}	0.98×10^{-7}	4.6×10^{-9}

plexes of plutonium(IV) corresponding to LiF/PuF_4 ratios of 1:1 ($LiPuF_5$) and 4:1 (Li_4PuF_8) can be formed by the reaction of PuF_6 and LiF. Recovery of plutonium from the complexes is essential to keep process losses within acceptable limits. Therefore, additional experimental work has been done to study the rate of PuF_6 volatilization from the complexes when they are reacted with fluorine. The effects of temperature, partial pressure of fluorine, and partial pressure of PuF_6 on the rate of PuF_6 volatilization are discussed in this report.

The basic components of the apparatus train were a boat reactor, a trap containing NaF to absorb excess PuF_6, and a trap containing alumina to absorb excess fluorine. The procedure consisted of passing reactant gases over 40 to 280 mg of a mixture of LiF and a complex contained in the boat and then, after a reaction period, measuring the weight loss of the solid phase and mixing the solids before the succeeding reaction period. The fluorination of each sample was carried out in a series of successive reaction periods until the plutonium in the sample was nearly exhausted.

In the reaction of a complex with pure fluorine (1 atm) at various temperatures, a flow rate of 300 ml/min (STP) was used since the reaction rate was found to be independent of flow rates equal to or greater than 300 ml/min. The rates of fluorination observed were not suitably represented by models for which the rate of diminution of an unreacted spherical core is controlled by (1) gas film diffusion, (2) diffusion through ash, or (3) chemical reaction.[37] Rather, the data indicate that the reaction rate remained constant during the course of the reaction even though the plutonium content of the sample decreased. Thus, the rate of the reaction might be described as zero order with respect to the concentration of PuF_4 in the solid phase; the data can be represented by the equation, $FW_o = kt$, where F is the fraction of PuF_4 reacted after time t, W_o is the initial weight of PuF_4 in the complex, and k is the rate constant.

When plutonium was initially present as $LiPuF_5$, however, the fluorination rate underwent a sharp change at the point where the total composition of the remaining solid was Li_4PuF_8. Also, X-ray patterns analogous to X-ray patterns for the corresponding uranium complexes have shown that the solid compounds are $LiPuF_5$ before the change in reaction rate and Li_4PuF_8 after the change in reaction rate. Graphical fitting of the equation $FW_o = kt$ to the data for the reaction of $LiPuF_5$ with fluorine (1 atm) yielded the rate constants 1.36, 0.7, and 0.32 mg PuF_4/min at 450, 400, and 350°C, respectively. A similar fitting of the data for the reaction of Li_4PuF_8 with fluorine (1 atm) to the same equation yielded the rate constants 0.49, 0.3, and 0.14 mg PuF_4/min at 450, 400, and 350°C, respectively. Graphical fitting of the Arrhenius equation to the data yielded activation energies of 12 kcal/mol PuF_4 for the reaction of $LiPuF_5$ with fluorine (1 atm) and 10 kcal/mol PuF_4 for the reaction of Li_4PuF_8 with fluorine (1 atm). These activation energies are within the range listed in the chemical literature for the reaction of PuF_4 with fluorine (1 atm).[38]

To obtain information on the effect of varying the partial pressure of fluorine on the rate of PuF_6 volatilization at a constant temperature of 400°C, nitrogen-fluorine mixtures with partial pressures of 0.3 to 0.6 atm fluorine were passed over solid mixtures that were initially $LiPuF_5$ and LiF (corresponding to a PuF_4 concentration of 30 mol %). The partial pressure of fluorine was regulated by keeping the fluorine flow rate constant at 300 ml/min and varying the nitrogen flow rate. Graphical fitting of the equation $FW_o = kt$ to the data for the reaction of $LiPuF_5$ with fluorine yielded the rate constants 0.39 and 0.22 mg PuF_4/min at 0.6 and 0.3 atm of fluorine, respectively. A similar fitting for the reaction Li_4PuF_8 with fluorine yielded the rate constants 0.21 and 0.12 mg PuF_4/min at 0.6 and 0.3 atm of fluorine, respectively.

The order n of the reaction with respect to fluorine pressure was obtained by graphically fitting the equation $k = (p_{F_2})^n$ to the data obtained at 1, 0.6, and 0.3 atm fluorine. Since the slopes of the graphs yielded values for n of 1 and 0.8 for the reactions of fluorine with $LiPuF_5$ and Li_4PuF_8, respectively, the rates can be considered to be of first order with respect to fluorine pressure.

The relative effect of back reaction on the rate of fluorination of both complexes at 400°C was determined by measuring the rates of reaction of the solid complexes with PuF_6-fluorine mixtures. The experimental system was the same as in previous experiments except that there were two additional vessels; one vessel was used to contain the PuF_6 supply and the other (a coiled trap of ⅜-in. dia nickel tubing) was used to regulate gas stream temperature and thereby obtain the selected vapor pressures of PuF_6. The gas stream was prepared by passing fluorine at 300 ml/min (STP) first through the PuF_6 supply vessel at a convenient temperature, T, and then through the coil trap at a selected temperature lower than T. The resulting gaseous mixture of fluorine and PuF_6 was then passed over a mixture of $LiPuF_5$ and LiF (corresponding to 30 mol % PuF_4) at 400°C. After a period of fluorination, the boat was reweighed and the solids were mixed

[37] O. Levenspiel, *Chemical Reaction Engineering*, p. 338, John Wiley & Sons, New York (1962).

[38] L. Trevorrow, T. Gerding, M. Steindler, *J. Inorg. Nucl. Chem.* **30**, 2671 (1968).

prior to the next fluorination period. The vessel supplying PuF_6 and the coil trap were weighed at intervals, and by means of the ideal gas law the average pressure of PuF_6 in the fluorinating gas stream was determined.

Fitting of the equation $FW_o = kt$ to the data for the reaction of $LiPuF_5$ with fluorine (1 atm) at 400°C yielded a rate constant of 0.7 mg PuF_4/min for six different pressures of PuF_6 over the range 1.7×10^{-2} to 5.1×10^{-1} Torr. Since this value of the rate constant is the same as that obtained for pure fluorine, it is concluded that the back reaction, $3PuF_6 + Li_4PuF_8 \rightarrow 4(LiPuF_5) + F_2$, has no effect on the fluorination of $LiPuF_5$ at PuF_6 pressures up to 5.1×10^{-1} Torr. On the other hand, the rate of reaction of Li_4PuF_8 with fluorine (1 atm) was found to depend on the pressure of PuF_6 within a certain range; a rate constant of 0.32 mg PuF_4/min was observed for PuF_6 pressures of 1.7×10^{-2}, 9.3×10^{-2}, and 1.1×10^{-1} Torr. A second trial at a PuF_6 pressure of 1.1×10^{-1} yielded a rate constant of 0.24 mg PuF_4/min. Also, rate constants of 0.2, 0.18, 0.14, and 0.09 mg PuF_4/min were observed for PuF_6 pressures of 0.23, 0.29, 0.41, and 0.47 Torr, respectively. A graphical smoothing of these data shows that the effect of PuF_6 pressure on the rate constant ($d \log k/d \log p_{PuF_6}$) is essentially zero for PuF_6 pressures less than 10^{-1} Torr. Since estimates of the partial pressures of PuF_6 in the product stream for the reaction of complexes with pure fluorine indicate that they are all less than 10^{-1} Torr, the back reaction can also be ignored in the treatment of the rates of reaction of the complexes with pure fluorine (reported above).

The rate constant for the reaction $Li_4PuF_8 + F_2 \rightarrow PuF_6 + 4LiF$ should approach zero as the pressure of PuF_6 approaches the equilibrium pressure of PuF_6 in the presence of fluorine (1 atm), Li_4PuF_8, and LiF. Smoothing of the graph of reaction rate as a function of PuF_6 pressure (data given in previous paragraph) shows that the rate constant approaches zero at PuF_6 pressures of about 0.6 Torr. Also, for PuF_6 pressures of 7.6×10^{-1} and 1.0 Torr, no net forward reaction occurred. Therefore, the equilibrium PuF_6 pressure at 1 atm fluorine is between 0.6 and 0.76 Torr. The equilibrium constant (p_{F_2}/p_{PuF_6}) for the reaction $Li_4PuF_8 + F_2 \rightleftarrows PuF_6 + 4LiF$ is therefore between 1.3×10^3 and 1×10^3. Katz and Cathers[39] also reported values for the same reaction at 400°C. Their graph of individual results indicates that the equilibrium constant is between 4×10^3 and 15×10^3, and their analytically smoothed value is 7.25×10^3.

d. Ultraviolet-Activated Synthesis of PuF_6 at Room Temperature (*T. J. Gerding, L. E. Trevorrow*)

During experiments to compare the relative tendencies of NpF_6, PuF_6, and UF_6 to decompose by various energy stimuli, it was discovered that PuF_6 can be formed at room temperature by ultraviolet irradiation (3125 Å) of the system solid PuF_4-gaseous fluorine (300 Torr). Spectrophotometric measurements of the quantity of PuF_6 produced and actinometric measurements of the number of light quanta incident on the static system were used to estimate an apparent yield of 4×10^{-3} molecules of PuF_6 per quantum, i.e., 7×10^{-2} kilowatt-hour of energy was required per gram of PuF_6 produced. Possibly, the apparent quantum yield could be increased by optimizing the mechanics of exposing this heterogeneous system to light. A more detailed account of this work has been accepted for publication.[40]

[39] S. Katz, G. I. Cathers, *Nucl. Appl.* **5**, 5 (1968).

[40] L. E. Trevorrow, T. J. Gerding, M. J. Steindler, "Ultraviolet-Activated Synthesis of Plutonium Hexafluoride at Room Temperature," *Inorg. Nucl. Chem. Letters* **5**, 837 (1969).

2. Engineering-Scale Investigations (*N. M. Levitz*)

a. Conceptual Fluoride Volatility Process for Fast-Reactor Fuels

A conceptual design study was carried out to assess the potential of a fluoride volatility plant for reprocessing LMFBR fuels. The design basis was 1 metric ton of actinides per day from combined core and blanket fuel [15,000 MW(e) equivalent]. The flowsheet was described in detail in the preceding annual report (ANL-7575, pp. 68–71). Since the results of this study are presented in a topical report,[41] only the conclusions of the study are presented here.

The application of fluoride volatility processing to LMFBR fuels is supported by a substantial body of basic and technological information that has been generated in reprocessing work on other nuclear fuel materials and in related processes. Existing information coupled with several innovative design features provided the basis for the design of a reference process and a reference plant for LMFBR fuel reprocessing. The reference process shows a high potential for handling highly radioactive, short-cooled fuel, as well as considerable flexibility in processing feed materials with a wide range of fissile material concentrations. The conceptual plant has a practical size, comparable to the size of existing plants that process LWR fuels.

[41] N. M. Levitz et al, "A Conceptual Design Study of a Fluoride Volatility Plant for Reprocessing LMFBR Fuels," USAEC report ANL-7583 (July 1969).

With optimization, a substantially improved process should be expected.

The uniquely difficult characteristics of LMFBR fuels (namely, high plutonium content, high heat load, and high fission product content) can be accommodated by appropriate design. In the reference process, use is made of continuous, slab-shaped fluorination reactors. The continuous system minimizes plutonium inventory and permits operating conditions that promote high plutonium throughput. The slab shape eases the heat-removal problem (provides higher wall area-to-bed volume ratios) and provides geometric control of criticality. The high content of volatile fission products in the fuel is accommodated by utilizing a "total containment" concept. Volatile wastes are converted to a solid waste form by sorption; rare gases are separated, compressed, and stored.

The process appears feasible since the techniques employed—continuous fluidized-bed fluorination, hexafluoride cold trapping, fractional distillation, and pneumatic conveying of solids—are basic to other nuclear and chemical processes. It is in their application to highly radioactive, high-plutonium fuel that uncertainty arises. Key problems can be summarized as follows:

1) The mechanical decladding procedure should be studied because of possible difficulties owing to the high rate of heat generation. Also, it may be difficult to ensure that all fuel oxide is removed from the fuel hulls by the conceptual ball-milling procedure; supplementary cleanup of hulls may be required.

2) The continuous fluorination step requires development of reliable solids-feeding devices and unique equipment such as slab-shaped fluorinators and dual-stage reaction vessels. A requirement is that plutonium losses in the alumina waste from fluorination be low.

3) Further development and testing is needed to determine whether plutonium decontamination will meet requirements.

4) The preparation of mixed fuel oxides by direct fluid-bed conversion of the mixed hexafluorides should be studied on an engineering scale since work to date has been on separate conversion of UF_6 to UO_2 and PuF_6 to PuO_2.

5) Total containment of process gases, although not an essential requirement, is a highly desirable goal. This concept needs development.

6) Further work is needed to insure that criticality safety and containment of PuF_6 will meet all requirements.

7) The role of sodium in the process and its possible effect on plutonium losses requires additional study, since it is known that PuF_6 can be sorbed irreversibly on sodium fluoride.

These key problems, which have been defined by analysis of one reference process that has not been optimized, are representative of problems existing in some alternative volatility flowsheets that also use fluorine gas as the sole fluorinating agent. These other flowsheets were examined only very qualitatively, since available time did not permit a more complete study.

The conceptual plant design study has defined some areas of work involving the investigation and confirmation of concepts that are already partially developed but not fully proven. Work on these problems would represent the first stage of a development program on the fluoride volatility process.

b. Continuous-Feed, Two-Stage Slab Fluid-Bed Reactor (*J. D. Gabor, A. A. Chilenskas, J. Hepperly, R. V. Kinzler, L. Marek*)

In the conceptual study of a fluoride volatility processing plant for fast breeder fuels (Section B.2.a), a slab-shaped, 4-in.-thick fluorination reactor was adopted to meet criticality and heat-removal requirements. The conceptual process incorporates a single-stage reactor for uranium fluorination and a two-stage reactor for plutonium fluorination. Because of the lack of information on the practical design and operation of slab reactors of approximately 4-in. thickness, exploratory tests were conducted, first on gas-distributor designs, then on mocked-up reactor sections made of Lucite. In all tests, alumina was fluidized with air at ambient temperature.

Gas-distributor tests. Particle movement was observed in initial tests in a "two-dimensional" (⅜-in. thick by 12-in. wide) glass column. The gas distributors in these tests had a saw-tooth shape corresponding to a "slice" of the inverted-pyramid gas distributors used in three-dimensional columns. The bed consisted of nominal 48–100 mesh alumina. Gas inlets (1/16-in. dia holes) at the base of each tooth were on 2-in. centers, and "tooth" heights were ¾ in. (37° wall angle from the horizontal) in one test and 1½ in. (56° wall angle) in a second test. Stagnant regions of the fluidized bed observed in both tests were eliminated by changing the gas-distribution pattern: diamond-shaped inserts were positioned so that the lower tip of the insert was about ¾ in. above the gas inlet.

Further testing was performed with a 4-in.-square Lucite column having an inverted-pyramid-shaped gas distributor 3 in. deep. In tests with a 1/16-in. gas inlet, spouting occurred. Gas-distributor dimensions that appeared to give good fluidization in the 4-in.-square column were ½-in. dia gas inlet and 7-in. depth. Some downward flow of solids was observed when the ½-in. dia gas inlet was used at superficial gas velocities of about 1 ft/hr, indicating that continuous countercurrent solids flow might be possible without the use of downcomer pipes, thereby simplifying design.

Continuous-solids-flow tests were performed on a two-stage column by adding another stage having a 4-in.-square cross section above the original column. Each stage was 36 in. tall. The gas distributor for the upper stage was an inverted pyramid with the same nominal depth, 7 in., as the lower stage. Nominal 48–100 mesh alumina (20-in. deep beds) was the bed material. Flow of alumina from the upper to the lower stage through 7/16-in. dia and 1-in. dia gas inlets was monitored. The solids level in each stage was maintained constant by recycling solids from the lower stage to the upper stage via a pneumatic jet-conveyor device. Tests were also performed with a variable-position, truncated-pyramid-shaped plug (1-in. by 1-in. base, 2¾-in. by 2¾-in. top, 3⅛-in. height) inserted above the orifice of the upper stage. Results (Table I-18) show that control of solids flow through a 1-in. orifice can be achieved over the range from 10 to 9000 lb/(hr)(ft²) by adjustment of plug location and gas flow rate. Complete shutoff of downward solids flow was achieved by a sufficiently high gas velocity.

A two-stage, slab-shaped fluidized-bed column of 4-in. thickness and 2-ft width was next constructed of Lucite. Each stage had a gas-distributor section consisting of six inverted-pyramid sections with dimensions similar to those given above. Only brief qualitative tests were performed in which the downward flow of solids through the multiple orifices and the overall quality of fluidization were observed.

Complete fluidization, with all six gas inlets functioning simultaneously in both stages, was achieved for only short periods (30 min or less). More frequently, only four of the six inlet sections functioned. Poor operation was attributed to electrostatic charge effects and to a low-pressure-drop gas distributor (~1 in. H_2O at 0.4 ft/sec). The charge effect can be avoided by using an all-metal system. Since relatively large openings are needed to allow solids to pass downward from the upper stage, a "priming" device (such as an auxiliary gas jet) may have to be inserted in each opening. Reliable operation of such multistage units may be possible by proper design.

TABLE I-18. Solids Flow Rates at Various Orifice Sizes and Plug Positions

a. Solids Flow Rate as a Function of Orifice Size and Gas Flow Rate

Gas Flow Rate (ft/sec)	Solids Flow Rates [lb/(hr)(ft²)] at Given Orifice Sizes		
	1 in.	¾ in.	½ in.
0 to 1.45	9000 to 310	4000 to 56	—
0 to 1.05	—	—	3900 to 10

b. Solids Flow Rate Through a 1-in. Dia Orifice as a Function of Orifice Plug Position and Gas Flow Rate

Gas Flow Rate (ft/sec)	Solids Flow Rate [lb/(hr)(ft²)]		
	No Plug	Plug ½ in. Above Seat	Plug ¼ in. Above Seat
0.5	980	980	730
1.4	330	225	85

A two-stage fluid-bed reactor with overflow weirs. A second two-stage unit was constructed of Lucite for a brief study of the operating characteristics of a slab fluid-bed reactor with flat, drilled-plate (1/32-in. dia holes) gas distributors and with a weir section as a downcomer for the solids. The stages were each 36 in. tall and had a cross section 4 in. by 24 in. Nominal 48–100 mesh alumina beds (8- to 10-in. static depth) were used. The downcomer section had a 4-in. by 4-in. cross section. Solids were continuously recycled from the lower to the upper stage by pneumatic conveying, simulating a continuous feed. A cyclone was employed to trap solids entrained in the gas, which was fed on a once-through basis.

With a gas velocity of 0.75 ft/sec, fluidization quality was good in both stages during the 27-hr accumulative test period. At this velocity, the perforated distributor plate performed well; few or no static bed regions were observed in either plate. Solids recirculation with a jet conveyor was good, as was solids movement from the upper stage to the lower stage via the downcomer. Slugging, observed in the downcomer at this velocity, should be avoided in future designs.

Since overall evaluation of the tests was mainly by visual observations, visibility was critical and was considerably enhanced by the use of a new electrical grounding system tested for the first time in these studies. The grounding system consisted of a few widely spaced aluminum rods (connected to a ground) mounted vertically in the column. This device significantly reduced fine alumina buildup on the walls due to electrostatic charges, which severely hampered visual observance of beds in plastic and glass columns in the past.

Overall results indicate that fluidization quality and multistage contacting of gas and solids are satisfactory in slab-shaped fluid-bed reactors. Significant potential advantages are a higher wall area-to-volume ratio for heat transfer and a "critical" small dimension (thickness) that is important for nuclear criticality considerations.

c. Pulsed-Bed Studies[42] (*D. Ramaswami, M. Kobayashi,*[43] *W. T. Brazelton*[44])

The pulsed-bed approach to fluidization (a pulsed bed is achieved by controlled, intermittent gas flow) appears to have certain advantages in comparison with conventional fluidized beds for gas-solid contacting (see ANL-7575, p. 71). Although the number of applications of pulsed-bed operation has increased, pulsed-bed characteristics such as bed behavior, heat transfer, and mass transfer have not yet been elucidated. An important objective of this investigation is to explore these characteristics.

Four sizes of glass beads, with average diameters ranging from 73 μm to 580 μm, were tested in a 4-in.-OD and 1.25-in.-ID annular column to measure bed expansion and pressure drop. The following unique characteristics of pulsed beds were found:

1) Pressure-drop patterns for a given pulse cycle are reproducible.

2) Maximum pressure drop increases linearly as the pulsed-gas velocity is increased.

3) Bed-expansion ratio (maximum expanded bed height)/(static bed height) increases with (a) increasing gas velocity, (b) decreasing pulse frequency, and (c) decreasing fraction of on-period relative to off-period.

4) The characteristics of beds composed of large or heavy particles are more regular at a given set of pulsing conditions than are the characteristics of beds composed of small or light particles.

5) Good particle motion continues in a pulsed bed at average gas velocities lower than the minimum fluidizing velocity of a bed operated in a steady (non-pulsed) state of fluidization.

6) For pulsed-bed behavior to be fully controlled, the on-period should not exceed an upper limit that is equal to the time required for a gas bubble to form at the distributor and rise through the bed; nor should the off-period be below a lower limit equal to the time required for the bed to settle to its height at minimum fluidization. The bed-expansion ratio can be predicted from on-period, gas velocity, and minimum bubbling velocity.

The effects of pulsing conditions (gas velocity and on- and off-period), particle properties (size, density, thermal conductivity, and heat capacity), gas properties (density, viscosity, and thermal conductivity), heater position, heater length, and static bed height on heat transfer from a concentrically located heater to a pulsed bed also have been studied for four sizes of glass beads, aluminum shot, and copper shot. Heat transfer in pulsed beds was superior to that in conventional fluidized beds for beds consisting of large or heavy particles and for a short heater or a heater located in the upper part of the bed.

A model was proposed for the heat-transfer mechanism in gas-solid particle systems. The proposed model was used to calculate heat-transfer coefficients from particle residence times and particle fluxes (measured from high-speed motion pictures) in both conventional fluidized beds and pulsed beds. Comparison of the calculated data with experimental heat-transfer data showed satisfactory agreement. The proposed heat-transfer-mechanism model can be used to estimate the heat-transfer coefficients in a pulsed bed.

d. Dense-Phase Transport of Granular Solids (*D. Ramaswami, L. Marek*)

Dense-phase transport of granular solids through pipelines has a number of potential applications in the nuclear fuel cycle, e.g., in the handling of powdered nuclear fuels and of particulate waste. This method of transporting powders through pipes differs from the conventional dilute-phase model of pneumatic transport: in dense-phase transport, the solids are fed from a pressurized hopper, and the solids-to-gas ratio is comparatively very high. Also, in dense-phase transport, velocities for solids and for gas are low, which may result in less attrition of solids and less erosion of piping than in dilute-phase transport.

Exploratory studies of the effects of motivating air pressure and discharge orifice diameter on the transport rate of solids were conducted in an apparatus consisting of a 20-liter pressurized solids-feed vessel, a ⅜-in.-ID, 55-ft-long polyethylene transport line (that permitted visual observations) with an orifice at the tip, a solids-collection vessel, and gas-flow instrumentation. Discharge orifices were 3/32, 3/16, or ⅜ in. in diameter. Nominal 48–100 mesh alumina was the test solid.

Operating conditions and results (summarized in Table I-19) show that higher pressures in the solids-feed vessel gave higher solids transport rates. For motivating pressures of 41.9, 49.7 and 60 psig in the solids reservoir, the transport rates for alumina were 127, 238, and 694 g/min at 0.02, 0.042, and 0.088 cfm of air flow at 78°F and 1 atm.

Higher transport rates were also achieved with greater discharge orifice diameters. With air pressures

---

[42] Fully reported as ANL-7592, a dissertation submitted to the Graduate School of Northwestern University in partial fulfillment of the requirements for the degree of Doctor of Philosophy, Chemical Engineering.

[43] Resident student associate from Northwestern University. Candidate for a doctorate in chemical engineering.

[44] Faculty associate from Northwestern University.

TABLE I-19. OPERATING CONDITIONS AND RESULTS FOR TESTS OF DENSE-PHASE TRANSPORT OF SOLIDS (NOMINALLY 48–100 MESH ALUMINA)

Discharge orifice diameter, in.	3/32[a]	3/16	3/16	3/16	3/8
Motivating air pressure, psig	50.1	41.9	49.7	60	46.2
Air flow rate, cfm, at 78°F and 1 atm	0.042	0.02	0.042	0.088	0.042
Solids transport rate, g/min	167	127	238	694	329

[a] The inside of the orifice was tapered with an angle of 60°.

in the feed vessel of 50.1, 49.7, and 46.2 psig, the transport rates for the alumina at 0.042 cfm (at 78°F and 1 atm) were 167, 238, and 329 g/min, respectively, with discharge-orifice diameters of 3/32, 3/16, and 3/8 in.

Visual observations indicated that inside the transport line the bulk density of the moving solids was close to the packed-bed density. Additional preliminary data indicated that solids transport rates increased with the volume flow rate of air through the orifice. For a particular size of granular solids and transport line, an empirical relation may exist among the rate of solids transport, the motivating air pressure, the discharge orifice diameter, and the volume flow rate of gas through the orifice. Overall results show that this technique is applicable to the transport of particulate materials typical of those contemplated for use in fluoride volatility processes.

e. Alpha Facility Maintenance (*N. M. Levitz, J. Kincinas, R. Kinzler, C. Wach*)

Useful information on the durability of gloves has been obtained during the course of approximately 3½ years of operations in the two gloveboxes that comprised the engineering-scale alpha facility.[45] The smaller glovebox, a 3-module by 4-module unit, housed off-gas scrubbers, AEC filters, and process gas (oxygen and fluorine) manifolds, which supplied the process equipment located in the larger glovebox. The smaller glovebox was exposed mainly to filtered ventilation air at near-ambient temperatures. The larger glovebox, a 5-module by 8-module unit, housed two pilot-scale fluidized-bed reactors and associated equipment. The large box was also exposed mainly to once-through filtered air, although, on occasion, very small amounts of fluorine and UF_6 and PuF_6 were released into the box atmosphere. At glove ports near heated equipment, temperatures above 50°C were noted.

In the smaller glovebox, 41 of the 95 seamless, milled-neoprene gloves deteriorated, mostly by cracking at folds and creases after relatively long periods of nonuse. Polymer-coated neoprene gloves (installed in 39 of the 95 positions) showed no deterioration except discoloration. Little damage to gloves due to abrasion or wear was evident, although fairly heavy mechanical work had been performed in this box.

Similar results were noted for the larger glovebox—135 of the 303 gloves needed replacement. In contrast to experience with the smaller glovebox, however, about one-fourth of the polymer-coated gloves (35 out of 149) showed deterioration. Defects noted near the clamped ends of the gloves were attributed to deterioration caused by room illumination and ozone attack. The polymer-coated gloves showed less attack on the coated side.

It was concluded that gloves should be left fully extended when not in use. Annual inspections are recommended. Polymer-coated neoprene gloves, although somewhat thicker and stiffer, appear to be superior to uncoated neoprene gloves. Both inside and outside coatings might be desirable in some applications. Thinner neoprene gloves (gloves in current usage are nominally 30 mils thick and have a 5-mil coating) are available and should be field-tested.

In response to a directive from the AEC, the fluoride volatility work in the Chemical Engineering Division will be phased out in FY 1970. Cleanup and decontamination of the engineering-scale alpha facility[45] will be carried out as part of the close-out effort. The gloveboxes will be left in a clean, safe standby condition.

Decontamination of the boxes is proceeding. Both the large glovebox and the small glovebox have been cleared of equipment, none of which is being reclaimed. Electrical and pneumatic lines at the end walls have been disconnected. It is intended to remove and salvage the windows, and to leave the boxes open for ready installation of new equipment when the need arises.

A new method of bagging out equipment from a contaminated glovebox has been developed that involves the use of a sturdy fiber carton. The carton, inside a plastic bag, is supported on a lift at a bagout port while it is loaded with items from the glovebox. The procedure, which was successfully tested, requires fewer bag seals, reduces the possibility of puncture by sharp objects, reduces the amount of sawing and cutting of equipment in preparation for removal, requires fewer man-hours, and allows storage of dry waste at higher density.

[45] G. J. Vogel, E. L. Carls, W. J. Mecham, "Engineering Development of Fluid-Bed Fluoride Volatility Processes. Part 5. Description of a Pilot-Scale Facility for Uranium Dioxide-Plutonium Dioxide Processing Studies," ANL-6901 (December 1964)

3. Basic Mechanisms of Fluidization (*N. M. Levitz*)

a. Basic Mechanisms of Fluidized-Bed Heat Transfer (*J. D. Gabor, J. Hepperly*)

The high rate of heat transfer at heating and cooling surfaces is probably the single most important property of fluidized beds. Despite the significance of this property and the relatively large effort expended in measuring fluidized-bed heat-transfer rates, correlations of heat-transfer coefficients have remained empirical and generally limited to the specific apparatus involved in the measurements.

A mechanistic approach to the correlation of fluidized-bed heat transfer is confronted with the complexity of fluidization dynamics. The column geometry and dimensions, the geometry and dimensions of the heat-transfer surface, the gas distributor design, and the properties of the particles and fluidizing gas are all factors in the heat-transfer process.

As a first step in investigating the mechanism of heat transfer in a fluidized bed, the rate of heat transfer to the bed as a function of fluidized-particle residence time at a heater surface was considered. Two aspects of this problem were studied: (1) the case of infinite particle residence time (the bed at minimum fluidization with little or no particle motion) and (2) the case of finite particle residence time (fluidized bed with particles in motion).

Heat transfer to particle beds at minimum fluidization. A model[46] was proposed for predicting the rate of heat transfer from a heater to a bed of particles for gas flow through the bed equal to that required for minimum fluidization. The basis of the model is that all heat transfer by conduction is normal to the heater and can be defined by an effective bed thermal conductivity for an orthorhombic array of spherical particles and that all of the heat is removed by the flowing gas. Predicted heat-transfer coefficients for both cylindrical and flat heaters were in good agreement with experimental data. It was also determined that the model adequately predicts heat-transfer rates for gas flows through the particle bed less than that required for minimum fluidization (packed-bed case).

Heat transfer to fluidized beds. Two models[47] were proposed for heat transfer from a wall to particles moving past a heater within a fluidized bed. One model, based on spheres in an orthorhombic array, was geometrically more accurate but required a large computational effort. The second model approximated a bed of spheres by a series of alternate slabs of gas and solids to represent the gas and solid phases of a fluidized bed. The heat-transfer rates predicted by the second model were in good agreement with (1) rates predicted by the first model and (2) reported data for moving packed beds, which have similar features to particles moving past a heater in a fluidized bed. The equations describing both models were solved by numerical analysis.

[46] J. D. Gabor, "Heat Transfer to Particle Beds with Gas Flows Less than or Equal to that Required for Incipient Fluidization," *Chem. Eng. Sci.* (in press).

[47] J. D. Gabor, "Wall-to-Bed Heat Transfer in Fluidized and Packed Beds," *Chem. Eng. Progr. Symp. Ser.* (in press).

C. PREPARATION OF FUEL MATERIALS

1. Oxidation of Uranium to UO_2 in a Fluidized Bed (*S. Vogler, P. A. Nelson*)

Currently, UO_2 is the favored fuel for nuclear power reactors. After UO_2 reactor fuel is irradiated in a reactor, the uranium is separated from fission products and recovered—at present, by a solvent extraction process. Other recovery processes, such as the Salt Transport Process which yields a metallic product, have been investigated. The necessity of converting the metallic product of a pyrochemical process to the oxide resulted in this investigation of the oxidation of uranium metal.

Considerable information on the reaction of uranium with water, steam, and CO_2 has been obtained by other experimenters whose interest was reactor safety. Because of criticality limitations, it was decided to investigate the CO_2-uranium reaction.

The available data indicated that the rate of reaction of bulk uranium with CO_2 is low, and this was confirmed in a preliminary experiment. To increase the reaction rate, the bulk metal was hydrided prior to oxidation to obtain fine particles with a large reacting surface. Hydriding and a subsequent oxidation were carried out in a 2-in. diameter fluidized-bed reactor

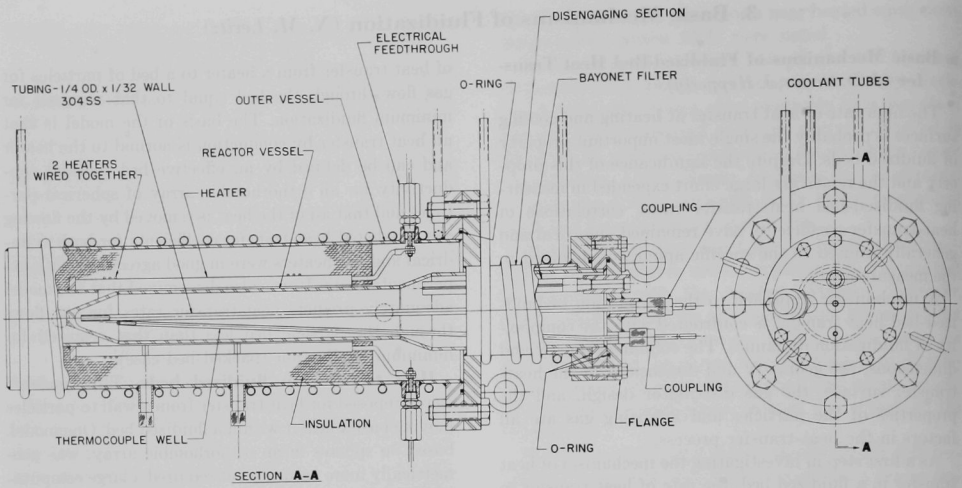

308-2164

FIG. I-25. Fluidized-Bed Reactor for Uranium Oxidation.

that was electrically heated (Fig. I-25). The outer secondary vessel and the disengaging section of the reactor were water-cooled by means of copper coils soldered to the units.

Hydrogen, helium, nitrogen, and carbon dioxide were passed from cylinders through rotameters and a manifold into the fluidized-bed reactor at appropriate rates. The fluidizing gas was heated before it was fed into the reactor.

The reaction was carried out as follows: approximately 300 g of massive uranium metal pieces were cleaned in a 1:1 nitric acid-water solution, rinsed in water, and dried with acetone. The metal was placed in the reactor, and helium was passed through the reactor for approximately 10 min to displace the air. Then hydrogen flow and heating were started to initiate hydriding. Reaction at 275°C and 2-atm pressure was continued for about 5 hr to insure that reaction was completed. (In experiments discussed later, a nitriding step was interposed between the hydriding step and the oxidation step.) Next, oxidation was carried out in the fluidized bed by passing CO_2 in a diluent through the heated fluidized particles. As the bed temperature reached approximately 420°C, the uranium hydride decomposed to metal. Reaction was usually carried out for 4 to 9 hr, sometimes over a period of two days of operation. Different reaction temperatures, ranging from 400 to 825°C, were used in the experiments.

Samples of the oxidized powder produced each day were analyzed for carbon content and extent of oxidation. The carbon content of the product material was determined by comparing the residue after the soluble portion of the sample had been dissolved in 1:1 nitric acid with the original weight of the sample. The extent of oxidation was determined by comparison of sample weights before and after ignition[48] of a sample of the product at 925°C for about 20 hr (appropriate corrections were made for the carbon content of the product).

The results of these experiments (Table I-20) indicate that a temperature of about 500°C is required for oxidation to UO_2 to be completed in 4½ to 5 hr. The carbon contents of the products were too high, reaching 1.55 wt % in one run. Lower contents were obtained (1) after longer reaction time and (2) when higher CO_2 concentrations were used at lower temperatures (<500°C); however, the latter conditions resulted in incomplete oxidation for this set of runs. The reduction of the carbon content during the second half of the reaction period was attributed to volatilization of the deposited carbon by reaction with CO_2 to produce CO. The results shown in Table I-20 agree with other data[49] that showed the carbon content of the product varying with the duration of reaction time, but not with temperature above a threshold temperature.

In an effort to reduce the carbon content of the product, runs were conducted in which the oxidation step was carried out after the hydride had been partially converted to nitride. Nitriding was performed as follows: Uranium hydride prepared in the manner

[48] E. A. Schaeffer, J. O. Hibbits, *Anal. Chem.* **41**, 254 (1969).

[49] J. J. Stobbs, A. J. Woodward, *Corrosion Science* **6**, 499 (1966).

described above was fluidized with nitrogen gas while the reactor was gradually heated to 650°C in about 1 hr. The partially nitrided product was subsequently reacted with 5 or 9 vol % CO_2 diluted with either nitrogen or helium. Four such experiments are summarized in Table I-21.

These results demonstrate the effectiveness of this technique for preparing UO_2 with a satisfactorily low carbon content. As expected, the percent conversion to UO_2 increased with reaction temperature, and at the higher temperatures the product was slightly hyperstoichiometric. It was also apparent that after the bulk of the uranium oxide had been formed, continued reaction resulted in the carbon content of the product being reduced. The reaction was more rapid with a fluidizing gas containing 9 vol % CO_2 than with 5 vol % CO_2. Nitrogen would probably be a satisfactory carrier gas if used at 750°C or above.

The lower carbon content of the UO_2 product when uranium nitride was oxidized than when uranium was oxidized may be explained as follows: Uranium metal reacts so rapidly with CO_2 during the initial stages of the reaction that free carbon is released. (The high reaction rate was sometimes indicated by a temperature spike on the recorder trace during heatup.) Carbon deposition probably continues for several hours. When uranium nitride reacts with CO_2, one of the products is nitrogen gas, which blankets the uranium nitride particles, thus reducing the probability of CO (another product of the reaction) reacting with the uranium nitride to produce carbon. Thus the following reaction is postulated

$$U_2N_3 + 4CO_2 \rightarrow 2UO_2 + 4CO + 1\tfrac{1}{2}\,N_2$$

The UO_2 was further characterized by obtaining the X-ray diffraction patterns of the products of several of the runs. The results in all cases showed the product to be essentially UO_2, except that the product derived from the incomplete oxidation at 650°C (Table I-21) was found to contain U_2N_3 also. The stoichiometry of the products can be narrowly defined from their X-ray lattice parameters; the accepted room temperature lattice parameter for stoichiometric UO_2 is 5.4705 Å.[50] The measured X-ray lattice parameters of the products indicated a stoichiometry of $UO_{2.00\pm0.007}$.

The products from the last group of experiments (Table I-21), especially those from reaction at 750 and 825°C, were reddish-brown, which is typical of UO_2. In earlier experiments, the products were black with a reddish cast.

These experiments have demonstrated the feasibility of preparing UO_2 from uranium in a fluidized bed. A stoichiometric product can be achieved with an acceptably low carbon content, perhaps less than 100 ppm.

TABLE I-20. Reaction of Uranium Metal with CO_2 in a Fluidized Bed

Charge: 300 g uranium hydrided to produce a fine powder
Pressure: 2 atm
Superficial velocity of fluidizing gas: 15 cm/sec

Expt.	Reaction Temp. (°C)	Reaction Time (hr)	Gas Comp. (vol % CO_2 in H_2)	Product	
				C(wt %)	Mole Ratio, O/U
4	510	4½	9	1.55	1.997
		5	9		2.041
3	575	4	9	1.08	2.020
5	650	5	9	1.51	2.034
6	740	5	9	1.46	2.10
		4½	9	0.77	2.007
7	740	5	18[a]	0.70	1.89
		4½	18[a]	0.32	1.92
8	400	6	9	0.29	0.63
		5	9	0.24	0.99
9	400	5½	18	0.17	0.96
		4½	18	0.16	1.28
11	465	5	9	0.27	1.31

[a] Helium was the diluent gas.

TABLE I-21. Reaction of Partially Nitrided Uranium with CO_2 in a Fluidized Bed

Charge: 300 g uranium, hydrided to form a fine powder, then partially reacted with nitrogen
Pressure: 2 atm
Superficial velocity of fluidizing gas: 15 cm/sec
Duration of reaction: approximately 9 hr during a period of two days

Reaction Temp. (°C)	Gas Conc.[a] (vol % CO_2)	Carbon Content (wt %)		% Conversion[b] to UO_2		X-Ray Lattice Parameter (Å)
		1st Day Product	2nd Day Product	1st Day Product	2nd Day Product	
650	9 (N)	0.055	0.061	65	89	5.4707
750	9 (He)	0.15	0.061	75	100.5	5.4702
825	9 (He)	0.12	<0.0005	87	101	5.4712
750	5 (He)	0.085	0.039	65	92	[c]

[a] Diluent gas was nitrogen (N) or helium (He).
[b] A conversion greater than 100% indicates that hyperstoichiometric UO_2 formed.
[c] Not obtained.

[50] L. Lynds, W. A. Young, J. S. Mohl, G. G. Libowitz, in *Advances in Chemistry Series*, Vol. 39, *Nonstoichiometric Compounds*, p. 58, American Chemical Society, Washington, D. C. (1963).

2. Conversion of FBR Oxide Fuel to Carbide Fuel (*D. Ramaswami, J. Pavlik*)

Studies of the use of an inductively heated plasma-torch reactor for the conversion of FBR oxide fuel to carbide fuel have been initiated. The current work is devoted to the conversion of uranium oxide to uranium monocarbide, but the process is expected to be applicable to the production of (U-Pu)C in equipment installed in an alpha-tight enclosure. The method involves making small (~100 mesh) composite particles of uranium oxide and graphite and reacting the particles by passing them through the plasma flame of an inductively coupled plasma torch point downward. The carbide product, in the form of small, free-flowing spheres, is collected in a product receiver at the bottom of the reactor. The CO reaction product is removed from the reaction chamber along with the inert plasma-forming gas. Development of this process to a full-scale continuous process that is critically safe is expected to be accomplished more readily than would development of the standard carbothermic reduction technique for the preparation of (U-Pu)C or the fluid-bed process investigated previously (ANL-7575, p. 128) at this site.

The objective of the current work is to determine the operating conditions required to produce high yields of reactor-grade uranium monocarbide in order to assess the feasibility of a continuous production process using a plasma-torch reactor.

A 25-kW, inductively heated plasma-torch[51] reactor has been installed.[52] A schematic diagram of the installed equipment is shown in Fig. I-26. The equipment consists of four major parts: the plasma torch, the reaction chamber, the high-frequency power "tank" and power supply, and the powder feeder.

In preliminary experiments,[53] crushed alumina was used as a stand-in for the composite particles of uranium dioxide and graphite. The percentage of alumina particles melted was used as the measure of heat transferred to the solid, indicating the extent of reaction to be expected in the processing of UO_2-graphite particles. The independent variables investigated included gas composition, gas velocity, power level, and powder feed rate. It was found that the percentage of melted alumina particles was greatly increased by adding a small percentage of a diatomic gas, such as 4 vol % hydrogen, to the argon carrier gas; more than 90% of the alumina particles were spheroidized. The other variables had minor effects.

The ranges of operating conditions that had been established to be optimum in the experiments with crushed alumina were used in exploratory experiments for the preparation of UC. Agglomerated particles (~100 mesh) of UO_2 and graphite were fed into the plasma flame. The carbon content of the powder decreased from 8.7 wt % in the feed to 5.0 to 6.5 wt % in the product, with solids feed rates of 0.6 to 0.9 kg/hr, whereas uranium monocarbide contains 4.8 wt % C. In general, the carbon content of the product was lower at a higher power level (20 kVA), with a lower gas flow rate (132 scfh), and with a higher hydrogen concentration in the plasma gas (6 vol %). However, the oxygen content of the product was nearly the same as that in the feed, indicating that the hot particles emanating from the torch might have reacted with atmospheric oxygen in the reaction chamber. Equipment improvements are under way to exclude oxygen and maintain an atmosphere of argon in the reaction chamber.

Mixtures of uranium oxides and graphite will be reacted at various operating conditions with an argon atmosphere in the plasma-torch reactor to examine the effects of variables on the product characteristics. The effectiveness of recycling the product to improve the yield will also be determined. The results from these experiments are expected to provide a basis for process evaluation.

[51] Manufactured by TAFA, a division of Hemphrey's Corporation, Concord, N. H.

[52] During installation of the plasma-torch equipment, J. T. Holmes participated in this program.

[53] During the initial experiments, T. R. Johnson participated in this program.

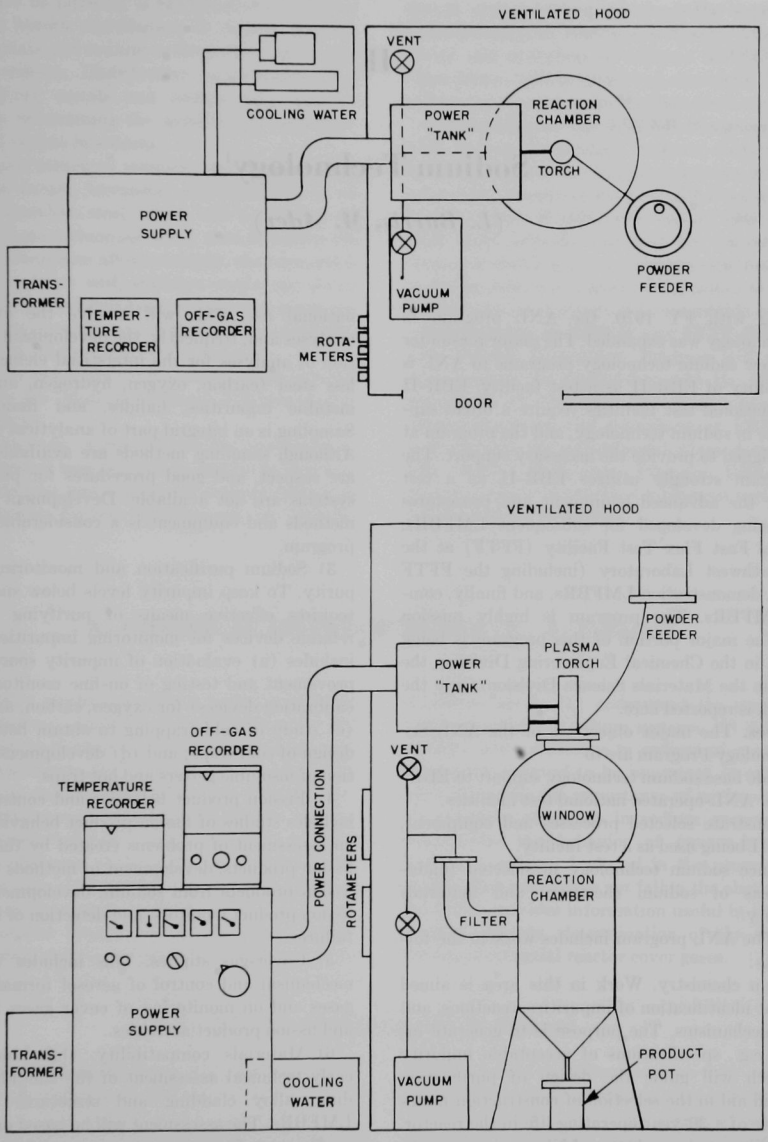

308-1678

FIG. I-26. Plasma-Torch Installation for Studying the Conversion of Uranium Oxide to Uranium Carbide.

II

Sodium Technology[1]

(*L. Burris, M. Ader*)

Beginning with FY 1970, the ANL program in sodium technology was expanded. The major reason for assigning new sodium technology programs to ANL is the availability of EBR-II as a test facility. EBR-II and other national test facilities require a broad supporting base in sodium technology, and the program at ANL is designed to provide the necessary support. The ANL program strongly utilizes EBR-II as a test facility for the advanced equipment and procedures that are being developed for subsequent LMFBRs, namely, the Fast Flux Test Facility (FFTF) at the Pacific Northwest Laboratory (including the FFTF test loops), demonstration LMFBRs, and finally, commercial LMFBRs. The program is highly mission oriented. The major portion of this program is being carried out in the Chemical Engineering Division, the remainder in the Materials Science Division. Only the former work is reported here.

Objectives. The major objectives of the ANL Sodium Technology Program are to

1) Provide base sodium technology support to EBR-II and other ANL-operated national test facilities.

2) Demonstrate selected processes and equipment, with EBR-II being used as a test facility.

3) Advance sodium technology in selected fundamental areas of sodium chemistry and materials compatibility.

Scope. The ANL program includes work in the following areas:

1) Sodium chemistry. Work in this area is aimed primarily at identification of impurities, reactions, and corrosion mechanisms. The purpose is to generate information, e.g., specifications of acceptable impurity levels, which will guide the design of purification methods and aid in the selection of construction materials capable of a 30-year operating life in the reactor.

2) Sampling and analyses. ANL will have the responsibility for establishing reference and standard analytical procedures and for certifying them for national use. This will involve the evaluation of analyses and, frequently, the development or modification of analyses for the interstitial elements of stainless steel (carbon, oxygen, hydrogen, and nitrogen), metallic impurities, halides, and fission products. Sampling is an integral part of analytical development. Although sampling methods are available, often they are suspect, and good procedures for practical plant systems are not available. Development of sampling methods and equipment is a considerable part of the program.

3) Sodium purification and monitoring of sodium purity. To keep impurity levels below specified limits requires effective means of purifying sodium and reliable devices for monitoring impurities. The work includes (a) evaluation of impurity sources; (b) improvement and testing of on-line monitors (including calibration devices) for oxygen, carbon, and hydrogen; (c) study of cold trapping to obtain better bases for design of cold traps; and (d) development and evaluation of insoluble getters and hot traps.

4) Fission product behavior and control. This area includes studies of fission product behavior in sodium, an assessment of problems created by the presence of fission products, development of methods for removing fission products from sodium, development of on-line fission product monitors, and detection of fuel-cladding failures.

5) Cover-gas studies. This includes work on the mechanism and control of aerosol formation in cover gases and on monitoring of cover gases for hydrogen and fission product activities.

6) Materials compatibility. One objective is an early technical assessment of the candidacy of vanadium alloy cladding and structural materials in LMFBRs. The assessment will be based on distribution coefficients of oxygen, nitrogen, and hydrogen (to the extent that information on nitrogen and hydrogen is available) between sodium and vanadium alloys, kinetics of dissolution of vanadium alloys, and mechanical-property effects. An outgrowth of this work,

[1] A summary of this section is given on pages 8 to 9.

which also will be pursued, is the analytical potential of using the known distribution of oxygen between refractory metals and sodium to determine the oxygen activity in sodium. Distribution measurements between refractory metals and sodium may also be applicable to determining the activities of hydrogen, nitrogen, and carbon in sodium.

Intergranular attack of stainless steel is also under study. In the future, increasing emphasis will be on corrosion of stainless steel, which will be studied by some of the same techniques being used to assess the candidacy of vanadium alloys; namely, the interaction of sodium impurities with stainless steels, the determination of their equilibria between stainless steels and sodium, and the measurement of the kinetics of dissolution of stainless steel constituents in sodium.

Much of the materials compatibility work is being carried out in the Materials Science Division and is not reported here.

In the above work, Argonne's role lies principally in the development of base technology and in the development of procedures and equipment through testing of prototype models. Further development for installation in large operating systems is the responsibility of industry and AEC laboratories directly concerned with design and operation of national LMFBR facilities. Close liaison with industry and other AEC laboratories will be maintained to assure that needs are being met.

Relationship to the LMFBR Program Plan. The ANL Sodium Technology Program contains subtasks from seven of the nine major task areas in the sodium technology element of the LMFBR Program Plan [see USAEC report WASH-1105, Vol. 5 (1968)]. Taken in total, these subtasks deal with the interaction of sodium and cladding or construction materials and with achieving sufficient control of impurities in the sodium to keep such interactions at an acceptable level.

Relationship to EBR-II and FFTF Projects. The ANL Sodium Technology Program will maintain a close, cooperative relationship with the EBR-II Project and FFTF. The EBR-II Project is responsible for testing equipment and procedures at EBR-II in accordance with the experimental plans designed in the ANL Sodium Technology Program. EBR-II will be used extensively to prooftest equipment and procedures for eventual use at FFTF.

A. CHEMICAL DEVELOPMENTS (*F. A. Cafasso*)

The chemistry program on liquid sodium is directed toward developing a sound scientific foundation for (1) understanding the behavior of sodium's common nonmetallic contaminants (C, O, H, N), (2) interpreting and evaluating existing corrosion data, and (3) predicting potential corrosion problems in reactor sodium systems. Of special interest, therefore, are the reactions of structural elements, such as iron and nickel, with elements that can enter metals interstitially, such as carbon, oxygen, hydrogen, and nitrogen. Current research is centered largely on the elements carbon, oxygen, and iron, and their compounds. The immediate objectives are to (1) understand the mechanisms of carbon transport in sodium systems, (2) determine the stability and solubilities in sodium of carbon-bearing compounds believed to be important in carbon transport, (3) assess the importance of surface diffusion in the corrosion of metals in sodium systems, and (4) characterize the behavior of oxygen-bearing compounds in sodium. Included in the program is a research effort which does not fall in the above categories but which provides information useful in the design of reactors, namely, determination of the solubility in sodium of potential reactor cover gases.

1. Sodium Chemistry (*F. A. Cafasso*)

a. Studies on Carbon Transport in Sodium-Steel Systems (*E. Veleckis, R. Wolson*)

A model for carbon transport has been developed.[2] It involves the formation of disodium acetylide (Na_2C_2) by the reaction of sodium with carbon at the appropriate carbon activity in steel and the transport of carbon between steels by dissolved acetylide. To verify this model, the dependence of acetylide concentration in sodium on temperature, time, and activity of carbon in selected iron-carbon binary alloys or ferritic steels is being studied.

As a first step, experiments are being performed to

[2] C. Luner, H. M. Feder, F. A. Cafasso, "Carbon Transport in Liquid Sodium," in *Proceedings of the International Conference on Sodium Technology and Large Fast Reactor Design*, USAEC report ANL-7520, Part I, p. 455 (1968).

determine whether an equilibrium involving acetylide exists between the sodium and the iron-carbon alloy or ferritic steel. Approximately 1 g of steel or alloy foil and 10 g of sodium are sealed in copper crucibles and heated for various periods of time at temperatures ranging from 400 to 650°C. The acetylide content of the sodium is determined by dissolving the entire sample of sodium in water and analyzing the off-gas by gas chromatography. The change in carbon content of the foil is determined by combustion analysis.

In initial experiments with an iron-carbon binary alloy (α-iron in coexistence with Fe_3C) containing 0.11 wt % carbon, significant amounts of acetylide were found in the equilibrated sodium: 8 ± 3 ppm at 650°C and 0.13 ± 0.04 ppm at 400°C. These levels were obtained within 24 hr and did not vary significantly over periods up to 5 days. Apparently, an equilibrium or steady-state concentration of acetylide was established rapidly in the liquid sodium. Analysis of the foils for total carbon after the equilibrium experiments indicated significant decreases, namely, from 0.11 to 0.05 wt % carbon. The bulk of this carbon appeared in the sodium as particles, which presumably were produced by graphitization of the iron-carbon alloy and subsequent dislodgement.

Similar equilibration experiments are being performed with ferritic steels. Preliminary results with Croloy 2¼ show that at 400°C a small but significant amount of acetylide is produced.

b. Characterization of the Disodium Acetylide-Sodium System (*J. Ackerman, J. Allen*)

As noted above, the decarburization of ferritic steels by liquid sodium may involve formation of Na_2C_2. Accordingly, information on the stability and solubility of Na_2C_2 in sodium is being obtained. A brief description of the experimental methods and of the preliminary findings is presented below.

Stability of Na_2C_2. The thermal stability of solid Na_2C_2 (99.5% purity) is being studied by differential thermal-thermogravimetric analysis (under 1 atm of helium pressure) and by high-temperature X-ray powder diffraction. Differential thermal analysis revealed a reversible endothermic change at 275°C. This change was shown by the X-ray study to be associated with a transition of the solid from tetragonal (low-temperature) to cubic (high-temperature) symmetry. No other significant features appeared in the thermogram up to about 700°C, where vaporization and consequent loss of sodium became significant.

X-ray patterns were obtained up to about 450°C. The cubic structure of the high-temperature modification of Na_2C_2 persisted, suggesting that this compound is stable to at least 450°C. The X-ray study is being extended to higher temperatures to define better the limits of Na_2C_2 stability. In addition, experiments to test the stability of the acetylide in the presence of sodium are planned.

Solubility of Na_2C_2 in sodium. An attempt is being made to measure the solubility of Na_2C_2 in liquid sodium over the temperature range in which it is stable. The method involves equilibrating reactor-grade sodium with excess Na_2C_2 at a preselected temperature, pressurizing a sample of the melt through a nickel-frit drain into a collector, dissolving the sample in water, and assaying the resulting off-gas for acetylene by gas chromatography. Preliminary results indicate that the acetylide ($C_2^=$) content in sodium is about 10 ppm near 550°C and that this level is invariant over a period of at least 70 hr.

c. Solubility of Helium in Liquid Sodium (*E. Veleckis, G. Redding*)

Information on the solubility in sodium of potential cover gases is needed by reactor designers and engineers to evaluate the possibility that exsolution of gas in the coolant circuit could lead to cavitation and/or bubble formation and thus result in diminished sodium flow. Of the three potential cover gases, argon,[3] nitrogen,[4] and helium, the solubilities in sodium of the first two have already been measured. This work was undertaken to provide solubility data for helium.

The measurements with helium were carried out in the same apparatus previously used to measure the solubility of argon and nitrogen in sodium. The experimental procedure, adapted from a method due to Grimes *et al*,[5] was as follows. Approximately 2.5 liters of cold-trapped sodium was saturated with ^3He-enriched helium gas in a stainless steel vessel (saturator) at a preselected temperature and pressure by circulating the gas through the metal for 2 hr. The saturated metal was allowed to stand overnight in the saturator at the same temperature and pressure. Approximately 2 liters of the equilibrated sodium was then transferred into another vessel (stripper) where the dissolved helium was stripped from the liquid sodium by sparging with an excess of recirculating argon. The argon-helium mixture in the stripper was

[3] E. Veleckis, R. Blomquist, R. Yonco, M. Perin, "Solubility of Argon in Liquid Sodium," in ANL-7325, p. 128 (1967).

[4] E. Veleckis, K. Anderson, F. A. Cafasso, H. M. Feder, "Solubilities of Nitrogen Gas and Sodium Cyanide in Liquid Sodium," *Proceedings of the International Conference on Sodium Technology and Large Fast Reactor Design*, USAEC report ANL-7520, Part 1, p. 295 (1968).

[5] W. R. Grimes, N. W. Smith, G. M. Watson, *J. Phys. Chem.* **62**, 862 (1958).

then drawn by a Toepler pump through a liquid-nitrogen-cooled Molecular Sieve trap[6] into a calibrated bulb. Helium passed unadsorbed through the trap, whereas the argon was retained. The contents of the bulb were then assayed with a mass spectrometer. Helium-3 was included in the saturating gas to distinguish between soluble helium and helium that was introduced inadvertently during the stripping step as a contaminant of the argon.

The removal of argon by the Molecular Sieves concentrated the helium and thereby improved the analysis for helium. Tests were made to determine if helium was lost in this step. Known quantities of ^{3}He gas were introduced into the stripper, and the sequence outlined above, beginning with sparging, was carried out. The results of these tests, given in Table II-1, show that (a) 100% recovery of helium was obtained when the total amount of helium in sodium exceeded 20 μmol, and (b) below 20 μmol, the recovery decreased rapidly with decreasing helium content. In the actual solubility measurements, helium recoveries ranged from 8 to 120 μmol. For the few experiments (at 350 and 400°C) that yielded <20 μmol of helium, corrections were applied for partial recovery.

Solubilities were measured as functions of both pressure and temperature. The pressure dependence was determined from 14 experiments carried out at ~500°C and at pressures ranging from 2 to 9 atm. Figure II-1 shows the variation of the mole fraction solubility of helium (corrected to exactly 500°C) with helium pressure. The experimental points were fitted by the method of least squares to a linear equation with a slope (the Henry's law constant K_H) of 1.56×10^{-7} atm^{-1}. On the basis of a statistical F-test made on the value of the intercept, the displacement of the line from the origin is insignificant. This can be seen in Fig. II-1 by the position of the 95% confidence limits. The solubility data, therefore, obey Henry's law.

The temperature dependence of the solubility was determined from about 30 experiments carried out at approximately 50-degree intervals between 350 and 550°C. The data, shown in Fig. II-2 in terms of the Ostwald coefficient λ (volume of helium dissolved per unit volume of sodium) and temperature in degrees Kelvin, were fitted by the method of least squares to a linear equation of the form $\log \lambda$ vs $1/T$. The regression line[7] in Fig. II-2 can be represented by

$$(350\text{–}550°\text{C})\ \log \lambda = 0.511 - 3070\ T^{-1} \qquad (1)$$

[6] The trap consisted of a coiled copper tube filled with ~100 g of Linde Molecular Sieve Type 5A.

[7] Equation 1 can also be expressed by log (He solubility, ppb/atm) = $5.08 - 2840\ T^{-1}$, with the atomic weight of natural helium taken as 4.003.

TABLE II-1. HELIUM RECOVERY TESTS

Helium-3 Injected into Stripper (μmol)	Helium-3 Recovered (%)
1.3	67 ± 7
4.8	84 ± 7
11.6	87 ± 5
22.6	100
56.4	100

Error analysis showed that at the 95% confidence level the deviation of the mean value of $\log \lambda$ is ±0.015; the corresponding error in λ is ±3.6%.

The heat of solution was calculated by differentiating Eq. 1 with respect to $1/T$. For the standard state defined as one gram-atom of ideal gas compressed at temperature T into the molar volume of sodium at that temperature (a standard state useful in theoretical calculations), the heat of solution is 14.1 ± 0.6 kcal/mol. For the standard state defined as one gram-atom of ideal gas at one atmosphere pressure, the heat of solution is 13.0 ± 0.4 kcal/mol.

No reported experimental measurements of the solu-

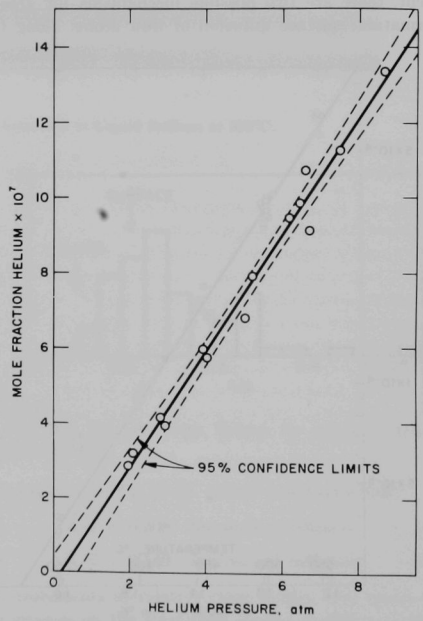

308-2096

FIG. II-1. Pressure Dependence of the Solubility of Helium in Sodium at 500°C.

bility of helium in sodium exist with which to compare the present data. A theoretical model that satisfactorily accounts for the measured helium solubility, however, has been developed in this laboratory. A description of this theoretical work appears in Section V.A.1.e.

d. Surface Diffusivity Studies (*J. G. Eberhart, W. Kremsner*)

This study was undertaken to determine the importance of surface diffusion in the corrosion and transport of α-iron in a liquid sodium environment. The technique employed is to observe by interference microscopy the development of grain-boundary grooves on polished α-iron surfaces. Experiments are carried out at temperatures between 600 and 880°C. Preliminary data on groove profiles and on the kinetics of their development have been collected at 800°C. These data and their significance are discussed below.

Groove growth. The kinetics of groove growth may be conveniently described in terms of the width of the groove, w, shown in the schematic drawing of a groove profile in Fig. II-3. In a liquid metal environment, there are two possible mechanisms for groove formation: surface diffusion of iron atoms along the

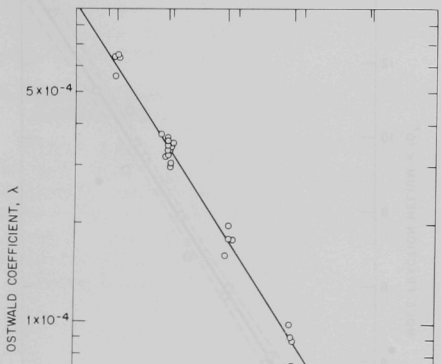

308-2165

FIG. II-2. Temperature Dependence of the Solubility of Helium in Sodium.

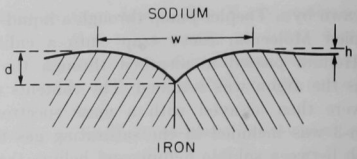

308-2166

FIG. II-3. Schematic of Grain-Boundary Groove Profile (w = width, d = depth, h = ridge height).

solid-liquid interface and volume diffusion of iron atoms through either the bulk solid or the bulk liquid. Mullins[8, 9] has shown that these two mechanisms lead to different grooving kinetics, namely,

$$w = 4.6(Bt)^{1/4} \quad \text{for surface diffusion} \qquad (2)$$

$$w = 5.0(At)^{1/3} \quad \text{for volume diffusion} \qquad (3)$$

where B and A are constants at a given temperature and t is time.

Eight different α-iron specimens were heated at 800°C for various times from 1 to 8 days. Many grooves on each specimen were examined. A typical interferogram is shown in Fig. II-4. The widest groove observed on each sample was selected for the kinetic analysis, and Fig. II-5 shows a log-log plot of the groove width versus time at temperature. The linear relationship between log w and log t was fit by the method of least squares. A slope of 0.22 with a standard deviation of 0.04 was obtained, in reasonable agreement with the exponent ¼ that Eq. 2 indicates is appropriate for surface diffusion. Thus, surface rather than volume diffusion is indicated as the mechanism of mass transport responsible for groove formation.

Mullins' analysis of grain-boundary grooving showed that the parameter B in Eq. 2 is

$$B = (D_{SL})(\nu)(\gamma_{SL})(\Omega^2)/kT \qquad (4)$$

where D_{SL} is the diffusion coefficient for iron atom movement along the solid-liquid interface, ν is the surface atom concentration of iron, γ_{SL} is the solid-liquid interfacial tension, Ω is the atomic volume, k is the Boltzmann constant, and T is the absolute temperature. A surface diffusion coefficient of $D_{SL} = 3 \times 10^{-6}$ cm²/sec is obtained from Eq. 4 by using the least-squares value $B = 5.3 \times 10^{-21}$ cm⁴/sec and assuming $\gamma_{SL} = 2000$ erg/cm², $\Omega = 7.8 \times 10^{-24}$ cm³/atom, and a bcc closest-packed surface plane with $\nu = 2^{-1/6}\Omega^{-2/3}$. This result is somewhat larger than the surface diffusion coefficient obtained by Blakely and Mykura[10] in

[8] W. W. Mullins, *J. Appl. Phys.* **28**, 333 (1957).
[9] W. W. Mullins, *Trans. Met. Soc. AIME* **218**, 354 (1960).
[10] J. M. Blakely, H. Mykura, *Acta Met.* **11**, 399 (1963).

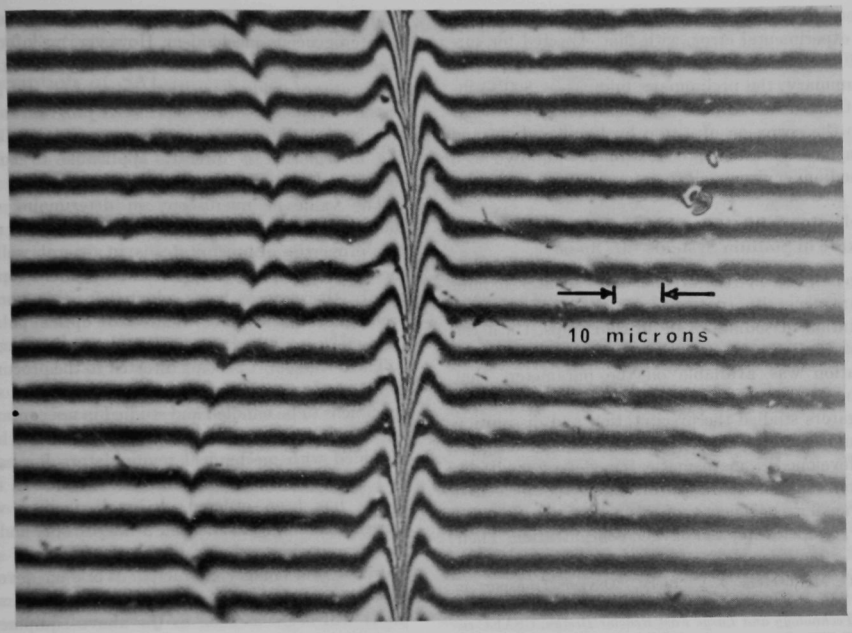

308-2046

FIG. II-4. Interferogram of an α-Iron Surface Annealed in Liquid Sodium at 800°C.

their study of α-iron grooving in vacuum, namely $D_{sv} = 5 \times 10^{-7}$ cm²/sec at 800°C.

Groove profile. According to Mullins' theory, the profile of a grain-boundary groove formed by surface diffusion is different from one formed by volume diffusion. This difference is conveniently characterized by the relative ridge height of the groove, h/d, where h is the height of the groove ridge and d is the depth of

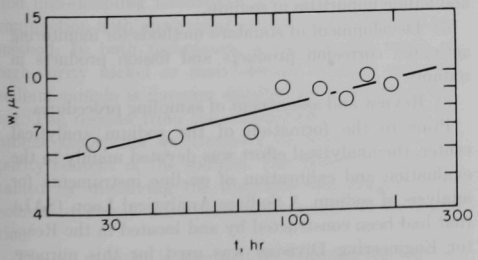

308-2167

FIG. II-5. Maximum Groove Width Versus Time for α-Iron in Liquid Sodium at 800°C.

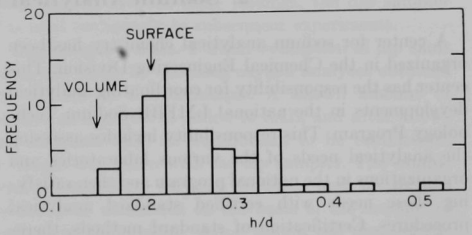

308-2168

FIG. II-6. Relative Ridge Heights for α-Iron in Liquid Sodium at 800°C.

the groove (see Fig. II-3). Allen[11] has shown that

$$h/d = 0.208 \quad \text{for surface diffusion} \tag{5}$$

$$h/d = 0.149 \quad \text{for volume diffusion} \tag{6}$$

Measurements of relative ridge height were made for 59 grooves on the specimens heated at 800°C. A histogram of the results is shown in Fig. II-6. The dis-

[11] B. C. Allen, *Trans. Met. Soc. AIME* **236**, 915 (1966).

tribution has a maximum at $h/d = 0.23$, which agrees, within experimental error, with that expected for surface diffusion.

In summary, the preliminary findings at 800°C indicate that surface diffusion is an important mechanism in the corrosion of α-iron by liquid sodium and that surface diffusion proceeds more rapidly in a liquid sodium environment than in vacuum.

e. Nucleation Kinetics and Morphology of Sodium Oxide in Sodium Systems (*M. Adams*)

Oxygen levels in reactor and experimental sodium loops are generally controlled by the dissolution or precipitation of sodium oxide in cold traps. Until the work of McPheeters and Biery,[12] little quantitative information was available on the parameters that might be important in the design of cold traps. These investigators studied the precipitation and dissolution of sodium oxide in unpacked regenerative cold traps. They developed a mathematical model of cold-trap operation that successfully correlated the measured mass-transfer coefficients of oxygen with Reynolds number, temperature, and oxygen concentration. Their findings suggested that oxide precipitation occurs by a heterogeneous mechanism. However, no information was generated on the effects of the nature of the surface, rates of oxide deposition, rates of crystal growth, or the morphology of the deposits. A program to collect this kind of information is being undertaken because the information is directly applicable to cold-trap design and operation.

The value of microscopy in determining crystal morphologies, kinetics of crystal growth, and nucleation properties of precipitates is, in general, well documented. An approach that is largely microscopical in nature, therefore, is being adopted for this work. The techniques that will be evaluated are optical polarized-light microscopy and scanning electron microscopy.

The initial effort is being directed to the procurement or development of equipment that will permit sodium specimens to be handled and studied in noncontaminating environments. An ultrahigh-vacuum chamber provided with mechanical manipulators for handling and preparing specimens and for conducting experiments has been ordered. A small facility with a refrigeratable microtome and a microscope, and capable of preparing carbon replicas of surfaces of sodium specimens, is being constructed. Work on developing expertise in sodium microscopy (a virtually unexplored area) will begin as soon as the above equipment becomes available.

[12] C. C. McPheeters, J. C. Biery, "Oxygen Transport in Sodium," in *Proceedings of the International Conference on Sodium Technology and Large Fast Reactor Design*, USAEC report ANL-7520, Part I, p. 471 (1968).

2. Sodium Analytical Development (*R. J. Meyer*)

A center for sodium analytical chemistry has been organized in the Chemical Engineering Division. This center has the responsibility for coordinating analytical developments in the national LMFBR Sodium Technology Program. This responsibility includes assessing the analytical needs of the various laboratories and organizations in the national program and then satisfying these needs with certified standard analytical procedures. Certification of standard methods, therefore, will be an important part of the center's program. The certification process is expected to involve either evaluation and improvement of existing analytical methods or development of new ones.

Recent effort has been devoted to (1) establishing avenues of communication with sodium analytical laboratories throughout the country for the purpose of assessing their needs, (2) establishing a mechanism by which standard methods may be certified and effectively implemented through the LMFBR Sodium Technology Program, and (3) initiating work in the following areas:

a) Development of reference methods to calibrate on-line monitors, to determine whether sodium meets procurement specifications, and to evaluate other standard methods.

b) Development of standard methods for oxygen, carbon, hydrogen, and nitrogen species in sodium.

c) Development of standard methods for metallic and halide impurities in sodium.

d) Development of standard methods for monitoring activated corrosion products and fission products in sodium.

e) Review and assessment of sampling procedures.

Prior to the formation of the sodium analytical center, the analytical effort was devoted mainly to the evaluation and calibration of on-line instruments for analysis of sodium. A Sodium Analytical Loop (SAL) that had been constructed by and located in the Reactor Engineering Division was used for this purpose. The following contains a description of the SAL facility and some preliminary experiments with it.

a. Sodium Analytical Loop (*S. Skladzien, P. Vilinskas, L. Bartholme*)

(1) Description of SAL

The Sodium Analytical Loop is shown schematically in Fig. II-7. It is constructed of type 304 stainless steel and is designed for operation at 600°F with a sodium capacity of 15 gal. The SAL facility consists of a main vessel and three small, individually pumped side loops. One loop contains an absolute resistance meter in series with two United Nuclear Corporation (UNC) oxygen cells, a heat exchanger, and a cold trap. The second loop contains a heat exchanger and a plugging indicator valve. Conoseal connections are used in this loop to enable substitution of the plugging indicator valve with a hot trap. The purpose of the third loop is to eliminate local temperature and impurity gradients by recirculating sodium from the upper to the lower region of the main vessel via the loop. The return line of this loop terminates at the throat of an eductor positioned near the bottom of the main vessel.

Two devices are provided for taking liquid sodium samples, the dip sampler and the line sampler. An important feature of the apparatus is the viewing port, which permits observation of the dip-sampling operation as well as the surface condition of the sodium in the main vessel.

(2) Preliminary Experiments with SAL

The initial activities with SAL were the following: (a) a comparison of dip sampling with line sampling was made; (b) dip sampling was further evaluated by comparing the results of oxygen analysis of dip samples with those obtained by gettering the oxygen in sodium with uranium; and (c) two UNC oxygen cells were calibrated. The oxygen-cell calibration is discussed in Section II.B.1.a.

Comparison of dip and line sampling. The dip- and line-sampling techniques are intended for use in conjunction with analysis of sodium by the distillation method. In both techniques, a sample cup made of high-purity nickel or molybdenum is used, and the sodium sample is vacuum distilled by induction heating. The residue from the distillation is analyzed by atomic absorption spectrometry to determine the impurity content of the sodium. The sample size is obtained by dissolving the distillate and assaying for sodium by atomic absorption spectrometry or by titration.

The dip sampler is operated by lowering the sample cup into the sodium and then raising it to the level of the induction coil. This is done manually by moving

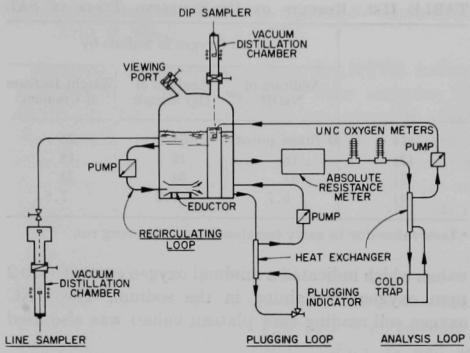

308-2169

FIG. II-7. The Sodium Analytical Loop (SAL).

a temperature-sensing rod, to which the cup is attached, through a sliding seal located at the top of the sampler. The line sampler uses a geared mechanism to raise the sample cup into a fill chamber. A stream of flowing sodium is directed into the cup, the excess spilling into an overflow reservoir. The line is valved off, which stops flow, and the cup is lowered into position for vacuum distillation.

The dip sampler was found to be superior to the line sampler in two respects: the sample size was more reproducible, and the operation had fewer mechanical problems. In view of these findings, the dip sampler was used exclusively in subsequent experiments.

Dip-sampling tests. Further evaluation of dip sampling was made by checking oxygen analyses obtained by the use of this technique. A known amount of oxygen as NaOH was added to SAL, and after allowing sufficient time for equilibrium to be established, a sample was taken with the dip sampler. The sample was subsequently vacuum distilled, and its oxygen content was calculated on the basis of the amount of sodium in the residue. After taking the dip sample, sodium flow was started through a uranium getter trap that had been substituted for the plugging indicator shown in Fig. II-7. The trap consisted of a removable section of pipe in which strips of uranium metal were suspended and maintained at 1020°F throughout a gettering run. At the end of a gettering run, flow through the side loop containing the trap was stopped, the trap was frozen and disconnected, and the uranium strips were removed, cleaned, and weighed. The weight increase was a measure of the oxygen pickup. The gettering runs were terminated when the emf reading of the UNC oxygen cell reached a (high) plateau

TABLE II-2. RESULTS OF DIP-SAMPLING TESTS IN SAL

	Ppm Oxygen in Sodium by		
	Addition of NaOH	Analysis of Dip Sample	Weight Increase of Uranium
(1)	0 (base point)	31	28[a]
(2)	16	12	18
(3)	31	34	34
(4)	6.7	7.2	7.8

[a] Low value due to early termination of gettering run.

value, which indicated a minimal oxygen content (<0.2 ppm oxygen) remaining in the sodium. The UNC oxygen cell reading (low plateau value) was also used to determine when equilibrium had been reached after addition of NaOH.

The results of four consecutive gettering runs are shown in Table II-2. Because good material balances were obtained, it can be concluded that the dip-sampling technique provides satisfactory samples of sodium for analysis of impurities.

After completion of the three activities discussed above, SAL was shut down. As part of the LMFBR Program Plan to centralize the work on sodium technology, SAL was moved from the Reactor Engineering Division and rebuilt (without the line sampler) in the Chemical Engineering Division, where it is once again in operation.

B. ENGINEERING DEVELOPMENTS (*P. A. Nelson*)

1. Monitoring of Sodium Purity (*J. T. Holmes*)

Work has been initiated on the development, testing, evaluation, and improvement of on-line monitors for impurities in sodium. On-line monitors for measuring the concentration of oxygen, carbon, and hydrogen are needed to study the chemistry of these impurities in sodium as well as to monitor their presence in LMFBR sodium coolant. The ability to detect abnormally high buildup of oxygen or carbon in sodium is required so that corrective action may be taken to avoid excessive corrosion of reactor components. On-line hydrogen monitors are needed for rapid detection of small water leaks into sodium from the steam-generator tubes. Thus, the reactor can be shut down before the leak propagates and causes widespread or catastrophic damage.

Monitors and monitoring systems (which include means for on-line calibration), after being fully tested and certified in the ANL Sodium Technology Program, will be prooftested at EBR-II and other national test facilities.

Work on the characterization of cold-trapped sodium is planned.

a. Oxygen-Activity Meter (*S. Skladzien, P. Vilinskas, L. Bartholme*)

The oxygen meter currently under test at ANL is the electrochemical cell developed by the United Nuclear Corporation (UNC). This meter is based on a galvanic cell having a ThO_2-15 wt % Y_2O_3 solid electrolyte, a Cu-Cu_2O reference electrode, and a recommended operating temperature of 600°F (315°C). The cell develops a voltage dependent on the activity of oxygen in the sodium. Possible improvements in the cell, such as replacement of the Cu-Cu_2O reference electrode with Na-Na_2O or oxygen gas, are being studied at Brookhaven National Laboratory. As improvements are developed, they will be tested in the ANL program.

Two UNC electrochemical oxygen cells were tested and calibrated prior to shipment to EBR-II early in 1969. The cells were calibrated in the Sodium Analytical Loop (SAL) described above in Section II.A.2. The calibration involved monitoring the steady-state cell output after various levels of oxygen were introduced into the loop by the decomposition of NaOH. Hydrogen from this decomposition was removed by gettering with zirconium. Prior to each addition of NaOH, oxygen was reduced to below 1 ppm by gettering with uranium. The technique of dip sampling and vacuum distillation, described in Section II.A.2, was used to measure the Na_2O concentration.

The data yielded the following calibration equations relating oxygen concentration to cell voltage at 600°F:

$$\text{Cell TP-285 ln O(ppm)} = 54.2 - 45.0\,V$$

$$\text{Cell TP-286 ln O(ppm)} = 56.4 - 46.9\,V$$

where V is the cell output in volts. The theoretical value for the slope at 600°F is −39.4. The higher values (−45.0 and −46.9) observed experimentally cannot be accounted for at present. The cells were shipped to EBR-II where they will be installed in the secondary sodium system.

Two other uncalibrated UNC cells have been operated in static sodium at EBR-II, one in a radiation field (cold-trap room), the other isolated from the radiation. Periodically, the placement of the cells is reversed to determine if measurable effects of radiation have taken place rather than normal drift or aging. To date, no effects of radiation have been observed. These results do not completely agree with earlier tests (possibly with earlier cell models) at Atomic Power Development Associates in which significant radiation effects were noted occasionally.

Additional experience on long-term operation of the UNC oxygen cells in flowing sodium is needed as well as information on the effects of higher radiation levels. Therefore, plans are being made to test cells in the Radioactive Sodium Chemistry Loop (RSCL) that is being constructed for the EBR-II primary sodium system. During these tests, calibrations of cell output will be made by comparison with the results of on-line distillation analyses, rates of oxidation of uranium metal tabs, and analyses for oxygen in equilibrated refractory metal wires. Two calibrated cells will be shipped to EBR-II in mid-1970 for testing in the RSCL. Additional calibrated cells will be supplied to EBR-II as required.

b. Carbon-Activity Meter (*C. Luner, N. Chellew, D. Raue, P. Mack*)

Knowing the activity of carbon in LMFBR sodium is important to reactor operators since corrosion by abnormally high carbon activity can adversely affect the strength of construction and cladding materials. UNC has developed an on-line carbon-activity monitor that measures the flux of carbon diffusing through an iron membrane immersed in sodium at about 1400°F (760°C). The Chemical Engineering Division has one of the three carbon-activity meters made available by UNC for field testing. This meter will be tested to determine its reliability of operation and its response to the typical steady-state conditions (e.g., temperature, impurity levels) of EBR-II sodium as well as abnormal releases of carburizing agents into the sodium. For these experiments, the meter is being incorporated into the Test and Evaluation Apparatus (TEA), which is shown schematically in Fig. II-8.

TEA is a small, type 304 stainless steel loop with a capacity of 40 to 50 lb of sodium and a maximum pumping rate of 8.5 gpm in the ½-in. Schedule 40 pipe of the main loop. The loop is of welded construction for operation at temperatures up to 1200°F. There is an

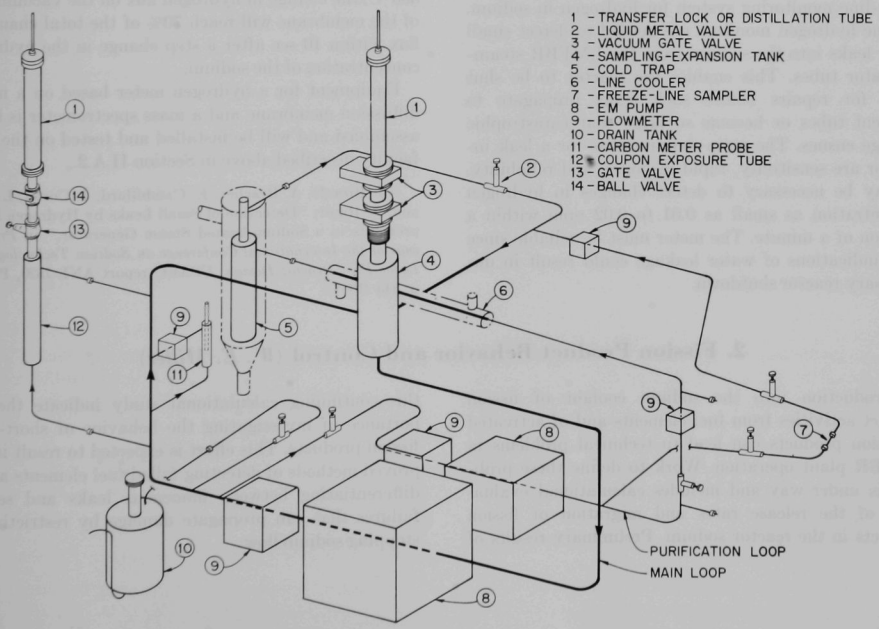

308-2092

FIG. II-8. Test and Evaluation Apparatus (TEA)

on-line distillation sampler (dip type) in the main loop and a freeze-line sampler in the purification loop. The response of the carbon-activity meter will be correlated with the rate of carburization of metal specimens mounted in a test section adjacent to the meter. During the course of these experiments, various changes in the design of the iron-membrane probe and the detector system will be tested in an effort to improve the meter.

Attempts to improve the meter are also being made by experiments in which probes are tested in sodium contained in stirred vessels. This type of equipment is also being used to determine meter response to various carbon-bearing species that may be important in carbon transport in sodium systems.

The most reliable model of the carbon-activity meter that is developed in this program will be prooftested at EBR-II in the Radioactive Sodium Chemistry Loop (RSCL). Methods of on-line calibration and of checking meter response to a sudden change in carbon activity will be developed by work on the TEA. Later, these methods will be incorporated into the operation of the carbon-meter station at RSCL.

c. Hydrogen-Activity Meter (*D. R. Vissers*)

Design and calculational studies are under way on an on-line monitoring system for hydrogen in sodium. On-line hydrogen monitors are needed to detect small water leaks into the sodium from the LMFBR steam-generator tubes. This enables the reactor to be shut down for repairs before such leaks propagate to adjacent tubes or become so large that catastrophic damage ensues. The main requirements for a leak indicator are sensitivity, rapid response, and reliability. It may be necessary to detect changes in hydrogen concentration as small as 0.01 to 0.02 ppm within a fraction of a minute. The meter must be reliable since false indications of water leakage could result in unnecessary reactor shutdown.

Oxygen-activity meters could also be used for detection of water leaks into sodium. Such meters have fast response and high sensitivity and may eventually be superior to hydrogen meters as leak detectors. However, oxygen meters are not as reliable at the present stage of development as hydrogen meters.

To respond to the immediate needs of facilities using sodium-heated steam generators, the aim of the initial work on hydrogen detectors will be to develop an on-line hydrogen monitor similar to that tested extensively at Electricité de France.[13] This monitor is based on diffusion of the hydrogen in the sodium through a nickel membrane and detection of the hydrogen with a mass spectrometer. A vacuum is drawn at a steady rate on the membrane, thereby creating a hydrogen activity gradient from the sodium side to the vacuum side and causing the hydrogen to diffuse. The partial pressure of hydrogen on the vacuum side, determined with the mass spectrometer, is a measure of the hydrogen flux through the membrane. A rapid increase in hydrogen flux through the mebrane would be an indication of a water leak into the sodium.

Response rates for the nickel membranes used in such hydrogen meters have been calculated. These calculations indicate that, for a 10-mil membrane at 500°C, the change in hydrogen flux on the vacuum side of the membrane will reach 70% of the total change in flux within 10 sec after a step change in the hydrogen concentration of the sodium.

Equipment for a hydrogen meter based on a nickel diffussion membrane and a mass spectrometer is being assembled and will be installed and tested on the SAL facility described above in Section II.A.2.

[13] J. Birault, A. Brachet, E. Cambillard, J. Coron, L. Lannou, C. Rault, "Detection of Small Leaks by Hydrogen Measurements in a Sodium-heated Steam Generator," in *Proceedings of the International Conference on Sodium Technology and Large Fast Reactor Design*, USAEC report ANL-7520, Part I, p. 345 (1968).

2. Fission Product Behavior and Control (*W. E. Miller*)

Introduction into the sodium coolant of fission product activities from fuel elements and of activated corrosion products can lead to technical problems in LMFBR plant operation. Work to define these problems is under way and includes calculational evaluations of the release rates and migration of fission products in the reactor sodium. Preliminary results of this continuing calculational study indicate the importance of investigating the behavior of short-lived fission products. This effort is expected to result in improved methods of detecting failed fuel elements and of differentiating between innocuous leaks and serious failures that can propagate damage by restricting or stopping sodium flow.

3. Nature and Control of Sodium Aerosol Formation (*R. W. Kessie, W. E. Miller*)

The objective of this work is to assess the magnitude of formation of sodium aerosol at proposed LMFBR conditions. Proposed LMFBR sodium temperatures during normal reactor operation range from about 425 to 650°C. The corresponding range of sodium vapor pressure is 0.73 to 52 Torr. In the pool-containment approach (used at EBR-II and proposed for LMFBRs), the cover gas is exposed to the full range of sodium temperatures.

The fraction of sodium vapor condensed to aerosol on cooling the sodium vapor-carrier gas mixture will depend on the ratio of thermal diffusivity to mass diffusivity in the mixture. High mass diffusivity will tend to promote direct condensation on the cooler surfaces above the sodium pool, whereas a low mass diffusivity will tend to promote aerosol formation within the cool gas-boundary layers. However, no experimental data on the diffusivity of sodium vapor has been found. For nonpolar simple gases, diffusivities may be estimated from viscosities; correlations for making such estimates for sodium are being examined.

The first experiments will be done in an inert-atmosphere glovebox. Sodium will be heated in a long tube cooled at one end, and an attempt will be made to view aerosol formation through a Pyrex window in the tube. The gas phase will be sampled and analyzed to determine the mass concentration of sodium aerosol.

III

Materials Chemistry and Thermodynamics[1]

(A. D. Tevebaugh, J. D. Bingle)

A. HIGH-TEMPERATURE THERMODYNAMIC STUDIES *(P. E. Blackburn)*

The objective of this program is to obtain phase-diagram, thermodynamic, and chemical data that can be used to interpret and evaluate performance of fast-breeder reactor fuels. This information will aid in understanding and in selecting methods for control of fission product distribution in the fuel, cladding attack by corrosive fission products, plutonium segregation, and fuel swelling. In addition, these data will help to identify phases formed in fuel under operating conditions and to choose additives for controlling the chemical potentials of fuel anions and those fission products which are deleterious to prolonged fuel pin lifetimes.

The high-temperature investigations of U-Pu-O and U-Pu-C fuel systems include mass-spectrometric vapor pressure measurements, phase-diagram studies, and activity measurements by transpiration experiments. The mass-spectrometric studies of the binary Pu-O and Pu-C systems are nearly complete, and the studies of the ternary U-Pu-O systems have been initiated. The first of several phase-diagram studies of the metal-rich limit in $(U,Pu)O_{2-x}$ has been completed. Measurements of the U-O system are being carried out to test the new plutonium transpiration equipment. The ultrahigh-vacuum effusion chamber has been fitted with a quadrupole mass spectrometer and measurements are under way to determine relative ion cross sections of uranium and uranium oxide molecules. Vapor transport experiments have been carried out to determine the mechanism of the attack of stainless steel cladding by fission product iodine. Experiments are being planned to establish the chemical factors necessary for the iodine attack. Carbon activities have been measured over the U-C system by a transpiration technique.

[1] A summary of this section is given on pages 9 to 11.

1. Volatilization Studies of Plutonium Oxide Compounds by Mass Spectrometry

(J. E. Battles, W. A. Shinn)

Mass-spectrometric studies of the volatilization behavior of the systems Pu-O and Pu-U-O are under way. The purpose of these studies is to determine (1) the composition of the vapor phase in equilibrium with the condensed phase(s), (2) the partial pressures of the vapor species as a function of temperature, and (3) the thermodynamic properties of the vapor species and condensed phases.

a. Plutonium-Oxygen System

The study of the volatilization behavior of the apparent congruently effusing plutonia ($\sim PuO_{1.83}$ at 2219°K) has been completed and the results previously reported (ANL-7575, p. 77). Also, data relating to the incomplete study of the binary condensed system $Pu_2O_3 + PuO_{1.61}$ were presented at that time. Additional mass spectrometric measurements to determine the enthalpies of reaction for

$$7.33\ Pu_2O_3(s) = 13.66\ PuO_{1.61}(s) + Pu(g) \quad (1)$$

$$2.77\ Pu_2O_3(s) = 4.54\ PuO_{1.61}(s) + PuO(g) \quad (2)$$

and

$$4.54\ PuO_{1.61}(s) = 1.77\ Pu_2O_3(s) + PuO_2(g) \quad (3)$$

have now been completed, concluding the study of the binary condensed system $Pu_2O_3 + PuO_{1.61}$. These measurements were made primarily to supplement the limited data previously obtained for Reaction 3.

TABLE III-1. HEATS OF REACTION TO PRODUCE GASEOUS Pu, PuO, AND PuO_2 FROM TWO-PHASE (Pu_2O_3 + $PuO_{1.61}$)

Run No.	Cell Material	Temperature Range[a] (°K)	Composition of Solid Material (O/Pu)	Heat of Reaction[c] (kcal/mol)		
				Pu	PuO	PuO_2
PW-5A	W	1704–2145	1.55	108.3 ± 1.5	116.4 ± 0.9	—
PR-5A	Re	1797–2134	1.60[b]	111.9 ± 1.6	114.4 ± 0.8	—
PR-6A	Re	1685–2147	1.56	111.2 ± 1.3	120.9 ± 1.1	—
PR-6C	Re	1657–2148	1.54	111.5 ± 2.8	119.1 ± 0.7	—
PR-6D	Re	1735–2147	1.56	109.9 ± 1.8	118.8 ± 0.6	126.2 ± 4.9
PR-8B	Re	1648–2224	1.55_0	113.1 ± 1.0	120.6 ± 0.5	136.3 ± 2.1
PR-8C	Re	1803–2212	1.54_7	109.1 ± 1.5	120.7 ± 1.0	131.7 ± 6.3
PR-9A	Re	1812–2216	1.56_1	105.2 ± 1.0	116.6 ± 0.7	133.8 ± 2.0
			Average	110.0 ± 1.7	118.4 ± 1.0	132.0 ± 4.4

[a] The measurements for PuO_2^+ covered the temperature range 1950°K to the maximum listed.
[b] Analysis is believed to be incorrect.
[c] The errors listed are standard deviations; an ionizing electron energy of 11 eV was used for measurements of Pu^+ and PuO^+, and 16 eV for measurements of PuO_2^+.

The results from these latest experiments (Runs PR-8B, PR-8C, and PR-9A), along with results from the previous experiments, are summarized in Table III-1. The experimental details and treatment of data were previously reported (ANL-7575, p. 81). The data in Table III-1 (heats of reaction) relate to condensed materials with O/Pu atom ratios of 1.54 to 1.56. The enthalpies of reaction for Reactions 1 and 2, obtained from a numerical average of all the data, differ insignificantly from the values reported in ANL-7575. For Reaction 3, an enthalpy of reaction of 132.0 ± 4.4 kcal/mol is obtained from an average of the four values; this differs considerably from the value (126.2 ± 4.9 kcal/mol) obtained initially (one experiment). The large standard deviations exhibited in the data for Reaction 3 are due primarily to the small ion intensity of PuO_2^+ which is the minor vapor species.

The partial pressures of Pu(g), PuO(g), and PuO_2(g) over (Pu_2O_3 + $PuO_{1.61}$) as a function of temperature were redetermined so as to incorporate the enthalpies of reactions listed in Table III-1 and are represented by the equations

$$\log P_{Pu}\,(\text{atm}) = -\frac{(24{,}040 \pm 370)}{T} + (5.240 \pm 0.190)\ (1648\text{–}2224°\text{K}) \quad (4)$$

$$\log P_{PuO}\,(\text{atm}) = -\frac{(25{,}870 \pm 220)}{T} + (7.140 \pm 0.120)\ (1648\text{–}2224°\text{K}) \quad (5)$$

$$\log P_{PuO_2}\,(\text{atm}) = -\frac{(28{,}850 \pm 960)}{T} + (6.130 \pm 0.480)\ (1950\text{–}2224°\text{K}) \quad (6)$$

b. Uranium-Plutonium-Oxygen System

Two preliminary experiments on the volatilization of 20 wt. % PuO_2-80 wt % UO_2 material at ~2260°K have been conducted. A tungsten effusion cell was used in the first experiment, whereas a rhenium effusion cell was used in the second experiment. The starting material had an oxygen-to-metal (O/M) atom ratio of 2.01_3. In these experiments, vapor species of W-O (tungsten effusion cell) and Re-O (rhenium effusion cell) were observed during the initial heating of the sample. The intensity of these vapor species decreased rapidly, thus indicating a reduction in the oxygen potential (O/M) of the samples.

In the second experiment, the sample (374 mg) was heated at about 1673°K until the Re-O vapor species were no longer detectable. The sample was than heated at about 2260°K for 20.5 hr. The variation of the ion intensities as a function of time is shown in Fig. III-1. At point A in Fig. III-1, a temperature decrease (10–15°) occurred, and at point B, a momentary high-voltage failure occurred. The points R_1 and R_2 indicate reheats after cooling the sample to room temperature. At point R_1 (9.5 hr), a sample was removed for oxygen analysis. The analysis yielded an O/M atom ratio of 1.92_0. The remainder of the material (~53 mg) was then reheated to 2260°K for an additional 11 hr. From point R_1 to the point marking the conclusion of the experiment, the ion intensities of the vapor species appear to have reached an approximate equilibrium condition. The residual material at the conclusion of the experiment (after 20.5 hr) had an O/M atom ratio of 1.86_5. Although PuO_2^+ was detected in the vapor phase in a minor amount, its concentration could not be evaluated because the mass spectrometer does not completely differentiate between $^{239}PuO_2^+$ and $^{238}UO_2^+$.

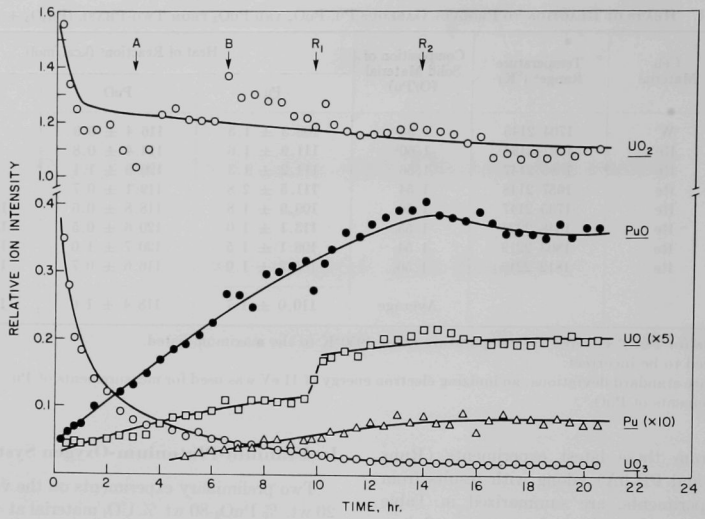

308-2170

FIG. III-1. Variation of the Ion Intensities of UO^+, UO_2^+, UO_3^+, PuO^+, and Pu^+ as a Function of Time at Constant Temperature (~2260°K).

The ion intensities of UO_2^+, UO^+, PuO^+, and Pu^+ were determined using an ionizing-electron energy of 11 eV, whereas 15 eV was used in the measurement of the ion intensity of UO_3^+.

Although considerable scatter exists in the data shown in Fig. III-1, the experiment did fulfill its purpose of establishing the relative abundance of the vapor species and the variation in the concentration of the species as a function of time at a constant temperature.

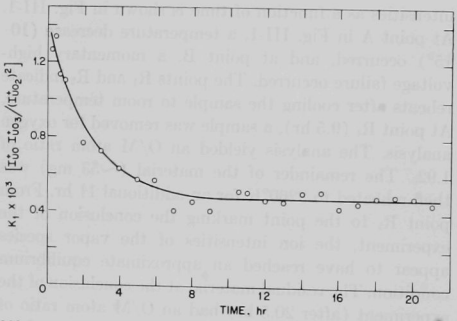

308-2211

FIG. III-2. Plot of the Equilibrium K_1 as a Function of Time at Constant Temperature (2260°K) for the Reaction $2UO_2(g) = UO(g) + UO_3(g)$.

The behavior exhibited in the initial portion of the experiment may be indicative of nonequilibrium in the vapor phase, or between the solid and vapor phases, or both. Similarly, the behavior in the latter portion may be indicative of equilibrium or near-equilibrium behavior. Another indicator of equilibrium or nonequilibrium behavior would be a plot of the equilibrium constants for the reactions

$$2UO_2(g) = UO(g) + UO_3(g),$$

$$K_1 = \frac{I_{UO^+} + I_{UO_3^+}}{(I_{UO_2^+})^2} \quad (7)$$

and

$$2PuO(g) = Pu(g) + PuO_2(g),$$

$$K_2 = \frac{I_{Pu^+} + I_{PuO_2^+}}{(I_{PuO^+})^2} \quad (8)$$

Under equilibrium conditions and constant temperature, the equilibrium constants K_1 and K_2 should remain constant when plotted as a function of time. In Fig. III-2, the equilibrium constant K_1 has been plotted as a function of time (K_2 could not be evaluated because the ion intensity of PuO_2^+ could not be measured). As shown in Fig. III-2, the equilibrium constant changed appreciably during the initial portion of the experiment and then remained constant during the latter part of the

experiment, thus indicating that equilibrium was achieved during this time. The behavior of the equilibrium constant shown in Fig. III-2 closely parallels the behavior of the ion intensities shown in Fig. III-1.

In future experiments, reaction with the cell material will be eliminated by using iridium effusion cells, which have been shown to be nonreactive with plutonia (see ANL-7575, p. 77). The problem of differentiating between $^{239}PuO_2^+$ and $^{238}UO_2^+$ will be resolved by substituting ^{235}U for ^{238}U. The Materials Science Division has prepared batches (~25 g each) of the following material using enriched uranium: 5 wt % PuO_2-95 wt % UO_2, 10 wt % PuO_2-90 wt % UO_2, and 20 wt % PuO_2-80 wt % UO_2.

2. Phase Diagram of the Ternary Oxide System U-Pu-O (*A. E. Martin, F. C. Mrazek*)

The dominant feature of the U-Pu-O ternary phase diagram[2] is the existence of a fluorite solid-solution phase field which extends across the diagram from the uranium-oxygen side to the plutonium-oxygen side. The hypostoichiometric boundary of this phase field at elevated temperatures, although of considerable interest in the field of fast reactor fuels, had not been established except at the two sides of the diagram. The establishment of this boundary was chosen as the major goal of our study of the U-Pu-O system, following some initial work on the Pu-O binary diagram that was previously reported (ANL-7575, p. 84).

The hypostoichiometric portion of the U-Pu-O ternary system, where the oxygen-to-metal ratio is less than 2.00, can conveniently be represented by rectangular coordinates, as for example in Fig. III-3. In this case, the ordinate is the oxygen-to-metal ratio, O/(U + Pu), and the abscissa is the atomic percent of plutonium with respect to the two major cationic constituents, [Pu/(U + Pu)] × 100. For convenience, the latter will be referred to as at. % Pu. As a practical matter, impurity elements are disregarded when computing either the O/M ratio or the at. % Pu.

It can be inferred from a study of the U-UO_2 phase diagram[3] that a high-temperature section through the uranium-rich portion of the U-Pu-O ternary phase diagram probably has the simple form shown in Fig. III-3. The temperature here might be in the range from 1200 to 2300°C. If this is the form of the phase diagram, then the only condensed phase in equilibrium with an oxide of the hypostoichiometric boundary composition is a uranium-plutonium alloy. This diagram also serves to point out that the tie lines in the two-phase field are not necessarily vertical. For convenience, the tilt of the tie lines will be given by the "tie-line-plutonium ratio," the ratio of the atomic percent of plutonium in the oxide phase to that in the liquid alloy phase. The tie line will be tilted if this ratio is other than 1.00.

It appeared to be likely that the hypostoichiometric boundary of the fluorite phase shown in Fig. III-3 could be established by equilibrating uranium-plutonium oxide crucibles with liquid plutonium-uranium alloys at various temperatures and subsequently analyzing the crucibles. This had been the method which was used in the establishment of the hypostoichiometric boundary of the urania fluorite phase in the U-UO_2 system.[3] How far into the ternary system the phase diagram would have the form shown in Fig. III-3 is uncertain, perhaps to as far as 40 to 50 at. % plutonium for temperatures below 2100°C. The initial goal was to establish the hypostoichiometric boundary of the fluorite phase at about 20 at. % plutonium. Coprecipitated oxide was available which contained 19.8 at. % plutonium. Subsequently, coprecipitated mixed-oxide powders with 44.1, 64.3, and 80.4 at. % plutonium were also obtained.

Crucibles were prepared from the oxide powder containing 19.8 at. % plutonium by pressing in a 0.50-in. die at 51,000 psi. In order to avoid contamination, no binder or die lubricant was used. The crucibles were sintered for one hour in vacuum at 1370°C followed by four hours in helium at 1685°C. The uranium-plutonium alloys were prepared by melting uranium with portions

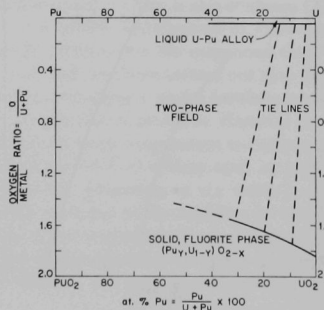

308-2171

FIG. III-3. Probable Form of High Temperature Section Through the Uranium-rich Portion of the U-Pu-O Ternary Phase Diagram.

---

[2] T. L. Markin, R. S. Street, *J. Inorg. Nucl. Chem.* **29**, 2265 (1967).

[3] R. K. Edwards, A. E. Martin, "Phase Relations in the Uranium-Uranium Dioxide System at High Temperatures," *Thermodynamics*, Vol. 2, p. 423, IAEA, Vienna (1966).

of a 40 at. % U-60 at. % Pu alloy in an arc furnace on a water-cooled copper hearth. (The 60 % plutonium alloy had been formed by arc melting uranium and plutonium. The plutonium was 99.99 % material obtained from Los Alamos whereas the uranium was the 99.9 % material previously used in the U-UO_2 study.[3]) The equilibration between alloys and crucibles was carried out in the Brew furnace (see ANL-7575, p. 83) in a helium atmosphere. The average charge in one of these experiments was 5.5 g, about 2.3 g of alloy and a 3.2-g crucible.

The initial equilibration tests were carried out at about 2000°C. After cooling, the products were mounted in a cold-setting resin, sectioned with a 10-ml diamond saw, polished, and then examined metallographically. Many similarities to comparable products from equilibrations of uranium with uranium dioxide crucibles were apparent. Oxide growths had formed between the alloys and the crucibles. Numerous metallic particles were observed in both the crucibles and the oxide growths; the particles were primarily located at grain boundaries of the fluorite oxide phase. Apparently, the oxide crucible and the oxide growth had both been single-phase fluorite oxide at the temperature of the equilibration, and the metallic particles, identified by electron-probe microanalysis (EPM) as U-Pu alloys, had precipitated during cooling to room temperature. The O/M analysis of the crucible products ranged from 1.64 to 1.73.

These results were encouraging in several respects. There was no evidence that a third phase, in addition to the solid fluorite oxide phase and the liquid alloy, had been present at the equilibrium temperatures. Moreover, no evidence was present that any liquid alloy had penetrated into the crucibles. The eventual success of the equilibration method in establishing the hypostoichiometric boundary for the mixed oxide containing 19.8 at. % plutonium seemed likely.

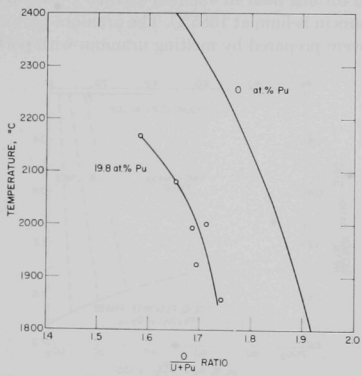

308-2172

FIG. III-4. Hypostoichiometric Boundary of the Fluorite Phase in the U-Pu-O System at High Temperature at 0 and 19.8 at. % Pu.

However, EPM examination of the products disclosed that the experimental conditions needed to be modified in order to produce valid hypostoichiometric boundary data. The tie-line-plutonium ratio was 2.0 with this oxide composition at this temperature. As a result, during the equilibration process, the plutonium concentration of each layer of oxide growth was twice that of the alloy from which it was formed. (The oxygen content of the oxide growth was, of course, supplied by the crucible.) Thus, a selective and accumulative loss of plutonium from the alloy to the oxide growth occurred. Successive layers of growth contained less and less plutonium as the alloy became further and further depleted in plutonium. Consequently, the plutonium content of the final alloy was too low for proper equilibration with the oxide crucible.

One possible way of overcoming this difficulty would be to use an initial alloy sufficiently high in plutonium to compensate for the plutonium loss to the oxide growth. The required alloy composition can be calculated from the weights of crucible and alloy and an assumed approximate final O/M composition for the crucible. However, when this method was attempted, the initial layers of oxide growth contained so much more plutonium than the crucible that an appreciable amount of plutonium diffused from the growth to the crucible. This, of course, led to a crucible having a concentration gradient of plutonium as disclosed by EPM examination.

A second method of overcoming the difficulty was apparent, namely, to use a two-stage equilibration process. This proved to be a practical method. During the first stage, the crucible is reduced nearly to the hypostoichiometric boundary composition. The alloy, then depleted in plutonium, is removed and replaced by fresh alloy of the proper plutonium concentration for equilibration with the crucible. During the second stage of the process, only a minor additional oxide growth formation occurs, hence the alloy composition changes very little and satisfactory final conditions for equilibration are achieved. In two separate experiments, crucibles with O/M compositions of 1.686 and 1.713, an average of 1.700, were obtained at 2000°C.

Before proceeding with similar two-stage equilibration processes at other temperatures, the tie-line-plutonium ratio was established as a function of temperature for oxides containing 19.8 at. % plutonium. This was accomplished by the EPM examination of

alloys and oxide growths formed between the alloys and oxide crucibles in relatively short-term tests at 1588, 1801, and 2215°C. It was found that the tie-line-plutonium ratio was almost independent of temperature for this temperature range.

With the tie-line information from these tests, specific alloy compositions for equilibration at four additional temperatures with oxide crucibles containing 19.8 at. % plutonium were calculated and prepared. These experiments were successfully carried out at 1858, 1925, 2082, and 2168°C. Crucible samples from these tests were analyzed in duplicate for oxygen. The data, which represent points on the hypostoichiometric boundary of the fluorite phase at a 19.8 at. % plutonium section of the oxide, are shown in Fig. III-4. For reference purposes, the data from the U-UO_2 system,[3] which can be considered to be at a section through the ternary system where the at. % plutonium is zero, are included in Fig. III-4. Thus, it is apparent that the hypostoichiometric boundary at 19.8 at. % plutonium is more hypostoichiometric than the boundary at 0 at. % plutonium by 0.17 to 0.20 O/M units in the temperature range of this study.

It is planned next to study the hypostoichiometric boundary of the oxide containing 44.1 at. % plutonium and subsequently that of the oxides containing 64.3 and 80.4 at. % plutonium. In addition, a study of the hyperstoichiometric boundary of the oxide containing 19.8 at. % plutonium has begun; this study will later be extended to the oxides of higher plutonium content.

3. Phase Diagram of the U-Pu-O System Containing Nonradioactive Fission Products (*H. Chen, P. E. Blackburn*)

The objective of this study is to obtain, for the chemical interactions among fast breeder reactor fuel, its fission products, and the cladding material, thermodynamic data which may be useful in designing a fuel system having a suitably long lifetime.

Analyses of irradiated fuels suggest that cesium and its compounds, which can penetrate the grain boundary of stainless steel (ANL-7575, p. 103), are closely related to the corrosion of the cladding. The Cs-O and Cs-U-O systems will, therefore, be investigated with an emphasis on the variation of oxygen activities with composition and temperature. The experimental scheme calls for the use of the Knudsen effusion technique and a microbalance. The oxygen potential will be determined from the vapor pressure of cesium over the Cs-O system using the Gibbs-Duhem equation. Work on the Cs-U-O system will follow that on Cs-O. A work chamber opening to a dry box has been constructed to house the balance, so that samples can be handled under a controlled atmosphere.

In connection with the interaction of stainless steel and cesium compounds, a preliminary examination has been carried out by chemical transport experiments and by thermodynamic calculations to assess the possibility of a chemical transport of iron by iodine (Van Arkel process). Although results indicate that iodine vapor can transport iron from stainless steel against a temperature gradient, free iodine should not be available for such transport in the presence of Cs_2O, since Cs_2O should react with I_2 to form the very stable CsI compound. However, it was also observed experimentally that free iodine was released from CsI and UO_{2+x} at about 900°C when $x \geq 0.18$ (the lowest value of x yet studied). The released iodine attacked stainless steel extensively, but did not transport iron efficiently unless the remaining UO_{2+x} was removed. When transport did not occur, an unidentified white deposit was observed.

A plausible explanation for these observations is as follows. Formation of a ternary Cs-U-O compound more stable than Cs_2O could cause the release of iodine from CsI. Under the high oxygen potential over $UO_{2.18}$, the iodine will attack stainless steel and form an Fe-O-I compound instead of FeI_2, which is essential in the transport of iron. This model, which assumes that Cs_2O can be stabilized by the formation of a ternary compound with UO_{2+x}, provides an explanation for the observation that there is cesium in the center of the irradiated fuel where the temperature is much higher than the boiling point of either CsI or Cs_2O (see Section IV-A of this report). There is also evidence (ANL-7575, p. 102) that similar stabilization of Cs_2O can proceed through the formation of the compound Cs_2O-Al_2O_3.

The work that has been carried out thus far has been helpful in constructing a model for the corrosion of the cladding by the fission products. However, it is evident that additional work is necessary to further the understanding of the Cs-U-O system and, in particular, the thermodynamic properties of its ternary compounds. To prevent corrosion of the cladding by fission product iodine, an oxygen content in the fuel must be found that will make cesium available to iodine for the formation of CsI, which is not corrosive chemically to stainless steel.

More experiments are being planned to identify the new compounds formed and to determine their thermodynamic properties.

4. Total Effusion of Pu-O and U-Pu-O Systems (*R. K. Edwards, P. M. Danielson*)

An effusion apparatus, previously used to determine the congruently vaporizing compositions of urania (see ANL-7325, p. 103), has been modified in order that studies may be carried out on the Pu-O and U-Pu-O systems. As previously used, the apparatus consisted of an ultrahigh-vacuum system in which an induction coil could be used to heat the effusion cell to high temperatures. The principal external modification required was coupling to a glovebox to protect personnel from contamination because of the anticipated radiation hazard. To increase the information output from the study while also reducing the time required for experimentation, two internal modifications were designed into the apparatus: (1) a quadrupole mass-spectrometer sensing probe that can be moved at will during an effusion run so that it either continuously or periodically intercepts the effusing gas beam, and (2) a quartz-crystal sensing head of a microbalance that can also, either continously or periodically, intercept the effusing gas beam and yield high-sensitivity measurements of the total effusive loss in terms of the effusate condensed. Theoretical analyses as well were directed toward increasing the efficiency of the experiments. It has been established that compositions of the condensed phase should be determinable from a mathematical analysis of the mass-spectrometric ion-current data more accurately than from time-consuming chemical analyses.

The mass-spectrometer installation has been completed, and initial testing and calibration runs (with urania materials) are under way. The preliminary performance appears excellent, in particular the temperature constancy of the effusion cell as deduced from the constancy of the species ion currents during congruent effusion. The quartz-crystal microbalance performs satisfactorily in tests external to the effusion apparatus; it will be installed at the appropriate time during the continuation of the testing. During the testing with urania materials, it will also be our objective to determine the relative ionization cross sections of the vapor species (U, UO, UO_2, UO_3), both so that these values may be better known and to guide us for the analogous evaluations in the Pu-O system. The values are needed to establish more reliably the partial pressures over the U-Pu-O system by mass spectrometric measurements (see Section III.A.1 of this report). Plutonium studies will begin after full plutonium capability for the glovebox has been achieved.

As was noted above, theoretical analyses were developed to guide the design of the apparatus so that the measurements to be carried out would efficiently lead to the desired objectives. The theoretical analyses have been focused on an evaluation of the new mass spectrometric "traverse" technique first proposed by R. K. Edwards (ANL-6925, p. 168) and preliminarily "proven" in limited tests (ANL-7225, p. 135). The results of the analyses have confirmed the desirability of using the technique in this work and as a new approach to measurements in related binary systems in general. The extension of this approach to ternary systems (such as U-Pu-O) is, in principle, obvious; but the mathematical formulations are more complex, and are yet to be thoroughly evaluated to establish their limits of reliability. A brief description of the technique is given below.

The traverse technique for a given binary phase with congruently effusing compositions, such as plutonia, consists of conducting two continuous isothermal effusion runs in which the composition of the sample changes (traverses), firstly, from the hyperstoichiometric phase boundary to the congruently effusing composition, and secondly, from the hypostoichiometric phase boundary to the congruently effusing composition. During the continuous effusion, mass spectrometric measurements of the species ion currents are measured either continuously or semicontinuously to yield curves and equations of their interdependencies. The derivative of the ion current of any one species with respect to that of any other species (excluding polymer pairs) determines the composition of condensed phase that is in equilibrium with the species partial pressures corresponding to the ion currents at that point (see ANL-6925, p. 168). Thus, for any generalized pair of species, $A_{a'}B_{b'}$ and A_aB_b ,

$$\left(\frac{\partial \ln I_{A_{a'}B_{b'}}}{\partial \ln I_{A_aB_b}}\right)_{T,\mathrm{oc}} = \frac{b' - a'r}{b - ar} \tag{9}$$

where I represents the ion current of the species, r is the atom ratio B/A in the solid phase, and T and oc imply that temperature and operating conditions of the mass spectrometer are to be held constant during the traverse. Consequently, the ion currents *vs* composition curves may be determined without interruption or need for chemical analyses.

A simulated experiment has been carried out by computer analysis. It has been shown with "data" of realistic error that compositions can be evaluated with both smaller precision errors and much smaller absolute errors than can be achieved by chemical analysis.

Once the ion current *vs* composition isotherms have been established for a series of temperatures, the partial molar enthalpies of vaporization can be evaluated by the second-law method. However, to get the partial molar free energies or entropies, the ion currents must

be converted to partial pressures. To effect this conversion, the ionization cross sections for the gaseous species need to be known. It is most desirable to experimentally determine the ionization cross sections since none of the existing methods for their estimation has been shown to be reliable for molecular species. Consequently, the apparatus discussed above has been designed with the capability of providing measurements of the total effusive loss from a sample via the collection of the effusate on the quartz crystal of the microbalance. If a curve of the weight of effusate *vs* time is then established from either a continuous or semicontinuous record from the microbalance, the slope of this curve may be related to the partial pressures of the species via the Knudsen effusion equations and, with the ion current relations already established above, the ionization cross sections may be evaluated.

Some alternate routes to obtaining the ionization cross sections are apparent and will be subjected to computer analyses for evaluation.

5. Oxygen Gradients, Total Vapor Pressures, and Oxygen Potentials in Reactor Fuels (*A. J. Becker, P. E. Blackburn*)

Assembly and testing of the high-temperature transpiration apparatus for study of the Pu-O and U-Pu-O systems (see ANL-7575, p. 87) have been completed. The apparatus is shown schematically in Fig. III-5.

During the transpiration experiments, a H_2O-H_2 gas mixture is recirculated over the Pu-O or U-Pu-O sample, which is suspended from a Cahn electrobalance, until the mixture reaches a fixed composition in equilibrium with the sample. The H_2O/H_2 ratio, as measured by an electrolytic hygrometer, establishes the oxygen potential for the sample. For higher oxygen pressures, mixtures of inert gas and oxygen are recirculated over the sample and oxygen potentials monitored by an oxygen concentration cell. Continued gas circulation transpires metal and oxide vapor. The rate of transpiration is monitored with the electrobalance which measures weight changes of the oxide sample. Alternatively, the overall rate of transpiration is obtained at the conclusion of the experiment by chemically analyzing the condensed oxide vapor.

It has been established that the balance (the noise level of which is ± 2 μg at room temperature) will operate at temperature in flowing gases with a noise level of ± 30 μg. The equipment is designed to operate with iridium tubes and sample crucibles at temperatures up to 2000°K and at high oxygen pressure, i.e., up to 0.2 atm. Measurements at higher temperatures will be obtained at low oxygen levels with tungsten tubes.

Initial experiments in which O_2 and $UO_3(g)$ pressures are measured over single-phase UO_{2+x} and two-phase U_4O_9-U_3O_8 are currently in progress. This system was chosen because oxygen levels and oxide pressures should be comparable to those in the Pu-O and U-Pu-O systems.

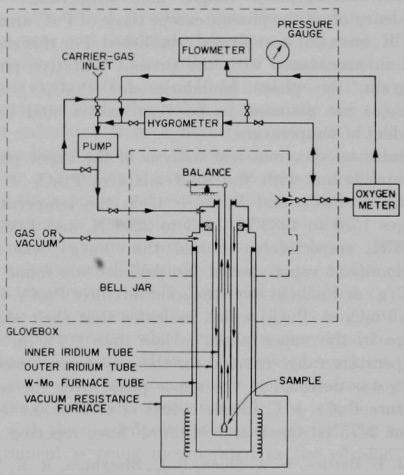

308-2173

FIG. III-5. Schematic of the Core of the Recirculating Transpiration Apparatus for Studies on U-Pu-O.

6. Volatilization Studies of Plutonium Carbide Compounds by Mass Spectrometry (*J. E. Battles, R. K. Edwards, W. A. Shinn*)

As part of an investigation of the thermodynamic properties of mixed carbides, the volatilization behavior of the plutonium carbides has been investigated by combined mass-loss and mass-spectrometric Knudsen effusion studies. These studies were conducted to determine (1) the composition of the vapor phase in equilibrium with the condensed phase(s), (2) the partial pressures of the vapor species as a function of temperature, and (3) the thermodynamic properties of the vapor species and condensed phases. In particular,

attention was focused on the univariant condensed systems Pu_2C_3 + C, PuC_2 + C, and Pu_2C_3 + PuC_2. Preliminary results obtained for the condensed systems Pu_2C_3 + C and Pu_2C_3 + PuC_2 were previously reported (ANL-7575, p. 82). The investigation of the three condensed systems noted above has now been completed and a paper entitled "A Mass Spectrometric Study of the Volatilization Behavior in the Plutonium-Carbon System"[4] has been written. A summary of this study follows:

According to the Pu-C phase diagram[5] which is based mainly on the original work of Mulford *et al.*,[6] there are, at selected temperatures, five thermodynamically invariant two-phase fields consisting of solids only: Pu_3C_2 + PuC,[7] PuC + Pu_2C_3, Pu_2C_3 + C, Pu_2C_3 + PuC_2, and PuC_2 + C. The condensed systems Pu_2C_3 + PuC_2 and PuC_2 + C are stable only at temperatures above 2023°K. However, more recent data[8] indicate that the eutectoid decomposition of PuC_2 occurs at 1933 ± 15°K, rather than at 2023°K. In fact, the precise homogeneity ranges and temperature dependency of all the phases, except those of PuC around 875°K, have not been firmly established. For this study and in accordance with the present tentative phase diagram, the phase boundaries for Pu_2C_3(s) and PuC_2(s) are assumed to be very narrow and independent of temperature.

Our mass-spectrometric analysis of the vapor phase in equilibrium with the solid mixtures Pu_2C_3 + C, Pu_2C_3 + PuC_2, and PuC_2 + C in the temperature ranges 1579 to 1933°K, 1933 to 2299°K, and 1933 to 2348°K, respectively, showed that Pu(g) was the predominant vapor species. No evidence was found for PuC(g) or PuC_2(g) over the solid mixtures Pu_2C_3 + C and Pu_2C_3 + PuC_2, which indicates that their abundance in the vapor phase is less than 0.1% in the temperature range covered for these systems. Gaseous PuC_2 was detected in the vapor phase over the solid mixture PuC_2 + C to the extent of 0.05 to 0.1% at about 2275°K. Olson and Mulford[9] have reported observing about 0.1% of PuC_2(g) in the vapor phase over condensed Pu_2C_3 + C at about 1990°K.

From considerations of the mass spectrometric data, X-ray diffraction and chemical analyses of sample residues, and the phase diagram, we have concluded that vaporization of Pu(g) occurs primarily by the following reactions,

$$\tfrac{1}{2}\,Pu_2C_3(s) = Pu(g) + \tfrac{3}{2}\,C(s) \qquad (10)$$

$$2\,Pu_2C_3(s) = Pu(g) + 3\,PuC_2(s) \qquad (11)$$

and

$$PuC_2(s) = Pu(g) + 2C(s) \qquad (12)$$

although, as noted above, the exact composition of each of the condensed phases is, as yet, unknown.

The enthalpies of reaction for the three reactions were determined by the second-law method from mass spectrometric measurements of the ion intensity of Pu^+ as a function of temperature. The averaged enthalpies of reactions from the several runs are 97.59 ± 1.08, 118.72 ± 1.10, and 88.29 ± 0.55 kcal/mol Pu(g) for Reactions 10, 11, and 12, respectively.

The rate of mass effusion was determined at 2127°K for the solid mixture Pu_2C_3 + PuC_2 and at 2170°K for the solid mixture PuC_2 + C. Vapor pressures were then calculated by applying the Knudsen equation for molecular effusion

$$P(\text{atm}) = (2.256 \times 10^{-2})\,\frac{w}{Atk}\sqrt{\frac{T}{M}} \qquad (13)$$

where w/At is the rate of effusion (w is the mass loss through orifice area A in time t, in g/cm^2-sec), T is the absolute temperature, M is the molecular weight of the vapor species, and k is the Clausing correction factor.[10] The average value of the vapor pressure, calculated from four measurements of the effusion rate in each system, was 5.11×10^{-6} atm at 2127°K for Reaction 11 and 3.62×10^{-6} atm at 2170°K for Reaction 12. When the values for the vapor pressures and the slopes derived from the temperature-dependence data are used to evaluate the intercepts, the following equations for the vapor pressures as a function of temperature are derived for Reactions 11 and 12, respectively:

$$\log P(\text{atm}) = (6.910 \pm 0.140) - \frac{(25{,}940 \pm 240)}{T}\ (1933\text{–}2299°\text{K}) \qquad (14)$$

[4] J. E. Battles, W. A. Shinn, P. E. Blackburn, R. K. Edwards, *High Temperature Science*, in press.

[5] D. T. Livey, P. Fischotte, *Atomic Energy Review* **4**, Special Issue No. 1, 53 (1966).

[6] R. N. R. Mulford, F. H. Ellinger, G. S. Hendrix, C. D. Albrecht, "The Plutonium-Carbon System," *Plutonium 1960*, p. 301, Cleaver-Hume Press, London (1961).

[7] It should be noted that the designation PuC represents a compound with a fairly wide range of composition, but less than the stoichiometric value.

[8] J. G. Reavis, Los Alamos Scientific Laboratory, private communication (1969).

[9] W. M. Olson, R. N. R. Mulford, "Thermodynamics of the Plutonium Carbides," *Thermodynamics of Nuclear Materials, 1967*, p. 467, IAEA, Vienna (1968).

[10] P. Clausing, *Ann. Phys.* **12**, 961 (1932); see also S. Dushman, *Scientific Foundations of Vacuum Technique*, pp. 80-117, John Wiley & Sons, Inc., New York (1962).

and

$$\log P(\text{atm}) = (3.450 \pm 0.090) - \frac{(19{,}290 \pm 120)}{T} \quad (1933\text{–}2348°\text{K}). \tag{15}$$

The errors indicated for the intercepts in the above equations are the standard deviations in the enthalpies combined with an estimated uncertainty of 7 % in the measurement of mass-effusion rates.

The eutectoid temperature, i.e., the temperature at which Pu_2C_3(s), PuC_2(s), and C(s) are in equilibrium, was estimated to be 1932°K from averaging the following four values. From two different experiments, the values 1952 and 1883°K were obtained from the intersections obtained by plotting log IT *vs* $1/T$ for the solid mixtures PuC_2 + C and Pu_2C_3 + C (C/Pu ~2.5). Similarly, the intersection obtained by plotting log IT *vs* $1/T$ for the solid mixtures Pu_2C_3 + C and Pu_2C_3 + PuC_2 (C/Pu ~1.8) yielded 1969°K. Equating Equations 14 and 15 for the solid mixtures Pu_2C_3 + PuC_2 and PuC_2 + C and solving for T yielded 1924°K. The estimated eutectoid temperature of 1932°K, derived from the average of the four values given, supports well the recent value of 1933 ± 15°K determined by Reavis.[8]

The pressure-temperature relationship for Reaction 10

$$\log P(\text{atm}) = (4.510 \pm 0.140) - \frac{(21{,}330 \pm 240)}{T} \quad (1579\text{–}1933°\text{K}) \tag{16}$$

was obtained by equating the vapor pressures for the solid mixtures Pu_2C_3 + C and PuC_2 + C (Equation 15) at 1933°K and utilizing the enthalpy of vaporization (97.59 kcal) obtained for Reaction 10. This method was selected since the rate of effusion in the solid mixture Pu_2C_3 + C is not sufficient for accurate measurement by the weight-loss technique using our present equipment, and since, at the eutectoid temperature, the vapor pressures for the two solid mixtures must be equal.

The equations for the vapor pressures obtained in each univariant system are plotted in Fig. III-6. The datum point on the line for the PuC_2 + C mixture and the one on the line for the PuC_2 + Pu_2C_3 mixture represent averages obtained from four measurements of the rate of mass effusion. The vapor pressure data for Reactions 10, 11, and 12 reported by previous investigators[9, 11, 12] have also been included in Fig. III-6. The enthalpy and entropy of formation of $PuC_{1.5}$(s) from the elements were evaluated at the reference temperature 298°K by combining vapor pressure data with $H_T^o - H_{298}^o$ and $S_T^o - S_{298}^o$ data. The values are $\Delta H_{f,298}^o = -16.14 \pm 1.10$ kcal/mol and $\Delta S_{f,298}^o = +5.09 \pm 0.60$ eu.

The enthalpy of formation for $PuC_{1.5}$(s) at 298°K (−16.14 kcal/mol) obtained in this study is more negative than the value (−12.3 kcal/mol) obtained by Olson and Mulford[9] from their vapor pressure measurements of condensed Pu_2C_3 + C and is also more negative than the value −13.7 kcal/mol which we calculate from their vapor pressure data for condensed PuC + Pu_2C_3. On the other hand, the value of $\Delta H_{f,298}^o = -17.3$ kcal/mol for $PuC_{1.5}$(s) derived from the data of Harris *et al.*[11] agrees well with the value obtained in this study. La Page,[13] from combustion calorimetry measurements, has obtained a preliminary value of −21 ± 2 kcal/mol. Huber and Holley[14] reported a "very preliminary value," $\Delta H_{f,298}^o = 1.7$ kcal/mol for Pu_2C_3(s) based on combustion measurements. Assessment of this value is not possible, since the experimental details were not reported; however, it appears to be seriously in error. The enthalpy of formation obtained in this study [$\Delta H_{f,298}^o = -16.14$ kcal/mol of $PuC_{1.5}$(s)] is preferred since this value is essentially the same as that calculated from a numerical average of all the values listed above (−16.1 kcal/mol), if the value of Huber and Holley is excluded. However, it is evident from the range of values that definitive measurements of the heat of combustion would be desirable.

Since plutonium dicarbide is unstable below 1933°K, the calculation of thermodynamic values at the reference temperature (298°K) was not attempted.

This work was carried out with a Bendix time-of-flight mass spectrometer which had been converted to plutonium capability. However, projected work on the ternary U-Pu-C system, which is being directed toward obtaining the relative activities of U/Pu, is to be carried out with the quadrupole mass spectrometer. The latter instrument is being incorporated in the effusion apparatus (see Section III.A.4 of this report), and experiments will begin when this total apparatus achieves

[11] P. S. Harris, B. A. Phillips, M. H. Rand, M. Tetenbaum, "The Volatility of Plutonium Carbides, Part I," UKAEA Report AERE-R 5353 (1967).

[12] R. N. R. Mulford, J. O. Ford, J. G. Hoffman, "The Volatility of Plutonium Carbide," *Thermodynamics of Nuclear Materials*, p. 517, IAEA, Vienna (1962).

[13] R. LaPage, private communication from UKAEA, Aldermaston, Berkshire, England (1969).

[14] E. J. Huber, C. E. Holley, Jr., "The Thermodynamic Properties of the Actinide Carbides Including New Measurements of the Heats of Formation of Some Thorium, Uranium and Plutonium Carbides," *Thermodynamics of Nuclear Materials*, p. 581, IAEA, Vienna (1962).

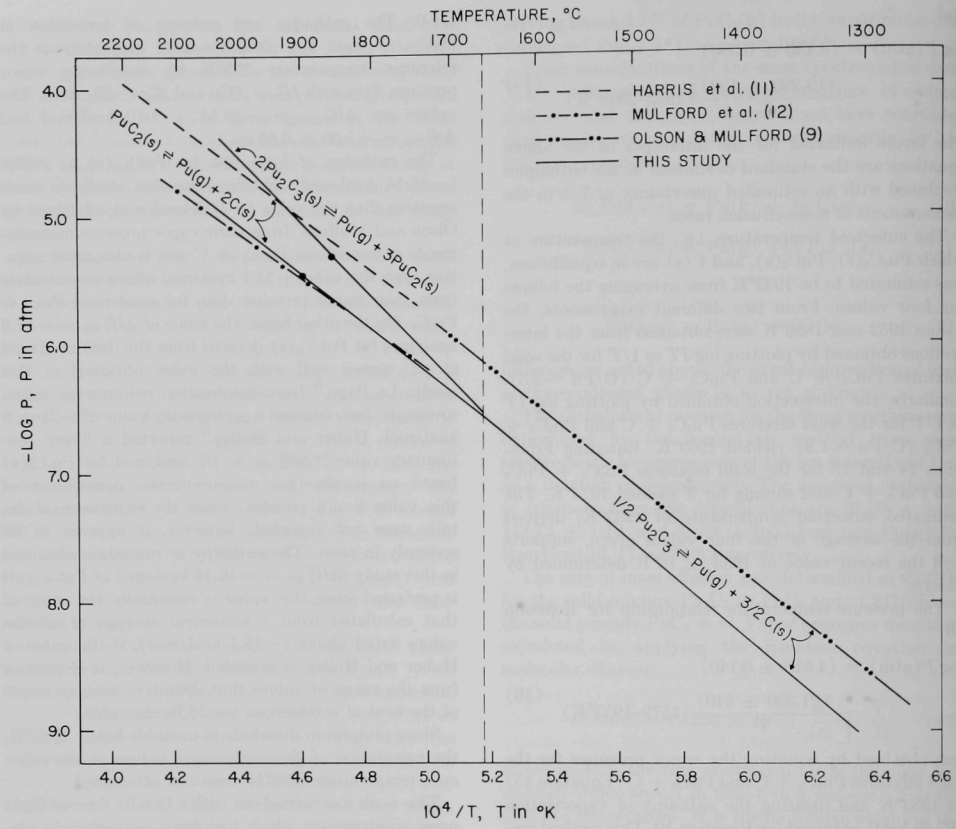

308-1983

FIG. III-6. Vapor Pressure of Pu(g) Over the Solid Mixtures Pu_2C_3 + C, PuC_2 + C and Pu_2C_3 + PuC_2.

plutonium capability. The higher sensitivity of this instrument is needed to get significant measurements of the partial vapor pressure of uranium at the same time as those of the partial vapor pressure of plutonium (the partial vapor pressure of uranium is anticipated to be much smaller than that of plutonium).

7. Transpiration Studies of the Uranium-Carbon System (*M. Tetenbaum, P. D. Hunt*)

The study of the vaporization behavior of the uranium-carbon system (ANL-7575, p. 86) is continuing. Measurements of the total pressure of uranium-bearing species and carbon activity are being made as functions of temperature and UC_x composition, using the transpiration method with hydrogen-methane mixtures as carrier gases. Emphasis has been placed on measuring carbon activities in the uranium-carbon system. These measurements will ultimately be extended to the plutonium-carbon and U-Pu-C systems. The effects of oxygen as an impurity, as well as fission product carbides on carbon activity in these systems will also be considered.

The results of the latest measurements of carbon activity as functions of UC_x composition at 2155, 2255, 2355, and 2455°K are shown in Fig. III-7. Although

the exact shapes of the isotherms should be considered tentative, they are consistent with expectations, namely, a sharp decrease in carbon activity near the stoichiometric composition of uranium carbide as the composition of the condensed phase is reduced toward the lower phase boundary [U(l) + UC(s)] in the hypostoichiometric region. The plateaus of the 2155, 2255, and 2355°K isotherms are consistent with the miscibility gap (UC + βUC_2) shown by the phase diagram proposed by Storms[15] for the uranium-carbon system. Over the composition range investigated at 2455°K, the shape of the carbon activity curve is typical of bivariant behavior and is also consistent with the phase diagrams, which show a single-phase region above the miscibility gap, with a critical temperature of ~2100°C (~2373°K) at C/U $\simeq$ 1.3. Compositional values for the boundaries of the UC + βUC_2 diphasic region at 2155, 2255, 2355°K derived from our measurements are given in Table III-2. The low-carbon values are in good agreement with the compositions estimated from the phase diagram at these temperatures. The shallowness of the isotherms at the higher carbon compositions makes it difficult to estimate the terminal compositions of the UC + βUC_2 diphasic region from our data.

Calculated values for the free energies and heats of formation are given in Table III-3. The free energy of formation values were calculated from our carbon-activity measurements shown in Fig. III-7, the adjusted uranium vapor pressure values of Storms,[15] and 126.3 kcal/mol as the heat of vaporization of uranium.[16] Heat of formation values (at 298°K) were estimated from the calculated free energy of formation values and the known free energy functions[15, 17] for U(l), $UC_{1.00}$(s), "UC_2"(s), and graphite. The $\Delta(G_T^o - H_{298}^o/T)$ values for UC_x compositions were interpolated on the assumption that a linear relationship exists for these values between $UC_{1.00}$ and $UC_{1.93}$.

The heats of formation of $UC_{1.00}$ and $UC_{1.85}$ found by averaging values in Table III-3 are −22.6 ± 0.5 and −23.7 ± 1.0 kcal/mol, respectively. The value chosen by the Vienna Panel[18] for $UC_{1.00}$ is −21.7 ± 1.0 kcal/mol; for $UC_{1.91}$, the value of −23 ± 2 kcal/mol was adopted. A more recent value of −23.2 ± 1.0 kcal/mol was estimated for $UC_{1.00}$ by Storms and Huber;[19] they obtained values of −23.2 ± 0.9 and −23.0 ± 1.0 kcal/mol for the heats of formation of $UC_{0.996}$ and $UC_{1.032}$, respectively, from combustion measurements.

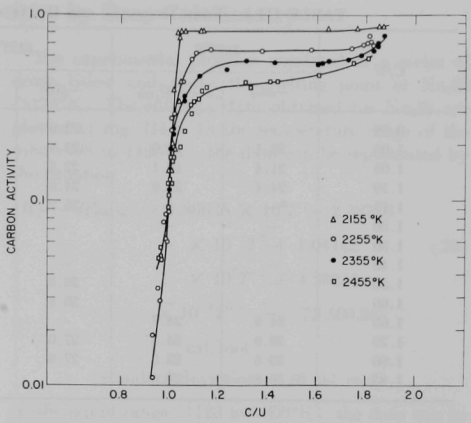

308-2174

FIG. III-7. Activity of Carbon as a Function of Composition.

The free energy of formation values given in Table III-3 are in reasonable agreement with the values derived from the mass-spectrometric measurements of Storms[15] at 2100 and 2300°K. For $UC_{1.00}$, Storms obtains ΔG_f^o values of −25.2 and −25.4 kcal/mol at 2100 and 2300°K, respectively; for $UC_{1.80}$, he obtains ΔG_f^o values of −27.0 and −28.0 kcal/mol at the same two temperatures. Values for the enthalpy of vaporization of uranium monocarbide were calculated, assuming monatomic carbon as the principal gaseous carbon species, from the reaction

$$UC_{1.00}(s) = U(g) + C_1(g) \qquad (17)$$

and the relationship

$$\Delta H_{298}^o = -RT \ln K - T\Delta\left(\frac{G_T^o - H_{298}^o}{T}\right) \qquad (18)$$

TABLE III-2. Low- and High-Carbon Compositions for Diphasic Region, UC + βUC_2

	Temperature (°K)	Composition (C/U)	
		This Work	Phase Diagram
Low Carbon	2155	1.05	1.13
	2255	1.15	1.14
	2355	1.25	1.20
High Carbon	2155	<1.65	1.61
	2255	<1.65	1.50
	2355	<1.60	1.35

[15] E. K. Storms, *The Refractory Carbides*, Chap. XI, pp. 205–213, Academic Press, New York (1967).

[16] R. J. Ackermann, E. G. Rauh, *J. Phys. Chem.* **73**, 769 (1969).

[17] H. L. Schick, *Thermodynamics of Certain Refractory Compounds*, Vol. II, Academic Press, N. Y. (1966).

[18] Vienna Panel, Technical Series No. 14, *The Uranium-Carbon and Plutonium-Carbon Systems*, IAEA, Vienna (1963).

[19] E. K. Storms, E. J. Huber, *J. Nucl. Mater.* **23**, 19 (1967).

TABLE III-3. FREE ENERGIES AND HEATS OF FORMATION FOR UC_x (ALL VALUES IN KCAL/MOL)

C/U	2155°K		2255°K		2355°K		2455°K	
	$-\Delta G_f^o$	$-\Delta H_{f(298)}^o$	$-\Delta G_f^o$	$-\Delta H_{f(298)}^o$	$-\Delta G_f^o$	$-\Delta H_{f(298)}^o$	$-\Delta G_f^o$	$-\Delta H_{f(298)}^o$
0.98	—	—	23.6	21.6	23.4	21.5	24.4	22.7
1.00	25.1	23.0	24.8	22.7	24.7	22.7	24.5	22.0
1.05	21.4	19.1	22.5	20.2	23.1	20.8	23.6	21.3
1.10	24.4	21.9	24.6	22.0	25.4	22.8	25.8	23.0
1.15	—	—	25.2	22.4	25.8	22.9	26.8	23.9
1.20	—	—	—	—	25.8	22.6	26.7	23.5
1.30	—	—	—	—	—	—	27.3	23.4
1.40	—	—	—	—	26.3	22.0	27.8	23.3
1.50	—	—	26.3	21.7	27.0	22.1	28.3	23.2
1.60	—	—	26.8	21.7	27.9	22.5	29.0	23.2
1.65	24.9	24.7	—	—	—	—	—	—
1.70	29.9	24.4	27.0	21.4	28.4	22.4	29.0	22.6
1.80	30.6	25.0	27.9	21.8	28.4	21.8	28.8	21.7
1.85	30.8	25.0	—	—	29.3	22.3	—	—

where the equilibrium constant $K = p_U g_C$. The partial pressure of $C_1(g)$ was estimated from our carbon activity measurements and the pressure of $C_1(g)$ in equilibrium with graphite.[17] Storms'[15] adjusted vapor pressure measurements were used to estimate the total pressure of U(g). The appropriate free energy function values were obtained[15, 17] for $C_1(g)$, U(g), and $UC_{1.00}$. The results of these calculations, for the temperatures of our carbon activity measurements, are as follows:

Temperature (°K)	ΔH_{298}^o (kcal/mol)
2155	322.4
2255	322.5
2355	320.0
2455	321.9
	Ave. 322.2 ± 1.2

For comparison, the enthalpy of vaporization was also derived from the following thermodynamic cycle for $UC_{1.00}$:

Reaction	ΔH_{298}^o (kcal/mol)
UC(s) = U(s) + C(s)	23.2 ± 1
U(s) = U(g)	126.3 ± 1
C(s) = C_1(g)	170.9 ± 0.5
UC(s) = U(g) + C_1(g)	320.4 ± 1.5

It should be noted that the measurements of Pattoret, Drowart, and Smoes[20] yield $\Delta H_{298}^o = 128.5 \pm 2.0$ kcal/mol for the heat of sublimation of uranium; the enthalpy of vaporization calculated via the above cycle using this value would be $\Delta H_{298}^o = 322.6 \pm 1.9$ kcal/mol. The enthalpy of vaporization values obtained via the thermodynamic cycle are decreased by ~1.5 kcal/mol if the Vienna Panel heat of formation value of -21.7 ± 1.0 kcal/mol is used in the calculations. The agreement between the enthalpy of vaporization for $UC_{1.00}$ based on carbon activity measurements and the values derived from the above thermodynamic cycle are encouraging.

[20] A. Pattoret, J. Drowart, S. Smoes, *Trans. Faraday Soc.* **65**, 98 (1969).

B. REACTOR SAFETY AND PHYSICAL PROPERTY STUDIES (*M. G. Chasanov*)

The primary objective of these studies is to provide physical property data for use in evaluating the safety of various prospective fast-breeder reactor materials. It is expected that these data obtained at temperatures above normal operating conditions can be suitably extrapolated to the very high temperatures involved in accident situations. In addition, physical property data in support of other Divisional programs are being obtained.

1. Enthalpies and Heat Capacities by Drop Calorimetry

Three complementary calorimetric systems for the measurement of high-temperature enthalpy increments by the method of mixtures (the "drop method") are in operation (see ANL-7575, p. 89): One uses resistance heating to achieve temperatures to 1600°K, the second utilizes electron-beam heating for temperatures to 2500°K, and the third employs induction heating for temperatures to 3600°K.

a. Resistance-heated and Electron-beam-heated Calorimetric Systems (*D. R. Fredrickson, R. D. Barnes*[21])

(1) Uranium Diboride ($UB_{1.98}$)

Enthalpy measurements made on $UB_{1.98}$ over the range 600–1500°K, employing the resistance-heated calorimetric system (ANL-7575, p. 89), were presented in the open literature[22] along with a description of the apparatus. Extension of the $UB_{1.98}$ data using the electron-beam-heated calorimetric system has been carried out at temperatures from 1300 to 2300°K. The data in the region of overlap (1300 to 1500°K) showed excellent agreement with those obtained using the resistance-heated system. The following equation summarizes the enthalpy values of $UB_{1.98}$ over the entire temperature range studied (600 to 2300°K) using both calorimetric systems:

$$H_T^\circ - H_{298}^\circ = 3.83605T + 2.00514 \times 10^{-2}T^2 - 1.04778 \times 10^{-5}T^3 + 2.18407 \times 10^{-9}T^4 - 2665.71 \text{ cal/mol} \quad (19)$$

(standard deviation = 34 cal/mol)

(2) Sodium-Bismuth (Na_3Bi)

The resistance-heated calorimetric system was used to obtain enthalpy increments (referred to 298.15°K) and the enthalpy of fusion of the intermetallic compound Na_3Bi.

The Na_3Bi was prepared by reacting sodium and bismuth in stoichiometric amounts in a tantalum capsule.[23] After confirming proper stoichiometry by thermal analysis, the calorimetric experiments were performed with the same sample and capsule.

The experimental program consisted of a series of drops below and above the melting point of Na_3Bi (1123°K). The enthalpy data obtained for Na_3Bi are plotted in Fig. III-8. In the temperature range of the solid (488 to 1123°K), the data can be represented by the equation

$$(H_T^\circ - H_{298.15}^\circ) = 1.86638 \times 10^2 T - 2.38758 \times 10^{-1}T^2 + 1.04442 \times 10^7 T^{-1} + 4.29343 \times 10^{-3}T^{5/2} - 73{,}500.95 \text{ cal/mol} \quad (20)$$

(standard deviation = 26 cal/mol)

In the liquid range (1123 to 1300°K), the data can be represented by the equation

$$(H_T^\circ - H_{298.15}^\circ) = 41.6431T - 13.942.38 \text{ cal/mol} \quad (21)$$

(standard deviation = 38 cal/mol)

Extrapolation of Eqs. 20 and 21 to the melting point gives a value of 7085 cal/mol for the enthalpy of fusion of Na_3Bi at 1123°K.

To provide an equation applicable down to 298.15°K, the constraint $(H_T^\circ - H_{298.15}^\circ) = 0$ when $T = 298.15$°K was added. The following equation applies over the

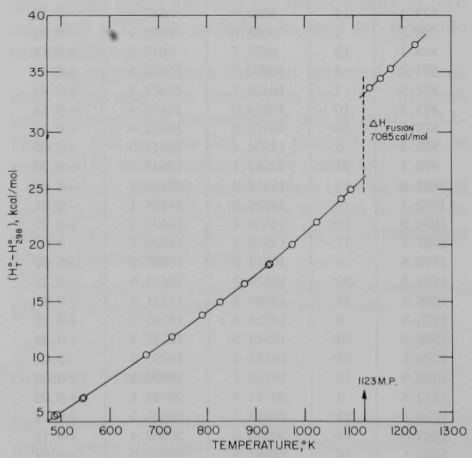

308-2048 Rev. 1

FIG. III-8. Enthalpy of Na_3Bi.

[21] Co-op Student from University of Missouri.

[22] D. R. Fredrickson, R. D. Barnes, M. G. Chasanov, R. L. Nuttall, R. Kleb, W. N. Hubbard, "The Enthalpy of UB_2 from 600–1500°K by Drop Calorimetry," *High Temp. Sci.* 1(3), 373 (1969).

[23] Na_3Bi prepared and analyzed by S. Johnson (see Section V.A.1.a of this report).

temperature range 298 to 1123°K:

$$(H_T^\circ - H_{298.15}^\circ) = 24.2289T - 2.72298 \times 10^{-3}T^2 + 6.30853 \times 10^{-6}T^3 - 7049.00 \quad (22)$$

cal/mol

(standard deviation = 70 cal/mol)

The heat capacity obtained from the derivative of Eq. 22 is

$$C_p^\circ = 24.2289 - 5.44596 \times 10^{-3}T + 18.92559 \times 10^{-6}T^2 \text{ cal/(mol)(°K)} \quad (23)$$

(3) Uranium Dioxide (UO_2)

The resistance-heated calorimetric system was used to obtain enthalpy increments (referred to 298.15°K) for $UO_{2.005}$ over the range 675 to 1434°K. For this work, two samples of powdered UO_2 differing only in their mass (27.54473 and 6.39206 g) were used. In each case, the sample was heated for 16 hr at 1940°C in a vacuum furnace and then sealed (under vacuum) in a tantalum capsule of 15-mil wall thickness. Analysis of the UO_2 by oxidation to U_3O_8 gave duplicate results for the O/U ratio of 2.0049 and 2.0053.

TABLE III-4. ENTHALPY OF URANIUM DIOXIDE ($UO_{2.005}$)

Temperature (°K)	Order of Experiments	$(H_T - H_{298})$ obs. (cal/mol)	$(H_T - H_{298})$ Calcd., Eq. 24 (cal/mol)	% Dev. from Eq. 24
674.5	11	6660.9	6667.8	−0.10
780.5	1	8685.6	8689.1	−0.04
828.1	12	9631.7	9618.2	+0.14
871.3	5	10503.7	10470.5	+0.32
871.4	2	10476.7	10472.4	+0.04
871.7	10	10514.0	10478.4	+0.34
873.9	18[a]	10479.6	10522.0	−0.41
973.4	3	12504.4	12513.0	−0.07
975.1	21[a]	12511.1	12547.3	−0.29
1021.8	13	13486.6	13492.8	−0.05
1073.1	4	14536.3	14538.1	−0.01
1076.0	19[a]	14636.4	14597.3	+0.27
1087.7	17	14828.3	14836.7	−0.06
1173.8	6	16611.2	16607.2	+0.02
1174.5	26[a]	16576.3	16621.6	−0.27
1228.6	14	17686.2	17741.5	−0.31
1275.0	8	18724.8	18705.9	+0.10
1276.5	20[a]	18849.0	18737.2	+0.59
1279.1	25[a]	18781.4	18791.3	−0.05
1328.9	15	19765.4	19830.5	−0.33
1372.8	9	20754.4	20749.5	+0.02
1376.9	23[a]	20885.2	20835.5	+0.24
1383.0	24[a]	20990.0	20963.4	+0.13
1434.1	16	21984.9	22037.0	−0.24

[a] Data from 6.39206-g (0.023672 mol) sample; other data from 27.54473-g (0.102006 mol) sample.

The experimental enthalpy data are given in Table III-4. To eliminate systematic errors, the data were taken in random order of temperature for the two different sample weights used. The following equation, with the constants determined by the method of least squares, represents the unweighted data over the range 675 to 1434°K:

$$(H_T^\circ - H_{298.15}^\circ) = 21.0203T + 2.09152 \times 10^{-4}T^2 + 1.18786 \times 10^6T^{-1} - 9366.64 \quad (24)$$

cal/mol

(standard deviation = 42 cal/mol)

The enthalpies calculated from Eq. 24, along with their deviations from the observed data, are included in Table III-4.

To provide an equation applicable down to 298.15°K, a computer program[24] was used which contained the following constraints:[25] $(H_T^\circ - H_{298.15}^\circ) = 0$, $C_p = 15.20$ cal/(mol) (°K), and $S^\circ = 18.41$ cal/(mol) (°K), when $T = 298.15$°K. The derived equation for temperatures from 298 to 1500°K is

$$(H_T^\circ - H_{298.15}^\circ) = 18.2426T + 1.12307 \times 10^{-3}T^2 + 3.29998 \times 10^5T^{-1} - 6645.68 \quad (25)$$

cal/mol

(standard deviation = 41 cal/mol)

The derivative of Eq. 25 gives the heat capacity as

$$C_p^\circ = 18.2426 + 2.246 \times 10^{-3}T - 3.29998 \times 10^5T^{-2} \text{ cal/(mol)(°K)} \quad (26)$$

(4) Sapphire (Al_2O_3)

As a check on the accuracy of the resistance-heated drop calorimetric system, enthalpy measurements were made on standard sapphire crystals obtained from the National Bureau of Standards. Table III-5 summarizes and compares this work with that of other investigators. The good agreement between the data establishes confidence in our system.

[24] Program HINC, developed by D. W. Osborne of the Chemistry Division.

[25] "Thermodynamic and Transport Properties of Uranium Dioxide and Related Phases," Technical Reports Series No. 39, p. 25, IAEA, Vienna (1965).

b. Induction-heated Calorimetric System

(1) Enthalpy and Heat Capacity of Uranium Dioxide (*L. Leibowitz, L. W. Mishler, D. F. Fischer*)

Work is continuing on the program to determine the heat capacity of liquid uranium dioxide, an important quantity in fast reactor safety calculations. Accurate values of the heat capacity and heat of fusion of molten UO_2 will facilitate estimation of the total energy released and the temperatures attained in the reactor core during destructive nuclear excursions. Induction heating in conjunction with a drop calorimeter is being used for measurements at temperatures that have not been previously explored.

In an experiment, a sample sealed in a tungsten capsule is suspended by tungsten wire in an induction coil and is heated to the desired temperature. For the temperature measurement, a disappearing-filament-type optical pyrometer is sighted on a blackbody cavity (length-to-diameter ratio of ten) extending into the capsule. When the temperature equilibrium has been reached (~20 min), the suspension wire is vaporized by means of a condenser discharge and the hot capsule falls into a modified Parr adiabatic calorimeter. The temperature rise is measured with a quartz thermometer.

TABLE III-5. SAPPHIRE COMPARISONS

Temperature (°K)	$(H_T^\circ - H_{298.15}^\circ)$ (cal/mol)			Deviation (%)	
	This Work[a]	Ginnings[b]	Chekhovskii[c]	from Ginnings	from Chekhovskii
500	4581	4581	4583	—	−0.04
600	7197	7197	7195	—	+0.03
700	9936	9941	9935	−0.05	+0.01
800	12766	12776	12768	−0.08	−0.01
900	15666	15678	15673	−0.07	−0.04
1000	18626	18631	18634	−0.03	−0.04
1100	21637	21624	21641	+0.06	−0.02
1200	24695	24647	24687	+0.20	+0.03

[a] $(H_T^\circ - H_{298.15}^\circ) = 27.6002T + 1.61393 \times 10^{-3}T^2 + 9.65836 \times 10^5T^{-1} - 11{,}554.31$ cal/mol.

[b] D. C. Ginnings, *J. Phys. Chem.* **67**, 1917 (1963).

[c] V. Ya. Chekhovskii, *Teplofizika Vysokikh Temperatur* **2**, 296 (1964).

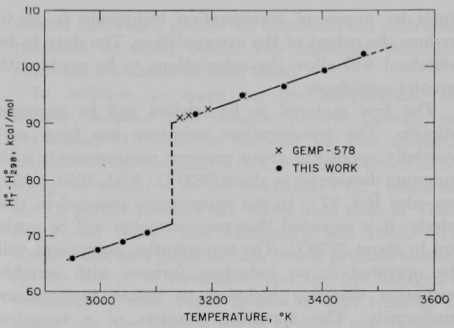

308-2175

FIG. III-9. Enthalpy of UO_2.

The procedure is repeated with an empty capsule and the enthalpy of the sample found by difference.

Data have already been reported (ANL-7575, p. 90) on the enthalpy of tungsten (a calorimetric standard) to 3594°K and of UO_2 to 3329°K. The UO_2 enthalpy measurements have now been extended to 3475°K; the data obtained to date at temperatures above the melting point are shown in Fig. III-9.

The liquid enthalpies are in good agreement in the region overlapping those reported by other workers.[26] These measurements extend previously available data by over 200°K. The heat of fusion of ~18 kcal/mol is also in good agreement with the literature[26] value of 18.2 kcal/mol. A straight line fits the liquid enthalpy data within about 1%, and the heat capacity of 33.6 cal/(mol) (°K) can probably be used for moderate extrapolations.

These enthalpies have not been corrected for tungsten, which may have dissolved in the UO_2. Although indications are that the correction will be small (ANL-7225, p. 198; see also Ref. 26), tungsten analyses as well as O/U determination will be performed.

At present, the calorimeter system is being modified for use with $(U,Pu)O_2$. Attempts will also be made to extend the liquid UO_2 data to still higher temperatures when this conversion is complete.

[26] R. A. Hein, P. N. Flagella, "Enthalpy Measurements of UO_2 and Tungsten to 3260°K," GEMP-578 (1968).

2. Other Physical Property Studies

a. Vapor Pressure over UO_2 at High Temperatures (*M. G. Chasanov, G. T. Reedy*)

An important input parameter for equation-of-state calculations for reactor fuels is vapor pressure of the fuel. Presently available data must be extrapolated over many orders of magnitude to obtain vapor-pressure values at the temperatures of interest in reactor-safety calculations. Consequently, a program has been initiated to measure vapor pressures over liquid reactor

fuels by means of transpiration techniques so as to reduce the extent of the extrapolation. The data to be obtained will allow the calculations to be made with greater confidence.

The first material to be studied will be uranium dioxide. The transpiration technique has been successfully applied to vapor pressure measurements with uranium dioxide up to about 2600°C (ANL-7055, p.165; see also Ref. 27). In the experiments planned in this study, it is expected that measurements will be made up to about 3250°C. The transpiration equipment will be operated in an induction furnace with suitable radiation shielding included to insure temperature uniformity. The apparatus consists of a tungsten susceptor-sample container, within which is a concentric tungsten condenser; this assembly is positioned within the induction heating coil of a 25-kW generator. The coil and susceptor are inside a high-vacuum chamber equipped with a prism and viewports for determining the sample temperature using optical pyrometry. The carrier gas may be either high-purity argon or a mixture of hydrogen and water vapor.

To date, vapor pressure measurements have been performed for testing purposes at about 2350°C. Satisfactory agreement has been found with literature values.[27, 28] Further tests of reproducibility and of several experimental parameters are planned before proceeding to higher temperatures.

b. Matrix-Isolation Spectroscopy of UO_2 (*S. D. Gabelnick*)

Calculations (both our own and others[29]) of fuel and fission product vapor pressures based on presently available thermodynamic data indicate that, at normal fuel operating temperatures, the greatest contributions are due to such species as xenon, cesium, barium oxide, and tellurium. However, at the temperatures likely to be reached under hypothetical reactor accident conditions (up to 10,000°K) estimates of the thermodynamic functions of the gas-phase oxides of uranium and of the condensed phase indicate that the predominant vapor species will be the oxides of the fuel itself. To predict these pressures more accurately, reliable values of the thermodynamic functions of the gaseous oxides of uranium (and of plutonium) must be used. Existing tabulations of these thermodynamic functions[30, 31] are based on statistical mechanical treatments of spectroscopic constants estimated by De Maria *et al.*[32] The fact that the vibrational frequencies given by De Maria are estimates only is not always sufficiently emphasized.

A program to carry out experimental determinations of the appropriate molecular parameters of uranium and plutonium oxides has been started. Adequate concentrations of these molecules for gas-phase spectroscopic studies are available only at very high temperatures; consequently only low-resolution infrared spectra could be obtained because of thermal populations of numerous rotational states. However, by employing the matrix-isolation technique,[33] in which species of interest and an inert diluent gas are co-condensed on a substrate at cryogenic temperatures, high-resolution (0.5 cm^{-1}) infrared spectra can be obtained. The observed frequencies can be assigned to the various species by varying the relative concentrations of the vapor species in the effusing stream; this, in turn, is achieved by varying the O/U ratio of the condensed urania in the evaporation cell. A study of ^{18}O-substituted urania will also be undertaken to calculate such parameters as the bond angle of gaseous UO_2.

Future work will include visible and ultraviolet emission-spectroscopic studies of these same vapor species. The purpose will be to determine the energies and other spectroscopic parameters of low-lying electronic states, which strongly contribute to the thermodynamic properties of these molecules at the high temperatures of interest to the reactor safety program.

c. Theoretical Extrapolation of Measured Physical Property Data to Higher Temperatures (*S. D. Gabelnick*)

Knowledge of the pressure within an operating fuel pin is of importance both to the reactor designer and to the safety analyst. For the designer, the internal pressure at projected operating temperatures is a factor in determining the thickness of the cladding material of the fuel. At normal operating temperatures, the major contribution to the internal pressure comes from buildup

[27] C. A. Alexander, J. S. Ogden, G. W. Cunningham, "Thermal Stability of Zirconia- and Thoria-Base Fuels," BMI-1789 (Jan. 6, 1967).

[28] M. Tetenbaum, P. D. Hunt, "Total Pressure of Uranium Bearing Species over Oxygen-Deficient Urania," *J. Nucl. Mater.* **34,** 86–91 (January 1970).

[29] W. A. Paulson, R. H. Springborn, "Estimation of Fission-Product Gas Pressure in Uranium Dioxide Ceramic Fuel Elements," NASA TN D-4823.

[30] H. Schick, ed., *Thermodynamics of Certain Refractory Compounds*, Vols. I & II, Academic Press, New York (1966).

[31] M. H. Fontana, "The Chemical Equilibria of Fission-Product-Nuclear Fuel Mixtures: The Uranium-Oxygen and the Uranium-Oxygen-Strontium System," Ph.D. thesis, ORNL-TM 2105 (July 1968).

[32] G. De Maria, R. P. Barnes, J. Drowart, M. G. Inghram, *J. Chem. Phys.* **32,** 1373 (1960).

[33] E. D. Becker, G. C. Pimentel, *J. Chem. Phys.* **25,** 224 (1956).

of gaseous fission products in the void region of the fuel pin. Calculation of these vapor pressures is possible using currently available thermodynamic data. The safety analyst, however, must be concerned with the projected behavior of the fuel pin at temperatures reached under accident conditions—temperatures that may be several thousand degrees Kelvin above the normal center-line temperature of the fuel pin. Under these circumstances, the combined vapor pressures of the fission products and fuel may serve as a gas ballast causing molten fuel to be extruded through a cladding rupture if one should occur. Thus the vapor pressure is one of the factors that need to be considered in determining the extent of fuel-coolant interaction as well as in establishing the total pressures generated under accident conditions.

The thermodynamic data needed for calculation of partial vapor pressures of the fission products and of the fuel at these high temperatures cannot be directly obtained by experimental means. Consequently, it is necessary either to find some basis on which to extrapolate existing experimental data taken at low temperatures to higher temperatures or to perform statistical mechanical calculations of the thermodynamic properties based upon observed spectroscopic parameters.

Efforts have initially been devoted to the development of a basic computer program for calculating vapor pressures of fuel and fission products at temperatures for which thermodynamic data are presently available. Although the fuel pin is a highly complex multicomponent system operating under a strong temperature gradient, the following simplifying assumptions, similar to those employed by Paulson and Springborn,[29] make the problem amenable to solution:

1) The central void and surrounding system of cracks in the fuel matrix are considered to be freely accessible to vapor species and to be at uniform temperature.

2) The condensed fuel and fission product species are considered to be immiscible and to have unit activity coefficients.

The major difference between our treatment and that of Paulson and Springborn is that oxide fission products are not neglected in the present work. Although the oxide partial pressures are all not important at normal operating temperatures, they become quite significant at the higher temperatures for which this basic program will later be employed. Since many of the fission product oxides decompose into gaseous oxygen and simpler oxides upon evaporation, the coupling effect of the oxygen concentration would cause erroneous vapor pressures to be predicted if extrapolations of total vapor pressures over condensed fission product phases were made. Only in the cases of fission products whose condensed and vapor phases are nonoxides can such extrapolations be safely made. The following variational approach has therefore been taken.

In addition to specifying the temperature, fuel density, relative void volume, percent burnup, and pre-burnup O/U ratio of the fuel, the user makes an estimate of the resultant UO_{2-x} stoichiometry. The free energy of formation of the condensed UO_{2-x} phase and the O_2 partial pressure are taken from data of Tetenbaum and Hunt[34] and Hagemark and Broli.[35] The stable condensed phase of each fission product element, its free energy of formation, and the free energies of formation of each vapor species of that element are taken from the compilation of Bedford and Jackson.[36] Concentrations of the vapor species are determined from equilibrium constants based on these data and on the oxygen partial pressure. The amount of the condensed phase of each fission product is calculated from mass constraints imposed by the fast neutron fission product yields of Varteressian.[37] If the amount of the condensed phase is determined to be negative (which occurs if the equilibrium vapor pressure exceeds the ideal gas pressure resulting from all of the fission product having evaporated), the vapor pressures are recalculated, the relative amounts of each vapor species being fixed by the vapor-phase free energies alone. From conservation of the total amount of oxygen in the system, the amount of oxygen available for bonding with uranium to form the condensed phase is calculated and a new value of x in UO_{2-x} determined. The trial O/U ratio is then varied until the calculated and trial values agree to within any desired accuracy.

Future work in this area will include updating and extension to higher temperature of the thermodynamic data compiled by Bedford and Jackson,[36] accounting for the possibility of compound formation between several fission product elements, and attempts to improve upon the simplifying assumptions enumerated above. Specifically, changes will be made to allow for the fact that under normal operating conditions rare earth fission product elements do not exist as separate sesquioxide phases but rather occupy lattice sites in the fuel matrix.

---

[34] M. Tetenbaum, P. D. Hunt, *J. Chem. Phys.* **49**, 4739 (1968).

[35] K. Hagemark, M. Broli, "Equilibrium Oxygen Pressures over Nonstoichiometric Uranium Oxides UO_{2+x} and U_3O_{8-z} at Higher Temperatures," Kjeller Report KR-102 (May 1966).

[36] R. G. Bedford, D. D. Jackson, "Volatilities of the Fission Product and Uranium Oxides," University of California, Lawrence Radiation Laboratory Report UCRL-12314 (January 1965).

[37] K. A. Varteressian, Argonne National Laboratory, "Fission Product Spectra of 2-Mev Neutron Fission of ^{239}Pu and ^{235}U" (unpublished).

This will change the calculated post-burnup O/U ratio and will consequently affect the determined oxygen activity. Further, it is known that cesium forms rather stable complexes such as $Cs_2O \cdot UO_{2\pm x}$ with the fuel material. Incorporation of this type of compound formation into the program not only will alter the calculated post-burnup O/U ratio but also will greatly reduce the calculated partial pressure of cesium vapor species. Finally, account will be taken of the fact that the oxygen activity in the mixed fuel $(Pu,U)O_{2\pm x}$ will differ from that in pure urania.

d. Speed of Sound in Molten Reactor Materials (*L. Leibowitz*)

An experimental program has been initiated to measure the speed of sound in liquid sodium, liquid UO_2, and other molten materials of importance in reactor safety. A knowledge of the sound velocity itself and of the compressibility of these materials will be of considerable value in certain reactor hazards analyses. Initial efforts will be directed toward measuring the speed of sound in sodium to high temperatures. At present, data are available[38] to 700°C, although these measurements do not agree well at lower temperatures with other workers. It should be possible for us to extend these measurements by several hundred degrees at least. We are currently evaluating various molybdenum, tantalum, and tungsten alloys as materials of construction in the sodium work. Electronic equipment has been purchased, a suitable furnace has been acquired, and sonic cell and furnace modification designs are in progress.

[38] G. H. Golden, J. V. Tokar, "Thermophysical Properties of Sodium," ANL-7323, p. 64 (August 1967).

3. Segregation in Ceramic Fuels: Fuel Migration Studies (*M. G. Chasanov, D. F. Fischer*)

Migration and segregation of fissile and fertile materials within a fast reactor fuel during its operational lifetime could have significant effects on the operational safety of the fuel. Redistribution of plutonium in $(U,Pu)O_2$ fuels might change the chemical and physical properties of the affected regions enough to alter the neutronics of the system, affect fuel-cladding compatibility, and change the resultant fission product distribution. Investigation of the migration of plutonium and fission products in a thermal gradient has been underway for mixed-oxide fuels. These experiments were performed to evaluate the extent of migration and to elucidate the mechanisms involved in the migration processes.

Experiments on mixed-oxide specimens were carried out with right-circular cylindrical pellets, ½ in. high by ½ in. in diameter, that were prepared from coprecipitated UO_2-PuO_2; the pellets are all nominally $(U_{0.8}Pu_{0.2})O_{2\pm x}$. The studies were performed in the thermal-gradient furnace described earlier in ANL-7425, p. 167. Samples were annealed in the gradient furnace for the desired time period, after which they were sectioned and analyzed for uranium and plutonium using an electron microprobe analyzer.

Results reported previously (ANL-7575, p. 94) indicated that, for specimens (initial O/M ratios of 2.01) heated in thermal gradients of the order of 1000°C/cm, enhancement of plutonium concentration occurred in the hottest regions. The concentration increases observed were small (~2 wt % PuO_2 increase), and the annealing times required were quite long (1020 hr for a sample with a top surface temperature of 1970°C, and 123 hr for a sample with a top surface temperature of 2350°C).

Additional experiments were done using similar specimens whose initial O/M ratios were 1.97. Each pellet was heated in an inverted tungsten crucible, which served as a barrier to evaporative losses during the annealing period; a similar procedure had been used with the hyperstoichiometric specimens. The samples were annealed at the temperatures and times indicated:

P-10: T_{top} = 2330°C, T_{bottom} = 1120°C, 262 hr
P-11: T_{top} = 2360°C, T_{bottom} = 1310°C, 125 hr
P-12: T_{top} = 2350°C, T_{bottom} = 1180°C, 97 hr

Electron microprobe analyses were then performed on these specimens; there appeared to be no significant plutonium concentration changes throughout these specimens' longitudinal sections.

Thus, in our experiments with mixed-oxide specimens, we have observed apparent changes in plutonium concentration at the hotter end of hyperstoichiometric pellets annealed in a thermal gradient, but no such change for slightly hypostoichiometric samples. This implies that the oxygen activity of the specimen could be involved in the mechanism for plutonium concentration enhancement. It also may imply that vaporization processes play a significant role in the observed changes.

Several preliminary experiments were performed in a similar fashion using mixed-carbide fuel pellets of approximate composition $(U_{0.85}Pu_{0.15})C$. These cylindrical pellets were 0.43 in. in diameter and 0.42 in. long, just slightly smaller than the oxide specimens used earlier. The composition of the carbide pellets

was 80.99 wt % U, 14.4 wt % Pu, and 4.61 wt % C. Four experiments similar to those performed on the oxide pellets were carried out. Sample top-surface temperatures averaged around 2000°C, and the gradients were of the order 700°C/cm. To date, electron microprobe analytical data are available on the two longest-term annealed specimens. These are pellets P-14 (T_{top} ~2000°C, T_{bottom} ~1370°C, 437 hr) and P-16 (T_{top} ~2000°C, T_{bottom} ~1320°C, 460 hr). Pellet P-14 was annealed without a vaporization barrier, while P-16 used the inverted tungsten crucible. The probe results indicate that considerable loss of plutonium occurred in the upper (hottest) region of P-14 (plutonium concentrations reduced to a few percent) while virtually no loss was observed for P-16. This is not too surprising, since it is known that plutonium is the chief high-temperature vapor species over such mixed carbides. Ceramographic examination showed considerable densification and columnar grain growth in the top portion of P-14 with little evident change in P-16.

No further experimental work is planned in this program. A final report embodying the experimental details of these studies is being written.

C. CALORIMETRY (*W. N. Hubbard*)

The calorimetry program is directed toward the experimental, empirical, or theoretical determination of thermodynamic properties of substances that are of interest in high-temperature chemistry and nuclear technology. Room-temperature enthalpies of formation (ΔHf_{298}) are being measured; complementary experimental determinations of high-temperature increments ($\Delta H_T - \Delta H_{298}$) are reported in Section III.B.1; complementary low-temperature thermal measurements (C_p^o, ΔH_{tr}^o, S^o) are being performed in the Chemistry Division and elsewhere.

The method of fluorine bomb calorimetry was developed for measurements on substances not amenable to more conventional calorimetric techniques and has now been used to determine the enthalpies of formation of 35 elemental fluorides and 21 other compounds. The more conventional oxygen bomb calorimetry has been used for studies of 12 reactions and solution calorimetry for measurements of six aqueous reactions.

The data and results presented in this report are to be considered preliminary; when published in their final form in a journal article, they may be slightly different owing to refinements in the calculations.

1. Thermochemistry of Uranium Compounds (*P. A. G. O'Hare, J. L. Settle*)

a. Enthalpy of Formation of Uranium Diboride

As part of the continuing program to obtain thermodynamic data for uranium compounds, the enthalpy of formation of uranium diboride was determined by fluorine bomb calorimetry. Complementary high-temperature enthalpy increment (see Section III.B.1.a of this report) and low-temperature thermal[39] measurements were also carried out. The fluorine bomb and low-temperature calorimetric work are described in a paper titled "Uranium Diboride: Preparation, Enthalpy of Formation at 298.15°K, Heat Capacity from 1° to 350°K, and Some Derived Thermodynamic Properties."[40] The work may be summarized as follows:

A sample of uranium diboride was prepared and characterized as $UB_{1.979\pm0.006}$ with 0.06 ± 0.03 wt % of identified impurities. The standard enthalpy of combustion in fluorine was determined to be −1021.2 ± 1.1 kcal mol^{-1}. The heat capacity was measured from 0.84 to 350°K. At 298.15°K, the heat capacity (C_p^o), entropy (S^o), and enthalpy increment ($H^o - H_0^o$) are 13.23 ± 0.03 cal °K^{-1} mol^{-1}, 13.17 ± 0.03 cal °K^{-1} mol^{-1}, and 2108 ± 4 cal mol^{-1}, respectively. The following values were obtained for the standard enthalpy, entropy, and Gibbs energy of formation of UB_2 at 298.15°K: $\Delta Hf^o = -39.3 \pm 4.0$ kcal mol^{-1}, $\Delta Sf^o = -1.54 \pm 0.05$ cal °K^{-1} mol^{-1}, and $\Delta Gf^o = -38.8 \pm 4.0$ kcal mol^{-1}. These agree within experimental error with values calculated from high-temperature effusion measurements.[41] The heat capacity results below 4.2°K

[39] Performed by H. E. Flotow and D. W. Osborne of the ANL Chemistry Division.

[40] H. E. Flotow, D. W. Osborne, P. A. G. O'Hare, J. L. Settle, F. C. Mrazek, W. N. Hubbard, *J. Chem. Phys.* **51**(2), 583 (1969).

[41] C. Alcock, P. Grieveson, "Study of Uranium Borides and Carbides by Means of the Knudsen Effusion Technique," *Thermodynamics of Nuclear Materials*, p. 563, IAEA, Vienna (1962).

follow the equation $C_p = (9.40 \pm 0.01)T + (3.18 \pm 0.14) \times 10^{-2}T^3$ mJ °K^{-1} mol^{-1}. The relatively high value for the coefficient of the linear term indicates that uranium diboride is a good electrical conductor. There seems to be an anomaly in the heat capacity between 40 and 100°K; this may be due to a two-level Schottky anomaly with the upper level having a degeneracy twice that of the lower level and a separation of the levels equal to 175 ± 5°K or 122 ± 4 cm^{-1}.

b. Enthalpy of Formation of $US_{1.9}$ (Tetrag.)

Measurements of the energy of combustion of $US_{1.9}$ in fluorine have been initiated. Combination of previously obtained values for $\Delta Hf°(UF_6, c)$[42] and $\Delta Hf°(SF_6, g)$[43] with the enthalpy of combustion of $US_{1.9}(c)$ will yield the value of $\Delta Hf°(US_{1.9}, c)$.

The $US_{1.9}$ sample was prepared by F. Grønvold *et al.*,[44] who determined that this sample was of tetragonal structure with a = 10.278 Å and c = 6.347 Å. Wet chemical, inert gas fusion, and spectrochemical analyses have shown the sample to contain about 0.06 wt % impurities and the anion/cation ratio to be 1.888 ± 0.005. This ratio is well within the range of composition of the $US_{1.9}$ phase, which has been estimated[44] to extend from about $US_{1.80}$ to $US_{1.93}$.

Preliminary experiments in progress will determine the optimum conditions for burning $US_{1.9}$ in fluorine.

[42] J. L. Settle, H. M. Feder, W. N. Hubbard, *J. Phys. Chem.* **67**, 1892 (1963).

[43] P. A. G. O'Hare, J. L. Settle, W. N. Hubbard, *Trans. Faraday Soc.* **62**, 588 (1966).

[44] F. Grønvold, H. Haraldsen, T. Thurmann-Moe, T. Tufte, *J. Inorg. Nucl. Chem.* **30**, 2117 (1968).

2. Thermochemistry of Plutonium Compounds (*G. K. Johnson, E. H. Van Deventer*)

a. Enthalpy of Formation of Plutonium Monocarbide

As part of a continuing program to provide accurate thermochemical data for plutonium compounds, the standard enthalpy of formation of plutonium monocarbide was determined by oxygen bomb calorimetry. Plutonium monocarbide exists as a nonstoichiometric compound with a narrow range of composition near $PuC_{0.87}$. Holley and Storms[45] have recently reviewed the thermodynamic properties of actinide carbides and from consideration of high-temperature equilibrium studies concluded that $\Delta Hf°_{298}(PuC_{0.87}) = -10.2$ kcal mol^{-1}. They recommended, however, that the enthalpies of formation of all plutonium carbides should be measured, preferably by combustion calorimetry.

A sample of plutonium monocarbide was prepared[46] by arc melting high-purity plutonium and graphite. Metallographic analyses showed that the sample was single phase. Chemical and spark-source mass spectrometric analyses indicated a total impurity content of 0.35 wt % of which 0.30 wt % was tungsten, presumably introduced by the arc-melting electrode. The carbon content of the sample was found to be 4.20 ± 0.01 wt %, which gave a plutonium content, taken by difference, of 95.45 wt %. The C/Pu atom ratio was calculated to be 0.878 ± 0.001. The sample was stored and handled in a dry-helium atmosphere to avoid oxidation.

The combustion technique used was similar to that described previously for plutonium metal.[47] The product of combustion was PuO_2 with a small residue (10–20 mg out of an original ~3 g) of unreacted plutonium monocarbide, which was determined by carbon analysis.

The results of five acceptable combustion experiments were combined with the enthalpies of formation of the product oxides[47, 48] [$PuO_2 = -252.35 \pm 0.17$ kcal mol^{-1} and $CO_2(g) = -94.051$ kcal mol^{-1}] to yield $\Delta Hf°_{298}(PuC_{0.878\pm0.001}, c) = -11.53 \pm 0.64$ kcal mol^{-1} for the reaction

$$Pu(\alpha) + 0.878\ C\ (graphite) \rightarrow PuC_{0.878}(c)$$

This result is in reasonable agreement with previous high-temperature equilibria studies,[45] but is subject to much less uncertainty.

b. Enthalpy of Formation of Pu_2C_3

Dr. R. A. Kent[49] is preparing a sample of Pu_2C_3 that is expected to be suitable for bomb calorimetric measurements. If so, the enthalpy of formation of Pu_2C_3 will be determined by techniques similar to those used for plutonium monocarbide.

[45] C. E. Holley, Jr., E. K. Storms, "Actinide Carbides: A Review of Thermodynamic Properties," *Thermodynamics of Nuclear Materials, 1967*, p. 397, IAEA, Vienna (1968).

[46] By O. L. Kruger of the ANL Materials Science Division.

[47] G. K. Johnson, E. H. Van Deventer, O. L. Kruger, W. N. Hubbard, *J. Chem. Thermodyn.* **1**, 89 (1969).

[48] D. D. Wagman, W. H. Evans, V. P. Parker, I. Halow, S. M. Bailey, R. H. Schumm, NBS Technical Note 270-3, U.S. Government Printing Office, Washington, D. C. (1968).

[49] Los Alamos Scientific Laboratory, Los Alamos, New Mexico.

3. Thermochemistry of Hydrogen Fluoride

In spite of the importance of hydrogen fluoride as a key thermochemical compound, its enthalpy of formation is uncertain by approximately 0.5 kcal mol^{-1}. This is especially serious when the value enters a thermochemical cycle several times; e.g., in the cycle involving the solution of UF_6, in which HF is formed, the enthalpy of formation of aqueous HF enters six times.

Much of our work with fluorine bomb calorimetry is related to the thermochemistry of hydrogen fluoride. The enthalpies of combustion in fluorine of Si and SiO_2 led to a paper on the enthalpy of formation of gaseous hydrogen fluoride.[50] Similarly, the combustions of boron, boric oxide, carbon, silicon, silicon dioxide, iodine, magnesium, uranium, and other compounds in fluorine can be used to calculate values for the enthalpy of formation of aqueous HF; the values for the first three of these have in fact been published.[51-53] Most of the values obtained for $\Delta Hf(HF \cdot 10H_2O)$ indicate that the selected values tabulated by the National Bureau of Standards[48] and by the Soviet Academy of Sciences[54] are too positive by 0.5 kcal or so. In an effort to clear up the discrepancy, the enthalpy of formation of liquid HF and its enthalpy of solution have been measured.

a. Enthalpy of Formation of Liquid Hydrogen Fluoride (*E. Greenberg*)

The enthalpy of formation of liquid hydrogen fluoride was determined by measuring the energy evolved on reaction of fluorine with hydrogen in a bomb calorimeter whose combustion chamber had been presaturated with gaseous HF (by addition of liquid HF). With this technique, the only product of combustion was liquid HF. This work is reported in detail in a paper titled "The Thermochemistry of HF: The Enthalpy of Formation of Liquid HF." [55] In summary, the standard enthalpy of formation of liquid HF, $\Delta Hf^{\circ}_{298}(HF, l)$, was calculated to be -71.98 ± 0.05 kcal mol^{-1}. However, it should be noted that because of experimental evidence of a positive bias in this value, it should be considered tentative at this time. In any case, owing to the greater ease and convenience in definitively establishing an enthalpy of formation for HF in its liquid state rather than in its gaseous state, it is advocated that the standard reference state of HF be taken as the liquid.

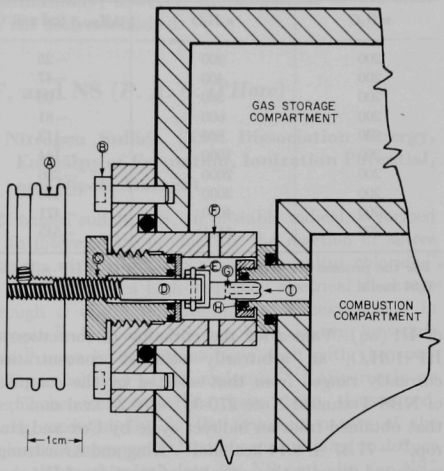

308-1959 Rev. 1

FIG. III-10. Improved Interconnecting Valve for Two-Compartment Calorimetric Bomb. (A, pulley; B, bolt; C, double-lead threads; D, stem; E, flexible joint; F, gas passage through valve housing; G, transverse hole; H, O-ring; I, longitudinal hole.)

Because the hypergolic gas-phase reaction between hydrogen and fluorine began at the valve between the two compartments of the calorimeter, the design of the valve was changed from that described earlier[56] to minimize attack on its seat. This modification, shown in Fig. III-10, is detailed in a note titled "An Improved Interconnecting Valve for a Two-Compartment Calorimetric Bomb." [57]

b. Enthalpy of Solution of Liquid Hydrogen Fluoride (*G. K. Johnson, P. N. Smith*)

The enthalpy of solution of HF(l) in water according to the reaction

$$HF(l) + nH_2O(l) \rightarrow HF \cdot nH_2O(l)$$

when combined with the enthalpy of formation of HF(l) discussed above, yields the enthalpy of formation

[50] H. M. Feder, S. S. Wise, J. L. Margrave, W. N. Hubbard, *J. Phys. Chem.* **67**, 1148 (1963).

[51] G. K. Johnson, H. M. Feder, W. N. Hubbard, *J. Phys. Chem.* **70**, 1 (1966).

[52] G. K. Johnson, W. N. Hubbard, *J. Chem. Thermodyn.* **1**, 459 (1969).

[53] E. Greenberg, W. N. Hubbard, *J. Phys. Chem.* **72**, 222 (1968).

[54] V. A. Medredev *et al*, *Thermochemical Constants of Substances*, Vol. 1, *Acad. Sci., High Temp. Institute, Moscow* (1965), p. 42.

[55] E. Greenberg, H. M. Feder, W. N. Hubbard, presented at the First International Conference on Calorimetry and Thermodynamics, Warsaw, Poland, Aug. 31–Sept. 4, 1969.

[56] J. L. Settle, E. Greenberg, W. N. Hubbard, *Rev. Sci. Instrum.* **38**(12), 1805 (1967).

[57] T. Denst, E. Greenberg, J. L. Settle, W. N. Hubbard, *Rev. Sci. Instrum.* **41**, 588 (1970).

TABLE III-6. ENTHALPIES OF DILUTION OF AQUEOUS HF SOLUTIONS

n_1H_2O	n_2H_2O	ΔH_{Diln}[a] (cal mol^{-1})
200	300	−25
200	400	−47
200	500	−66
200	600	−81
200	800	−113
200	1000	−144
200	2000	−286
200	3000	−400
200	4000	−471
200	5551[b]	−545

[a] For the process $HF \cdot n_1H_2O + (n_2 - n_1)H_2O \rightarrow HF \cdot n_2H_2O$.
[b] 0.01 molal.

of HF(aq). Values for the enthalpy of formation of $HF \cdot 10H_2O$, an arbitrarily selected concentration, currently ranged from that selected by the compilers of NBS Technical Note 270-3,[48] −76.24 kcal mol^{-1}, to that obtained from an indirect cycle by Cox and Harrop,[58] −77.37 ± 0.14 kcal mol^{-1}. King and Armstrong[59] measured directly the enthalpy of reaction of $H_2(g) + F_2(g) + H_2O(l)$ and obtained −76.60 ± 0.09 kcal mol^{-1} for $\Delta Hf(HF \cdot 10H_2O)$. The JANAF Thermochemical Tables[60] have recently selected a value in agreement with the direct measurement −76.70 ± 0.10 kcal mol^{-1}. In addition to these results, there are some ten cycles which yield ΔHf(HF, aq) indirectly. These cycles are, in general, based on fluorine bomb calorimetric data and yield ΔHf(HF, aq) values that are in surprisingly good agreement with each other considering the complexity of many of the cycles. The value for $\Delta Hf(HF \cdot 10H_2O)$, based on our assessment of the indirect cycles only, is −76.9 ± 0.1 kcal mol^{-1}.

The experimental part of this research was conducted in two parts: First, the enthalpy of solution of HF(l) was established at the concentration $HF \cdot 200H_2O$. Second, through additional solution experiments, the enthalpies of dilution of HF(aq) were obtained in the range $HF \cdot 200H_2O$ to $HF \cdot 5551H_2O$. (Enthalpies of dilution from $HF \cdot 10H_2O$ to $HF \cdot 200H_2O$ are already well established.[58, 61, 62])

The solution measurements were conducted in an LKB-8700 calorimeter equipped with a gold reaction vessel. A sample of pure, anhydrous liquid HF (conductivity, 1×10^{-6} ohm^{-1} cm^{-1}) was obtained from Argonne's Chemistry Division. The HF was distilled into small ampoules constructed entirely of Kel-F plastic. The ampoules were made by hot-air welding a ⅛-in. OD filling tube to a ⅜-in. OD tube and then heat sealing 3-mil film windows over the open ends of the larger tube. When the ampoule was charged with HF, the filling tube was sealed with hot pliers. The reaction was initiated in the calorimeter by puncturing the film windows.

The average of six measurements of the enthalpy of solution according to

$$HF(l) + 200H_2O(l) \rightarrow HF \cdot 200H_2O(l)$$

was −4506.1 ± 2.0 cal mol^{-1}. Some 35 additional measurements of the enthalpy of solution were performed in which the final product was varied from $HF \cdot 200H_2O$ to $HF \cdot 5551H_2O$. From these measurements, the enthalpies of dilution of aqueous HF, as given in Table III-6, were obtained.

The standard state for solutions is generally taken as a hypothetical ideal solution at unit molality. In this standard state, the apparent molal enthalpy of the solute is the same as it is in an infinitely dilute real solution. Thus, to obtain the standard enthalpies of solution and formation, it is necessary to extrapolate to infinite dilution. This is not a simple procedure for aqueous HF as even at 0.01 molal approximately 75% of the HF is still undissociated. From selected values of the equilibrium constants for the two equilibria present in HF solutions

$$HF \rightleftarrows H^+ + F^-$$
$$HF + F^- \rightleftarrows HF_2^-$$

and selected values of the enthalpies of the reactions, based on the temperature dependence of the equilibrium constants, it was possible to calculate the enthalpy of dilution from $n = 5551$ (0.01 molal) to $n = \infty$. The resulting value is −2349 ± 64 cal mol^{-1}, which gives the standard enthalpy of solution of liquid HF in infinite H_2O as −7400 ± 65 cal mol^{-1}.

Additional enthalpies of dilution were obtained from the literature[58, 61, 62] for concentrated HF solutions ($n = 200$ to $n = 2$). For example, the enthalpy of dilution from $n = 10$ to $n = 200$ was selected as −99 cal mol^{-1}, which yields the enthalpy of solution of HF(l) in 10 moles of H_2O as −4407 cal mol^{-1}.

These results can be combined with the enthalpy of formation of HF(l) reported above, −71.98 ± 0.05 kcal mol^{-1}, to yield $\Delta Hf^\circ_{298}(HF \cdot \infty H_2O) = -79.38 \pm 0.08$ kcal mol^{-1}, $\Delta Hf_{298}(HF \cdot 200H_2O) = -76.49 \pm 0.05$ kcal mol^{-1}, and $\Delta Hf_{298}(HF \cdot 10H_2O) = -76.39 \pm 0.06$ kcal mol^{-1}. Thus, our result would seem to substantiate

[58] J. D. Cox, D. Harrop, *Trans. Faraday Soc.* **61**, 1328 (1965).
[59] R. C. King, G. T. Armstrong, *J. Res. Nat. Bur. Stand.* **72A**, 113 (1968).
[60] The JANAF Thermochemical Tables, Dow Chemical Co., Midland, Michigan.
[61] W. A. Roth, H. Pahlke, A. Bertram, E. Borger, *Z. Electrochem.* **43**, 350 (1937).
[62] H. Schafer, F. Kahlenberg, *Z. Anorg. Allg. Chem.* **294**, 242 (1958).

the selected value of the National Bureau of Standards.[48] Our results, however, must be considered preliminary and subject to revision. Both the solution results and the ΔHf^{o}(HF, l) result are being carefully scrutinized for evidence of a systematic bias. As noted above, a positive bias in ΔHf^{o}(HF, l) has been shown experimentally; however, the magnitude of the error has not been established.

4. Chemical Bonding in NSF_3, NSF, and NS (*P. A. G. O'Hare*)

a. The Enthalpies of Formation of NSF_3 and NSF and the N≡S Bond Strengths

The sulfur-nitrogen halides, for which there are few thermodynamic data, have been the subject of several physicochemical investigations in recent years.[63] The multiplicity of nitrogen-sulfur bonds, up to and including formal triple bonds, is of considerable interest. The compounds NSF_3 and NSF, with formal triple bonds, have N—S bond orders of 2.7[64] and 2.4,[65] respectively, which were deduced from spectroscopic and bond-length data. Calorimetric measurement of the enthalpy of fluorination of NSF_3 was undertaken to determine a reliable value for $\Delta Hf^{o}(NSF_3)$, the standard enthalpy of formation.

The results of this investigation are presented in a paper titled "Thiazyl Tri- and Monofluorides: Enthalpies of Formation and Dissociation Enthalpies of the N≡S Bonds." [66] In brief, the work may be described as follows:

The energy of combustion of thiazyl trifluoride (NSF_3) in fluorine was measured calorimetrically, and a value of -85.2 ± 0.5 kcal mol^{-1} was derived for $\Delta Hf^{o}_{298}(NSF_3, g)$. Combination of this result with reported mass spectrometric appearance-potential data[67] yielded $\Delta Hf^{o}_{298}(NSF, g) = +41 \pm 2$ kcal mol^{-1}, $\Delta Hf^{o}_{298}(SF_4, g) = -162$ kcal mol^{-1}, and N≡S bond dissociation enthalpies of approximately 93 and 71 kcal mol^{-1} for NSF_3 and NSF, respectively. The result for $\Delta Hf^{o}_{298}(SF_4, g)$ is substantially different from previously reported values,[68-70] and indicates that it should be redetermined by a direct technique such as the fluorination of SF_4 to SF_6.

b. Nitrogen Sulfide (NS): Dissociation Energy, Enthalpy of Formation, Ionization Potential, and Dipole Moment

Nitrogen sulfide, NS, an unstable radical, is formed as an intermediate product by the reaction of active nitrogen with sulfur vapor[71] or with sulfur chloride,[72] or by passage of a high-frequency electrical discharge through a dilute mixture of sulfur hexafluoride in nitrogen.[73] Although NS has been known for some time,[74] most investigations have dealt with the spectroscopic behavior of the molecule.[72-77] Apparently no thermochemical properties have been determined, owing, undoubtedly, to the transient nature of the molecule. Consequently, a study was initiated to deduce some thermochemical data for NS and also for NS^+ (the latter ion was first observed spectroscopically by Dressler[78]). The study is detailed in a paper under the title, "Dissociation Energies, Enthalpies of Formation, Ionization Potentials, and Dipole Moments of NS and NS^+," [79] which may be summarized as follows:

A dissociation energy of 4.8 ± 0.25 eV at 0°K has been deduced for NS($^2\pi$) from spectroscopic data in the literature;[72-77] the corresponding value for $\Delta Hf^{o}_{0}(NS)$ is 2.91 ± 0.26 eV. Recent experimental results for $\Delta Hf^{o}(NSF)$ reported above indicate $\Delta Hf^{o}_{0}(NS^+, {}^1\Sigma^+) = 12.72 \pm 0.10$ eV. Thus, the ionization potential of NS is 9.81 ± 0.28 eV. A Hartree-Fock-Roothaan *ab initio* calculation for NS yielded an ionization potential of 10.10 eV, based on Koopmans' theorem, in good agreement with the experimental value, and a dipole moment of 1.732 D. Combining the value of $\Delta Hf^{o}_{0}(NS^+)$ with enthalpies of formation of the assumed products, $S^+(g)$ and N(g), gives the previously unreported dissociation

---

[63] O. Glemser, M. Fild, in *Halogen Chemistry*, Vol. II, Chap. 1, V. Gutmann, ed., Academic Press, New York (1967).

[64] H. Richert, O. Glemser, *Z. Anorg. Allg. Chem.* **307**, 328 (1961).

[65] A. Müller, G. Nagarajan, O. Glemser, S. J. Cyvin, *Spectrochim. Acta* **23A**, 2683 (1967).

[66] P. A. G. O'Hare, W. N. Hubbard, O. Glemser, J. Wegener, *J. Chem. Thermodyn.* **2**, 71 (1970).

[67] O. Glemser, A. Müller, D. Böhler, B. Krebs, *Z. Anorg. Allg. Chem.* **357**, 184 (1968).

[68] M. J. Nichols, Ph.D. thesis, The University of Durham, England (1958).

[69] J. D. Vaughn, E. L. Muetterties, *J. Phys. Chem.* **64**, 1787 (1960).

[70] J. Kay, F. M. Page, *Trans. Faraday Soc.* **60**, 1042 (1964).

[71] J. A. S. Bett, C. A. Winkler, *J. Phys. Chem.* **68**, 2501 (1964).

[72] P. Goudmand, O. Dessaux, *J. Chim. Phys.* **63**, 136 (1967).

[73] M. Peyron, Lam Thanh-My, *ibid.* **63**, 130 (1967).

[74] A. Fowler, C. J. Bakker, *Proc. Roy. Soc. London* **136**, 28 (1932).

[75] P. B. Zeeman, *Can. J. Phys.* **29**, 174 (1951).

[76] R. F. Barrow, A. R. Downie, R. K. Laird, *Proc. Phys. Soc. London* **A65**, 70 (1952).

[77] R. F. Barrow, G. Drummond, P. B. Zeeman, *ibid.* **A67**, 365 (1954).

[78] K. Dressler, *Helv. Phys. Acta* **28**, 563 (1955).

[79] P. A. G. O'Hare, *J. Chem. Phys.* **52**, 2992 (1970).

energy of NS^+ as 5.31 ± 0.31 eV. It is not surprising that the dissociation energy for NS^+ is greater than that for NS, since the latter contains one more antibonding electron.

5. Enthalpy of Formation of Molybdenum Disulfide (*P. A. G. O'Hare, G. Kuzmycz,*[80] *F. Cheng,*[80] *E. Benn*[80])

Molybdenum disulfide, MoS_2, has a low friction coefficient at room temperature, and this property is substantially retained at relatively high temperatures.[81, 82] Consequently, MoS_2 has been suggested as having potential applications in the aerospace industry.[82] A process for the production of high-purity molybdenum by the thermal dissociation of MoS_2 has been developed by Scholz *et al.*[83] Thus, for these and other reasons the thermodynamic properties of MoS_2 are of interest.

The value for one of the basic thermal quantities, namely the enthalpy of formation at 298.15°K, is still in doubt. Several years ago at this Laboratory, an oxygen bomb study was carried out on MoS_2 (see ANL-6029, p. 65). However, the chemical processes in the bomb were very difficult to define and, consequently, a reliable result for $\Delta Hf°(MoS_2)$ could not be obtained. There are also several conflicting values in the literature[84-86] for $\Delta Hf°(MoS_2)$, ranging all the way from −91 to −48 kcal mol^{-1}.

Since MoS_2 burns completely in fluorine to yield only MoF_6 and SF_6, and since a calorimetric-grade sample of MoS_2 was available, a study of the heat of combustion was undertaken. Preliminary results indicate a value for $\Delta Hf°(MoS_2)$ of about −65 kcal mol^{-1}. This result is subject to substantial change depending on analytical results not yet available.

[80] Summer Engineering Practice School students from State University of New York (Buffalo), Massachusetts Institute of Technology, and University of Arizona, respectively.

[81] M. T. Lavik, T. E. Medved, G. D. Moore, *ASLE Transactions* **11**, 44 (1968).

[82] W. A. Brainard, NASA Technical Note, NASA TN D-5141 (1969).

[83] W. G. Scholz, D. V. Doane, G. A. Timmons, *Trans. Met. Soc. AIME* **221**, 356 (1961).

[84] I. A. Makolkin, *Acta Physicochimica U.S.S.R.* Vol. XIII, p. 361 (1940).

[85] J. R. Stubbles, F. D. Richardson, *Trans. Faraday Soc.* **56**, 1460 (1960).

[86] H. R. Larson, J. F. Elliott, *Trans. Met. Soc. AIME* **239**, 1713 (1967).

6. Miscellaneous Fluorine Bomb Calorimetric Studies

a. Enthalpy of Formation of Silicon Carbide (*E. Greenberg, C. Natke*)

Earlier reports (ANL-6925, p. 177, and ANL-7055, p. 171) have discussed the determination of the enthalpy of formation of α- and β-silicon carbide. This work has now been summarized in a paper titled "The Enthalpy of Formation of Silicon Carbide."[87] The abstract is as follows:

> The energy of combustion of silicon carbide in fluorine was measured with samples of both hexagonal and cubic crystalline modifications. The standard enthalpies of formation, $\Delta Hf°(298.15°K)$, of alpha (hexagonal) and beta (cubic) silicon carbide were calculated to be −17.23 ± 0.46 and −17.49 ± 0.43 kcal mol^{-1}, respectively.

b. Enthalpy of Formation of Phosphorus Trifluoride (*E. Rudzitis, E. H. Van Deventer*)

The potential of PF_3 as a fluorine stripper in calorimetry (ANL-7225, p. 152) and the determination of its enthalpy of formation (ANL-7325, p. 121) were discussed previously. The work has recently been reported in a paper titled "The Enthalpy of Formation of Phosphorus Trifluoride,"[88] the abstract of which reads as follows:

> The energy of the reaction $PF_3(g) + F_2(g) \rightarrow PF_5(g)$ was determined by the combustion of PF_3 in excess fluorine in a bomb calorimeter. The standard enthalpy of this reaction, −635.94 ± 0.67 kJ mol^{-1}, was used to derive the standard enthalpy of formation, $\Delta Hf°_{298.15}(PF_3, g) = -957.4 \pm 1.4$ kJ mol^{-1}.

c. Enthalpy of Formation of Iodine Pentafluoride and Iodine Heptafluoride (*J. L. Settle, J. H. E. Jeffes,*[89] *P. A. G. O'Hare*)

Previous reports (ANL-7425, p. 120, and ANL-7575, p. 114) have discussed the determination of the enthalpies of formation of IF_5 and IF_7. This work has been completed and can be summarized as follows:

[87] E. Greenberg, C. A. Natke, W. N. Hubbard, *J. Chem. Thermodyn.* **2**, 193 (1970).

[88] E. Rudzitis, E. H. Van Deventer, W. N. Hubbard, *J. Chem. Thermodyn.* **2**, 221 (1970).

[89] Resident research associate, Imperial College, London.

The energy of combustion of iodine in fluorine was measured in a bomb calorimeter, and the standard enthalpy of formation, $\Delta Hf^{\circ}_{298.15}$, of liquid iodine pentafluoride (IF_5) was calculated to be -210.9 ± 0.3 kcal mol^{-1}. A linear least-squares analysis of the combustion data enabled a value of -229.7 ± 0.6 kcal mol^{-1} to be deduced for $\Delta Hf^{\circ}_{298.15}$ of gaseous iodine heptafluoride (IF_7).

Details of the work will be available in a paper being prepared for publication.

d. Enthalpies of Formation and Solution of Boric Oxides (*G. K. Johnson*)

The determination of the enthalpies of formation and solution of boric oxide (ANL-7225, p. 147, and ANL-7575, p. 115) has been published under the title "The Enthalpies of Formation of Crystalline and Amorphous Boric Oxide and Orthoboric Acid." [62] The abstract of this paper is as follows:

The energy of combustion in fluorine of crystalline boric oxide was measured in a bomb calorimeter to be -239.12 ± 0.39 kcal mol^{-1}. The enthalpies of solution in water of B_2O_3(c) and B_2O_3(amorph) to form $H_3BO_3 \cdot 341H_2O$(l) were measured to be -3.54 ± 0.05 and -7.98 ± 0.04 kcal mol^{-1}, respectively. These data were used to calculate the standard enthalpies of formation of crystalline and amorphous boric oxide, namely, $\Delta Hf^{\circ}(B_2O_3, \text{c}, 298.15°\text{K}) = -304.48 \pm 0.59$ kcal mol^{-1} and $\Delta Hf^{\circ}(B_2O_3, \text{amorph}, 298.15°\text{K}) = -300.04 \pm 0.59$ kcal mol^{-1}. The values were further combined with data reported in the literature to derive $\Delta Hf^{\circ}(H_3BO_3, \text{c}) = -261.71 \pm 0.31$ kcal mol^{-1} and $\Delta Hf^{\circ}(HF \cdot 3H_2O, \text{l}) = -76.71 \pm 0.08$ kcal mol^{-1}.

7. Thermochemistry of Aqueous Xenon Trioxide (*P. A. G. O'Hare, G. K. Johnson*)

Xenon trioxide, XeO_3, and its derivatives are perhaps the most unexpected of the noble gas compounds. Solid xenon trioxide is explosively unstable and has an enthalpy of formation of 96 ± 2 kcal mol^{-1}.[90] Solutions of XeO_3 in dilute aqueous acid, although they are potent oxidizers,[91] show no evidence of spontaneous decomposition; because of this, they have received more experimental attention than has the dangerous solid. A reliable quantitative determination of the thermodynamic oxidizing power of these solutions is therefore of considerable practical value. Inasmuch as reactions of aqueous XeO_3 are irreversible, this oxidizing power can only be measured thermodynamically.

The present investigation was undertaken to obtain a precise value for the enthalpy of formation of aqueous XeO_3, $\Delta Hf^{\circ}(XeO_3, \text{aq})$, from calorimetric measurements of the enthalpies of the reactions between XeO_3(aq) and HI(aq) and between I_2(c) and HI(aq) according to the processes:

$$XeO_3(\text{aq}) + 9I^-(\text{aq}) + 6H^+(\text{aq}) \rightarrow Xe(\text{g}) + 3I_3^-(\text{aq}) + 3H_2O(\text{l})$$
$$I_2(\text{c}) + I^-(\text{aq}) \rightarrow I_3^-(\text{aq})$$

The results of the above investigations are described in a paper titled "The Thermochemistry of Aqueous Xenon Trioxide." [92] The work reported therein may be summarized as follows:

Solution calorimetric measurements of the enthalpies of the reactions of XeO_3(aq) with HI(aq) and of I_2(c) with HI(aq) have been used to obtain a value of 99.94 ± 0.24 kcal mol^{-1} for $\Delta Hf^{\circ}_{298}(XeO_3 \cdot 96.15\ H_2O)$. The electrode potentials of the Xe-XeO_3 couple in acidic solution and of the Xe-$HXeO_4^-$ couple in basic solution were deduced to be 2.10 ± 0.01 V and 1.24 ± 0.01 V, respectively.

[90] S. R. Gunn, in *Noble Gas Compounds*, p. 149, H. H. Hyman, ed., University of Chicago Press, Chicago, Ill. (1963).

[91] E. H. Appelman, J. G. Malm, *J. Amer. Chem. Soc.* **86**, 2141 (1964).

[92] P. A. G. O'Hare, G. K. Johnson, E. H. Appelman, *Inorg. Chem.* **9**, 332 (1970).

8. Enthalpies of Formation of $KBrO_4$(c) and $KBrO_3$(c) and the Thermodynamic Properties of the Perbromate and Bromate Ions (*G. K. Johnson, P. N. Smith*)

The recent discovery of preparative methods[93, 94] for perbromic acid and perbromates has ended a long search for these compounds. The determination of the energies of decomposition to KBr and the enthalpies of solution in H_2O of $KBrO_4$(c) and $KBrO_3$(c) was carried out to help in the exploitation of these new compounds and in the explanation of the past difficulties encountered in their synthesis. The results of this study also bear on the contention that the highest oxidation states of the nonmetals of the first long period are less stable than the corresponding oxidation states of the preceding and succeeding periods.

[93] E. H. Appelman, *J. Amer. Chem. Soc.* **90**, 1900 (1968).

[94] E. H. Appelman, *Inorg. Chem.* **8**, 223 (1969).

The results of this work are presented in a paper under the title, "The Thermodynamic Properties of the Perbromate and Bromate Ions."[95] The work may be briefly described as follows:

The energies of decomposition of $KBrO_4(c)$ and $KBrO_3(c)$ to $KBr(c)$ plus $O_2(g)$ were measured in a bomb calorimeter. These data were used to derive the standard enthalpy of formation (ΔHf°_{298}) of $KBrO_4(c)$, -68.74 ± 0.14 kcal mol^{-1}, and of $KBrO_3(c)$, -86.02 ± 0.12 kcal mol^{-1}. The enthalpies of solution of $KBrO_4(c)$ in 2144 moles of water and of $KBrO_3(c)$ in 1808 moles of water were measured to be 11,606 ± 20 and 9,765 ± 42 cal mol^{-1}, respectively, at 298.15°K. The above values were combined with other data to derive standard thermodynamic properties at 298.15°K for the perbromate ion: $\Delta Hf^\circ = 3.19 \pm 0.15$ kcal mol^{-1}, $S^\circ = 44.7 \pm 2.0$ cal deg^{-1} mol^{-1}, and $\Delta Gf^\circ = 29.18 \pm 0.63$ kcal mol^{-1}; and for the bromate ion: $\Delta Hf^\circ = -15.95 \pm 0.13$ kcal mol^{-1}, $S^\circ = 38.6 \pm 0.3$ cal deg^{-1} mol^{-1}, and $\Delta Gf^\circ = 4.55 \pm 0.14$ kcal mol^{-1}. The standard electrode potential of the bromate-perbromate couple in acid solution was calculated to be 1.763 ± 0.014 V at 298.15°K.

Selected values for the thermodynamic properties of the halates and perhalates of chlorine and iodine are also tabulated in Ref. 95. Although the perbromate ion is more oxidizing then either perchlorate or periodate ion, the difference is not great enough to explain why the synthesis of perbromates has been so difficult.

[95] G. K. Johnson, P. N. Smith, E. H. Appelman, W. N. Hubbard, *Inorg. Chem.* **9**, 119 (1970).

9. Enthalpy of Formation of Disodium Acetylide (*E. H. Van Deventer, G. K. Johnson*)

Disodium acetylide, Na_2C_2, has been postulated as the species responsible for carbon transport in liquid sodium systems (see ANL-7575, p. 120). The transport of carbon from ferritic to austenitic steels, with subsequent degradation of both, is a problem of some importance in the liquid-sodium-cooled reactor program. The thermodynamic properties of Na_2C_2 as they relate to the thermal stability of this compound are therefore important.

The present value for $\Delta Hf^\circ(Na_2C_2)$, +4.2 kcal mol^{-1}, is based on the old solution measurements of Matignon[96] and De Forcrand.[97] It is doubtful if this value is accurate owing to the likelihood of a high impurity level in the samples. Therefore, a program was initiated to determine a more reliable value for $\Delta Hf^\circ(Na_2C_2)$.

A sample of Na_2C_2 has been received and is being analyzed. Trial experiments suggest that either of the reactions

$$Na_2C_2(c) + Cl_2(g) \rightarrow 2NaCl(c) + 2C(amorph)$$
$$Na_2C_2(c) + 5F_2(g) \rightarrow 2NaF(c) + 2CF_4(g)$$

would be feasible for bomb calorimetry.

[96] C. Matignon, *C. R. Acad. Sci., Paris, Ser. AB* **124**, 1026 (1897).

[97] De Forcrand, *ibid.* **120**, 1215 (1895).

IV

Analytical and Reactor Chemistry[1]

A. CHEMISTRY OF IRRADIATED FAST REACTOR FUELS AND MATERIALS (*C. E. Crouthamel*)

The study of the chemical behavior of irradiated fast reactor fuels has as its principal objective the collection of chemical data that will aid in the understanding of the complex chemical processes that take place in these fuels. The current program is primarily directed toward the study of uranium-plutonium oxide fuels, with emphasis on fuel-cladding interactions and fission product migration and interaction; however, some work is also being done on mixed uranium-plutonium carbides.

Studies of the retention of fission gases by ceramic fuels have recently been initiated. These studies will be important to the understanding of fuel swelling mechanisms and should aid in the formation of associated modeling codes for mixed-oxide fuels. The main emphasis of current studies of irradiated fuels by electron microprobe analysis is on the investigation of fuel-cladding interactions.

[1] A summary of this section is given on pages 11 to 12.

1. Chemical Studies of Irradiated Ceramic Fuels (*H. S. Edwards, P. K. Hon, L. E. Ross, C. C. Honesty, G. E. Staahl*)

a. Fuel-Evaluation Facility

An existing shielded cell in the cave complex of the Chemistry Division has been modified for studies of irradiated ceramic fuels. Work on the facility was completed with the installation of a Leitz metallograph and its associated shielding. A helium atmosphere was established in the enclosure after repair of major leaks in the storage pit and the gas blowers. The moisture level, 0.5 ppm, and the oxygen level, 3 ppm, are lower than the design specifications of 5 ppm moisture and 10 ppm oxygen.

Shakedown tests of the equipment for cutting, grinding, polishing, ultrasonic coring, and micro drilling of irradiated fuel specimens have been completed. Operations will proceed with irradiated fuel as needed and as other priorities in the program will allow.

The pneumatic sample-transfer tube (ANL-7575, p. 95) is complete except for the installation of diverter switches at the ends of the tube in the cave and in the analytical complex. A prototype "rabbit" has been tested in the mockup facility.

b. Spark-Source Mass Spectrometry

A technique that combines laser-microsampling and spark-source mass spectrographic analysis of the vaporized sample was investigated as a means of studying the microstructure of fuel materials. The utility of a ruby laser for microsampling has been demonstrated,[2] and with sensitivities at the nanogram level, the spark-source mass spectrograph provides a sensitive means of ion detection.

Two different laser-sampling techniques were tested. In the first, the vaporized sample was condensed on the flattened ends of two gold wires (0.025-in. dia) which had been placed very close to the focal spot of the laser beam. The condensed samples were then transferred to the spark-source mass spectrograph for examination. In the second method, the laser-microscope combination was coupled to the spark-source mass spectrograph by replacing the inspection lamp of the source chamber with the laser-microscope. After a specimen was mounted in the source chamber, the laser beam was

[2] M. D. Adams, S. C. Tong, *Anal. Chem.* **40**, 1762 (1968).

focused on the specimen and the chamber evacuated. The laser was then fired, and the ions produced were accelerated by a 2-kV potential through the spectrograph slit system.

Mass-spectrographic examination of laser-vaporized samples indicated that, in general, the two sampling methods provided about the same sensitivity; however, in the direct examination of laser-produced ions, the number of ions detected was strongly dependent on the proper orientation of the sample in the source chamber. Specimens of normal uranium metal,[3] normal UO_2, and type 308 stainless steel[4] were sampled by both methods. When craters of ~60 μm dia were produced by the laser, the ^{235}U line was observed in both the UO_2 and uranium metal and lines of ^{50}Cr, ^{52}Cr, ^{53}Cr, ^{55}Mn, ^{54}Fe, ^{56}Fe, ^{57}Fe, ^{58}Ni, and ^{60}Ni were observed in type 308 stainless steel. These data indicate that for laser samples ~60 μm in diameter an isotope present at concentrations of ~1 wt % or more could be detected. Without a great improvement in sensitivity, the method would find limited application in the study of irradiated fuels, where laser samples ~4–8 μm in diameter would be required.

Development work on improving the sensitivity of the laser-sampling method has been terminated as a result of a decision to transfer the spark-source mass spectrograph to the EBR-II Project in Idaho. Arrangements have been made, however, with the Analytical Group in Idaho to provide mass-spectrographic analysis of our samples, on a limited basis, as the need arises.

c. Determination of Fission Gases

Knowledge of the radial distribution of fission gases in ceramic fuels would be of considerable value in fuel modeling and swelling studies. Work is in progress on the development of a technique for microsampling and analysis of fission product gases retained in irradiated ceramic fuels. Microsampling is accomplished by laser-beam vaporization of selected areas of a fuel sample held in a vacuum chamber; the released fission gases are identified and measured by means of a quadrupole mass spectrometer.

[3] Normal uranium contains ~0.7% ^{235}U.

[4] Composition of type 308 stainless steel: Mn, 2%; Cr, 19–21%; Ni, 10–12%; remainder Fe.

Preliminary measurements were made of the radial distribution of fission gases in a transverse section of an irradiated UO_2 fuel pin clad with type 304 stainless steel. The fuel material, which had an overall enrichment of 13%, was produced by blending fully enriched and depleted UO_2 powders. The fuel pin had been irradiated to 6.0 at. % burnup in MTR. The calculated surface and centerline temperatures at the start of the steady-state irradiation were 1350° and 2400°C, respectively. Post-irradiation estimates, based on the behavior of fission gases in other irradiated UO_2 fuels, indicated that the total amount of fission xenon and krypton remaining in the fuel was about 0.5 mmol/cm^3 UO_2. This represents ~50% of the total produced during irradiation.

Laser samples of the fuel-pin cross section were taken in the columnar grains and the unrestructured regions of the fuel; the craters produced were 60 to 70 μm in diameter. Fission gas was readily detectable in all locations. There were indications that the fission-gas concentration was higher, by a factor of two or three, in the outer, unrestructured regions than in the columnar grains. The average concentration of fission gas in samples taken from the columnar grains was about 0.1 mmol/cm^3 UO_2. This is about 10% of the total produced in fission.

The test pointed out several factors that need consideration before the method can be fully evaluated. First, it should be noted that the columnar-grain region of this fuel specimen shows progressively less complete isotopic exchange of ^{235}U and ^{238}U from the central void to the equiaxed-grain region and little or no isotopic exchange in the unrestructured region. These local variations in isotopic composition could lead to local variations in fission gas concentration that would tend to obscure any systematic trends across the radius of the fuel pin. Additionally, these preliminary experiments revealed limitations associated with the detection system that may have caused large systematic errors. In future experiments, the fission gases will be determined by isotope-dilution analysis, a method that is expected to provide increased accuracy and precision. The detection apparatus is presently being modified to accommodate this change.

2. Electron Microprobe Analysis of Irradiated Fuels (*C. E. Johnson, N. R. Stalica, C. A. Seils, K. E. Anderson*)

The electron probe microanalyzer, which accomplishes microsampling and microanalysis directly, is being used to study the distribution of fission products, fuel-cladding interactions, and the formation of inclusions in irradiated fuels. The instrument used in these studies, an Applied Research Laboratories EMX electron probe microanalyzer, provides adequate shielding for handling specimens having gamma activity as

great as 1 R/hr at 1 ft. Complete cross sections of irradiated fuel pins having the requisite activity level have been examined. A newer, shielded instrument (Applied Research Laboratories EMX-SM), presently in the final stages of installation and testing, will greatly enhance our capabilities in electron microprobe analysis by providing (1) increased shielding and, therefore, increased capability for handling highly radioactive samples, (2) modest electron microscope capabilities, (3) increased sensitivity and speed of analysis by a solid-state-detector, multichannel-analyzer system, and (4) interface of the detectors with paper-tape readout to allow a computer calculation of the elemental concentrations.

a. Uranium-Plutonium Oxide Fuels

A variety of fuel pin sections have been examined; however, the greatest emphasis has been placed on the study of a UO_2-PuO_2 fuel pin designated SOV-3. This fuel pin was fabricated by vibratory compaction of fully enriched UO_2-20 wt % PuO_2 in type 304 stainless steel cladding. The pin had been irradiated in EBR-II to a maximum burnup of 3.7 at. %; the maximum linear power rating was 21.4 kW/ft. The centerline temperature of the fuel was estimated to be 2790°C; the fuel surface temperature, 1060°C; and the cladding temperature, 600°C.

Distribution of noble metal fission products. Many metallic inclusions varying in size from 3 to 30 μm, were found in SOV-3. The elemental composition of the inclusions differed significantly depending on their location in the body of the fuel. Inclusions near the central void contained molybdenum, ruthenium, rhodium, and technetium, lesser concentrations of iron, and traces of palladium. Inclusions near the columnar-equiaxed grain boundary consisted largely of palladium and iron, with lesser quantities of molybdenum, ruthenium, rhodium, and technetium. Some inclusions in this area were pure iron, and a few contained only iron and palladium. At one location near the cladding, a large (~30 μm) inclusion of pure molybdenum was found.

Microprobe analysis of metallic inclusions in coprecipitated uranium-plutonium oxide fuel[5] was also carried out. This fuel had been irradiated to a 5.6 at. % burnup at a power density of 16 kW/ft. Large metallic inclusions were found in a band in the unrestructured region of the fuel near the boundary between this region and the equiaxed-grain region, generally at the cooler end of a void. These inclusions were largely iron and palladium with lesser amounts of tin, antimony, indium, tellurium, and chromium. In general, the particles were homogeneous; however, in one case the iron and chromium were segregated at one end of the inclusion with the other metals being distributed throughout the inclusion.

Oxide inclusions. Metallographic photographs of a midplane cross section of SOV-3 showed large particles of a gray non-metallic phase located in a band at the end of the columnar grains. Electron microprobe examination of inclusions of the gray phase identified the principal constituent as alumina. The presence of this phase is the result of an Al_2O_3 impurity introduced into the fuel in a ball-milling operation. Alumina that was in the columnar-grain region near the center of the fuel was not soluble in the solid UO_2-PuO_2 matrix and migrated outward to the cooler equiaxed-grain region.

X-ray scanning images of a typical alumina-containing particle are shown in Fig. IV-1. This particular particle was located at the cooler end of a long columnar grain, 0.55 mm from the cladding wall. The tip of the columnar grain is outlined at the right in the specimen current image, Fig. IV-1a (the brightness in the specimen current image is inversely proportional to the mean atomic number of the elements present). Two longer columnar grains form the upper and lower boundaries of the particle. The particle shown in the figure had collected around a metallic iron inclusion. The alumina acted as a getter for barium oxide, cesium oxide, and tellurium. It has not been established whether this gray phase is a solid solution or a mixture of compounds such as $BaO \cdot 6Al_2O_3$ and $Cs_2O \cdot Al_2O_3$.

In a cooler location at the top of the SOV-3 pin, the alumina particles contained significant quantities of cesium only, but the cesium had not totally penetrated the larger particles, as evidenced by the small, dense core of cesium-free alumina that was found in these particles. The alumina, which apparently melted and collected in a circular band of inclusions at the end of the columnar grains, was relatively free of both uranium and plutonium and showed no evidence of any rare earth oxide components. A very low level of strontium is evident in some of the inclusions containing barium, cesium, and tellurium.

Fuel-cladding interaction. Electron microprobe examination of metallic inclusions in SOV-3 indicated that constituents of the stainless steel cladding had been transported into the fuel. As discussed above, metal inclusions containing iron were found near the boundary of the equiaxed and columnar grains; frequently, these inclusions were pure iron. However, in cooler temperature regions of this fuel, iron was often found alloyed with palladium or molybdenum. In contrast, chromium penetrated into the fuel only slightly and was found primarily as an oxide, associated with barium and cesium oxides in the outer regions of the

[5] Sample obtained from General Electric Co., Vallecitos Laboratory.

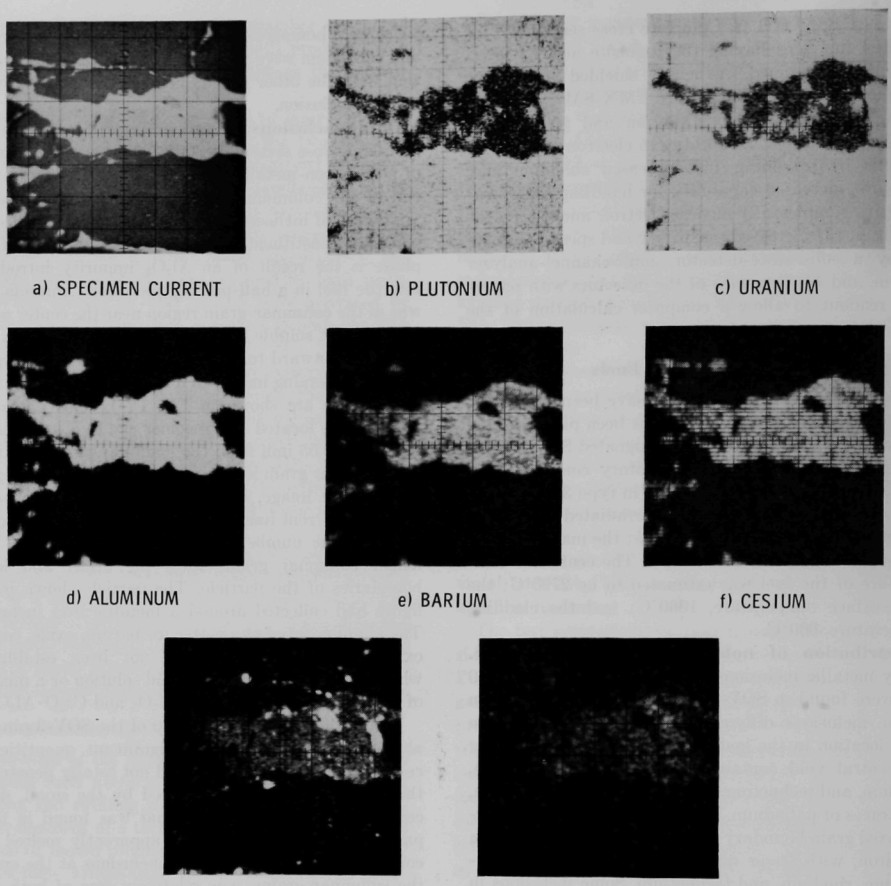

308-1919 T-1

FIG. IV-1. Electron Microprobe Scanning Images of Alumina Inclusions in a UO_2-20 wt % PuO_2 Fuel Pin (SOV-3). (All images represent areas 45 μm square.)

fuel pin near the fuel-cladding interface. Nickel was found segregated in the cladding grain boundaries, and, in general, did not migrate into the fuel matrix.

Electron microprobe examination of the fuel-cladding interface showed that intergranular attack of the cladding had occurred. In SOV-3, the average depth of cladding attack was ~90 μm. A typical area of intergranular attack is shown in the X-ray scanning images of Fig. IV-2. The feature of greatest interest in this fuel can be seen in Fig. IV-2g, which shows, for the first time, the presence of iodine in the area of intergranular attack. The other X-ray scans show the distribution of iron, nickel, chromium, cesium, barium, and tellurium at the fuel-cladding interface.

The presence of iodine in the area of intergranular attack has led to the hypothesis that iodine is contributing significantly to the mechanism of metal transport from the cladding to the fuel matrix. It is suggested that the transport mechanism is similar to that of the van Arkel-deBoer[6] process, in which purification

[6] A. E. van Arkel, J. H. de Boer, *Z. Anorg. Chem.* **148**, 345 (1925).

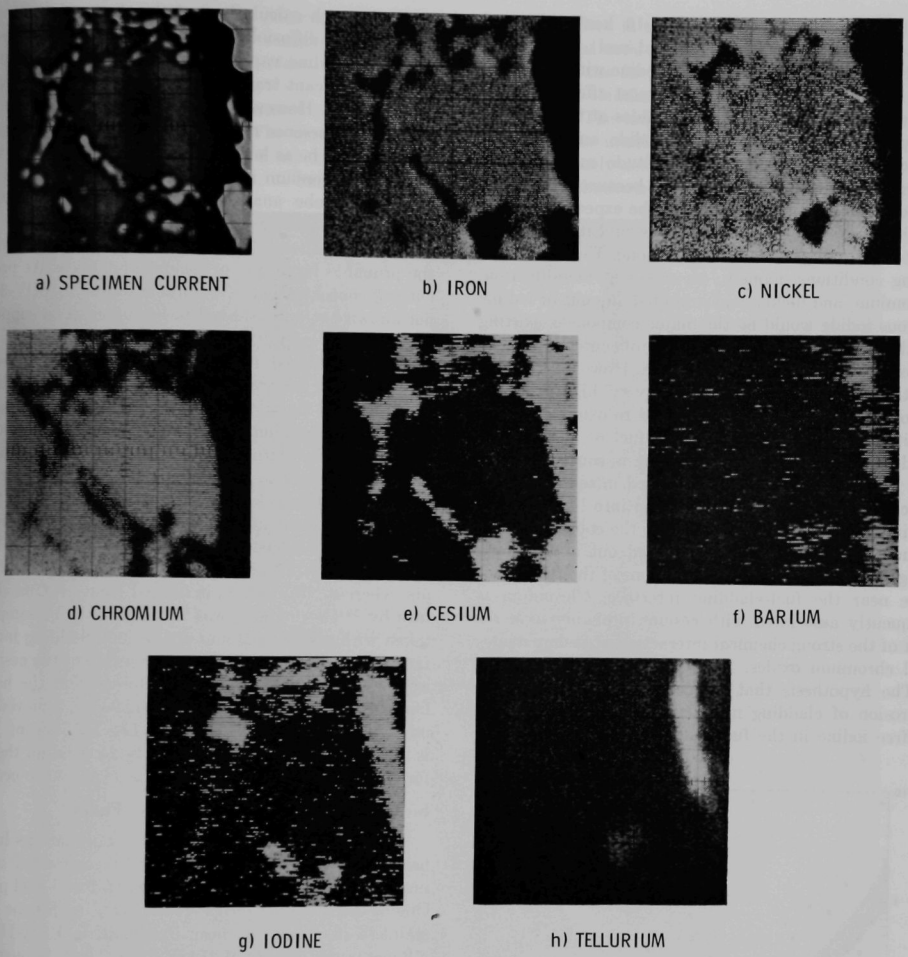

308-1918 T-1

FIG. IV-2. Electron Microprobe Scanning Images of Fuel-Cladding Interface of a UO_2-20 wt % PuO_2 Fuel Pin (SOV-3) Clad with Type 304 Stainless Steel. (All images represent areas 45 μm square.)

and vapor deposition of a metal is achieved by thermal decomposition of the metal iodide. In the fuel during irradiation, the transport mechanism could involve an iodine-cycling process in which fission product iodine migrates to the fuel-cladding interface and reacts with the cladding, and the metal iodides formed vaporize and are transported to high-temperature zones in the fuel matrix where iodide decomposition occurs. The process appears to be initiated only if the cladding temperature is high enough to produce (1) appreciable iodine attack on the stainless steel and (2) vaporization of the metallic iodides.

The iodides of the three stainless steel components have stabilities at 1000°K[7] that decrease in the following order: chromous iodide ($\Delta G^{o}f$ = −26 kcal/

[7] C. E. Wicks, F. E. Block, "Thermodynamic Properties of 65 Elements, Their Oxides, Halides, Carbides, and Nitrides," Bureau of Mines Bulletin 605 (1963).

mol), ferrous iodide ($\Delta G^o f = -16$ kcal/mol), and nickelous iodide ($\Delta G^o f = -2$ kcal/mol). The extent of the reaction of fission product iodine with the stainless steel components is probably most affected by the relative vapor pressure of their iodides at the cladding temperature; at 900°K ferrous iodide and nickelous iodide are three orders of magnitude more volatile than chromous iodide. However, because of its low iodide stability, nickel would not be expected to exist in the vapor phase, and therefore would not be transported to a higher temperature zone. Under the existing conditions, namely, an excess of metallic iron, chromium, and nickel, and a limited amount of iodine, ferrous iodide would be the major component existing in the vapor phase although a significant quantity of chromous iodide would be expected. However, the stabilities of chromium oxides are very high, and the chromous iodide would be expected to oxidize and deposit in the cooler region of the fuel or at the fuel-cladding interface. This hypothesis is consistent with our observations of other irradiated mixed-oxide fuel specimens. Iron is transported deep into the equiaxial grain structure and sometimes into the columnar grain structure. Chromium is transported out of the cladding, but remains in the outer regions of the fuel structure near the fuel-cladding interface. Chromium is frequently associated with cesium, probably as a result of the strong chemical interaction of cesium oxides and chromium oxides.

The hypothesis that iodine is responsible for the corrosion of cladding materials requires the presence of free iodine in the fuel during operation in the reactor. A rough calculation[8] of the chemical transport by gas-phase diffusion in a porous medium has shown that if the iodine vapor pressure is greater than 10^{-6} atm, a significant transport of iron could be observed in 100 days. However, further calculations indicate that in the presence of cesium oxide, the iodine vapor pressure may be as low as 10^{-22} atm as a result of the formation of cesium iodide. However, data from electron microprobe analyses suggest that in the SOV series of fuel pins cesium is stabilized chemically by interaction with an alumina impurity in the fuel, with the probable formation of cesium aluminate. At present the concentration of available iodine in SOV-3 is not known but is considered to be sufficient to support the overall transport mechanism.

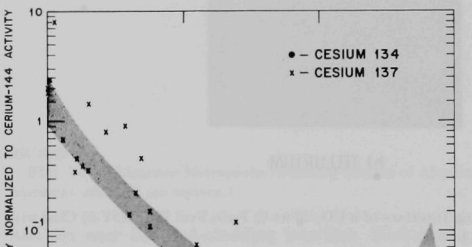

308-2176

FIG. IV-3. Radial Distribution of ^{137}Cs and ^{134}Cs in a UO_2-PuO_2 Fuel Pin (SOV-6).

Results obtained from laser sampling and gamma spectrometric analysis of another fuel cross section (SOV-6; UO_2-20 wt % PuO_2, 2.7 at. % burnup) have provided information that lends support to the above hypothesis. The data, shown in Fig. IV-3, indicate a marked difference in the ratio of ^{137}Cs to ^{134}Cs across the radius of the fuel pin. (The shaded areas in the figure represent estimated distributions of the two cesium isotopes, on the basis of overall uncertainties in the data.) Cesium-137 was distributed throughout the fuel pin, whereas ^{134}Cs, which is formed from neutron capture by ^{133}Cs (stable), was detected only in samples taken within about 0.2 mm of the fuel-cladding interface. This sharp difference in distribution of the cesium isotopes could result from the differences in the half-lives of their iodine precursors, which are believed to migrate rapidly to the cladding. The half-life of ^{133}I is 21 hr, whereas that of ^{137}I is only 24 sec, and therefore little migration of ^{137}I would be expected to occur.

b. Uranium-Plutonium Carbide Fuels

Preliminary electron-microprobe examinations have been carried out on two vibratorily compacted uranium-plutonium carbide (UC-20 wt % PuC) fuel pins. One of the fuel pins (SMV-1) was clad with type 316 stainless steel and had been irradiated in EBR-II, at a linear power density of 21 kW/ft, to 2.6 at. % burnup. The second fuel pin (SMV-2) was clad with type 304 stainless steel and had been irradiated in EBR-II, at a linear power density of 24 kW/ft, to 6.9 at. % burnup. The temperatures of the fuel-cladding interfaces for SMV-1 and SMV-2 during irradiation were 625 and 675°C, respectively. Both the UC and PuC fractions of the fuel materials were hyperstoichiometric, the UC containing UC_2 and the PuC containing Pu_2C_3. The average particle size of the PuC was <44 μm and that of the UC was 500–1700 μm. As a

[8] Dr. Lloyd Zumwalt, University of North Carolina, private communication (1969).

result of this large difference in particle sizes and the method of fabrication (vibratory compaction), the fuel material at the fuel-cladding interfaces was primarily the more finely divided PuC.

Both fuel pins showed minor attack of the cladding at the fuel-cladding interface. The depth of reaction was about 7 μm for SMV-1 (2.6 at. % burnup) and about 15 μm for SMV-2 (6.9 at. % burnup). The reaction resulted in the formation of separated bands of the stainless steel components and the migration of nickel into the fuel matrix. A composite X-ray image of the fuel-cladding interface of SMV-2 is shown in Fig. IV-4. The large particle seen in the fuel matrix (A to B) is uranium carbide; the remainder of the matrix is finely divided PuC. In the region B to C, the light areas indicate nickel that has moved out into the

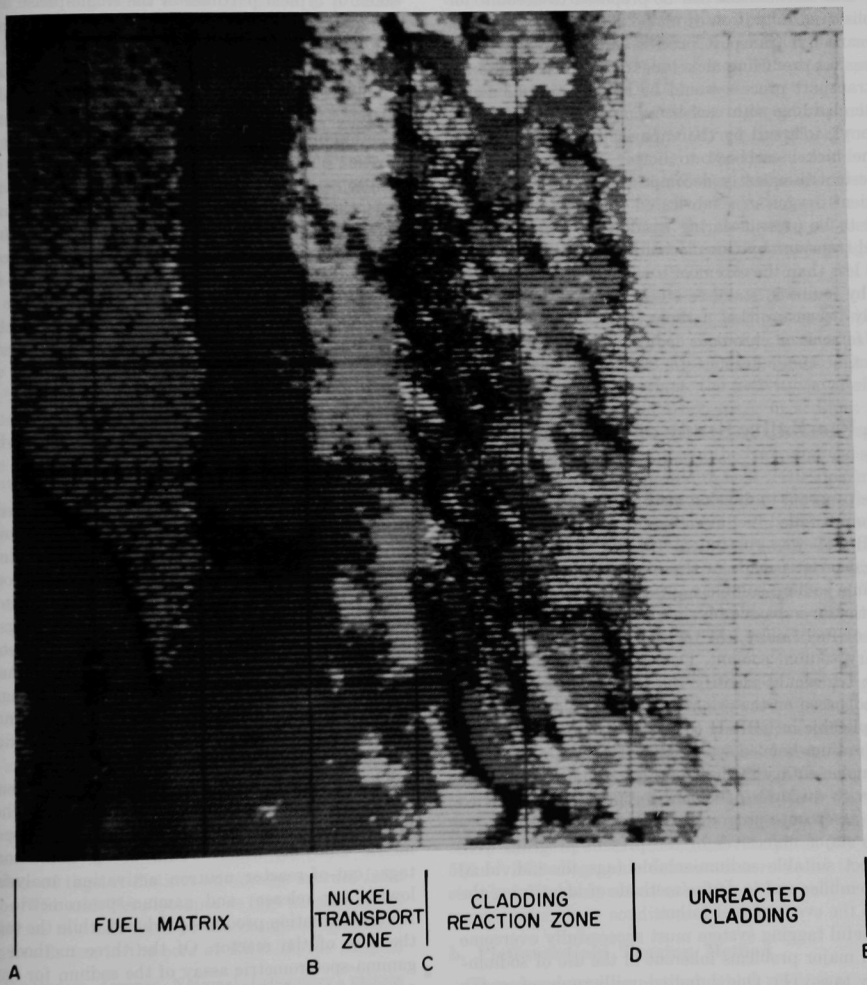

308-2062 A

FIG. IV-4. Electron Microprobe X-ray Image of Fuel-Cladding Interface of a UC-20 wt % PuC Fuel Pin (SMV-2) Clad with Type 304 Stainless Steel. (Image represents an area 45 μm square.)

fuel matrix. The separated band of stainless steel components is present in the reaction zone (C to D). Within this band, the variations in brightness are caused by variations in the nickel and chromium contents; the black areas are voids. The area of the figure from D to E is unreacted cladding. The cladding interface regions of both pins were free of both cesium and iodine fission products.

Several mechanisms can be proposed to account for the observed migration of nickel. The first mechanism is a carbonyl transport process, similar to the Mond process for producing nickel metal. In the carbide fuel, the transport process would be the reaction of nickel in the cladding with carbon monoxide to form nickel carbonyl, followed by the vaporization and migration of the nickel carbonyl to hotter areas of the fuel, where it subsequently decomposes. There is probably sufficient oxygen in a fabricated fuel for carbon monoxide to be present during irradiation. The extent of nickel transport by this mechanism would be expected to be less than the extent of iron and chromium transport by iodine in stainless steel-clad oxide fuels, principally because nickel carbonyl has a lower stability than ferrous or chromous iodide. The second mechanism that could account for nickel migration is the reaction of the carbide fuel (containing a slight excess of carbon) with nickel in the cladding to form a mixed plutonium-nickel carbide. Further investigations are planned to establish the exact nature of the mechanism for nickel transport.

Preliminary studies of SMV-2 have also been conducted to determine the distribution of fission products within the carbide fuel. Spectral profiles were taken of typical particles of the single-phase uranium carbide (average size, ~700 μm) located near the center and near the periphery of the fuel pin. Zirconium and molybdenum were present in detectable quantities in all of the particles examined. No concentration difference was observed for either element as a function of (1) location within a given particle or (2) location of the particle in the fuel pin.

Spectral analysis of the porous plutonium carbide phase indicated the presence of neodymium and palladium, as well as cesium. Cesium was observed throughout the plutonium carbide in localized concentrations. This is in contrast with the behavior of cesium in oxide fuels, where cesium is found primarily in the cooler zones (i.e., near the cladding) of the fuel.

Further studies of fission product distribution in the carbide fuels is in progress.

3. Feasibility Study of Fuel-Failure Detection: Sodium-Soluble Tags (*R. J. Meyer, C. E. Johnson*)

The program to develop methods for identifying the position of failed fuel in an operating fast reactor such as EBR-II was continued. In this program an investigation was made of the feasibility of introducing the same sodium-soluble tag into each fuel element of a particular subassembly in such a way that, in the event of fuel failure, the tag will be discharged to the primary sodium coolant. Detection and identification of the tag would identify the faulty subassembly. A method based on the use of sodium-soluble tags would be applicable in EBR-II to sodium-bonded driver fuel or to sodium-bonded, encapsulated experimental fuel. A complementary technique for tagging gas-bonded fuels with mixtures of xenon isotopes is being carried out in a separate program (see Section IV.B).

The major objectives of the present program were to select suitable sodium-soluble tags for individual subassemblies and to devise methods of identifying the tags in the event of fuel failure.

A useful tagging system must successfully overcome several major problems inherent in the use of sodium-soluble tags. (1) One hundred milligrams of a tag charged to the bond sodium of a driver fuel element would result in a concentration below the part-per-billion level when the tag was completely mixed with the primary coolant; detection at this level would be a difficult analytical problem. (2) Only eleven elements have a solubility such that 100-mg quantities would be soluble in the 0.8 g of bond sodium at the reactor operating temperature. Consequently, multiple tags must be devised from this limited number of elements. (3) No purification of EBR-II sodium, other than cold trapping, is presently being effected. Thus, a tag, once released, would probably remain in the sodium and constitute a potential interference to the identification of the next failed fuel.

The detection methods capable of providing the necessary sensitivity for identifying a tag in the primary sodium coolant are spark-source mass spectrometric analysis, which would detect nonradioactive tags; out-of-reactor neutron activation analysis following tag release; and gamma-spectrometric assay for tag activation products produced while the tag is in the core of the reactor. Of the three methods, only gamma-spectrometric assay of the sodium for reactor-activated tags has the capability of satisfying the detection requirements (this subject is discussed in the next subsection).

Two tagging methods have been devised that should overcome the major difficulties associated with the use of sodium-soluble tags. The first involves the use of mixtures of gold and antimony and the second, mixtures of gold and platinum.

a. Antimony-Gold Tagging Method

In the proposed gold-antimony method, the weight ratios of ^{121}Sb and ^{197}Au would be varied to produce a series of tags. Each fuel element in a subassembly would then be tagged with a unique mixture having a fixed ratio of ^{121}Sb and ^{197}Au. While in the core of EBR-II, these tag mixtures would be activated to ^{122}Sb (2.8 days) and ^{198}Au (2.7 days). Because of the varying weight ratios, each tag mixture would have a distinctive activity ratio. In the event of a fuel failure, the active isotopes would be discharged to the primary coolant. After appropriate sampling and separation procedures, the ^{122}Sb-^{198}Au activity ratio would be determined by gamma-ray spectrometry, and this ratio would be used to identify the faulty subassembly. The details of the method are discussed below in relation to the problems that were enumerated previously.

Detection. Calculations were made of the level of activity of ^{198}Au that would be produced from irradiation of ^{197}Au in the core of EBR-II at full power; the value used for the capture cross section of ^{197}Au in EBR-II was 200 mb.[9] These calculations showed that (1) the saturation activity of ^{198}Au produced from 1 mg of ^{197}Au would be about 6×10^8 dps (~98% of saturation is achieved in 15 days) and (2) the activity produced in one day would be about 1.2×10^8 dps/mg of ^{197}Au. Release of 1 mg of ^{197}Au of the latter level of activity to the 3×10^8 g of sodium coolant would result in a sodium activity level of 0.4 dps/g of sodium. This level of activity should be more than adequate for detection in a 10-g sodium sample after appropriate radiochemical separations have been performed.

Because experimental data on the capture cross section of ^{121}Sb were not available, differential cross sections were estimated with the NEARREX computer code,[10] and these were summed over a typical EBR-II flux spectrum. The results of the calculations indicate a capture cross section for ^{121}Sb in EBR-II of about 70 mb, which should produce sufficient ^{122}Sb to be detectable.

Number of tags. A distinct advantage accrues from using the ^{121}Sb and ^{197}Au isotopes as tags because of the similarity in the half-lives of the daughter activities. During irradiation in the core of EBR-II, the ratio of ^{122}Sb to ^{198}Au activities produced would be nearly constant. For example, if one assumes that the saturation activity ratio will be 1.00, the activity ratio after one hour of irradiation would be 1.04, and, thereafter, would approach 1.00. The constancy of the activity ratio would permit numerous tags to be manufactured from these two isotopes. The exact number of tags that could be put into use depends on the constancy of the ratio of the capture cross sections of ^{121}Sb and ^{197}Au as a function of neutron energy and on the precision of the radiochemical separations used to isolate the active isotopes. It is estimated that at least 10 tags and possibly as many as 100 could be made.

Interference from previous tags or impurities. Until suitable methods of purifying the primary coolant are devised, any tagging method must consider the effects of previously released tags. Although most potential methods would require purification of the coolant to remove previous tags, the antimony-gold method is reasonably free from the effects of previous tags, as can be seen from the discussion below.

A fuel-element tag would reside in the core of the reactor 100% of the time and, as previously stated, would achieve a saturation activity level of about 6×10^8 dps/mg of ^{197}Au. Upon discharge of 1 mg of ^{197}Au to the primary coolant, the activity level of the tag in the sodium would be 2 dps/g of sodium. Any ^{197}Au already in the circulating sodium would spend only about $1/2000$ of the time in the core, and the saturation level would be expected to be 3×10^5 dps/mg of ^{197}Au. A simple calculation shows that the circulating sodium must contain approximately 2 g of ^{197}Au before the activity level will be equal to that produced in 1 mg of ^{197}Au tag. Furthermore, a tag that has achieved the saturation activity level of 6×10^8 dps/mg of ^{197}Au in the core will decay rapidly to the lower saturation level of 3×10^5 dps/mg of ^{197}Au once it is released to the sodium.

In selecting a tag, consideration must also be given to the corrosiveness of the tag toward the fuel cladding. In preliminary studies to test the corrosion characteristics of possible tags in a fuel-element environment, gold and antimony were among the elements tested. Mixtures of Na-2 wt % Sb and Na-2 wt % Au were placed in separate capsules of type 304L stainless steel, which were then sealed and rotated at 650°C for 500 hr. Metallographic examination revealed that the stainless steel was not attacked by either gold or antimony under these conditions.

b. Platinum-Gold Tagging Method

The second tagging method, which utilizes mixtures of isotopes ^{197}Au and ^{198}Pt, would operate on the same general principles as the antimony-gold method. In

[9] N. D. Dudey, Argonne National Laboratory, private communication (1969).

[10] P. A. Moldauer *et al*, "NEARREX, A Computer Code for Nuclear Reaction Calculations," ANL-6978 (1964).

TABLE IV-1. CALCULATED ACTIVITY RATIOS OF TAGS DURING A TYPICAL EBR-II OPERATING PERIOD[a]

Time Interval (days)	Power (MW)	Activity Ratio at End of Interval	
		$^{198}Au/^{122}Sb$	$^{198}Au/^{199}Au$
3.5	30	1.79	3.19
7.0	0	1.68	2.43
2.5	30	1.78	3.10
1.0	0	1.77	2.95
3.25	30	1.78	3.04
1.25	0	1.76	2.87
3.25	30	1.77	2.98
3.25	0	1.72	2.62
2.5	30	1.76	2.95
3.5	50	1.78	3.02

[a] Period from Oct. 1 to Oct. 31, 1968.

this case, however, tag identification would be made on the basis of the $^{198}Au/^{199}Au$ ratio. The ^{199}Au is produced by the reactions

$$^{198}Pt(n,\gamma)\ ^{199}Pt \xrightarrow[(31\ min)]{\beta^-} {}^{199}Au\ (3.15\ days)$$

Estimations of the capture cross section of ^{198}Pt in EBR-II, made by the method described above, indicate a value of the same magnitude as that of ^{121}Sb, namely, about 70 mb.

One attractive feature of the platinum-gold tagging method is that tag identification is made on the basis of the ratio of two isotopes of gold, and no difference would be expected in the behavior of the two isotopes in the sodium coolant. Therefore, a minor instability of gold in the reactor system would produce no alteration in the $^{198}Au/^{199}Au$ ratio of a released tag.

A possible disadvantage of the platinum-gold method is that, during variations in reactor operating conditions, the $^{198}Au/^{199}Au$ activity ratio would not be as constant as the $^{198}Au/^{122}Sb$ activity ratio. The reasons for the lesser variation in the $^{198}Au/^{122}Sb$ activity ratio are as follows: (1) The half-life of ^{122}Sb (2.8 days) is more nearly equal to the half-life of ^{198}Au (2.7 days) than is the half-life of ^{199}Au (3.15 days). (2) The formation of ^{199}Au is delayed by the 31-min half-life of the intermediate activation product ^{199}Pt.

To gain some insight into how much variation would be produced by reactor startups, shutdowns, and changes in power, calculations were made which permitted comparison of the performance of a ^{197}Au-^{198}Pt tag with that of a ^{197}Au-^{121}Sb tag during a one-month period of operation of EBR-II. The following assumptions were made in performing the calculations: (1) Each tag is composed of equal weights of ^{197}Au and the other isotope. (2) The capture cross sections are 200 mb for ^{197}Au, and 70 mb for both ^{198}Pt and ^{121}Sb. (3) The time to achieve the power level and the time to shutdown are insignificant.

The results of these calculations are given in Table IV-1. It is evident from these results that identification of a platinum-gold tag would be more difficult than identification of an antimony-gold tag because the variations in activity ratios are greater. However, with adequate fuel-failure detection equipment and a power record of the reactor, tag identification could be made.

Although both of these methods show promise as useful tagging methods, insufficient funding has required the termination of the program. The evaluations of tagging methods that have been made, however, may be useful for future fast reactors.

B. XENON TAGGING OF FUEL ELEMENTS IN EBR-II (*L. F. Coleman, G. J. Bernstein, E. R. Ebersole,*[11] *M. T. Laug,*[11] *R. E. Rice,*[12] *P. B. Henault,*[12] *W. J. Larson,*[12] *D. E. Walker*[13])

A program is under way to utilize mixtures of xenon isotopes as tags for the identification of experimental fuel elements that fail in EBR-II. Emphasis has been placed on the application of the xenon-tag method to the identification of unencapsulated gas-bonded fuel elements, most of which will contain UO_2-PuO_2.

[11] Idaho Division.
[12] EBR-II Project, Idaho.
[13] EBR-II Project, Illinois.

Fuel-cladding failures in EBR-II are presently detected by the following instruments: (1) a fuel failure rupture detector (FERD), (2) an on-line charged-wire fission gas monitor (FGM), and (3) a reactor cover gas monitor (RCGM). Although detection by these instruments is thorough, identification of the subassembly in which failure occurred has been difficult and time consuming. Implementation of the xenon tagging system will permit rapid identification of any

failed experimental fuel subassembly and will thus significantly increase the EBR-II plant factor.

In the xenon-tagging system, each fuel element in a subassembly is tagged with 1 ml of a mixture of xenon isotopes that is unique for a particular subassembly. If a cladding failure is indicated by one of the failure-detection instruments, a sample of the reactor cover gas will be analyzed mass spectrometrically to determine the ratios of xenon isotopes present. These ratios will provide an indication of the tagging mixture that has been released; positive identification will then be made by analyzing a master sample of the indicated mixture and comparing the two results. Positive identification of the released xenon mixture will permit identification of the affected subassembly and its location in the reactor. It is anticipated that identification can be accomplished within the 4-hr period required to prepare for removal of a subassembly.

Many features of the xenon-tagging system were discussed in the preceding annual report.[14] In the following discussion of the status and plans of the system, these features will be reiterated only where necessary to maintain clarity.

[14] ANL-7575, pp. 106–111 (1968).

1. Preparation of Tag Mixtures

Because xenon isotopes with mass numbers 131 through 136 are abundantly produced by fission, xenon-tag mixtures for failed-fuel identification must contain significant concentrations of the lower mass numbers 124 through 130. Mound Laboratory[15] is currently producing several different mixtures of xenon isotopes in which the lighter isotopes have been enriched by thermal diffusion. Table IV-2 shows the isotopic compositions of natural xenon and four enriched isotopic mixtures which have been purchased from Mound Laboratory for the preparation of tag mixtures.

Tag mixtures have been prepared as planned[14] by blending each of the Mound Laboratory Mixtures 1, 2, and 3 with natural xenon in preselected proportions. In the resultant tag mixtures, designated as subseries A1, A2, and A3, respectively, the $^{129}Xe/^{124}Xe$ isotopic ratios are normally stepped so that each ratio is 1.2 times the previous ratio; these ratios range from 4.9 to 75 (the ratio in natural xenon is 275). These tag mixtures will normally be identified by the $^{129}Xe/^{124}Xe$ isotopic ratio. There are five tag mixtures in subseries A1, eight in A2, and five in A3 for a total of eighteen prepared tag mixtures.

Because approximately twenty subassembly locations in the EBR-II core are available for experimental fuel irradiation and because tagging logistics require a greater number of tag mixtures than the peak number of in-core tagged subassemblies, the eighteen tag mixtures now prepared may eventually prove insufficient for EBR-II experimental fuel elements. Several alternatives are available to ensure an adequate number of tagging mixtures: consideration is being given to preparing new A-subseries tag mixtures as well as a series of tag mixtures (Series B) utilizing pure ^{128}Xe.

[15] Mound Laboratory, Miamisburg, Ohio; operated by the Monsanto Research Corporation for the USAEC.

In the thermal-diffusion enrichment of the light xenon isotopes (see Table IV-2), the $^{126}Xe/^{124}Xe$ isotopic ratio is a minimum at an intermediate enrichment. This feature permits preparation of additional A-subseries tag mixtures which can be identified by consideration of both the $^{129}Xe/^{124}Xe$ and $^{126}Xe/^{124}Xe$ isotopic ratios. This interrelationship is shown in Fig. IV-5, where the ranges of the existing subseries of tag mixtures, A1, A2, and A3, are shown, along with the ranges of the proposed subseries, A4 and A5. Subseries A4 would be prepared by blending Mound Mixture 4 (21.3 mol % ^{124}Xe) and Mound Mixture 3 (1.257 mol % ^{124}Xe) in preselected amounts. Subseries A5 would be prepared by blending Mound Mixture 2 (5.58 mol % ^{124}Xe), Mound Mixture 3, and natural xenon. For the ranges shown, subseries A4 would provide eighteen tag mixtures and subseries A5 would provide five tag mixtures. These twenty-three new tag mixtures and the eighteen previously prepared would

TABLE IV-2. Isotopic Composition of Natural Xenon and Four Light-Isotope-Enriched Mixtures from Mound Laboratory

Xenon Isotope Mass Number	Total Xenon[a] (mol %)				
	Mound Mixture				Natural Xenon
	No. 1	No. 2	No. 3	No. 4	
124	12.10	5.58	1.257	21.3	0.096
126	4.80	1.92	0.834	10.2	0.090
128	16.70	10.32	8.02	23.9	1.92
129	58.78	63.02	63.50	43.4	26.44
130	2.25	4.30	5.25	0.7	4.08
131	3.13	9.43	13.11	0.4	21.18
132	1.70	5.03	7.46	0.1	26.89
134	0.29	0.34	0.496	<0.1	10.44
136	0.25	0.026	0.080	<0.1	8.87

[a] Xenon purity $\geq$ 99.0%.

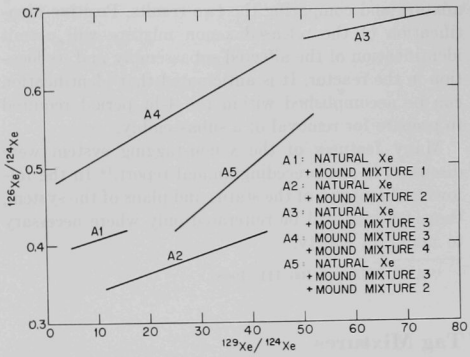

308-2177
FIG. IV-5. Isotopic Relationships of Series A Xenon Tags.

probably satisfy all EBR-II tag demands. Material for about seventeen new A-subseries tag mixtures is on hand or readily available from Mound Laboratory.

A very large number of tag mixtures can be made by blending Mound Laboratory enriched mixtures of xenon (or enriched plus natural xenon) with pure ^{128}Xe prepared by neutron irradiation of natural iodine.[16] In these tag mixtures, which will be designated Series B, each different $^{129}Xe/^{124}Xe$ ratio will form a subseries. Released tags from Series B mixtures will normally be identified by the $^{128}Xe/^{124}Xe$ isotopic ratio.

Argonne National Laboratory has awarded a contract to Douglas United Nuclear, Inc. to develop a method for preparing pure ^{128}Xe and to deliver 100 ml; the contract offers to buy an additional 1000 ml ^{128}Xe at a fixed price. The number of Series B tags that could be produced from a small quantity of pure ^{128}Xe would probably extend the available supply of tags sufficiently to meet all EBR-II demands. Availability of pure ^{128}Xe at a reasonable price could possibly permit application of xenon tagging to the next generation of fast reactors.

[16] Natural iodine is 100% ^{127}I; ^{128}Xe is formed by the reactions $^{127}I(n,\gamma)^{128}I \xrightarrow{\beta^-} {}^{128}Xe$.

2. Addition of a Tag to a Fuel Element

Gas-bonded fuel elements that are irradiated in EBR-II consist of a fuel region and a gas plenum to contain released fission gases. The inside diameter of the cladding is about ¼ in., the fuel length is about 14 in., and the gas plenum length is generally greater than 8 in. Although the method of transferring a xenon tag from the ANL-supplied container to a fuel element is the responsibility of the experimenter, tag-addition procedures have been devised by ANL and suggested to experimenters, and ANL personnel have provided aid to experimenters in developing or improving their tag-addition procedures.

Two basic techniques of xenon tag addition have been developed: hypodermic syringe and pre-mixed backfill. In the former method, a syringe is filled with several milliliters of xenon tag mixture and 1 ml is injected into each of several fuel elements by means of a long needle reaching near the bottom of the helium-filled gas plenum. In the latter method, the fuel element is evacuated and then backfilled with a mixture of helium and xenon tag. In each case, the fuel element is immediately capped and welded to prevent loss by diffusion.

Two methods have been developed for transferring xenon tag mixture from an ANL-supplied transfer container (usually of 30-ml capacity) to a hypodermic syringe for tag addition. The first method, which was previously described,[14] utilizes a manually operated mercury piston to remove tag gas from the transfer container at negative pressure and supply it at a slightly positive pressure to a chamber equipped with a needle-loading rubber septum. Because close observation of the mercury-gas interface is required, much of this apparatus must be of glass. An apparatus of this type was used by the General Electric Company[17] to prepare the first xenon-tagged fuel elements.

A cryogenic transfer technique for syringe loading was developed to overcome shortcomings in the mercury-transfer technique. The new technique eliminates the possibility of mercury contamination, and the all-metal construction of the system eliminates fragile components. Furthermore, the method provides a means of purifying the tag mixture of the common contaminants oxygen and nitrogen.

An apparatus utilizing this principle is shown in Fig. IV-6. The operating procedure is briefly as follows. With the 30-ml transfer cylinder isolated, the apparatus is purged of contaminants by repeated evacuations and helium backfills. The tag mixture is purified by immersing the transfer cylinder in liquid nitrogen, freezing the xenon, and pumping off the volatile contaminants. The xenon is then cryogenically transferred to the small charging cylinder, after which the tubing cross-connection is isolated from the pipe tee. The tub-

[17] D. M. Bishop, General Electric Company–Vallecitos, private communication.

ing cross-connection is attached by means of a flange to a rubber septum located in a helium-filled glovebox used for fuel element assembly. A hypodermic syringe with a long needle is used to withdraw tag mixture through the septum and discharge 1 ml into the plenum of each of several fuel elements. During syringe charge, the xenon is maintained at a slight positive pressure by manipulating the fine-control throttling valve. The charging cylinder and cross-connection have small internal volumes, and all but 4 ml of the tag mixture can be transferred to the syringe. The remaining 4 ml can be cryogenically transferred back to the transfer cylinder for use in subsequent tag mixture preparation. This apparatus was successfully used[18] to tag fuel elements for an instrumented subassembly.

In the pre-mixed backfill technique, the xenon-tag transfer cylinder is pressurized with helium to form a helium-xenon mixture. The mixture is then supplied to an evacuated fuel element to fill it to a pressure of 1 atm. The helium-to-xenon ratio in the mixture is selected so that the back-filled element will contain 1 ml of xenon tag. After backfilling, the fuel element is immediately capped and seal-welded. The primary advantage of this back-fill technique is that it eliminates use of the hypodermic needle. This technique has been used successfully at Pacific Northwest Laboratory[19] (PNL) to tag a large number of fuel elements.[20]

[18] D. E. Walker, P. J. Halfman, J. H. Sanecki, "Xenon Tagging of Instrumented Fuel Capsules for Use in EBR-II," presented at USAEC-NASA National Symposium on Developments in Irradiation Testing Technology, Sandusky, Ohio, Sept. 9–11, 1969.

[19] Operated by Battelle Memorial Institute for the USAEC.

[20] R. M. Crawford, PNL, private communication.

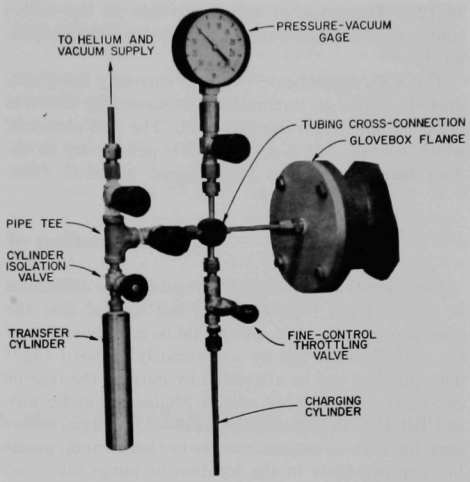

308-2225

FIG. IV-6. Cryogenic Syringe-Charging Apparatus for Purification and Transfer of Xenon Tags.

The three transfer techniques described above all have disadvantages in that special equipment is required by the experimenter and absolute certainty that an element has been tagged is not possible. These disadvantages might be overcome if tag gas for an individual fuel element could be provided in a sealed capsule which could be automatically opened after or at the time of final element closure. Preliminary development of a capsule technique is under way at ANL.

3. Possible Detrimental Effects of Xenon Tagging

Possible detrimental effects of the presence of a xenon tag in gas-bonded fuel elements were previously considered.[14] The only detrimental effect considered to be possible was a decrease in the thermal conductance of the fuel-to-cladding gap during the early stages of fuel-element irradiation. Examination of the literature indicated that this should not be a significant problem, but this indication was not considered sufficiently conclusive. Accordingly, experimental investigations of the thermal-conductance effect were independently planned by PNL and ANL.

In the PNL experiment,[21, 22] four gas-bonded fuel capsules were prepared with fuel, cladding, and fuel-to-cladding gaps representative of PNL fuel elements but with abbreviated lengths. The gas spaces of the capsules were filled with helium-xenon mixtures having xenon concentrations varying from 0 to 100%. The four capsules were irradiated concurrently for 4 hr in the rabbit facility of a thermal reactor under conditions that assured central melting of the fuel. Post-irradiation metallographic examination and measurement of the radius of the molten zone in each fuel pellet permitted calculation of the gap conductance for each case. For a 10% Xe-90% He mixture, the mixture most representative of proposed tagging conditions, the decrease in gap conductance attributed to xenon was only 4%. The experimenter estimated that operating under more representative conditions (no central melting) might cause decreases in the gap conductance of

[21] G. R. Horn, "The Effects of Xenon on Fuel-to-Cladding Gap Conductivity," *Trans. Amer. Nucl. Soc.* **12**(2), 607 (1969).

[22] G. R. Horn, private communication.

10–12%. Decreases of this magnitude in the early-stage gap conductance should not be a significant detriment.

The ANL experiment,[18] which is currently being conducted, utilizes an instrumented subassembly that was designed and constructed at ANL. The fuel elements, which contain 44.5%-enriched UO_2 pellets, are in sodium-bonded capsules. Four tagged elements (14% Xe-86% He), equipped with central thermocouples, are arranged to experience the same neutron flux as two untagged elements, which are also equipped with central thermocouples. This experiment will allow the effect of a xenon tag on the fuel-to-cladding gap conductance to be determined continuously for a wide range of power densities.

4. Identification of a Released Xenon Tag

Consideration of factors that could cause difficulties in identifying a released xenon tag showed that the most probable problem area would be contamination of the reactor cover gas by a previously released tag.[14] This problem can be alleviated by purging the reactor cover gas after each tag release. Studies are under way at EBR-II to determine the amount of purge gas necessary for various contaminant-reduction factors, possible improvements in the location of purge inlet and exhaust lines, and the advisability of providing interim storage capacity for the purged gas.

If any of the EBR-II on-line fission product monitors indicate that a cladding failure has occurred, a sample of the reactor cover gas will be analyzed for the presence and identity of a xenon tag. Three percent of the cover gas ($\sim$10 ft^3 at ambient conditions) will be passed over activated carbon at $-78°C$ to sorb the xenon. The sample will then be analyzed mass spectrometrically to identify the tag.

Experiments with activated carbon at $-78°C$ in a ¾-in. OD U-tube showed that essentially all of the xenon in a 10-ft^3 sample of reactor cover gas is collected in the first two inches of the carbon. A station for cover-gas sampling is available within the reactor containment shell, and a more convenient sampling station outside the containment shell is in an advanced construction stage.

Positive identification of the xenon tag will be accomplished by mass spectrometry. A mass spectrometer (Varian-MAT Model CH-7) designed for gas analysis has been installed at EBR-II for this purpose. Analytic data can be obtained by either of two collector systems: an electron-multiplier single collector or a dual cup-and-plate simultaneous detector. Potentiometric and galvanometric recorders are available for data display. The multiplier detector system scans the mass range 124–136 and records on either recorder. The dual collector consists of a collector plate with a precision slit focused upon a cup detector. A preselected isotope can be focused upon the slit and measured by the cup detector, with the remaining isotopes being measured by the plate. Thus, the ratio of any isotope to the balance of the isotopes can be measured directly within 0.05% and the ratio recorded on the potentiometric recorder.

The mass spectrometer is provided with a versatile source having three inlet systems: (1) a directly coupled gas chromatograph with a sample enricher, (2) a viscous-flow inlet system, and (3) a molecular-flow inlet system. A sample of the reactor cover gas introduced into the mass spectrometer through any one of the inlet systems can be analyzed by means of either collector system.

With the gas-chromatographic inlet system a reactor cover-gas sample from the activated carbon trap is introduced into the chromatograph, which separates the xenon component from the bulk argon in the trap. The separated xenon is then introduced into the mass spectrometer via the sample enricher, which removes the helium carrier gas used in the chromatographic separation.

The viscous-flow inlet system contains two small gas reservoirs (<50 ml), one for a reference sample and the other for a cover-gas sample. By utilizing the dual collector and the rapid sample interchange feature of the viscous-flow inlet system, a direct comparison can be made between the isotopic ratios of the cover-gas sample and the isotopic ratios of a reference sample. The molecular-flow inlet system, which is the simplest system to operate, contains a single large (2000 ml) sample reservoir. Because sample flow is molecular, some bias may develop in the flow of gases of different molecular weights and special calibration will be required for high precision. Use of either the viscous-flow or the molecular-flow inlet systems will probably require a separate step to concentrate the xenon from the xenon-argon mixture in the sample trap if the operating time for the spectrometer is to be kept to a reasonable level.

All three inlet systems are feasible for xenon-tag identification. The chromatographic inlet will obviate the need for sample concentration prior to analysis and, therefore, will give the most rapid analysis. The

viscous-flow inlet will provide immediate ability for comparison of a sample isotopic ratio with a reference isotopic ratio for rapid identification, but sample preparation time will be longer than for the chromatographic input. The viscous-flow system, with immediate referencing capability, also provides the greatest detection sensitivity. The molecular-flow input is the simplest mode to employ but is difficult to shield, when samples are highly radioactive, because of its large reservoir and configuration. Sample size, detection sensitivity and the amount of shielding required will dictate the input system to be used with a cover gas sample.

Implementation of the xenon-tagging system in EBR-II is well advanced. Eighteen tag mixtures have been prepared and material for seventeen new tag mixtures is on hand or readily available. A technique for producing pure ^{128}Xe is being developed and ^{128}Xe availability will greatly extend the possible number of tag mixtures. A large number of experimental fuel elements have been tagged, and in the near future the ratio of tagged to untagged experimental fuel subassemblies in the EBR-II core should increase to a point where the full value of the xenon-tagging program can be realized. The xenon-tagging program has essentially passed from a development stage to an operational stage and is now completely under the direction of the EBR-II Project.

C. FAST-REACTOR CROSS-SECTION MEASUREMENTS (*N. D. Dudey, C. E. Crouthamel*)

An understanding of fast-neutron processes is essential to the design and development of fast breeder reactors. The objective of the cross-sections program is to obtain data for neutron reactions occurring in fuel, structural, and control materials, and to apply these data to problems of interest to the overall fast breeder reactor program. In past work, a large part of the effort in the cross-sections program was directed toward determination of capture cross sections as a function of monoenergetic neutron energy; however, this portion of the work has now been completed. Recent efforts have been concentrated on the measurement of cross sections in the broad neutron-energy spectrum of EBR-II. These spectrum-averaged cross sections are of particular interest because they provide a means of characterizing the magnitude and the energy distribution of the neutron flux within an operating reactor.

Current progress is reported for spectrum-averaged measurements in EBR-II. These include (1) cross sections for (n,γ), (n,p), (n,α), (n,2n) reactions for materials of interest to the fast breeder reactor program and (2) capture-to-fission ratios (alpha) of principal fast breeder reactor fuels. The present status of neutron spectral characterization studies using foil-activation techniques is discussed. The status of the program to measure the fast fission yields of low-mass particles is also described.

1. Spectrum-Averaged Measurements (*N. D. Dudey, R. R. Heinrich, J. W. Williams*)

a. Flux Characterization Studies in EBR-II

A knowledge of the neutron flux as a function of position within an operating reactor is necessary in predicting the long-term behavior of fuels, cladding, and structural materials. In studies of radiation damage and in evaluations of models of fuel and cladding swelling, for example, an accurate means of monitoring the neutron flux is needed. The fast neutron flux and spectral distribution can be predicted by means of reactor physics calculations, but a comparison of these theoretical calculations with experimental data is also needed. An extensive program is presently being conducted in which flux values are being determined in EBR-II from activation-rate data of selected monitor foils. The method employed is described in detail elsewhere;[23] only a brief description will be given here.

Monitor reactions can be conveniently categorized into three classes: (1) low-energy reactions, which are predominately sensitive to neutrons below 1 MeV, for example, ^{45}Sc(n,γ) and ^{54}Fe(n,γ); (2) high-energy or threshold reactions such as ^{54}Fe(n,p), ^{58}Ni(n,α), or ^{197}Au(n,2n) reactions, which are characterized by a threshold energy (usually greater than a few hundred

[23] N. D. Dudey, R. R. Heinrich, "Flux Characterization and Neutron Cross Section Studies in EBR-II," USAEC report ANL-7629 (in press).

keV) below which the reaction does not take place; and (3) broad-spectrum reactions, such as $^{235}U(n,f)$ and $^{239}Pu(n,f)$, whose cross sections are relatively insensitive to variations in neutron energy between a few keV and 10 MeV.

To obtain activation-rate data, appropriate monitor foils are irradiated in various positions in EBR-II, and the number of reaction product atoms present at the end of the irradiation is determined by radiochemical analysis. A spectrum-averaged cross section is then computed for each monitor reaction at each sample location from published differential cross section data and from a two-dimensional diffusion-theory calculation of the neutron spectral distribution. From the measured reaction rates and the computed spectrum-averaged cross sections, values of the flux, ϕ, or flux per megawatt, ϕ/MW, are determined for each location. The reliability of the flux determinations can be increased by measuring several monitor reactions at each location and determining an average value of the flux.

The results of our flux measurements in EBR-II, based on five monitor reactions, are shown in Fig. IV-7, along with some measurements reported by PNL[24] and Ge.[25] The variations in the ϕ/MW values result principally from the fact that measurements were made in two different types of subassemblies: fuel subassemblies (designated by points in Fig. IV-7) and structural subassemblies (designated by x's), in which the samples were probably surrounded by neutron-scattering and neutron-absorbing materials, such as stainless steel. Other factors also contribute to the variations in results: (1) With present methods of flux determinations by foil-activation techniques, measurements based upon a single monitor reaction have uncertainties, in the best cases, of ±15%. (2) Changes in the composition of EBR-II occurred during the numerous experiments from which the data were obtained.

In addition to the obvious variations in Fig. IV-7, the measured flux values are, in general, about 20–25% lower than the flux values predicted by reactor-physics calculations; this difference results principally from the assumption in the reactor physics calculations that the reactor core is homogeneous.

If one takes into account all the factors discussed above, the data are qualitatively consistent within themselves and with the reactor physics calculations.

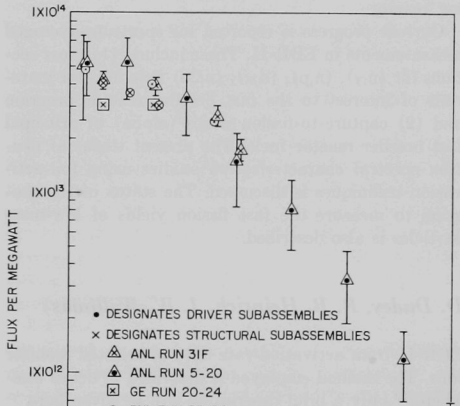

308-2064

FIG. IV-7. Flux per Megawatt as a Function of Radial Position in EBR-II.

TABLE IV-3. Spectrum-Averaged Cross Sections in EBR-II Calculated from Measured Reaction Rates and Experimentally Determined Fluxes

Reaction	Spectrum-Averaged Cross Sections (mb)			
	Row 2	Row 4	Row 6	Row 7
$^{54}Fe(n,\gamma)$	8.3	8.2	9.5	11
$^{62}Ni(n,\gamma)$	7.6	8.0	9.7	13
$^{45}Sc(n,\gamma)$	14	15	19	20
$^{58}Fe(n,\gamma)$	3.9	4.0	4.7	6.0
$^{59}Co(n,\gamma)$	14	14	18	23
$^{63}Cu(n,\gamma)$	—	19	26	—
$^{197}Au(n,\gamma)$	221	228	262	376
$^{54}Fe(n,p)$	16	16	13	7.3
$^{58}Ni(n,p)$	23	22	20	10
$^{46}Ti(n,p)$	2.0	2.0	1.7	0.93
$^{47}Ti(n,p)$	4.4	4.3	3.8	2.1
$^{48}Ti(n,p)$	0.052	0.050	0.041	0.021
$^{59}Co(n,p)$	0.27	0.27	0.24	0.12
$^{63}Cu(n,p)$	4.9	4.6	4.3	2.4
$^{32}S(n,p)$	3.5	3.4	3.0	1.7
$^{54}Fe(n,\alpha)$	0.18	0.18	0.15	0.073
$^{58}Ni(n,\alpha)$	0.90	0.87	0.78	0.41
$^{50}V(n,\alpha)$	0.21	0.079	0.099	0.073
$^{51}V(n,\alpha)$	0.0041	0.0041	0.0035	0.002
$^{63}Cu(n,\alpha)$	0.10	0.090	0.086	0.049
$^{197}Au(n,2n)$	0.56	0.66	0.50	0.39
$^{59}Co(n,2n)$	0.065	0.058	0.052	0.0021

[24] J. L. Jackson, J. A. Ulseth, *Nucl. Appl.* **5**, 275 (1968).

[25] A. Withop, B. A. Hutchins, G. C. Martin, "Analytical Procedures and Applications of Fluence Determinations from EBR-II Flux Wires," GEAP-5744 (1969).

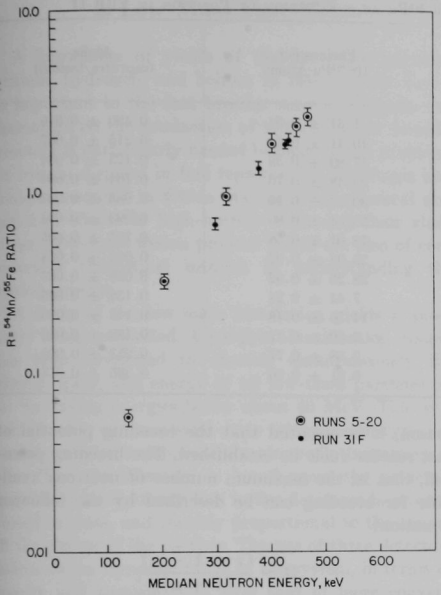

308-2065

FIG. IV-8. $^{54}Mn/^{55}Fe$ Ratio, R, *vs.* Median Neutron Energy in EBR-II.

The important conclusion to be drawn from analysis of these data is that future flux measurements intended to monitor irradiation experiments in EBR-II must be designed specifically to monitor the neutron flux and spectrum "seen" by the samples. Furthermore, the results of one experiment cannot be expected to agree with results of other experiments in which the flux monitors experience different conditions, nor can they be expected to agree with reactor-physics calculations in which a homogeneous reactor core is assumed. However, if the flux monitoring is reliable, the deviations should be predictable and understandable.

b. Spectrum-Averaged Cross-Section Measurements

The flux values determined by the method described above can be used to obtain spectrum-averaged cross sections of reactions for which appropriate differential cross-section data are not available. In this case, other selected foil materials are irradiated along with the monitor foils. The activation-rate data from these materials and the average flux values for each sample location, determined from the monitor foils, provide the necessary data to calculate spectrum-averaged cross sections. A summary of our spectrum-averaged cross-section data, measured at various positions in EBR-II during Run 31F, is presented in Table IV-3.

It must be recognized that if spectrum-averaged cross sections are to be applicable to other reactors or other reactor positions, the neutron spectral distribution in which the cross section was determined must be specified. It would, therefore, be desirable to be able to refer to a spectral index that, to some degree, describes the neutron spectral distribution. One such spectral index, which we have been examining, is the ratio of the reaction rates of the $^{54}Fe(n,p)^{54}Mn$ and $^{54}Fe(n,\gamma)^{55}Fe$ reactions. The $^{54}Fe(n,p)^{54}Mn$ reaction is sensitive only to neutrons above ~2 MeV, and the $^{54}Fe(n,\gamma)^{55}Fe$ reaction is, in general, sensitive only to neutrons below 2 MeV. The $^{54}Mn/^{55}Fe$ ratio, R, has been shown to be extremely sensitive to changes in the neutron spectral shape (see ANL-7575, p. 174). Additional measurements of this ratio were made in EBR-II in Run 31F, and all of the data obtained to date are shown in Fig. IV-8, where the ratio, R, is plotted against the median energy of the neutron spectrum as computed from reactor-physics calculations. The correlation between R and the median neutron energy is very encouraging; however, further work in reduc-

TABLE IV-4. CAPTURE-TO-FISSION RATIO (ALPHA) FOR ^{233}U AS A FUNCTION OF POSITION IN EBR-II

Distance from Core Center		Captures per 10^2 ^{233}U Atoms	Fissions per 10^2 ^{233}U Atoms	Alpha (captures/fissions)
Radial (cm)	Axial (cm)			
2.86	−17.0	1.77 ± 0.018	2.49 ± 0.072	0.0710 ± 0.0022
2.86	−8.5	2.16 ± 0.022	3.23 ± 0.093	0.0668 ± 0.0020
2.86	+0.0	2.30 ± 0.023	3.51 ± 0.101	0.0656 ± 0.0020
2.86	+8.5	2.14 ± 0.021	3.20 ± 0.093	0.0668 ± 0.0020
2.86	+17.0	1.68 ± 0.017	2.37 ± 0.067	0.0709 ± 0.0022
2.86	+51.5	0.464 ± 0.0046	0.495 ± 0.014	0.0937 ± 0.0029
21.25	−3.49	2.37 ± 0.024	3.28 ± 0.190	0.0723 ± 0.0044
40.83	−2.30	1.48 ± 0.015	1.73 ± 0.050	0.0856 ± 0.0026
61.23	−2.30	0.357 ± 0.0036	0.372 ± 0.011	0.0960 ± 0.0029

TABLE IV-5. CAPTURE-TO-FISSION RATIO (ALPHA) FOR ^{239}Pu AS A FUNCTION OF POSITION IN EBR-II

Distance from Core Center		Captures per 10^4 ^{239}Pu Atoms	Fissions per 10^3 ^{239}Pu Atoms	Alpha (captures/fissions)
Radial (cm)	Axial (cm)			
2.50	+72.9	6.30 ± 0.06	1.31 ± 0.04	0.480 ± 0.016
2.50	+30.2	22.40 ± 0.22	10.41 ± 0.34	0.215 ± 0.007
2.86	+17.0	22.05 ± 0.22	17.89 ± 0.58	0.123 ± 0.004
2.86	+8.5	24.30 ± 0.24	23.48 ± 0.76	0.104 ± 0.004
2.86	0.0	26.40 ± 0.26	30.93 ± 0.10	0.085 ± 0.003
2.86	−8.5	24.80 ± 0.25	26.53 ± 0.86	0.093 ± 0.003
2.86	−17.0	24.35 ± 0.24	18.01 ± 0.58	0.135 ± 0.005
10.21	+0.32	24.65 ± 0.25	29.93 ± 0.97	0.082 ± 0.003
21.25	+0.32	27.90 ± 0.28	28.26 ± 0.92	0.099 ± 0.003
30.62	+0.42	10.25 ± 0.10	7.44 ± 0.24	0.138 ± 0.005
40.83	+0.42	21.15 ± 0.21	14.76 ± 0.48	0.143 ± 0.005
51.03	+0.42	10.00 ± 0.10	5.30 ± 0.17	0.189 ± 0.006
61.24	+0.42	6.02 ± 0.06	2.38 ± 0.77	0.253 ± 0.009
71.45	+0.42	3.51 ± 0.04	0.91 ± 0.30	0.385 ± 0.013

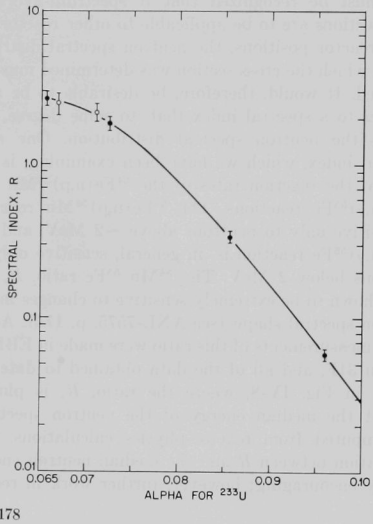

308-2178

FIG. IV-9. Correlation of Capture-to-Fission Ratio (Alpha) for ^{233}U and Spectral Index, R (R = ^{54}Mn/^{55}Fe).

ing experimental uncertainties will be required before a complete evaluation can be made of the ^{54}Mn/^{55}Fe ratio as a spectral index.

c. Capture-to-Fission Ratios in EBR-II

The purpose of a breeder reactor is to produce or breed more fissile fuel than it consumes; for this reason, it is essential that the breeding potential of fast reactor fuels be established. The breeding potential, that is, the maximum number of neutrons available for breeding can be described by the following equation:

$$B = \frac{(\nu - 1 - \alpha)}{(1 + \alpha)}$$

where ν is the number of neutrons emitted per fission of the reactor fuel and α is the capture-to-fission ratio of the fuel. Measurements of alpha (see ANL-7575, p. 174) have now been completed for samples of ^{233}U and ^{239}Pu irradiated in various positions (i.e., different spectra) of EBR-II. The samples were irradiated for periods ranging from 0.5 to 1.6 yr. The number of capture products (^{234}U or ^{240}Pu atoms) was determined by mass-spectrometric isotope-dilution analyses.[26] The number of fissions was determined by counting ^{137}Cs, using a fission yield of 6.51% for ^{233}U and a fission yield of 6.58% for ^{239}Pu. The results of these measurements for ^{233}U and ^{239}Pu are given in Tables IV-4 and IV-5, respectively.

The values of alpha for ^{233}U at four radial positions and four axial positions are shown as a function of the spectral index ^{54}Mn/^{55}Fe (R) in Fig. IV-9. Each open circle represents two axial measurements at symmetric points above and below the reactor midplane in Row 1. These results help to confirm the feasibility of correlating data by means of the spectral index.

[26] The mass spectrometry was performed by M. Laug, Idaho Division.

2. Low-Mass Fast-Neutron Fission Yields (*N. D. Dudey, A. A. Madson*)

A knowledge of yields of the low-mass particles tritium, hydrogen, and helium in fast-neutron fission is important to the fast breeder reactor program. Information on the production of tritium in fast breeder reactors is particularly needed because of the problems of tritium disposal in fuel reprocessing. Hydrogen and helium produced in fission may produce chemical and physical effects in high-burnup fuels and their claddings. Low-mass fission product yields are also of considerable theoretical interest in understanding the fission process.

A study of the low-mass fast-fission yields is presently being conducted. A particle identification system has been developed to identify simultaneously the charge, mass, and energy of all low-mass particles up to ^{7}Li having energies below about 40 MeV. This system consists of three solid-state transmission-type detectors coupled to appropriate electronic instrumentation. The identification is based upon the principle that the rate of energy loss in the detectors is proportional to mass, and roughly proportional to the square of the charge of the particle. The use of three detectors increases the dynamic range of the system, in terms of energy and particle type, over that of more conventional methods. This capability permits more information to be obtained in a single measurement.

Two experiments have been performed to test the particle identification system. The first was a study of the Bohr Independence Hypothesis; the purpose of the study was to demonstrate that the mode of decay of a compound nucleus is independent of its mode of formation. In this experiment the compound nucleus ^{63}Cu was formed in two ways, namely, by bombarding ^{59}Co with alpha particles and ^{62}Ni with protons. The energy and angular distribution of emitted protons, deuterons, and alpha particles were then determined. Although analysis of the resulting data is, at present, incomplete, the experiment demonstrated that the particle-identification system functioned properly. The purpose of the second experiment was to measure the energy distribution of all low-mass particles emitted in the spontaneous fission of ^{252}Cf. In this experiment the capabilities of the particle-identification method were verified: all low-mass particles up to ^{7}Li were individually identified and counted.

A preliminary experiment was also conducted to measure the fission yield of tritium for the ^{232}Th(α,f) reaction. Although no fission-yield data were obtained, the experiment provided information that will be very useful in designing future experiments. Two principal problems were disclosed: (1) radiation damage to the silicon fission detectors, and (2) strict requirements for setting the timing of the coincidence system. These problems were compounded by the extremely low tritium count rates. It has been concluded that, in spite of the deterioration of the silicon detectors, no better detectors are available; when the operating characteristics become degraded, they will be replaced. The timing problem can be solved by using a ^{252}Cf source in a special scattering chamber to set the timing before experimental measurements begin.

Because of budget restrictions within the program it is unlikely that the particle-identification experiments will be conducted according to the original plan. An alternative, simpler experiment is therefore being considered for determination of fast-neutron tritium yields. This experiment involves irradiation of gram quantities of fissile material in the Physics Division's neutron generator (Dynamitron), followed by radiochemical separation and counting of the tritium. The radiochemical and particle-identification methods, which employ widely different approaches, should ultimately supplement each other and add considerable confidence to the final values for tritium fission yields.

D. DETERMINATION OF BURNUP OF FAST REACTOR FUELS
(*R. P. Larsen, C. E. Crouthamel*)

The program for the development of methods for measuring burnup in fast reactor fuels is continuing. To achieve the program's objective it is necessary to develop accurate analytical methods for determining the concentration of fission products that can be used as burnup monitors and to establish accurate values for their fast fission yields.

1. X-Ray Spectrometric Determination of Rare Earth Fission Products (*R. D. Oldham, R. J. Meyer, R. V. Schablaske*)

A method is under development for the measurement of burnup in fast reactor fuels by X-ray spectrometric assay of the four principal rare earth fission products: lanthanum, cerium, praseodymium, and neodymium. The general analytical procedure to be used was described in ANL-7425, p. 194, and preliminary evaluations of the sensitivity and selectivity of the method were reported. Evaluations of the precision of the method (ANL-7575, p. 178) as a function of the amount of rare earths assayed showed that, in the range 30 to 90 μg of rare earths, an accuracy of $\pm$1–2% appeared feasible.

In the proposed procedure, terbium (a rare earth with a fission yield of less than 0.05%) is added to the sample as an internal standard; the rare earths as a group are separated from uranium, plutonium, and the high-activity fission products; and the separated rare earths are mounted on a metal plate and assayed by X-ray spectrometry. The use of terbium as an internal standard has the following advantages: (1) the need for a high degree of geometric reproducibility in sample mounting is minimized, and (2) the depressive effect of foreign materials on the X-ray intensities of the rare earths is largely compensated for. Moreover, quantitative recovery of the rare earths in the separation procedure may not be necessary, provided that the fission product rare earths and the terbium exhibit identical chemical behavior.

Separation of the rare earths. The advantages of the internal-standard method and the good discrimination from interferences that is afforded by X-ray spectrometric analysis place rather modest requirements on the separation procedure: the rare earths must be separated only from the bulk constituents of the fuel and from the more active gamma-emitting fission products. This separation is accomplished by converting the sample (which has been spiked with terbium) to 12*M* hydrochloric acid and passing it through a Dowex-1 ion-exchange column. Uranium, plutonium, ^{95}Zr, ^{95}Nb, ^{103}Ru, and ^{106}Ru are retained on the ion-exchange column and the rare earths are eluted. The long-lived fission products ^{90}Sr and ^{137}Cs are not separated from the rare earths, but these do not contribute significantly to the total activity of the rare earth sample.

Deposition of the rare earths for X-ray spectrometric assay. In preliminary tests of the plating procedure with a mixture of the fission product rare earths (inactive) and terbium, the rare earth chlorides were converted to nitrates by fuming to dryness with concentrated nitric acid and redissolving in dilute nitric acid; this solution was pipetted onto an aluminum plate and dried. However, when this technique was coupled with the ion-exchange separation, the plates were not of satisfactory quality (see ANL-7575, p. 180).

An electroplating technique, which was devised by Handley and Cooper[27] for the analysis of americium and curium by alpha spectrometry, has subsequently been adapted for preparing the rare earth sample mounts. The plating procedure is, briefly, as follows. After the ion-exchange step and subsequent conversion of the rare earth solution to a nitric acid medium (as described above), dimethyl sulfoxide is added, and the rare earths are electroplated onto an aluminum plate, which serves as a cathode. With a current density of 15 mA/cm^2 and a potential of ~100 V, complete deposition is achieved in 15 min. A significant improvement in the quality and reproducibility of the X-ray plates has been achieved by the electroplating technique. The deposition is uniform, the amount of solids on the plates is decreased, and the rare earths are completely adherent.

The revised procedure was tested in the following manner. Four samples consisting of 35 μg of terbium and 100 μg of a simulated mixture of fission product rare earths were carried through the ion-exchange procedure and electroplated on aluminum. These were treated as "unknowns" and were compared with two "standards" of the same composition that were electroplated directly. The average intensity ratios (rare earth-to-terbium) obtained for the standards and unknowns were as follows:

	Avg. Intensity Ratio		
	Standards	Unknowns	Rel. Std. Dev. (%)
La/Tb	0.161	0.162	1.7
Ce/Tb	0.275	0.273	2.6
Pr/Tb	0.218	0.217	1.6
Nd/Tb	0.483	0.482	0.5

The relative standard deviation is for a single determination; similar precision was obtained in duplicate experiments.

Interelemental effects in the X-ray spectrometric assay. Before the accuracy of the method could be evaluated, it was necessary to assess the magnitude of interelemental interferences on the X-ray measurements and to devise a method for corrections if the interferences were significant. Two types of interelemental effects were considered: (1) the effect of sec-

[27] T. H. Handley, J. H. Cooper, *Anal. Chem.* **41**, 381 (1969).

ondary and tertiary (Lβ and Lγ) emission lines of each rare earth on the intensity of the primary (Lα) emission line that is used in the assay and (2) the effect of the Lβ and Lγ emission lines of cesium and barium (fission products not removed in the ion-exchange separation) on the Lα lines of the rare earths. To establish the magnitude of these effects, mounts of the pure elements (~1 mg) were prepared and each was assayed at the wavelength of its primary emission line and also at each of the wavelengths used in the assay of the individual rare earths. Where significant interferences were observed (in one case, ~30%), intensity relations were established. These were used as coefficients in a set of simultaneous equations by which the necessary corrections were made. A small computer program was devised to handle data reduction.

Calibration. To obtain a calibration curve for each of the rare earths, aliquots of a standard mixture of the rare earths (in amounts proportional to their fission yields) were used to prepare plates containing a total of 44 to 217 μg of fission product rare earths; each plate also contained 40 μg of terbium. The line intensity of each rare earth was measured, the corrected line intensities were calculated using the computer program, and the rare earth-to-terbium line intensity ratios were plotted against weights of rare earths by a least-squares technique. The average divergence of the individual datum points over the entire concentration range was as follows: La, 1.5%; Ce, 3.0%; Pr, 0.2%; Nd, 1.2%. The maximum divergence obtained was for cerium (4%).

The standard rare earth mixture described above was also used to prepare two series of "unknown" samples, each sample containing 102 μg of rare earths. In the first series, the rare earths were electroplated directly. The plates were then assayed, and the amount of each rare earth determined from its calibration curve. In the second series, the rare earth "unknowns" were spiked with 100 mg of uranium and appropriate amounts of all the other major fission products (to simulate a 1 at. % burnup sample) and were carried through the ion-exchange separation prior to electroplating and assay. The results are summarized in the following table:

Rare Earth	Fission Yield from ^{239}Pu (%)	Recovery (%) Series I	Recovery (%) Series II
La	5.73	100.0 ± 3.9	99.3 ± 3.4
Ce	10.54	98.0 ± 6.6	94.5 ± 7.0
Pr	5.81	99.2 ± 5.2	93.5 ± 2.7
Nd	16.33	101.1 ± 0.9	99.4 ± 1.6
Total	38.63	99.6 ± 3.2	95.9 ± 2.5

The decrease in precision in the Series I results, as compared with previous results, has been attributed to instrumental difficulties. In Series II, the low and erratic results are believed to be due to losses in the procedure (probably by incomplete dissolution of the rare earths prior to the electroplating step); the fact that the absolute X-ray intensities were also relatively low substantiates this theory.

An experiment is presently being planned that should pinpoint the source of difficulty. Samples of the individual rare earths will be irradiated in the Juggernaut reactor, and the behavior of each rare earth in various steps of the procedure will be established by assays for ^{140}La (40 hr), ^{143}Ce (33 hr), ^{142}Pr (19 hr), ^{147}Nd (11 days), and ^{160}Tb (72 days). It is expected that, with minor refinements in the procedure, the accuracy of the method can be increased to the desired ±1%.

Analysis of irradiated fuel. The entire procedure was tested on a sample of irradiated UO_2 fuel (13% enriched, ~6.5 at. % burnup) to determine whether any problems, not previously considered, would be encountered in the analysis of an actual fuel sample. The sample had been previously analyzed for total rare earths (TRE) by a complexiometric titration with EDTA (see ANL-7575, p. 178). The concentrations of lanthanum, cerium, praseodymium, and neodymium, as determined by X-ray spectrometric analysis, were compared with the concentrations calculated (on the basis of fission yields of the individual rare earths) from the results of the total rare earth titration analysis. This comparison is given below.

Rare Earth	Concentration (μmol/ml) Calculated from TRE Analysis	Concentration (μmol/ml) Determined by X-ray Analysis
La	0.0842	0.0857
Ce	0.1752	0.1622
Pr	0.0762	0.0805
Nd	0.2706	0.2722
La+Ce+Pr+Nd	0.6062	0.6006

The agreement of these results indicates that the analysis of irradiated fuels presents no unforeseen problems and lends confidence to the potential applicability of the method to burnup analysis.

This sample was also analyzed for uranium, total neodymium, and ^{148}Nd by B. F. Rider of the General Electric Vallecitos Atomic Power Laboratory. The analyses were performed by a mass-spectrometric isotope-dilution (MSID) method. Rider's value for total neodymium, 0.2723 μmol/ml, is in excellent agreement with our X-ray value of 0.2722 μmol/ml.

A comparison was made of the burnup values obtained by the several rare earth methods that have been used to analyze this sample. These data and the fission yields used to calculate the burnups are given

TABLE IV-6. COMPARISON OF BURNUP ANALYSES OF IRRADIATED UO_2 BY SEVERAL METHODS

Rare Earths Determined	Fission Yield (%)	Analytical Method	Burnup (at. %)
Total	49.35	EDTA	6.75
La, Ce, Pr, Nd	45.20	X-ray	6.68
Total Nd	20.52	X-ray	6.61[a]
Total Nd	20.52	MSID[b]	6.65[a]
^{148}Nd	1.70	MSID[b]	6.62

[a] These values were corrected for the ^{144}Ce (285 days) that had not decayed to ^{144}Nd (stable).
[b] MSID = mass-spectrometric isotope-dilution.

in Table IV-6. Good agreement between the several methods is evident.

Neodymium as a burnup monitor. From the data presented above, it can be seen that the data for neodymium show consistently better precision and accuracy than those for the other rare earths or for the combined rare earths. Therefore, the X-ray spectrometric determination of neodymium is also being evaluated as a potential method of measuring burnup (the six isotopes of neodymium produced in the fissioning of ^{239}Pu have a combined yield of about 16%).

An X-ray spectrometric method based on neodymium alone has several advantages. Modifications could be made on the detection system of the X-ray spectrometer that would improve the signal-to-noise ratio by a factor of 5 or more. With this improvement, the sample size and, hence, the level of beta-gamma activity could be reduced significantly. The activity level of the sample could be reduced even further by adding a step to the procedure to remove cerium[28] as cerium (IV), probably by ion exchange in nitrate medium on a column of Dowex-1 and lead dioxide. The only disadvantage in the use of neodymium, rather than the combined rare earths, would be a greater variation in the fission yield as a function of fissioning nuclide.

A study will be made of the separation procedure and the X-ray assay to establish the optimum set of conditions for a burnup determination based upon a neodymium analysis.

[28] The two isotopes ^{141}Ce (32 days) and ^{144}Ce (285 days) are the principal sources of activity in the rare earth mounts.

2. Development of a New Method for the Determination of Fast Fission Yields

(R. J. Popek, R. J. Armani,[29] H. Okashita[30])

In the determination of fission yields, two techniques have been used to establish the number of fissions that have occurred in the irradiated sample. One technique[31] is to irradiate a known amount (about 20 mg) of fissile nuclide to a burnup of 20 to 30 at. % and determine the number of fissions by measuring the change in the actinide-atom content of the sample. The principal disadvantage of this technique is the length of the irradiation, for example 4 to 5 years in EBR-II. The other technique[32] is to irradiate gram amounts of the fissile nuclide to a burnup of 1 to 2 at. %, analyze the irradiated sample for all the fission product nuclides in the heavy mass peak, and sum the number of atoms of these nuclides. The principal disadvantage of this technique is the magnitude and complexity of the analytical effort.

A new technique for determining the number of fissions is under development. This technique is, by comparison, relatively easy to execute and will therefore be much more versatile. It is expected that this technique will provide the means for (1) determining fission yields of selected burnup monitors in the reactor for which burnup measurements are required and (2) determining fission yields as a function of neutron energy. Two irradiations are required: one of about 2-hr duration at a reactor power level of 50 kW and one of about 3-month duration at full reactor power.

Included in the short irradiation are fission-track counters[33] (mica disks alternately stacked with platinum disks on which are mounted nanogram amounts of the fissile material) and fission foils (milligram amounts of the fissile material). These samples provide data for establishing a factor relating the number of fissions that occurred to the count rate of a particular fission product, e.g., ^{144}Ce ($t_{1/2}$, 285 days). The fission tracks on the mica disks are counted under a microscope; the ^{144}Ce activity of the fission foils is determined by gamma spectrometry. Included in the 3-month irradiation are gram amounts of fissile material, which are subsequently analyzed for the fission product whose yield is being determined and for ^{144}Ce activity. The number of fissions that occurred is established from the ^{144}Ce activity and the previously determined fissions-to-^{144}Ce factor. It is expected that the accuracy in determining the number of fissions by

[29] Applied Physics Division.
[30] Resident Associate, Japan Atomic Energy Research Institute.
[31] ANL-7350, p. 94.
[32] F. L. Lisman *et al*, IN-1277, p. 7 (1968).
[33] R. Gold, R. J. Armani, J. H. Roberts, *Nucl. Sci. Eng.* **34**, 13 (1968).

this technique will be comparable with that of the other two techniques, namely, ±1%.

An evaluation of this approach has been made in support of an experiment of the Applied Physics Division in ZPR-3, which had as its primary objective the determination of the capture-to-fission cross-section ratios for ^{233}U, ^{235}U, and ^{239}Pu in a soft neutron spectrum. In this experiment, the length of the short (calibration) irradiation was 80 min, and that of the long irradiation was 5 days. The number of captures per atom of fissile nuclide that occurred in the long irradiation was determined by pre- and post-irradiation mass spectrometry of ^{233}U, ^{235}U, and ^{239}Pu samples of high isotopic purity.[34] The number of fissions per atom of fissile nuclide was determined on separate samples (15-mg foils) which were irradiated with the high-purity samples. Because the irradiation times in this experiment were considerably shorter than those proposed for fission-yield determinations, the activity of ^{140}Ba ($t_{1/2}$, 12.8 days) was used to establish the necessary relationships between the two irradiations.

Included in the short (80-min) calibration irradiation were 15-mg foils of the fissile nuclides (4 of each) and fission-track counters (7 of each). The amount of fissile nuclide on each platinum disk in the fission track counters was determined by alpha counting,[35] the amount of fissile nuclide in each 15-mg foil by weighing, and the ^{140}Ba activity by gamma-ray spectrometry using the 1.59-MeV gamma ray emitted by the ^{140}La ($t_{1/2}$, 40 hr) daughter.

The number of fissions that occurred in a 15-mg foil in the long irradiation is the product of three factors: the number of fissions per atom of fissile nuclide in the short irradiation, the ratio of the ^{140}Ba activities (cpm/mg of fissile material) in the two irradiations, and the number of fissile atoms in the foil. These three factors were determined with accuracies of ±0.6, ±1.4, and ±0.1%, respectively; therefore, the accuracy of determining the number of fissions was ±1.5%.

Obviously, the largest error in determining the number of fissions in the long irradiation resulted from the factors that related the ^{140}Ba activities per milligram of fissile nuclide in the two irradiations. In tests to determine possible sources of error in these measurements, the ^{239}Pu foils from the long irradiation were also analyzed for other short-lived activities, namely, ^{95}Zr, ^{103}Ru, and ^{141}Ce. A comparison with the ^{140}Ba data showed that the foils having the highest and the lowest values of ^{140}Ba per milligram of ^{239}Pu also had the highest and lowest values, respectively, of ^{95}Zr, ^{103}Ru, and ^{141}Ce per milligram of ^{239}Pu. These results demonstrate that the variability in the factor relating the number of fissions in the two irradiations was due to a variation in the neutron flux across the irradiation capsules and not to errors in the measurements. It is believed that with an improved geometric arrangement foils, the error in the relative number of fissions in the of the fission track detectors and the two sets of fission two irradiations can be reduced from ±1.4% to ±0.7%. This improvement would result in an overall accuracy of ±0.9%, which is comparable with that obtainable by other methods.

The feasibility of using this method for the determination of fission yields will be tested by (1) analyzing the 15-mg foils from the long irradiation for several of the radioactive fission products, ^{95}Zr, ^{106}Ru, ^{141}Ce, ^{144}Ce, and ^{137}Cs, (2) calculating the fission yields, and (3) comparing these data with published values.[36]

[34] This work was performed in the Chemistry Division.

[35] The specific alpha activities of the ^{235}U and ^{233}U were increased by the addition of ^{232}U. The small amounts of ^{232}U added had no significant effect on the determination of the number of fissions of ^{235}U or ^{233}U.

[36] F. L. Lisman *et al*, IN-1277, p. 64 (1968).

V

Chemistry of Liquid Metals and Molten Salts[1]

(*A. D. Tevebaugh, J. D. Bingle*)

Experimental and theoretical research efforts on molten metals and salts, which have been in progress for several years, have been directed toward (1) understanding the behavior of liquid sodium as a coolant in nuclear reactors, (2) conducting basic research relating to the development of electrochemical cells with liquid sodium and liquid lithium anodes, and (3) determining the thermodynamic and structural properties of fused salts.

The experimental program has centered around the determination of the thermodynamic properties and phase relationships for lithium- and sodium-containing binary systems and for fused alkali-halide systems by thermal-analysis, emf, solubility, and vapor-liquid equilibrium methods. In addition, measurements have been made of the ultrasonic properties of selected metallic liquids and of some structural and transport properties of fused alkali-halide mixtures. The electrochemistry of lithium/chalcogen cells is being investigated in some detail.

The theoretical program has been devoted to (1) developing a model for predicting gas solubilities in liquid metals, (2) developing an empirical equation which relates the surface tension of a liquid metal at absolute zero to its critical properties, and (3) applying and extending models for predicting phase diagrams of binary and multicomponent metal and salt systems.

Progress in these experimental and theoretical research efforts over the past year is summarized in the following paragraphs.

Much information has been gathered on the nature of binary intermetallic systems of elements having widely differing electronegativities such as lithium (or sodium) and elements of Groups IV-A, V-A, and VI-A. The phase relationships of such systems are not predictable *a priori* and the experimental results have shown considerable complexity. In the lithium-selenium and lithium-sulfur systems, for example, compounds of high stability are found in the lithium-rich regions of the phase diagrams and extended liquid-liquid immiscibility occurs throughout the chalcogen-rich regions. The need for synthesizing and characterizing high-purity single phases in these studies has been met with the development of several new experimental techniques.

A model for predicting gas solubilities in liquid metals has been proposed. This model successfully accounts for the molar excess Gibbs free energies of solution of rare gases (He, Ar, Kr) dissolved in sodium.

The principle of corresponding states, which provides a relationship between the surface tension of a liquid at absolute zero, the critical molar volume, and the critical temperature, was demonstrated not to be in accord with available data on liquid mercury and the alkali metals. A new empirical equation was developed which does relate these properties.

The absorption of sound in liquid gallium was measured as a function of temperature and was found to be anomalous in the temperature regions where curves of its density, viscosity, and surface tension exhibit discontinuities.

Studies of the thermodynamic and structural properties of molten salts by thermal-analysis and spectroscopic methods have continued. A polarization theory has been used for the calculation of phase diagrams essential to the identification of low-melting salt compositions for use in electrochemical devices. This method has greatly reduced the experimental effort needed to obtain phase diagrams. Exploratory studies by Raman spectroscopy into the nature of anion-cation interactions in molten salts have yielded information pertinent to the understanding of transport properties and distribution-coefficient data. Interactions between oxy-anions such as CO_3^{-2} and alkali metal cations appear to be of the contact "ion-pair" type. Much stronger and more covalent interactions exist between divalent cations (such as Mg^{+2} and Cd^{+2}) and halide anions.

Research in electrochemical energy conversion has been primarily in areas related to the investigation of systems that show promise of becoming a family of high-specific-power, high-specific-energy electrochemi-

[1] A summary of this section is given on pages 12 to 14.

cal cells (projected values of 500 W/kg and 300 W-hr/kg). This research is providing an understanding of the thermodynamic, electrochemical, chemical, and physical processes involved in the operation of electrochemical cells with liquid-metal anodes and molten-salt electrolytes. Several of the couples under investigation (e.g., Li/Sn, Na/Bi, Na/Pb) have physical and chemical properties which allow the cell products to be thermally decomposed, separated, and returned to the appropriate electrode compartment by the use of a regenerator, which acts as a single-stage distillation unit. The combination of cell and regenerator thus converts heat to electricity. The electrochemical properties of several new cathodes containing sulfur and mixtures of sulfur and phosphorus have been investigated. Some progress has been made in increasing the electronic conductivities of sulfur and selenium cathodes by the addition of Group V, VI, and VII elements.

Several goal-oriented secondary-battery programs are in progress. Specifically, they are the development of (1) an implantable lithium/selenium battery for powering artificial organs (National Heart and Lung Institute); (2) high-specific-power lithium/selenium batteries for military vehicle applications (U.S. Army, Ft. Belvoir, Va.); and (3) high-specific-power, high-specific-energy, versatile lithium/sulfur batteries for use in family automobiles (National Air Pollution Control Administration).

Various portions of our work on liquid metals and molten salts are discussed further in several recent publications in the open literature.[2-11]

[2] H. Shimotake, E. J. Cairns, "A Lithium/Sulfur Secondary Cell with a Fused-Salt Electrolyte," The Electrochemical Society New York Meeting, May, 1969 Abstr. No. 206; *Extended Abstracts of the Industrial Electrolytic Div.* **5**, 520, May 1969.

[3] E. J. Cairns, H. Shimotake, "High-Temperature Batteries," *Science*, **164**, 1347 (1969).

[4] V. A. Maroni, E. J. Cairns, "Studies of a Li/P_4S_{10} Electrochemical Cell," American Chemical Society, New York Meeting, Sept. 1969; Abstr. No. PHYS-113.

[5] H. Shimotake, A. K. Fischer, E. J. Cairns, "Secondary Cells with Lithium Anodes and Paste Electrolytes," in Proc. 4th Intersociety Energy Conversion Engineering Conference, American Institute of Chemical Engineers, New York (1969), p. 538.

[6] E. J. Cairns, H. Shimotake, A. K. Fischer, "Lithium/Chalcogen Electrochemical Cells for Energy Storage," *Argonne National Laboratory Reviews* **5**(2), 87 (1969).

[7] V. A. Maroni, E. J. Cairns, "Raman Spectra of Fused Carbonates," *J. Chem. Phys.* (in press).

[8] V. A. Maroni, E. J. Hathaway, "Raman Spectra of the $CdCl_2$-KCl System," *Electrochim. Acta* (in press).

[9] R. Sridhar, C. E. Johnson, E. J. Cairns, "Phase Diagrams of the Systems LiI-KI and LiI-RbI," *J. Chem. Eng. Data* **15**, 244 (April 1970).

[10] J. G. Eberhart, "The Surface Tension and Critical Properties of Liquid Metals," *J. of Colloid. and Interface Science* (in press).

[11] J. G. Eberhart, F. A. Cafasso, H. M. Feder, W. Kremsner, "The Grain Boundary Grooving of Iron in Liquid Sodium," *Proc. of the Symp. on Corrosion by Liquid Metals*, the Metallurgical Society, October 13–16, 1969, Philadelphia, Pa., Plenum Press (1970).

A. LIQUID METAL STUDIES (*E. J. Cairns, F. A. Cafasso*)

Research is being directed toward broadening and systematizing knowledge of the liquid metallic state. Experimental and theoretical programs are being undertaken which include (1) determination of the thermodynamic properties, including phase diagrams for binary metallic systems, gas solubilities, and surface tensions; (2) measurement of transport properties, such as electronic conductivities, of sulfur-, selenium-, and tellurium-containing liquids; and (3) measurement of the absorption of sound in liquid gallium as a means of studying its structure.

1. THERMODYNAMICS

a. The Sodium-Bismuth System

(1) Thermal Analysis Studies of Na_3Bi (*E. J. Cairns, S. A. Johnson*)

The preparation of pure compounds from the constituent elements and of mixtures having specific compositions is a necessary procedure in many of our investigations. Both the purity and the freezing point of single phases, which can provide a check on the preparations, can be determined with a high degree of accuracy from time-temperature cooling curves[12] by thermal analysis. To develop synthesis and thermal

[12] W. J. Taylor, F. D. Rossini, *J. Research Nat. Bur. Std.* **32**, 197 (1944).

analysis techniques, the compound Na_3Bi was chosen since both an accurate freezing point and the enthalpy of fusion were needed to complete the thermodynamic studies of the sodium-bismuth system.[13] (The enthalpy of fusion measurements, performed by drop calorimetry, are described in Section III.B.1a of this report.)

The preparation procedure which was developed consisted of loading pure sodium and bismuth, in amounts corresponding to the stoichiometry of Na_3Bi, into a tantalum capsule, and then sealing the evacuated capsule by welding. (The capsule was designed so that it could be used for the preparation of the Na_3Bi, for the thermal analyses, and also for the calorimetric studies, thus minimizing the possibility of contamination.) The sodium and bismuth react to form Na_3Bi during heat-up for the initial cooling curve measurements.

Cooling curves were run both before and after the calorimetric studies to check for any change in the impurity level. The shapes of the cooling curves indicated that the capsule design was appropriate for this use. No change in the impurity level, calculated to be 0.28 mol %, was noted. (Included in the designation "impurity" is any deviation from exact stoichiometry.) The value determined for the freezing point of Na_3Bi was $850.4^{+0.1}_{-0.3}$°C. The calorimetric studies reported in Section III.B.1.a yielded a value for the apparent enthalpy of fusion for Na_3Bi of 7.085 kcal/mol.

(2) The Sodium-Bismuth Phase Diagram (*C. E. Johnson, A. K. Fischer, M. S. Foster, E. J. Cairns*)

The sodium-bismuth system is of interest not only because of its potential application in energy conversion devices, but also because it provides an opportunity for testing a solution theory in liquid metals. A previous report (ANL-7575, p. 165) describes a preliminary attempt to apply the quasi-ideal solution theory to the sodium-bismuth system. A model that incorporates Na, Bi, Na_3Bi, and NaBi as species was used to construct a phase diagram. The phase diagram was divided into the regions Bi-NaBi, NaBi-Na_3Bi, and Na_3Bi-Na. The data used for each region of the phase diagram follow:

$$\text{Bi: } T_m = 271.3°\text{C} \quad \Delta H_m = 2.6 \text{ kcal/mol}$$

$$\text{NaBi: } T_m = 500°\text{C} \quad \Delta H_m = 3.6 \text{ kcal/mol}$$

$$Na_3Bi\text{: } T_m = 848.1°\text{C} \quad \Delta H_m = 11.1 \text{ kcal/mol}$$

Thermal analysis and solubility data were then compared with the calculated solid-liquid equilibrium curve. There was generally poor agreement at the sodium-rich end of the diagram. Since the deviation is consistent with association of sodium, the model was revised to include the dimer, Na_2, and the tetramer, Na_4, in addition to the species already postulated. Multiple regression analysis yielded equilibrium constants of formation for each of the species, as follows:

$$\ln K(Na_2) = 9.0981 + 6795.3/T$$

$$\ln K(Na_4) = 17.296 + 16083.8/T$$

$$\ln K(NaBi) = 10.057 + 30202.4/T$$

$$\ln K(Na_3Bi) = 3.2350 + 11790.9/T$$

The constants were used to recalculate the sodium-bismuth phase diagram which is shown in Fig. V-1. The calculated solid-liquid equilibrium curve agrees well with the experimental data even to the extent of reproducing the concave-upward characteristic in the Na-Na_3Bi region. Agreement in the Na_3Bi-NaBi region is excellent. The somewhat poorer fit for the bismuth-rich region suggests a possible dimeric character for bismuth. (Dimeric bismuth is known to exist in the vapor phase.[14])

As stated above, recent drop-calorimetry experiments have determined the apparent heat of fusion of Na_3Bi to be 7.085 kcal/mol; this value differs considerably from the value of 11.1 kcal/mol, determined from solubility experiments, that was used in the theoretical calculation. When the new calorimetric value is substituted in the calculation of the sodium-bismuth diagram, the agreement between the experimental data and the quasi-ideal solution model based on the previously mentioned species was not as good as that shown in the figure, particularly for the Na_3Bi compound peak. The calculated diagram shows a narrower compositional range for the liquid-solid peak defining the Na_3Bi compound region. Additional work is needed to resolve this difference between the model and the real system.

b. The Lithium-Tin System (*A. K. Fischer, S. A. Johnson*)

The lithium-tin system is one that was proposed for a thermally regenerative galvanic cell system. The bulk of work on this system was reported earlier (see ANL-7575, p. 137).

To conclude experimentation on liquid-vapor equilibria in the lithium-tin system and to allow an approximate temperature-composition phase diagram to be constructed, some additional transpiration experi-

[13] C. E. Johnson, A. K. Fischer, M. S. Foster, E. J. Cairns, "New Measurements for the Sodium-Bismuth Binary System," Abstracts of Papers, 156th Amer. Chem. Soc. Meeting, Atlantic City, Sept. 1968, PHYS-94; also C. E. Johnson, A. K. Fischer, "New Measurements for the Sodium-Bismuth Phase Diagram," *J. Less-Common Metals* **20**, 339 (April 1970).

[14] A. K. Fischer, *J. Chem. Phys.* **45**, 375 (1966).

ments have been carried out at 900°C for a composition of 40 at. % Li-60 at. % Sn. The total vapor pressure (all due to lithium) in the system was found to be 0.15 ± 0.07 Torr at 900°C.

It was reported in ANL-7575 that, for a pressure of 0.41 to 0.42 Torr, the phase diagram of the lithium-tin system should show the liquid-vapor loop tangent or almost tangent to the liquid-solid region. An outline of the shape of the liquid-vapor loop when it is in a nearly tangent position would provide a guide in designing the regenerator for a lithium-tin thermally regenerative galvanic cell. A temperature-composition diagram, shown in Fig. V-2, was constructed for a pressure of 0.705 Torr; this value represents the total vapor pressure at 20 at. % Li-80 at. % Sn (ANL-7575, p. 138) and is near the critical value of 0.41 Torr. Temperatures corresponding to vapor pressures of 0.705 Torr

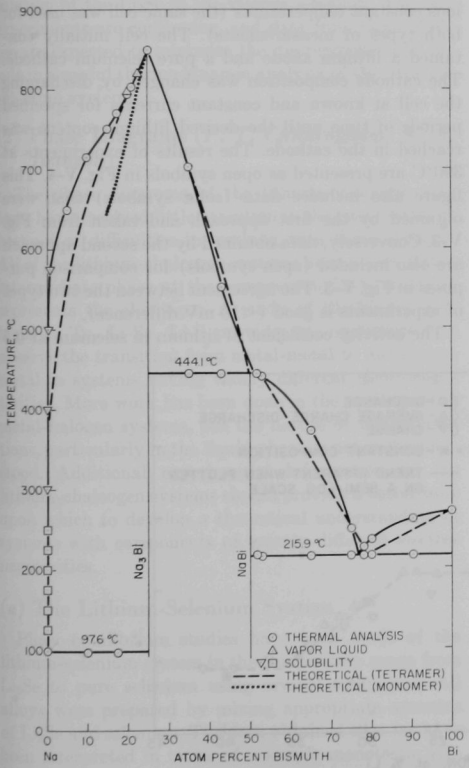

308-1743

FIG. V-1. Solid-Liquid Phase Diagram for the Sodium-Bismuth System.

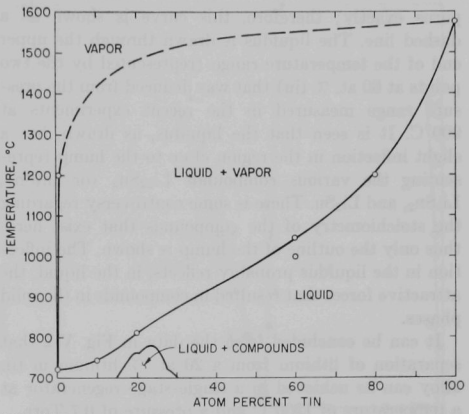

308-2179

FIG. V-2. Temperature-Composition Phase Diagram for the Lithium-Tin System at a Pressure of 0.705 Torr.

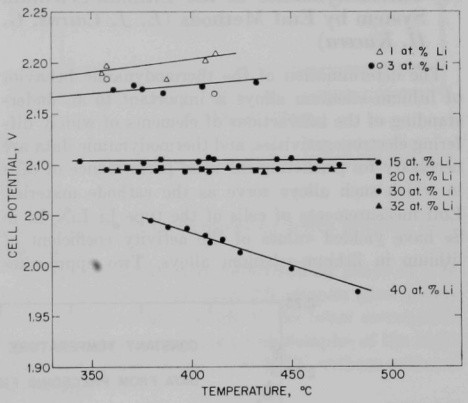

308-2180

FIG. V-3. Emf of the Cell Li(l)/LiF-LiCl-LiI(l)/Li in Se as a Function of Temperature (solid symbols indicate Li-Se alloys made by dissolving solid Li_2Se in selenium; others obtained by the controlled deposition of lithium in selenium).

were obtained from the literature[15, 16] for pure lithium and tin and from our previous data (ANL-7575, p. 140) for compositions of 80 and 90 at. % lithium. No data are available between 1200 and 1577°C (the boiling point of pure tin at 0.705 Torr) to define the va-

[15] T. B. Douglas, L. F. Epstein, J. L. Dever, W. H. Howland, *J. Amer. Chem. Soc.* **77**, 2144 (1955).

[16] R. Hultgren, R. L. Orr, P. D. Anderson, K. K. Kelley, *Selected Values of Thermodynamic Properties of Metals and Alloys*, John Wiley and Sons, New York (1963).

porus exactly; therefore, this curve is shown as a dashed line. The liquidus is drawn through the upper end of the temperature range (represented by the two points at 60 at. % tin) that was deduced from the pressure range measured in the recent experiments at 900°C. It is seen that the liquidus, as drawn, has a slight inflection in the region close to the hump representing the various compounds $Li_{22}Sn_5$ (or Li_4Sn), Li_7Sn_2, and Li_2Sn. There is some controversy regarding the stoichiometry of the compounds that exist here; thus only the outline of the hump is shown. The inflection in the liquidus probably reflects, in the liquid, the attractive forces that resulted in compounds in the solid phases.

It can be concluded from the data in Fig. V-2 that separation of lithium from a 20 at. % lithium in tin alloy can be achieved in a single-stage regenerator at a temperature of 1200°C and a pressure of 0.7 Torr.

c. Lithium-Chalcogen Systems

(1) Thermodynamics of the Lithium-Selenium System by Emf Methods (*E. J. Cairns, G. H. Kucera*)

The determination of the thermodynamic behavior of lithium-selenium alloys is important to an understanding of the interactions of elements of widely differing electronegativities, and thermodynamic data are necessary for predicting the ideal performance of cells in which such alloys serve as the cathode material. Emf measurements of cells of the type Li/LiX/Li in Se have yielded values of the activity coefficient of lithium in lithium-selenium alloys. Two approaches have been employed in performing emf measurements of lithium/selenium cells.

The first approach was the measurement of the emf of the cell Li(l)/LiF-LiCl-LiI(l)/Li in Se as a function of temperature at known and constant compositions of the cathode alloy. The cathode alloys were prepared by dissolving solid Li_2Se in molten selenium to form a mixture of the desired composition. The results of this first set of experiments, shown by solid symbols in Fig. V-3, indicate the following: (1) a single-phase liquid region extending from 0 to perhaps 10 at. % lithium in selenium, (2) a liquid-liquid immiscibility region from below 15 to about 32 at. % lithium, characterized by a constant emf over the indicated range of compositions, and (3) a liquid-solid region above 40 at. % lithium (for the temperature range 360 to 475°C).

The second approach was the measurement of the emf as a function of cathode alloy composition at various constant temperatures (the same cell was used for both types of measurements). The cell initially contained a lithium anode and a pure selenium cathode. The cathode composition was changed by discharging the cell at known and constant currents for specified periods of time until the desired lithium content was reached in the cathode. The results of experiments at 390°C are presented as open symbols in Fig. V-4. This figure also includes data (solid symbols) that were obtained by the first approach and taken from Fig. V-3. Conversely, data obtained by the second approach are also included (open symbols) for comparison purposes in Fig. V-3. The agreement between the two types of experiments is good (<10 mV difference).

The activity coefficient of lithium in selenium at 0.5

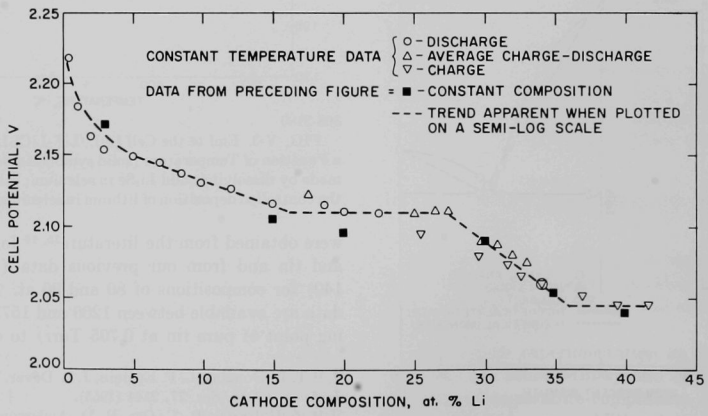

308-2146 Rev. 1

FIG. V-4. Emf of the Cell Li(l)/LiF-LiCl-LiI(l)/Li in Se as a Function of Cathode Composition (temperature = 390°C).

at. % lithium is 3.03×10^{-15} at 390°C, a value that is consistent with the formation of a very stable species in the cathode alloy. The emf plateau in Fig. V-4 that extends from 36 at. % lithium to higher concentrations corresponds to the precipitation of solid Li_2Se from the cathode alloy; this emf corresponds to a free energy of formation of −94.3 kcal/mol for the formation of solid Li_2Se from lithium and selenium in 36 at. % Li in Se at 390°C.

A more complete discussion of the lithium-selenium phase diagram is presented in the following subsection. At present, some discrepanices exist between the emf data and the phase-equilibrium data, particularly in the region of the selenium-rich boundary of the miscibility gap (~10–15 at. % Li from emf studies *vs.* ~2 at. % from phase-equilibrium studies). One possible source of error in the emf experiments by the first approach might be traced to incomplete and/or slow dissolution of the Li_2Se in the viscous selenium. The emf experiments are continuing, and data from these studies are expected to minimize the discrepancies and result in a useful thermodynamic analysis of the lithium-selenium system.

(2) Phase Diagrams (*P. T. Cunningham, S. A. Johnson*)

The phase diagrams of the lithium-chalcogen systems have received little attention in the past, partially because of difficulties in working with these systems. All of the lithium-chalcogen systems have a very stable intermediate phase at the composition Li_2Y, where Y represents the chalcogen. A study of the binary systems Li-Te, Li-Se, Li-S provides an opportunity to observe the transition from metal-metal to metal-nonmetal in systems having widely different electronegativities. More work has been done in the similar alkali metal-halogen systems, but the nature of the interactions, particularly in the liquid phase, is not well understood. Additional experimental information on the lithium-chalcogen systems should provide a better base upon which to develop a theoretical understanding of systems with components of greatly different electronegativities.

(a) The Lithium-Selenium System

Phase-equilibrium studies have been made of the lithium-selenium system in the composition range from Li_2Se to pure selenium using several techniques. All alloys were prepared by mixing appropriate amounts of Li_2Se and selenium. The data obtained thus far have been interpreted in terms of a simple monotectic system. The tentative phase diagram is shown in Fig. V-5; the figure also indicates the methods of analysis (thermal, chemical, or microscopic) by which the data were obtained.

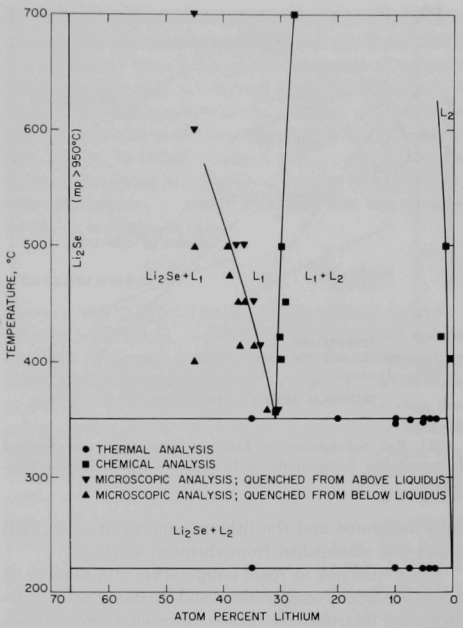

308-2181

FIG. V-5. Partial Phase Diagram for the Lithium-Selenium System.

Thermal analyses were performed on alloys of 3 to 55 at. % lithium in selenium. All samples gave arrests in the vicinity of 350 and 220°C, the latter corresponding to the selenium melting point. Samples of the Li_2Se phase were heated in quartz to 950°C without evidence of melting.

Microscopic analyses of alloys containing 32 to 45 at. % lithium which were quenched from several temperatures in the range 390 to 700°C have been used to place limits on the position of the upper liquidus in the proposed monotectic system. Although attack of polished surfaces by atmospheric moisture created some problems, the interpretation of the microscopic structure—that is, the determination of whether an alloy was quenched from above or below the liquidus—was not seriously impaired.

To set limits on the extent of the miscibility gap, alloys of 15 and 26 at. % lithium were quenched from various temperatures above the monotectic temperature. In each experiment, the two phases were physi-

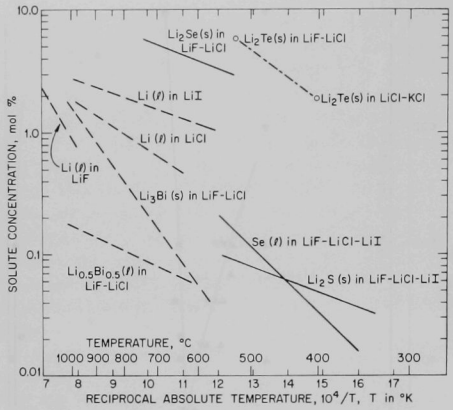

308-2182

FIG. V-6. Solubilities of Lithium, Selenium, and Several Intermetallic Compounds of Lithium in Alkali-Halide Mixtures.

cally separated and the lithium concentration in each phase was established from chemical analyses.

X-ray analyses at room temperature of a number of alloys of various compositions and thermal histories indicate no intermediate phases between Li_2Se and selenium.

The results of all the analyses, shown in Fig. V-5, indicate that the system has a monotectic temperature of 350°C and a monotectic composition of 32 at. % lithium. The miscibility gap extends to about 1.5 at. % lithium; no eutectic structure near pure selenium could be detected. The composition range from Li_2Se to pure lithium was not studied.

(b) The Lithium-Sulfur System

Only preliminary thermal analysis data have been obstained for the lithium-sulfur system. Samples of Li_2S were heated to 1025°C in an alumina crucible without evidence of melting. Thermal arrests at ~355°C were observed in the composition range 5 to 15 at. % lithium in sulfur, and X-ray analyses indicated no intermediate phases other than Li_2S. Pearson and Robinson[17] observed temperature arrests around 360°C for compositions in the region of 50-57 at. % lithium. This agreement in the thermal analysis data, together with the appearance of some quenched samples, suggests that the lithium-sulfur system may have a simple monotectic similar to that proposed for the lithium-selenium system.

[17] T. G. Pearson, P. L. Robinson, *J. Chem. Soc.* **1931**, 413.

d. Solubilities of Li_2S, Li_2Se and Selenium in Fused Lithium Halides (*V. A. Maroni, E. J. Hathaway*)

The solubilities of Li_2S, Li_2Se, and selenium in molten lithium halides have been measured at various temperatures. The metal or intermetallic compound was equilibrated at each temperature with the selected lithium halide salt, and filtered samples were taken. (The experimental apparatus provided a uniform temperature zone throughout the molten salt.) The solubilities of Li_2S, Li_2Se, and selenium, determined from chemical analysis of the samples, are given in Fig. V-6. Also included in the figure, for comparison, are (1) previously determined solubilities (ANL-7316, p. 119) for Li_2Te and two lithium-bismuth compounds and (2) the solubility of lithium from the data of Dworkin, Bronstein and Bredig.[18] Extrapolation of the results for Li_2Se, Li_2S, selenium, and lithium in molten lithium halides indicates that their solubilities are significantly lower in the temperature range below 400°C.

The solubility of selenium in molten LiF-LiCl was unexpectedly low ($<10^{-4}$ mol % at 500°C) compared with the solubilities for selenium in LiF-LiCl-LiI. Solubility measurements reported[19] for Na_3Bi in NaI and in NaCl-NaI indicate that the solubility of Na_3Bi at a given temperature increases with increasing concentration of NaI. It appears that the presence of iodide may increase the solubility or the heat of solution of some metals and intermetallic compounds in alkali-halide melts.

e. Theoretical Studies: Gas Solubility in Liquid Metals (*H. Schnyders, H. M. Feder*)

To begin to understand the complex corrosion phenomena associated with the use of sodium as a coolant in fast breeder reactors, its fundamental behavior as a solvent must be studied in detail. In turn, to unravel the interrelated factors involved in sodium's role as a solvent, it is desirable to begin with a study of the most simple solutes, namely, the noble gases. By so doing, the contributions to the work required for the insertion of a single atom of a neutral solute species into a liquid metal can be conceptualized and can be separated from the additional contributions to the work of solution that arise with more complex solutes. As a start, a simple model describing the thermodynamics of solution of noble gases in liquid sodium will be presented and compared with experimental results.

In this model, the excess free energy of formation of

[18] A. S. Dworkin, H. R. Bronstein, M. A. Bredig, *J. Phys. Chem.* **66**, 572 (1962).

[19] M. Okada, R. A. Guidotte, J. V. Corbett, *Inorg. Chem.* **7**, 2118 (1968).

a dilute solution is set equal to the difference of two terms: the electronic work done on the solvent in creating within it a cavity (or bubble) of appropriate size to accommodate the solute atom, less the attractive work done by the solute atom when on insertion into this cavity it polarizes the surrounding solvent atoms. The electronic work, being by far the larger term, will be given primary attention; for its calculation the work of Fumi[20] (on the formation energy of vacancies in solid metals) provides an excellent basis. Consider a monovalent metal to be a spatially uniform, immobile distribution of positive charge corresponding to N positive ions, neutralized by N free, mobile valence electrons, all contained in a spherical volume V.[21] (This is the well-known "jellium" model.) Now, remove from the center a small spherical volume, δV, of positive charge and distribute it uniformly over the surface of the sphere, leaving a cavity. Two effects occur. First, the excess negative charge in the cavity ($= \delta V/\Omega$, where Ω, the atomic volume, is V/N) repels, by a screened Coulombic potential, all the electrons in the conduction band and increases their potential energy. The amount of work done is equal to two-thirds the maximum kinetic or Fermi energy, E_f, per electron times the excess negative charge in the cavity:[22]

$$W_{\text{rep}} = \tfrac{2}{3}\, E_f \frac{\delta V}{\Omega} \tag{1}$$

Secondly, the expansion of the sphere reduces the average kinetic energy per electron of the valence electrons. For free electrons $\bar{E}_{\text{kin}} = 3/5\, E_f$, and since E_f varies as $V^{-2/3}$, $\delta E_f/E_f = -2/3(\delta V/V)$. Hence

$$\begin{aligned} W_{\text{kin}} &= \Delta\bar{E}_{\text{kin}} = \tfrac{3}{5}\, N\delta E_f \\ &= \tfrac{3}{5}\, N\left(-\tfrac{2}{3}\frac{\delta V}{V}\, E_f\right) \\ &= -\tfrac{2}{5}\, E_f \frac{\delta V}{\Omega} \end{aligned} \tag{2}$$

So in total,

$$W_{\text{cav}} = \tfrac{2}{3}\, E_f \frac{\delta V}{\Omega} - \tfrac{2}{5}\, E_f \frac{\delta V}{\Omega} = \tfrac{4}{15}\, E_f \frac{\delta V}{\Omega} \tag{3}$$

The Fumi model for the work of formation of a cavity in a monovalent metal has been shown[23] to be valid for solid metals by comparing W_{cav} to known vacancy formation energies. The result appears to be good to within ten percent provided allowance is made for the fact that in solid metals the lattice can relax in the neighborhood of the vacancy. Since the Fumi model is a reasonable description of the energetics of vacancy formation and does not depend on lattice structure, it may be directly applied to the problem of creating a cavity in a liquid metal to accommodate a solute molecule. In fact, to obtain a value for W_{cav}, one only needs a model describing the fractional volume change, $\delta V/\Omega$, upon introducing a solute molecule. For the present model, it is proposed that

$$\delta V/\Omega = 1 + \frac{\pi}{6}\frac{\sigma^3}{\Omega} - \eta \tag{4}$$

where η, the packing fraction of the solvent, is equivalent to $(\pi/6)(a^3/\Omega)$, a being the effective hard-sphere diameter of the solvent atoms, and σ the corresponding hard-sphere diameter of the solute atoms. The rationale of Eq. 4 is that the increase in volume on moving one solvent atom out to the surface is not just an atomic volume, but the atomic volume plus the increment due to the difference in hard-sphere volumes between the solute and solvent atoms. The validity of hard-sphere theory in this connection is supported by the correct prediction of the location and height of the first peaks in the experimental liquid structure factors $a(K)$ for both metals[24] and noble gases. These peaks are matched very well by the calculated $a(K)$ for fluids of hard spheres of appropriate diameters and number densities. Insertion of Eq. 4 into Eq. 3 gives

$$W_{\text{cav}} = \tfrac{4}{15}\, E_f\left(1 + \frac{\pi}{6}\frac{\sigma^3}{\Omega} - \eta\right) \tag{5}$$

If the Gibbs free energy of solution is considered to be very well approximated by the Helmholtz free energy of solution, then the excess molar Gibbs free energy of solution of the dissolved noble gas relative to its molar Gibbs free energy as an ideal gas at the same temperature is given by

$$\Delta G^{\text{xs}} = -Nk_BT \ln \lambda = NW_{\text{cav}} - NW_{\text{attr}} \tag{6}$$

where k_B is Boltzmann's constant, T the absolute temperature, λ the Ostwald solubility coefficient,[25] and W_{attr} the work of attraction by the solvent per atom of solute.

To evaluate Eq. 6, values for η and σ must be derived from appropriate experimental data. Values of η at various temperatures were conveniently obtained from the well-known thermodynamic limit ($K \to 0$) for the liquid structure factor and the limiting expression for $a(K)$ of a fluid of hard spheres,[24, 26] i.e.,

[20] F. G. Fumi, Phil. Mag. **46**, 1007 (1955).

[21] Atomic units are used throughout this discussion.

[22] N. H. March, *Liquid Metals*, Pergamon Press, London, p. 51 (1968).

[23] K. Mukherjee, *Trans. Met. Soc. AIME* **236**, 1324 (1966).

[24] N. W. Ashcroft, J. Lekner, *Phys. Rev.* **145**, 83 (1966).

[25] The Ostwald solubility coefficient is defined as the volume of dissolved gas per unit volume of solvent.

[26] M. S. Wertheim, *Phys. Rev. Lett.* **10**, 321 (1963).

TABLE V-1. MOLAR EXCESS GIBBS FREE ENERGIES OF SOLUTION OF NOBLE GASES DISSOLVED IN LIQUID SODIUM AT 400°C

Gas	ΔG^{xs}(exptl)[a]	NW_{cav}(calcd)[a]
He	12.5 ± 0.1[b]	14.6
Ar	17.1 ± 0.3[c]	19.2
Kr	19.1[d]	20.7

[a] In kcal/mol.
[b] E. Veleckis, ANL, private communication.
[c] E. Veleckis, R. Blomquist, R. Yonco, M. Perin, ANL-7325, p. 128.
[d] S. K. Dhar, ANL-6900, p. 125.

TABLE V-2. TEST OF THE PRINCIPLE OF CORRESPONDING STATES[a]

Metal	γ_o (erg/cm^2)	V_c (cm^3/mol)	T_c (°K)	$\gamma_o V_c^{2/3}/T_c$ [erg/(°K) (mol$^{2/3}$)]
Hg	545[31]	43[34, 35]	1763[33]	3.79
Li	470[32]	66[36]	3223[36]	2.38
Na	220[32]	116[36]	2573[36]	2.03
K	125[32]	209[36]	2223[36]	1.98
Rb	95[32]	247[36]	2093[36]	1.79
Cs	80[32]	311[36]	2057[36]	1.79

[a] Superior numbers in parentheses indicate references that were sources of data.

$$a(0) = \rho k_B T \chi_T = (1 - \eta)^4/(1 + 2\eta)^2 \qquad (7)$$

where χ_T is the isothermal compressibility of the solvent and ρ its number density. The length parameter in the Lennard-Jones 6–12 potential, which has been used to fit second virial coefficient data for the noble gases,[27] was chosen as the value for σ. This particular choice is justified because the location and height of the first peak in $a(K)$ for a fluid of hard spheres of this constant diameter matches that for liquid krypton at several intervals in the temperature range 117–183°K.[28]

Calculated values of NW_{cav} for helium, argon, or krypton dissolved in sodium are compared with experimental data for ΔG^{xs} in Table V-1. The errors assigned to the experimental data for helium and argon are our estimates; however, because of the possibility of systematic error in the krypton data, error limits were not assigned. The agreement between the experimental and calculated values is quite good with respect to sign, sequence, and magnitude. The results of similar calculations made for 300 and 500°C (not shown) indicate that the temperature dependence of ΔG^{xs} given by the NW_{cav} term is, at least, qualitatively in agreement with experiment. The overall agreement is particularly gratifying since previous theoretical models that ignored the specifically metallic nature of the solvent, e.g., the Hildebrand solubility parameter, failed to give even order-of-magnitude agreement for λ. Furthermore, the nature of the agreement encourages us to calculate Ostwald coefficients for xenon prior to actual measurement because of xenon's importance in nuclear reactor technology. The coefficients at 300, 400, and 500°C are 8.1×10^{-10}, 2.5×10^{-8}, and 3.3×10^{-7}, respectively, when the values calculated for NW_{cav} are decreased by 2 kcal/mol. This correction was made to compensate for the apparent systematic overestimate of ΔG^{xs} by this amount.

It is premature to conclude that the excess of NW_{cav}(calcd) over ΔG^{xs}(exptl) is, in fact, indicative of a term NW_{attr} of the order of 2 kcal/mol. NW_{attr} is difficult to calculate from simple principles. In addition, more detailed consideration must be given to the value 4/15 in Eqs. 3 and 5. However, the success of this simple model justifies refinements which could lead to better agreement with experiment for the monovalent metals, and which are considered essential to the extension of the model to polyvalent metals. The density of states for conduction electrons in metals is nonparabolic in the wave vector **k** as a result of the interaction of the electrons with locally attractive ionic potentials. Therefore, the valence electrons are not completely free in the metal, and their average kinetic energy relative to the bottom of the conduction band may be different from the free electron value of 3/5 E_f. Furthermore, the contribution of 2/3 E_f to Eqs. 1 and 3, arising from the screened repulsive interaction between the conduction electrons and the excess electronic charge in the cavity, is known to be correct to first order in perturbation theory, but higher order terms may be significant. Some or all of these approximations may not be valid for polyvalent metals, and this is being investigated.

f. The Surface Tension and Critical Properties of Liquid Metals (*J. G. Eberhart*)

In 1945, Guggenheim[29] applied the principle of corresponding states to the surface tension of liquids and obtained the relation:

$$\gamma_o V_c^{2/3} = KT_c \qquad (8)$$

where γ_o is surface tension extrapolated to absolute zero, V_c is the critical molar volume, T_c is the critical temperature, and K is a universal constant. By analysis of surface tension and critical property data, Gug-

[27] J. O. Hirschfelder, C. F. Curtiss, R. Bird, *Molecular Theory of Gases and Liquids*, Ch. 3, John Wiley and Sons, New York (1954).

[28] G. T. Clayton, LeRoy Heaton, *Phys. Rev.* **121**, 649 (1961).

genheim[29, 30] obtained 4.3 erg/(°K)(mol$^{2/3}$) as the value of K.

Surface tension and critical-property data have since become available for mercury and the alkali metals.[31-36] These are shown in Table V-2 together with the values for $\gamma_o V_c^{2/3}/T_c$ calculated according to Eq. 8. Clearly $\gamma_o V_c^{2/3}/T_c$ is not a constant for these liquid metals and has a value consistently smaller than that for the simple liquids. Thus, Eq. 8 is not valid for liquid metals, i.e., the surface tension of liquid metals does not follow the principle of corresponding states.

Because Eq. 8 cannot be applied to liquid metals, a new empirical relationship between γ_o, V_c, and T_c was sought. The equation

$$\gamma_o(V_c - B)^{2/3} = AT_c \tag{9}$$

where A and B are constants, was found to accurately relate these three properties. The equation may be rewritten

$$(T_c/\gamma_o)^{3/2} = A^{-3/2}(V_c - B) \tag{10}$$

Its validity for mercury and the alkali metals is evident in Fig. V-7 by the linearity of a plot of $(T_c/\gamma_o)^{3/2}$ versus V_c for the data in Table V-2. From the intercept of the line on the V_c-axis, the constant B is 31 cm^3/mol; from the slope of the line, the constant A is 1.67 erg/(°K)(mol$^{2/3}$). Both constants were derived by least-squares analysis. The dashed line in Fig. V-7 is for simple liquids that follow the principle of corresponding states. Equations 8 and 9 differ in that K is about 2.5 times larger than A, and $B = 0$ for simple liquids.

The critical volumes and temperatures of other liquid metals can be estimated from Eq. 9 and the law of the rectilinear diameter,[29] as follows. The value of γ_o, obtained by extrapolating the surface tension of the liquid metal to absolute zero, is inserted into Eq. 9 together with the values for the constants A and B. This fixes one relationship between T_c and the critical density $\rho_c = M/V_c$, where M is the molar mass. A second relationship between T_c and ρ_c is given by the law of the rectilinear diameter, which states that the average density of the liquid and vapor phases, $\bar{\rho} = (\rho_L + \rho_V)/2$,

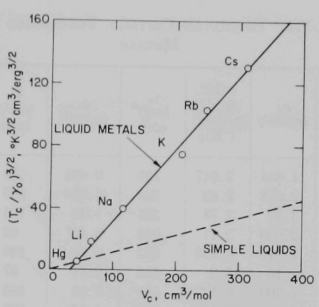

308-2183

FIG. V-7. $(T_c/\gamma_o)^{3/2}$ *vs.* V_c for Liquid Metals (included for comparison is a similar plot for simple liquids that follow the principle of corresponding states).

is a linear function of temperature and passes through the critical point (T_c, ρ_c). The latter relationship can be established from accurate low-temperature liquid density data, since at low temperatures $\bar{\rho} \approx \rho_L/2$, and it can be extrapolated reliably to higher temperatures because of its linearity. If the two relationships are constructed on a density *vs.* temperature plot, then ρ_c and T_c can be found from their intersection. This is illustrated in Fig. V-8 with data for liquid iron; the two curves intersect at $T_c = 6500$°K and $\rho_c = 1.42$ g/cm^3, giving $V_c = 39$ cm^3/mol.

This technique of solving two simultaneous equations in the critical properties was used to estimate ρ_c, V_c, and T_c for a variety of liquid metals whose densities and surface tensions as functions of temperature are known. The results are shown in Table V-3.

It is important that these estimates be put into

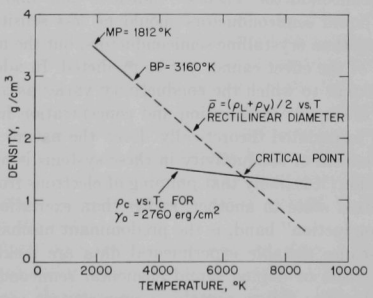

308-2184

FIG. V-8. Graphical Estimation of the Critical Density and Temperature for Liquid Iron from the Law of the Rectilinear Diameter and the Relationship between Surface Tension and Critical Properties for Liquid Metals.

[29] E. A. Guggenheim, *J. Chem. Phys.* **13**, 253 (1945).
[30] E. A. Guggenheim, *Proc. Phys. Soc.* **85**, 811 (1965).
[31] G. M. Zeising, *Aust. J. Phys.* **6**, 86 (1953).
[32] J. Bohdansky, H. E. J. Schins, *J. Inorg. Nucl. Chem.* **29**, 2173 (1967).
[33] E. U. Franck, F. Hensel, *Phys. Rev.* **147**, 109 (1966).
[34] J. Bender, *Ann. Phys. (Leipzig)* **16**, 246 (1915); **19**, 410 (1918).
[35] A. V. Grosse, *J. Inorg. Nucl. Chem.* **22**, 23 (1961).
[36] I. G. Dillon, P. A. Nelson, B. S. Swanson, *J. Chem. Phys.* **44**, 4229 (1966).

TABLE V-3. ESTIMATED CRITICAL PROPERTIES OF LIQUID METALS

Metal	ρ_o (g/cm³)	-10^4 $d\rho/dT$ [g/(cm³) (°K)]	γ_o (erg/cm²)	ρ_c (g/cm³)	V_c (cm³/mol)	T_c (°K)
Mg	1.834	2.647	721	0.438	56	3600
Sr	2.648	2.62	392	0.850	103	4000
Ba	3.59	2.74	351	1.36	101	3600
Al	2.659	3.11	996	0.427	63	6000
In	7.315	6.798	602	0.77	149	8600
Tl	12.15	15.2	536	2.11	97	5200
Sn	7.309	6.127	581	0.65	183	9900
Pb	11.469	13.174	538	1.94	107	5800
Bi	10.665	11.820	423	1.18	177	7000
Fe	8.618	8.83	2758	1.42	39	6500
Ni	9.908	11.589	2348	1.38	42	6100
Cu	9.007	4.003	1629	1.10	58	8600
Ag	10.465	9.067	1139	1.83	59	6200
U	19.356	10.328	1747	3.30	72	12400

proper perspective with respect to historical developments in this area and to their probable reliability. Until recent years, mercury was the only metal whose critical properties were known. Estimates[37] of the critical properties of other metals had been based on data for mercury and the principle of corresponding states. However, measurement of the critical properties of the alkali metals[36] showed that the liquid and vapor densities and the heats of vaporization of these metals were not related as predicted by the principle of corresponding states. Moreover, the present work extends this conclusion to the surface tension as well. Hence, application of the principle to estimation of critical properties is of dubious validity. The technique of estimation presented here is based not only on data for mercury but on data for all metals whose critical properties are known at this time. This is probably an improvement over corresponding-state methods, but there is no assurance that other liquid metals will have γ_o, V_c, and T_c values accurately related by Eq. 9. Thus the validity of this relationship should be reassessed as future measurements of the critical properties of metals are made. In the meantime, the approach outlined here provides critical-property estimates of sufficient reliability for many scientific and engineering purposes.

[37] A. V. Grosse, *J. Inorg. Nucl. Chem.* **22,** 23 (1961).

2. Transport Properties: Electronic Conductivity of Selenium- and Sulfur-Containing Cathode Alloys (*R. Sridhar, C. A. Trapp, L. W. Mishler, E. J. Cairns*)

Extensive data have been published on the electronic conductivity of solid (crystalline) elemental semiconductors and the effects of temperature and dopants on conductivity; however, little information is available on the electronic conductivity of liquid elemental semiconductors and the effects on conductivity of temperature, dopant composition, and dopant concentration in the semiconductor. Theory[38] indicates that amorphous and liquid semiconductors should be less sensitive to doping than crystalline semiconductors, but the magnitude of the effect cannot yet be predicted. In addition, the extent to which the conductivity varies as a function of dopant composition and concentration has not been formulated theoretically. Even the nature of the mechanism of conductivity in these systems is open to question; it is likely that jumping of electrons from one localized state to another, rather than excitation into a "conduction" band, is the predominant mechanism.

Because suitable experimental data are lacking on the effects of doping liquid elemental semiconductors and because future portable power sources may rely heavily on liquid semiconducting elements as cathode materials, the effects of doping on liquid selenium and sulfur are being studied.

[38] A. I. Gerbanov, *Quantum Electron Theory of Amorphous Conductors*, Consultants Bureau, New York (1965).

a. Selenium

The conductivities of liquid selenium and selenium-tellurium alloys containing up to 26 at. % tellurium have been measured. The conductivity cell consisted of a pair of spectrographic graphite rods sealed in quartz tubes. The tubes were fused parallel to one another and mounted on a micrometer-controlled stand to provide a constant interelectrode distance and a measurable immersion depth. For an immersion depth of 1.27 cm, a cell constant of 0.3150 cm^{-1} at 25°C was measured by means of standard KCl solutions. Conductivities were measured with an impedance bridge (Electro Scientific Industries, Model 290A) at an ac frequency of 1 kc; measurements were carried out in the temperature range 300 to 400°C in a high-purity helium atmosphere. The selenium and tellurium were obtained from American Smelting and Refining Company and were specified as 99.999% pure.

In Fig. V-9, our data for the conductivity of pure selenium as a function of temperature are compared with those of other workers.[39-43] Our results are in ex-

[39] H. W. Henkels, *J. Appl. Phys.* **21,** 725 (1950).
[40] H. W. Henkels, J. Maczuk, *J. Appl. Phys.* **24,** 1056 (1953).
[41] B. Lizell, *J. Chem. Phys.* **20,** 672 (152).
[42] E. H. Baker, *J. Chem. Soc.* **A1968,** 1089.
[43] O. Watanabe, S. Tamaki, *Electrochim. Acta* **13,** 11 (1968).

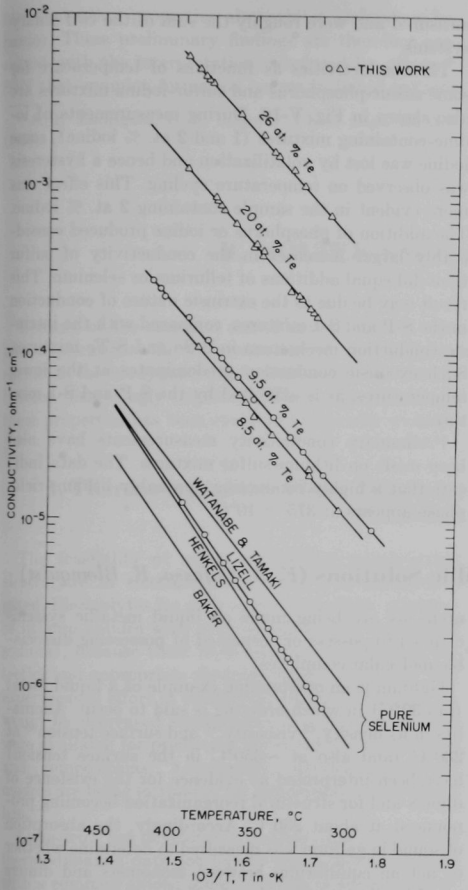

308-2185

FIG. V-9. Conductivity of Selenium and Selenium-Tellurium Alloys as a Function of Temperature.

cellent agreement with those of Henkels[39, 40] and Lizell,[41] whereas the values of Baker[42] and Watanabe and Tamaki[43] are lower and higher, respectively.

The conductivities of several selenium-tellurium alloys are also given as a function of temperature in Fig. V-9. These results were extrapolated to 500°C (assuming a constant activation energy for conduction in the range of 300 to 500°C), and compared with those of other workers.[44, 45] The extrapolated values from the

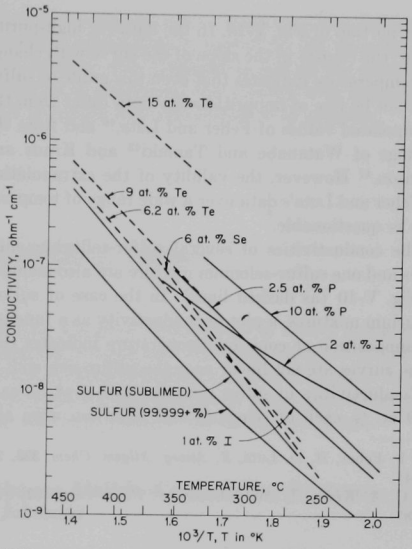

308-2186

FIG. V-10. Conductivity of Sulfur and Sulfur-Containing Mixtures as a Function of Temperature (mixtures made with sublimed sulfur except for 2% I mixture).

present study were in very good agreement with the data of Perron,[44] who studied the conductivities at the tellurium-rich concentrations.

b. Sulfur

The conductivities of liquid sulfur and sulfur-rich mixtures have been determined as a function of temperature and composition. Measurements were made with a Jones electrolytic bridge (Leeds and Northrup Co.) operated at an ac frequency of 1 kc. Most of the measurements were made in the temperature range 220 to 420°C. Experimental accuracies of the conductivity measurements were limited because of the high volatility of liquid sulfur; the error limits were estimated to be approximately ±10% at temperatures above 260°C and ±50% at temperatures below 260°C. (The larger error limits associated with the measurements below 260°C resulted from the use of a shunt in parallel with the cell.)

Conductivities were measured for two different grades of sulfur, namely, sublimed sulfur (N.F.) supplied by Mallinckrodt Chemical Works (no purity specification available) and sulfur of 99.999+% purity obtained from American Smelting and Refining Company. The results for both materials are given in the

[44] J. C. Perron, *Advan. Phys.* **16**, 657 (1967).

[45] A. I. Blum, A. R. Regel, *Zh. Tekhn. Fiz.* **23**(6), 964 (1953); data taken from D. M. Chizhikov and V. P. Schastlivyi, *Selenium and Selenides*, p. 362, Collett Publishers, London (1968).

lower portion of Fig. V-10. In the data for high-purity sulfur, the change in the slope of the curve with changing temperature indicates that even this grade of sulfur may not be free of impurities. Our data differ from the extrapolated values of Feher and Lutz,[46] and from the findings of Watanabe and Tamaki[43] and Kraus and Johnson.[47] However, the validity of the extrapolation of Feher and Lutz's data over a wide range of temperature is questionable.

The conductivities of several sulfur-tellurium mixtures and one sulfur-selenium mixture are also included in Fig. V-10 (as dashed lines). In the case of sulfur-tellurium mixtures, a plot of conductivity as a function of composition at constant temperature indicates that these curves are not linear near the sulfur-rich end.

Conductivities of sulfur mixtures with 5 at. % each or 9 at. % each of selenium and tellurium were also measured and were roughly the sum of the two binary systems.

The conductivities as functions of temperature for some sulfur-phosphorus and sulfur-iodine mixtures are also shown in Fig. V-10. During measurements of iodine-containing mixtures (1 and 2 at. % iodine), some iodine was lost by volatilization and hence a hysteresis was observed on temperature cycling. This effect was more evident in the sample containing 2 at. % iodine. The addition of phosphorus or iodine produced considerably larger increases in the conductivity of sulfur than did equal additions of tellurium or selenium. This result may be due to the extrinsic nature of conduction in the S-P and S-I mixtures, compared with the intrinsic conduction mechanism in S-Se and S-Te mixtures. Such extrinsic conduction predominates at the lower temperatures, as is exhibited by the S-P and S-I mixtures.

Preliminary conductivity measurements have also been made on lithium-sulfur mixtures. The data indicate that a highly conducting (probably lithium-rich) phase appears at 375 ± 10°C.

[46] F. Feher, H. D. Lutz, *Z. Anorg. Allgem. Chem.* **333**, 216 (1964).

[47] C. A. Kraus, E. W. Johnson, *J. Phys. Chem.* **32**, 1281 (1928).

3. Ultrasonic Measurements in Liquid Metallic Solutions (*F. A. Cafasso, R. Blomquist*)

Ultrasonic relaxation (absorption) spectrometry has proven to be a valuable tool for detecting and studying complex formation in nonmetallic systems. By virtue of its general sensitivity to the rate of transfer of energy between molecules in equilibrium, i.e., to structural relaxation processes in general, this tool may be expected to be sensitive to and thus enable detection of molecular ordering in liquid metals as well. To evaluate its potential in this connection, absorption measurements are being made on liquid metallic systems claimed to possess or suspected of possessing dissociable molecular complexes.

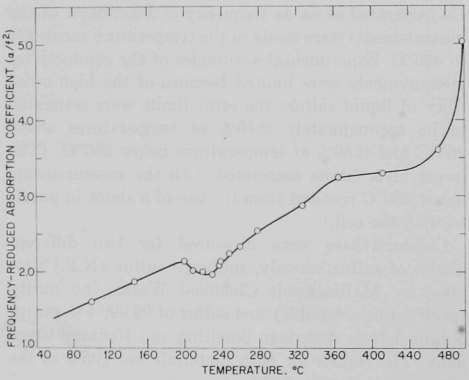

308-2187

FIG. V-11. Frequency-Reduced Absorption Coefficient (α/f^2) of Gallium versus Temperature (135 MHz).

Gallium is an outstanding example of a liquid metal (mp 30°C) in which ordering is said to occur. Anomalies in its density,[48] viscosity,[49] and surface tension[50] at 230°C (and also at ~350°C in the surface tension) have been interpreted as evidence for the existence of dimers and for structural reorganization becoming pronounced at about 230°C. Accordingly, the absorption of sound in gallium was measured to determine whether or not an equilibrium between monomers and dimers could be discerned by the absorption spectrum.

Measurements were made at 135 MHz between 100 and 500°C by the pulse-echo method,[51] the measurements alternating between high and low temperatures. The variation of the frequency-reduced absorption coefficient (α/f^2) with temperature is shown in Fig. V-11. A distinct anomaly at about 200°C, an apparent anomaly around 360°C, and a sharp increase in absorption from 400 to 500°C are the notable features of this curve. Of particular significance is the fact that the first two anomalies appear at about the same tempera-

[48] A. S. Bassin, A. H. Solov'ev, *Zh. Prikl. Mekh. Tekh. Fiz.* **6**, 83 (1967) [ANL Trans-677].

[49] G. I. Goryaga, M. F. Morgovova, *Nauch. Dokl. Vyoshei Shkoly, Fiz.-Mat. Nauk* **1**, (1958).

[50] O. A. Timofeevicheva, P. P. Pugacheivich, *Dokl. Akad. Nauk SSSR* **134**, (1960).

[51] ANL-7225, p. 159; ANL-7325, p. 131.

ture that other properties also exhibit anomalous behavior. These preliminary findings are therefore consistent with the interpretation, advanced by others,[48, 50, 52] that complex formation occurs in liquid gallium. Before this conclusion can be considered firm, however, supporting information is needed on the variation of sound velocity with temperature and on the variation of both sound absorption and velocity with frequency. Work to obtain this information is in progress.

[52] S. E. Rodriguez, C. J. Pings, *J. Chem. Phys.* **42**, 2435 (1965).

B. MOLTEN SALT STUDIES (*E. J. Cairns*)

Because of the extensive use of molten salts in various applications, the understanding of their physicochemical, thermodynamic, and structural properties has become increasingly important. The program to study these properties has been concerned primarily with determining the phase relationships of binary and multicomponent systems and with elucidating the structure of these systems. Attention has also been given to the characterization and analysis of paste electrolytes and filler materials (used in the battery program).

1. Thermodynamics: Phase Diagrams of Lithium Halide-Containing Systems (*R. Sridhar, C. E. Johnson*)

The feasibility of using low-melting mixed-cation electrolytes in electrochemical cells is being investigated. Electrolytes for such cells would utilize mixtures of lithium halides with other alkali halides (excluding sodium), because these have suitably low-melting eutectics and appropriate thermodynamic stabilities. The experimental effort in identifying suitable salt systems would be decreased significantly if a general method were available for predicting the eutectic temperatures and compositions. Accordingly, several theoretical models are being evaluated for application to this problem.

Lumsden[53] has developed a method of estimating the thermodynamic data for binary alkali halide systems with a common anion; these data can be used to calculate the requisite binary phase diagrams. (The technique is complementary to that presented in ANL-7575, p. 142.) Using a regular solution model, Lumsden expressed the liquidus temperature of component i as

$$T_i = \frac{KN_j + \Delta H_{mi}}{\Delta S_{mi} - R \ln N_i} \qquad (11)$$

where ΔH_{mi} and ΔS_{mi} are the heat and entropy of fusion of component i, N is the mole fraction, and K is an interaction parameter calculated from London forces, polarization forces, and the interionic distances for each salt.

Lumsden's model was used to calculate the phase diagrams for the LiI-KI and LiI-RbI systems.[9] A minimal number of thermal analysis data points were necessary to map the phase diagrams because of the guidance given by the calculated diagrams. The data for the LiI-KI system are given in Fig. V-12 along with

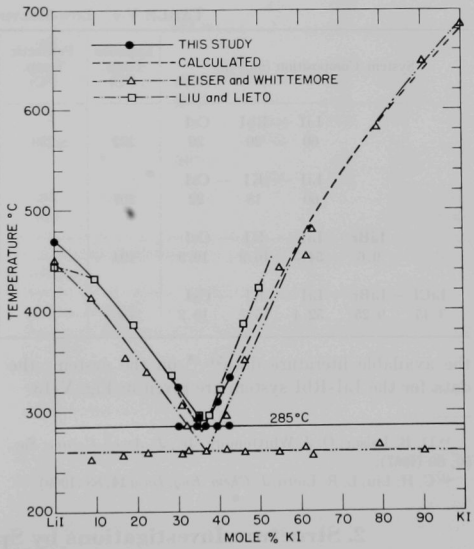

308-2094

FIG. V-12. Solid-Liquid Phase Equilibria for the LiI-KI System.

[53] J. Lumsden, *Discussions Faraday Soc.* **32**, 138 (1961).

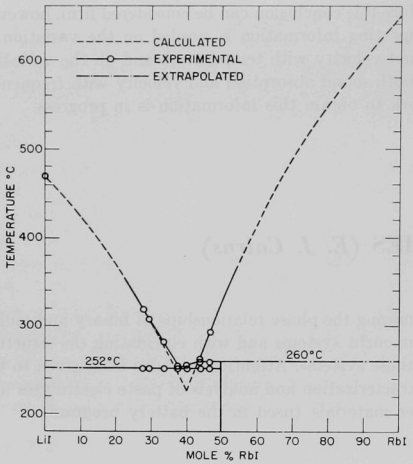

308-2095

FIG. V-13. Solid-Liquid Phase Equilibria for the LiI-RbI System.

The agreement between the calculated and experimentally determined phase diagrams is excellent, especially for the LiI-RbI system even though the 1:1 compound LiI·RbI forms. The compound LiI·RbI raises the minimum temperature only 25° above that obtained in the calculation. As seen in Fig. V-12, the data for the LiI-KI system obtained by Leiser and Whittemore[54] are in rather poor agreement with our experimental data. The temperature data that they obtained could have resulted from the presence of water in the lithium iodide that they used. Such an impurity could cause the temperatures that they observed to be low by the amounts shown.

Since the two binaries LiI-KI and LiI-RbI have low-melting eutectics, several ternary and multicomponent systems having these pairs as constituents were also investigated and mixtures having even lower melting points were identified. Only those compositions that were estimated to be close to the eutectic compositions were studied; the results to date are summarized in Table V-4.

It is clear that the model proposed by Lumsden can decrease significantly the experimental effort required the available literature data[54, 55] on the system; the data for the LiI-RbI system are given in Fig. V-13.

TABLE V-4. Low-Melting Lithium Halide Mixtures

System/Composition (mol %)	Liquidus Temp. (°C)	Peritectic Temp. (°C)	Eutectic Temp. (°C)	Remarks
LiI — RbI — CsI 60 20 20	232	≃230	≃227	Peritectic and eutectic occur close to each other.
LiI — KI — CsI 60 18 22	207	—	204	Composition close to eutectic composition.
LiBr — LiI — KI — CsI 9.6 54.3 16.2 19.9	194	—	189	Composition close to eutectic composition.
LiCl — LiBr — LiI — KI — CsI 3.45 9.25 52.4 15.7 19.2	186	—	184	Composition close to eutectic composition.

to select low-melting molten salt mixtures. Although this model is rigorously applicable only to simple eutectic systems, our work indicates that reasonable success can be expected in predicting the behavior of alkali halide systems even when compound formation occurs.

[54] D. B. Leiser, O. J. Whittemore, Jr., *J. Amer. Ceram. Soc.* **50**, 60 (1967).

[55] C. H. Liu, L. R. Lieto, *J. Chem. Eng. Data* **14**, 83 (1969).

2. Structure Investigations by Spectroscopic Methods (*V. A. Maroni, E. J. Hathaway, E. J. Cairns*)

a. Raman Studies

Several of the phosphorus-sulfur compounds under investigation as cathode substances for electrochemical cells have been investigated by Raman spectroscopy. Raman spectra of solid compounds were taken at room temperature and those of liquids at temperatures just above their melting points. The Raman spectra of elemental liquid sulfur and elemental liquid phosphorus are well known.[56, 57] Sulfur exists in the form of an S_8-

[56] A. T. Ward, *J. Phys. Chem.* **72**, 4133 (1968).

[57] C. W. F. T. Pistorius, *J. Chem. Phys.* **29**, 1421 (1958).

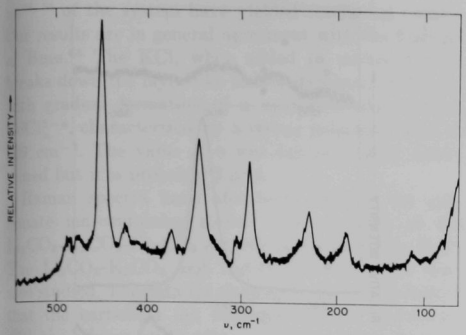

308-2188

FIG. V-14. Raman Spectrum of Liquid P_4S_3 (200°C).

puckered ring in the liquid state, whereas melts of the white modification of phosphorus contain P_4 tetrahedra. Phase diagram studies of the phosphorus-sulfur system[58] have indicated the formation of numerous compounds, the most stable of these being P_4S_{10}, P_4S_7, and P_4S_3.

The Raman spectra of solid and liquid P_4S_3 obtained in our laboratory are essentially the same except that several low-frequency lattice modes were observed for the solid. The spectrum of molten P_4S_3 is shown in Fig. V-14 and the frequencies are tabulated in Table V-5, column 3. The Raman spectrum for molten P_4S_{10} is shown in Fig. V-15 and the frequencies are tabulated, along with those for the solid, in Table V-5, columns 1 and 2. The Raman spectra of solid and liquid P_4S_3 and the spectrum of solid P_4S_{10} agree with previously reported results for these compounds.[59, 60] No previous investigations of molten P_4S_{10} have been reported in the literature.

Unlike P_4S_3, P_4S_{10} exhibits differences in the Raman spectra of the solid and liquid phases. The three bands of highest frequency in the spectrum of solid P_4S_{10}, namely, those at 726, 697, and 401 cm^{-1}, are absent in the spectrum of the liquid. These bands probably arise from stretching vibrations of terminal P-S bonds. In P_4S_{10}, six of the sulfur atoms are present in P-S-P bridges and four in terminal P-S bonds,[61] whereas in P_4S_3 all three sulfur atoms are present in P-S-P bridges.[62] The absence of any bands above 400 cm^{-1}

TABLE V-5. COMPOSITE OF RAMAN FREQUENCIES (cm^{-1}) FOR THE PHOSPHORUS-SULFUR SYSTEM[a]

P_4S_{10}		P_4S_3 Liquid	Liquid 85 at. % P-15 at. % S		Species Assignment
Solid	Liquid		Before Heating[b]	After Heating[c]	
42, 54, 66	—	—	—	—	Lattice modes
128	126 s	—	—	126	P_4S_{10}
—	—	—	151	—	S_8
163	163 m	—	—	(163)[d]	P_4S_{10}
185	183 m	187 m	—	185	P_4S_3, P_4S_{10}
197	202 s	—	—	202	P_4S_{10}
—	—	—	—	214	[e]
—	—	—	221	—	S_8
—	—	227 m	—	225	P_4S_3
—	—	—	—	233	[e]
—	—	—	—	238	[e]
—	—	—	—	244	[e]
—	—	—	—	262	[e]
274	268 m	—	—	267	P_4S_{10}
—	—	292 s	—	290	P_4S_3
310	308 m	—	—	305	P_4S_{10}
—	—	347 s	—	346	P_4S_3
—	—	—	—	358	[e]
—	—	—	366	366	P_4
—	—	377 w	—	375	P_4S_3
401	—	—	—	—	Solid P_4S_{10}
—	—	—	—	407	[e]
—	—	425 w	—	425	P_4S_3
—	—	451 s	—	451	P_4S_3
—	—	—	465	465	P_4
—	—	—	479	—	S_8
—	—	490 w	—	490	P_4S_3
—	—	—	605	605	P_4
697	—	—	—	—	Solid P_4S_{10}
726	—	—	—	—	Solid P_4S_{10}

[a] s = strong intensity, m = medium intensity, w = weak intensity.

[b] Spectrum of liquid eutectic at 25°C before temperature cycling to 200°C.

[c] Spectrum of liquid eutectic at 25°C after temperature cycling to 200°C.

[d] Observed as a shoulder on the 185 cm^{-1} band.

[e] Probably associated with polyphosphide or a phosphorus-sulfur compound other than P_4S_{10} or P_4S_3.

in the liquid indicates that, on melting, the terminal sulfur atoms in P_4S_{10} become at least partially dissociated from the inner P_4S_6 skeleton. However, this inner cage structure is not affected by heating, as evidenced by the similarity in the Raman data below 400 cm^{-1} for the solid and liquid phases. In P_4S_3, the bands below 400 cm^{-1} are also attributed to the P-S-P network and those in the region of 400 to 500 cm^{-1} are assigned to vibrations of the equilateral triangular base formed by three of the phosphorus atoms.

The eutectic 85 at. % P-15 at. % S has also been investigated by Raman spectroscopy. This mixture is a

[58] R. Förthmann, A. Schneider, *Z. Phys. Chem. (Frankfurt am Main)* **49**, 22 (1966).

[59] H. Gerding, J. W. Maarsen, P. C. Nobel, *Rev. Tran. Chem.* **76**, 757 (1957).

[60] D. H. Zijp, *Proc. 4th Intern. Meet. Mol. Spectroscop. Bologna, Italy*, 1959, Vol. 1, p. 345 (1962).

[61] A. Vos, E. H. Wiebenga, *Acta Cryst.* **8**, 217 (1955).

[62] Y. C. Leung, J. Waser, L. R. Roberts, *Chemistry & Industry* **74**, 948 (1955).

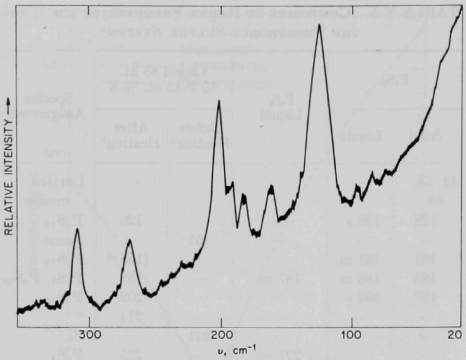

308-2189

FIG. V-15. Raman Spectrum of Liquid P_4S_{10} (340°C).

liquid at room temperature and can be formed by placing the elements in intimate contact at about 40°C. Spectral data at 25°C for the mixture (Table V-5, column 4) show that only P_4 and S_8 are present. Data taken at 25°C after the sample had been heated at 200°C for 20 minutes (Table V-5, column 5) are considerably different from those for the unheated sample

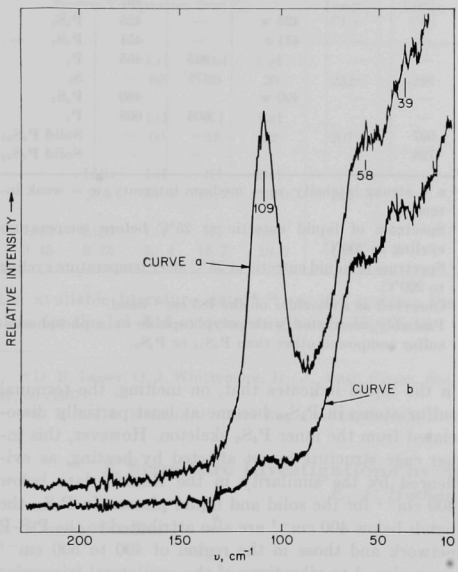

308-2190

FIG. V-16. Raman Spectrum of 40 mol % MgI_2-60 mol % KI (360°C).

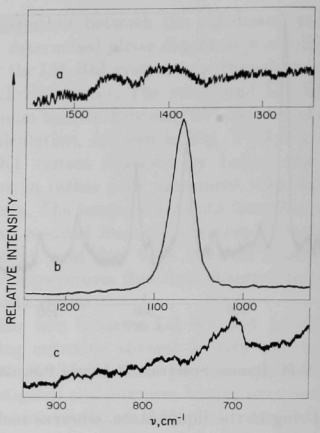

308-1973

FIG. V-17. Raman Spectrum of Molten Li_2CO_3-K_2CO_3-Na_2CO_3 Eutectic, 400°C. (Scan speed = 9 cm^{-1}/min; time constant = 20 sec; spectral band pass = 12.5 cm^{-1}. Curve a: ν_3 region, sensitivity = 10^{-11} amp; curve b: ν_1 region, sensitivity = 10^{-10} amp; curve c: ν_2 and ν_4 region, sensitivity = 3×10^{-11} amp.)

and indicate the formation of P_4S_{10}, P_4S_3 and possibly other phosphorus-sulfur compounds. Because of the large excess of phosphorus, P_4 molecules are still evident in the heat-treated sample but S_8 molecules are not.

The Raman studies of divalent metal ions in molten halide media have continued with studies of the MgI_2-KI and $CdCl_2$-KCl systems. Raman spectra of molten samples containing 40 and 50 mol % MgI_2 in KI were identical; the spectrum of the 40 mol % MgI_2 sample is shown in Fig. V-16. The band at 109 cm^{-1} is almost totally polarized, whereas the bands at 58 and 39 cm^{-1} are depolarized, as indicated by trace b in the figure. These results and those previously reported in ANL-7575, p. 144, for the $MgCl_2$-KCl and $MgBr_2$-KBr systems are very much the same. In each system two bands were observed: a strong polarized band and a broad depolarized band, which was less intense and occurred at a lower frequency. In the MgI_2-KI system, the lower-frequency band was resolved into two components. Although this band was not resolved in the $MgCl_2$-KCl and $MgBr_2$-KBr systems, it very probably contained two components in these systems as well. The Raman spectra for the magnesium halide systems are most consistent with the formation of tetrahedral MgX_4^{-2} (X = Cl, Br, or I).

A brief examination was made of the Raman spectra of the molten $CdCl_2$-KCl system.[8] Two previous stud-

ies[63, 64] of the system have yielded conflicting results. Our results are in general agreement with the findings of Bues.[63] The KCl, when added to molten $CdCl_2$, breaks down the layer-like lattice structure, $(CdCl_2)_n$, with gradual formation of a monomolecular species, $CdCl_n^{2-n}$, characterized by a strong polarized band at 259 cm^{-1}. The value of n was not accurately determined but it is probably 3 or 4.

Raman spectra have also been obtained for carbonate ion-containing melts.[7] The spectrum of the Li_2CO_3-K_2CO_3-Na_2CO_3 eutectic is shown in Fig. V-17. The Li_2CO_3-K_2CO_3 and Li_2CO_3-LiBr eutectics were also studied. The data for these systems have indicated that the carbonate ion undergoes strong interaction with the lithium ions leading to splitting of the Raman-active degenerate modes for CO_3^{-2}, $\nu_3(E')$ (Fig. V-17a) and $\nu_4(E')$ (Fig. V-17c). In addition, the frequency of $\nu_1(A_1')$ for CO_3^{-2} (Fig. V-17b) is measurably affected by the lithium ion concentration. These results show that carbonate ion-cation interactions in molten phases are closely analogous to those of nitrate ion-cation interactions in nitrate melts.[65]

[63] W. Bues, *Z. Anorg. Allgem. Chem.* **279**, 104 (1955).

[64] M. Tanaka, K. Balasubramanyam, J. O'M. Bockris, *Electrochim. Acta* **8**, 261 (1963).

b. Infrared Studies

A rapid method has been developed for analyzing lithium aluminate preparations by infrared spectroscopy. Samples of α-$LiAlO_2$, γ-$LiAlO_2$, α-Al_2O_3, and γ-Al_2O_3 each had a different characteristic spectrum, which was independent of the history of the sample.

Various samples have been examined by this technique to measure the extent of reaction of γ-Al_2O_3 with Li_2CO_3-Na_2CO_3 eutectic to form $LiAlO_2$ and to determine the crystalline form (α or γ) of the $LiAlO_2$ product. These measurements can be made with nearly the same sensitivity as the powder X-ray diffraction analysis previously used, and in all cases the two techniques have been in good agreement qualitatively.

[65] For a review of this subject see: V. A. Maroni, E. J. Cairns, "A Review of Raman Spectroscopy of Fused Salts and Studies of Some Halide-Containing Systems," in *Molten Salts: Characterization and Analysis*, p. 234, G. Mamantov, ed., Marcel Dekker, Inc., New York (1969).

C. ENERGY CONVERSION STUDIES (*E. J. Cairns*)

Studies of laboratory-scale secondary cells have been directed toward obtaining a better understanding of the electrochemical processes occurring in the cells. New and potentially useful cathode materials containing phosphorus and sulfur have been introduced, and the nature of the diffusion mechanism in these cathodes has been examined. The influence of the salt-to-filler ratios in paste electrolytes on cell performance has been investigated. Several promising low-melting mixed-cation electrolytes have evolved. In all of these studies, inert containment materials are needed to ensure that electrochemical measurements are thermodynamically meaningful; this need is being met by the materials research program.

1. Lithium/Chalcogen Cells

a. Lithium/Selenium Cells

(1) Cells with Liquid Electrolytes (*R. Sridhar*)

An attractive feature of the lithium/selenium cell is that both selenium and lithium have low melting points: 220 and 180°C, respectively. However, cell operating temperatures have been limited by the melting point, 341°C, of the commonly used electrolyte, the eutectic mixture composed of 11.7 mol % LiF-29.1 mol % LiCl-59.2 mol % LiI (see ANL-7425, p. 179). In an effort to achieve lower operating temperatures, lower-melting electrolytes for lithium/selenium cells have been sought.

For successful cell operation, the electrolyte should have a high lithium-ion content and lithium-ion mobility as well as a low melting point. At present, the adequacy of the lithium-ion flux can only be inferred from the results of cell operation and from the stability of other halides relative to LiI, the major component in most of the eutectics that have been used in cells. From a comparison of the standard free energies of formation at 600°C for all of the alkali metal halides,[66] electrolytes based on the binaries LiI-KI, LiI-RbI, and LiI-CsI seem attractive. With considera-

[66] JANAF Thermochemical Tables, Dow Chemical Co., Midland, Mich. (1962).

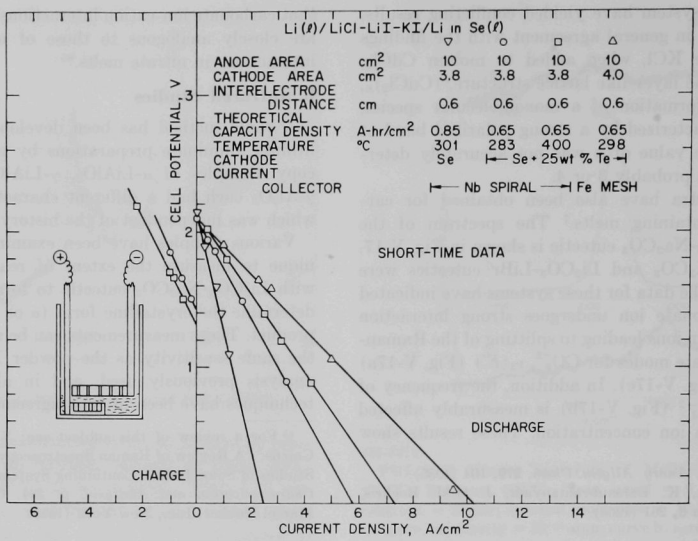

308-2191

FIG. V-18. Voltage-Current Density Characteristics of a Lithium/Selenium Cell with a Mixed-Cation Liquid Electrolyte.

tion of the additional requirement that the electrolyte have a high lithium-ion content, a eutectic composed of 8.5 mol % LiCl-59 mol % LiI-32.5 mol % KI, mp = 265°C (see ANL-7575, p. 142), was prepared for use in lithium/selenium cells.

Short-time voltage-current density data for several lithium/selenium cells with LiCl-LiI-KI electrolytes are given in Fig. V-18, together with a tabulation of the cell parameters and operating conditions. The effects of adding tellurium to selenium (to improve the conductivity) and of using an expanded-mesh current collector on the performance of these cells are well illustrated by the data.

It was not possible to achieve the full theoretical capacity in these cells operating at high current densities and low temperatures (below 300°C) because a solid product formed in the cathode (see lithium-selenium phase diagram, Fig. V-4, this report). However, it was possible to achieve 82% of theoretical capacity (1.22 A-hr) at 295°C at a current density of 0.125 A/cm² in a cell with an expanded-mesh cathode current collector; 70% of this capacity was achieved at a terminal voltage above 1 V.

Thermal analysis of the electrolyte used in these experiments indicated that its composition had not changed during the runs; thus it can be concluded that no reduction of potassium ion occurred during cell operation. It appears from these results that selected low-melting mixed-cation electrolytes can be used in lithium/selenium cells without significantly affecting cell performance relative to that of cells of the type Li/LiF-LiCl-LiI/Li in Se.

(2) Cells with Paste Electrolytes (*H. Shimotake, J. C. Cassulo*)

In the study of lithium/selenium cells with paste electrolytes, cell performance has been evaluated as a function of (1) composition of the paste electrolyte and (2) properties of the cathode current collector, including porosity, pore size, and configuration (metal felt or expanded mesh). (A further discussion of paste electrolytes is given below in Section V.C.2.) A diagram of the cell configuration used in these studies is shown in Fig. V-19 along with voltage-current density characteristics and the pertinent structural information for two of the cells. The maximum power density observed for these Li/Se cells was 2.7 W/cm² at 375°C, for the cell with a stainless steel Feltmetal cathode current collector. Discharge curves for one of the cells are given in Fig. V-20; the curves are typical of those obtained throughout the investigation. At a current density of 0.053 A/cm², an energy density of 0.3 W-hr/cm² was obtained. Data for the entire series of cells are summarized in Table V-6. It was generally

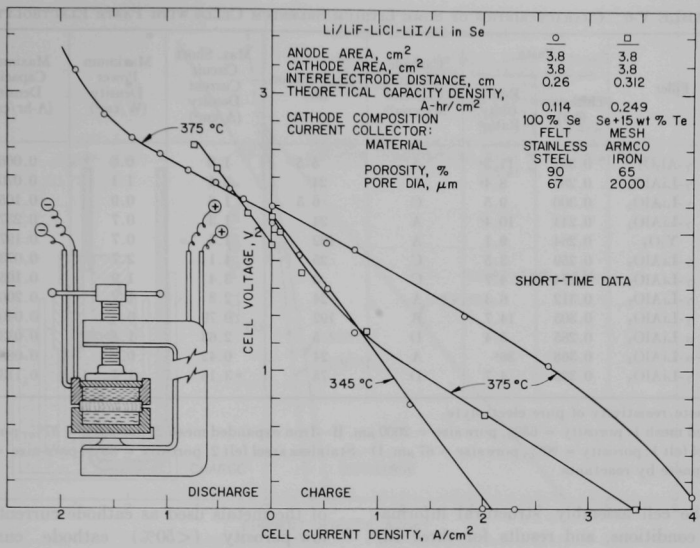

308-2192

FIG. V-19. Voltage-Current Density Characteristics of Lithium/Selenium Cells with Paste Electrolytes.

found that at low current densities (<0.1 A/cm²), high capacity densities were obtained with expanded-mesh current collectors, whereas at higher current densities (>0.25 A/cm²), metal-felt current collectors provided higher capacity densities. Pastes with high concentrations of electrolyte (≥70 wt %) experienced structural failure of the paste electrolyte owing to excessive softening. Pastes with ≤50 wt % electrolyte showed generally higher resistivity ratios (paste/pure electrolyte) and poor wetting at the electrolyte-electrode interfaces.

b. Lithium/Sulfur Cells (*H. Shimotake, R. Sridhar, J. C. Cassulo*)

A number of lithium/sulfur cells have been operated with liquid eutectic electrolytes.[2, 3] Fig. V-21 contains

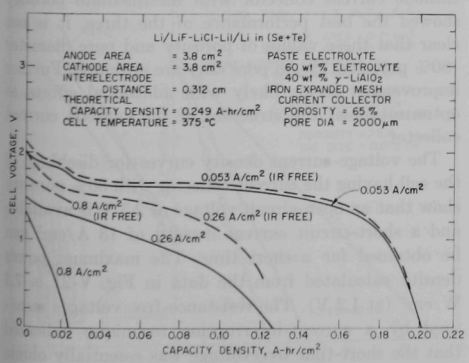

308-2193

FIG. V-20. Voltage-Capacity Density Characteristics for a Lithium/Selenium Cell.

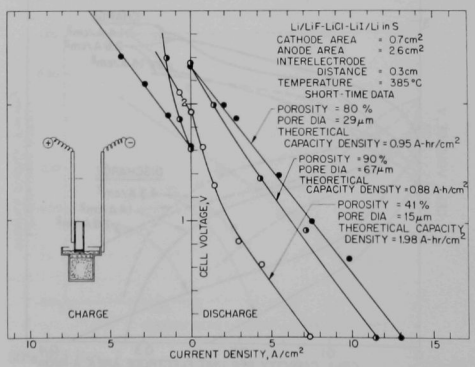

308-2194

FIG. V-21. Effect of Cathode Current Collector on Cell Performance of a Lithium/Sulfur Cell.

TABLE V-6. CHARACTERISTICS OF SOME LITHIUM/SELENIUM CELLS WITH PASTE ELECTROLYTES

Electrolyte Concentration (wt %)	Filler	Paste		Cathode Current Collector Material[b]	Test Duration (hr)	Max. Short Circuit Current Density (A/cm²)	Maximum Power Density (W/cm²)	Maximum Capacity Density (A-hr/cm²)	Theoretical Capacity Density (A-hr/cm²)
		Thickness (cm)	Resistivity Ratio[a]						
50	γ-Al_2O_3	0.302	11.3[c]	A	5.5	1.0	0.6	0.066	0.355
	γ-$LiAlO_2$	0.282	8.4[c]	A	24	2.1	1.1	0.070	0.585
	γ-$LiAlO_2$	0.300	9.5	C	6.5	1.6	0.9	0.105	0.451
	γ-$LiAlO_2$	0.244	10.4[c]	A	24	1.3	0.7	0.237	0.494
	Y_2O_3	0.264	9.1	A	192	1.3	0.7	0.197	0.494
60	γ-$LiAlO_2$	0.259	3.5	C	25	4.1	2.7	0.073	0.371
	γ-$LiAlO_2$	0.274	4.7	C	3	3.4	1.9	0.105	0.114
	γ-$LiAlO_2$	0.312	6.3	A	24	2.3	1.2	0.206	0.249
	γ-$LiAlO_2$	0.305	14.7	B	192	0.79	0.45	0.040	0.460
70	α-$LiAlO_2$	0.285	5.4	D	5	2.63	1.4	0.033	0.123
	$\gamma+\alpha$-$LiAlO_2$	0.368	36[c]	A	24	0.42	0.23	0.088	0.454
	γ-$LiAlO_2$	0.325	4.7	D	75	3.16	1.7	0.113	0.527

[a] Resistivity of paste/resistivity of pure electrolyte.
[b] A—Iron expanded mesh 1: porosity = 65%, pore size = 2000 μm. B—Iron expanded mesh 2: porosity = 57%, pore size = 1800 μm. C—Stainless steel felt 1: porosity = 90%, pore size = 67 μm. D—Stainless steel felt 2: porosity = 80%, pore size = 29 μm.
[c] Poor wetting of paste by reactants.

a diagram of the cell assembly, structural information, operating conditions, and results for three Li/LiF-LiCl-LiI/Li in S cells.

The performance of lithium/sulfur cells was closely related to the characteristics (porosity and pore size)

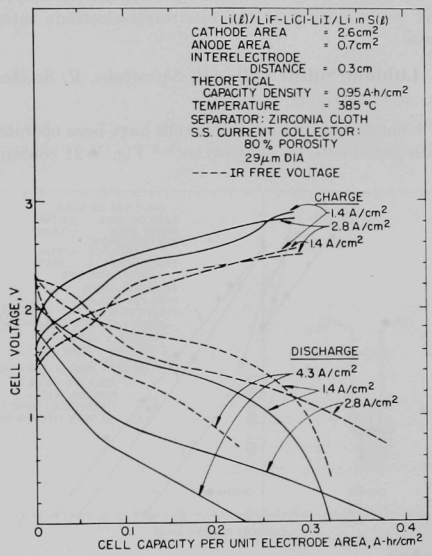

308-1748 T-1

FIG. V-22. Voltage-Capacity Density Curves at Constant Current for a Lithium/Sulfur Cell.

of the metals used as cathode current collectors. The low-porosity (<50%) cathode current collectors showed a low resistance overvoltage and a high diffusion overvoltage, whereas the converse was true for the high-porosity (>80%) materials. A current density of 3 A/cm² at 1 V was obtained from a cell that had sintered tungsten powder (41% porosity, 15-μm pore dia) as the cathode current collector; a current density of 6 A/cm² at 1 V was achieved from a cell with stainless steel felt (90% porosity, 67-μm pore dia) as the cathode current collector. The best performance, 7 A/cm² at 1 V, was obtained with stainless steel felt of 80% porosity and 29-μm pore dia. Although the cathode current collector with intermediate porosity showed the best performance of the three, it is not clear that these values of porosity and pore diameter (80% porosity, 29-μm pore dia) are optimum. Further improvement seems likely with additional efforts at optimization of the structure of the cathode current collector.

The voltage-current density curves for discharge of the cell having the current collector with 80% porosity show that an open-circuit voltage of 2.3 V is available and a short-circuit current density of 13 A/cm² can be obtained for a short time. The maximum power density calculated from the data in Fig. V-21 is 7.5 W/cm² (at 1.2 V). The resistance-free voltages measured by a current-interruption technique indicated that the short-time overvoltage was essentially ohmic and originated primarily in the electrolyte and the cathode current collector. The diffusion overvoltage increases during the discharge while the resistance

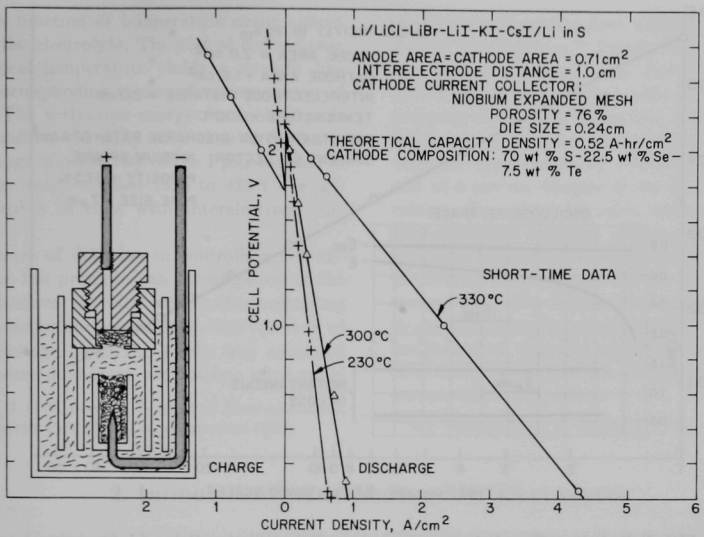

308-2195

FIG. V-23. Voltage-Current Density Characteristics for a Lithium/Sulfur Cell.

overvoltage remains approximately constant, as can be seen in Fig. V-22.

The overall cathode compositions at full discharge ranged from $Li_{0.5}S$ to LiS. Complete discharge of the cell to Li_2S was not possible at current densities near 1 A/cm² because of the high diffusion overvoltage. For this reason, the highest capacity density achieved at a current density of 1.4 A/cm² was 0.33 A-hr/cm² or 35% of the theoretical capacity density, based on Li_2S as the final cathode composition. The open-circuit voltage was stable in a 54-hr test, thereby indicating a low rate of self-discharge.

A lithium/sulfur cell was also operated with the low-melting (184°C) LiCl-LiBr-LiI-KI-CsI eutectic as the electrolyte. The sulfur cathode of this cell contained approximately 30 wt % of a selenium-tellurium alloy to aid in current collection. Figure V-23 gives the

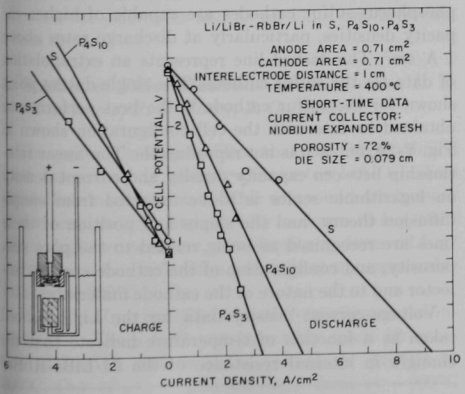

308-1979 Rev. 1

FIG. V-24. Voltage-Current Density Characteristics for Lithium/Sulfur, Lithium/P_4S_{10}, and Lithium/P_4S_3 Cells.

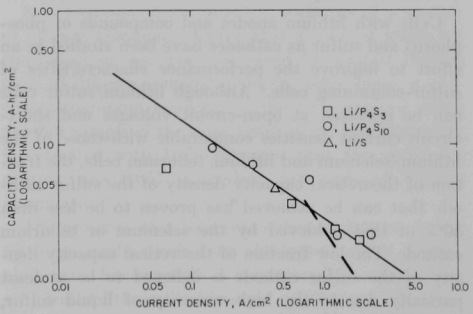

308-1975 Rev. 1

FIG. V-25. Capacity Density-Current Density Characteristics for Li/P_4S_3, Li/P_4S_{10}, and Li/S Cells at 400°C. (Dashed curve represents extrapolation of data for Li/S cells operated at current densities greater than 2 A/cm².)

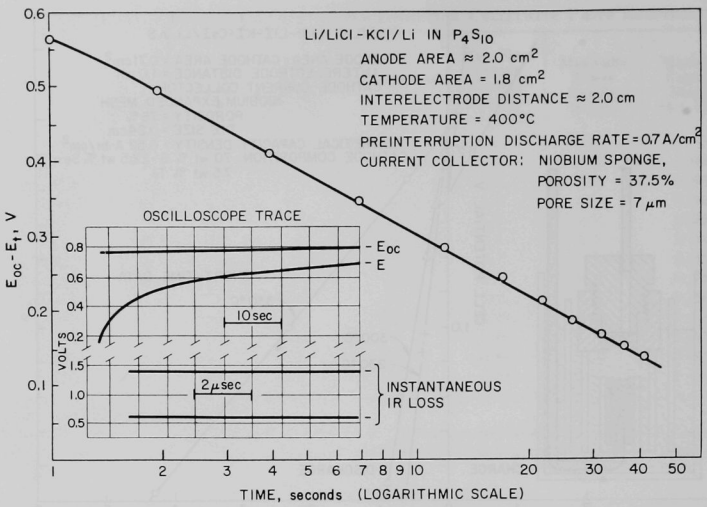

308-1980 Rev. 1

FIG. V-26. Voltage-Time Relations of a Lithium/P_4S_{10} Cell after Current Interruption.

cell design and voltage-current density characteristics for this cell at various temperatures. The performance of the cell is poor below 300°C, but improved appreciably at about 330°C. The poor performance at lower temperatures is attributed to the high viscosity of the cathode alloy and to solid formation in the cathode after addition of small amounts of lithium. At higher operating temperatures, the capacity of the cell is increased by the greater solubility of lithium in the cathode alloy.

c. Lithium/P_xS_y Cells (*V. A. Maroni*)

Cells with lithium anodes and compounds of phosphorus and sulfur as cathodes have been studied in an effort to improve the performance characteristics of sulfur-containing cells.[4] Although lithium/sulfur cells can be operated at open-circuit voltages and short-circuit current densities comparable with those of the lithium/selenium and lithium/tellurium cells, the fraction of theoretical capacity density of the sulfur cathode that can be achieved has proven to be less than 50% of that achieved by the selenium or tellurium cathode. The low fraction of theoretical capacity density of the sulfur cathode is believed to be at least partially due to the high viscosity of liquid sulfur, which inhibits the diffusion of cell products away from the cathode-electrolyte interface. Additives such as phosphorus are known to reduce the viscosity of the sulfur considerably.[67]

A comparison of instantaneous voltage[68]-current density characteristics for a Li/P_4S_3 cell, a Li/P_4S_{10} cell, and a Li/S cell is given in Fig. V-24 along with a diagram of the cell assembly and a summary of the operating conditions, which were the same for each cell. The sulfur cathode appears to be superior to the phosphorus-sulfur cathodes in producing a high instantaneous power density; however, a comparison of capacity density-current density data for these cathodes, which is shown in Fig. V-25, indicates that the phosphorus-sulfur cathodes are capable of higher capacity densities, particularly at discharge rates above 1 A/cm². The dashed line represents an extrapolation of data for the sulfur cathode. The single datum point shown for the sulfur cathode is the best performance obtained to date with the cell configuration shown in Fig. V-24, but it was not reproducible. The linear relationship between capacity density and current density on logarithmic scales is to be expected from simple diffusion theory, and the slopes and position of these lines are recognized as being related to the pore size, porosity, and configuration of the cathode current collector and to the nature of the cathode material.

Voltage-current density data for the Li/P_4S_{10} cell taken as a function of temperature indicate that the changes in internal resistance of the Li/LiBr-RbBr/

[67] J. R. Van Wazer, *Phosphorus and Its Compounds*, Vol. I, Chemistry, p. 300, Interscience Publishers, Inc., New York (1958).

[68] The instantaneous voltage is the cell terminal voltage a fraction of a second after initiation of current flow.

P_4S_{10} cell as a function of temperature occur almost exclusively in the electrolyte. The plot of conductance against reciprocal temperature yields a straight line with a slope corresponding to an activation energy of 3.6 kcal/mol. The activation energy for ionic liquids such as fused salts is normally very close to 3.6 kcal/mol.[69] The change in resistivity of the P_4S_{10} cathode in the temperature range studied (315 to 425°C) is apparently negligible in cells with interelectrode distances $\geqslant$1 cm.

The importance of diffusion in controlling cell capacity densities has prompted an investigation of the diffusion mechanism in cells with sulfur-containing cathodes. The instantaneous and long-time recovery of the terminal voltage of Li/P_4S_{10} cells was measured with a dual-beam dual-trace oscilloscope after rapid interruption of current flow, using a method similar to that of Trachtenberg.[70] Figure V-26 shows the results of a typical experiment. The short-time or IR-related overvoltage was measured with the lower beam by sweeping at a rate of 2 μsec/cm; the long-time or diffusion-related terminal voltage recovery was measured with the upper beam by sweeping at a much lower rate of 5 sec/cm. Graphs of the steady-state terminal voltage, E_{oc}, obtained after interruption, minus the time-dependent terminal voltage, E_t, plotted against time on a logarithmic scale have yielded straight lines in the time range of 1 to 100 sec after interruption of current flow (Fig. V-26). Work currently in progress to derive mathematical expressions for this behavior has indicated that the equations governing diffusion in a semi-infinite medium adequately predict the observed region of linearity.

[69] G. Kortum, J. O'M. Bockris, *Textbook of Electrochemistry*, Vol. I, p. 203, Elsevier Publishing Co., Amsterdam (1951).

[70] I. Trachtenberg, *J. Electrochem. Soc.* **111**(1), 110 (1964).

2. Immobilization of Molten-Salt Electrolytes

An important factor in the development of practical cell configurations is the immobilization of one or more of the three liquid phases. A program is in progress (ANL-7575, p. 158) to study immobilization of the electrolyte phase through the use of paste disks. The paste electrolyte disk is a pressed composite of an inert infusible filler and the electrolyte proper, which is an ionic lithium salt mixture. At the operating temperature of an electrochemical cell, the electrolyte is above its melting point; however, the paste, being a highly viscous material, behaves essentially as a solid. This pseudo-solid functions both as a mechanical separator between the electrodes and as an ionic conductor between them.

a. Studies of Filler Materials (*A. K. Fischer, L. E. Trevorrow, F. L. Ferry, J. G. Riha*)

The paste electrolyte filler that has been studied most extensively is lithium aluminate ($LiAlO_2$). Two crystalline modifications of this compound are known: a low-temperature, high-density α form (3.4 g/cm^3) and a high-temperature, low-density γ form (2.6 g/cm^3). The α-to-γ transition proceeds at an appreciable rate above 600°C.

Methods of preparation of both forms have been investigated. The γ form can be readily made by reaction of Li_2CO_3 with α-Al_2O_3, γ-Al_2O_3 or AlOOH at 800°C. Our efforts to prepare the α form at ~600°C have shown that the reaction between Li_2CO_3 and Al_2O_3 is slow, taking 4 to 5 days to reach 80% of completion. Faster reactions were observed when a Li_2CO_3-Na_2CO_3 mixture was used to provide a molten medium (see ANL-7575, p. 159), but the product was still contaminated with Al_2O_3, as shown by X-ray diffraction analysis.

In most of the preparations, the lithium aluminate product was washed with water at room temperature to remove any Li_2CO_3 remaining after the preparation reaction. Evidence has recently been obtained, however, which indicates that dissolution and hydrolysis may occur during the washing of lithium aluminate. Both processes may occur to a considerable extent because of the extremely small particle size of the lithium aluminate used in the present work.

Acid titration of the collected washings of a sample of lithium aluminate showed that a total of about 0.2 equivalent of aqueous base could be washed from a mole of lithium aluminate. On the other hand, a gas-chromatographic analysis of the CO_2 evolved when another sample of the same batch of lithium aluminate was treated with HCl indicated that the carbonate content was 0.057 equivalent per mole of lithium aluminate.

The presence of a base other than carbonate in the washings might result from the hydrolysis of lithium aluminate. For example, a recent study[71] reports that a hydrated lithium dialuminate results from the reaction

$$2(Li_2O \cdot Al_2O_3) + (x + 1)\ H_2O \rightarrow$$

$$Li_2O \cdot 2Al_2O_3 \cdot xH_2O + 2Li^+ + 2\ OH^-$$

Experimental evidence[71, 72] also indicates that only the γ structural modification is susceptible to hydrolysis. Consistent with these findings, our observations indicate that when lithium aluminate is washed with water at room temperature, the concentration of the γ modification decreases. If any of the dialuminate were introduced into the solid by hydrolysis at room temperature, however, its concentration was below the limit detectable by X-ray powder diffraction analysis.

In addition to the α and γ forms of $LiAlO_2$ discussed above, a third, previously unreported form has been discovered. The X-ray diffraction pattern is distinctive. This new material was first prepared by heating LiOH and α-Al_2O_3 at 500°C for about 1½ days, followed by washing with water. Subsequent experiments showed that LiOH is a more effective reagent than Li_2O for producing the new form of $LiAlO_2$. With Li_2O (and α-Al_2O_3), the product is a mixture, of variable proportions, of γ-$LiAlO_2$ and the new form of $LiAlO_2$. With LiOH, only the new compound was observed as a product, whether α-Al_2O_3, γ-Al_2O_3, or AlOOH was the co-reactant. At high temperatures (900°C, but possibly lower), the new compound transformed to γ-$LiAlO_2$.

Methods for the preparation of two other lithium-aluminum oxides, Li_5AlO_4 and $LiAl_5O_8$, have also been investigated. The compound Li_5AlO_4 was prepared by a known procedure[73] of heating a mixture of LiOH and α-Al_2O_3 in a 5:1 lithium-to-aluminum atomic ratio at gradually increasing temperature from 400 to 830°C, and by our own method, namely, heating a mixture of Li_2O and Al_2O_3 (5:1 molar ratio) at 800°C. X-ray diffraction analysis indicated our product was more nearly monophasic than the product obtained with Lehmann and Hesselbarth's procedure. It was also shown that this compound is hydrolyzable and cannot be washed with water to free it of unreacted reagents.

The compound $LiAl_5O_8$ was prepared by the reaction[74]

$$3LiF + 8Al_2O_3 \rightarrow 3LiAl_5O_8 + AlF_3$$

at 900°C. A new method of preparation of $LiAl_5O_8$ was also discovered during an attempt to form $LiAlO_2$ by the reaction

$$Li_2SO_4 + Al_2O_3 \rightarrow 2LiAlO_2 + SO_3$$

at 900°C. The $LiAl_5O_8$ product, after washing, was extremely pure. The actual reaction is postulated to be

TABLE V-7. Conditions of Preparation and Densities of 2.5-cm Diameter Paste Electrolyte Disks

Electrolyte[a] Content (wt %)	Electrolyte[a] Content (vol %)	Filler	Source[c]	Pressing[d] Atmosphere	Pressing Temperature (°C)	Density (g/cm³)	Percent of Theoretical Density
50	55	α-$LiAlO_2$	ANL-1	He	117	1.69	52
	49	γ-$LiAlO_2$	ANL-2	He	124	2.75	99
	"	"	ANL-2	Vac	105	2.70	97
	"	"	ESP	He	120	2.39	86
	"	"	ESP	Vac	102	2.48	89
	"	"	ESP	Vac[e]	25	2.72	98
	"	"	G & S	He	120	2.42	87
	64	Y_2O_3	ROI	He	125	3.16	81
	58	γ-Al_2O_3	VITRO	He	120	2.53	81
	"	"	VITRO	Vac	106	2.67	77
60	66[b]	α-$LiAlO_2$	ANL-3	Vac	25	2.79	80
	"	"	ANL-3	Vac	120	3.17	91
	65	"	ANL-1	He	120	2.74	84
	67	"	ANL-4	Vac	120	2.64	78
	"	"	ANL-4	Vac[e]	25	3.20	94
	"	"	ANL-3	Vac	180	2.64	78
	"	"	ANL-3	Vac[e]	25	3.22	95
	59	γ-$LiAlO_2$	ANL-2	He	120	2.51	85
	"	"	ANL-2	Vac	107	2.91	99
	"	"	ANL-5	He	120	2.66	91
	"	"	ESP	He	120	2.57	87
	68	γ-Al_2O_3	VITRO	Vac	105	2.89	85
	"	"	VITRO	He	118	2.69	79
	"	"	VITRO	He	300	2.96	87
	"	"	VITRO	He	340	>3.0	>88
70	74	α-$LiAlO_2$	ANL-1	He	120	2.79	74
	77	γ-Al_2O_3	VITRO	He	120	2.81	84

[a] LiF-LiCl-LiI eutectic except where indicated.
[b] LiCl-LiI-KI eutectic.
[c] ANL = Argonne National Laboratory; ESP = Electronic Space Products; G & S = Gallard and Schlesinger; ROI = Research Organic/Inorganic Chemical Co.
[d] Pressing force 1450 kg except where indicated.
[e] Pressing force 29,000 kg.

$$Li_2SO_4 + 5Al_2O_3 \rightarrow 2LiAl_5O_8 + SO_3$$

The reaction of Al_2O_3 with Li_2SO_4 and LiF prompted an investigation of its reaction with LiCl and LiBr. Experiments were conducted in which α-Al_2O_3 was heated for 5 days with LiCl or LiBr; the products were then washed and examined. The product of reaction with LiCl was a mixture of $LiAl_5O_8$, γ-$LiAlO_2$, and unreacted α-Al_2O_3. The product of reaction with LiBr was very pure $LiAl_5O_8$.

The reaction observed with LiCl further suggested that the paste electrolyte used in a cell is a potentially reactive system, being composed of $LiAlO_2$ and a ternary electrolyte of LiF, LiCl, and LiI. This possibility was confirmed in an experiment in which a mixture of γ-$LiAlO_2$ and LiCl (2:3 molar ratio) was

[71] I. S. Lileev, L. K. Sachenko-Sakun, I. V. Guseva, *Zh. Neorg. Khim.* (*The Chemical Society Translation*) **13**(2), 213 (1968).

[72] A. M. Lejus, *Rev. Hautes Temp. Refract.* **1**, 53 (1964).

[73] H. Lehmann, H. Hesselbarth, *Z. Anorg. Allgem. Chem.* **315**, 14 (1962).

[74] E. Kordes, *Z. Kristall.* **91**, 193 (1935).

heated: $AlCl_3$ was evolved at a temperature below 900°C, and complete reaction occurred upon heating at 900°C for about 5 days. Although this study has not been completed, the findings clearly indicate that a chance of a reaction within the paste electrolyte exists. The considerably lower operating temperature of the cells, ~375°C, may slow the reaction so that its effects in the pastes would take much longer to become apparent. Cells which are expected to operate for thousands of hours (1000 hr = 41.6 days) may well undergo chemical changes and, consequently, electrical and structural changes. These possibilities need to be evaluated experimentally.

The development of a practical cell requires a paste electrolyte that is chemically stable toward the lithium anode and the chalcogen cathode. Stability tests have, therefore, been conducted on materials of interest. After contact with lithium for 2 hr at 500°C, the surface of γ-$LiAlO_2$ powder was darkened (became gray). Under similar conditions Y_2O_3 was blackened. At 375°C, $LiAlO_2$ and MgO powders were both stable toward lithium in an 8-day test and were also stable toward molten selenium in a two-week test. However, the true utility of these materials in a secondary battery must be demonstrated in tests of longer duration. The compound Li_5AlO_4 gave indications of possible reaction in a test with lithium at 375°C for one week; Li_2ZrO_3 proved unacceptable in an 18-hr test with lithium at 500°C.

b. Paste Studies (*H. Shimotake, J. C. Cassulo*)

A necessary part of the development of cells employing paste electrolytes is the selection of pastes with suitable electrochemical and physical characteristics. Work has continued on the preparation of paste electrolyte disks of various compositions and the determination of the properties of the disks.

Recent efforts have been directed toward producing paste electrolytes of high density. Conditions of preparation and the resulting densities for several paste electrolytes are listed in Table V-7. The disks were all 2.5 cm in diameter and varied in thickness from 2 to 4 mm. The densities of the disks that were pressed without pre-evacuation of the mold were usually lower than the densities of those obtained when the mold was evacuated prior to pressing. The effects of pressing force and pressing temperature on disk density have not yet been investigated in detail; however, it has been established that high densities can be obtained even at room temperature if enough pressing force is used. For example, 98% of theoretical density was achieved for a disk containing 50 wt % γ-$LiAlO_2$ by pressing at 25°C under 29,000 kg force after mold evacuation. The effect of pressing temperature (at 1450-kg pressing force) on disk density was investigated with and without evacuation using γ-Al_2O_3 as the filler. At temperatures of 300 and 340°C, without evacuation, the disk density approached 90% of the theoretical value. These results can be compared with a value of 85% for an identical mixture pressed at only 105°C with evacuation. Evidently, evacuation is more important to the achievement of high disk density than is elevated temperature (above 105°C).

From the above experiments, it can be concluded that, for paste electrolyte disks of 2.5-cm dia, densities within a few percent of the theoretical value can be obtained by vacuum molding with a force of 29,000 kg at room temperature, or with a force of 1450 kg at 110°C.

3. Materials Stability (*M. L. Kyle, P. W. Krause*)

The chemical systems of interest in the research program on liquid metals and molten salts include several having high reactivity. Consequently, materials compatibility is being studied in the current program. Experimental apparatus must be constructed of stable materials to avoid contamination and corrosion, to allow thermodynamically meaningful results to be obtained, and to obtain long lifetimes of laboratory cells. Both metallic and ceramic (insulator) materials are required that are stable to molten alkali metals, fused alkali halides, and molten chalcogens. A continuing program is being carried out to identify metals, alloys, and ceramics that resist the corrosive action of the systems being investigated.

a. Corrosion by Molten Lithium

Although aluminum oxide (Al_2O_3) is suitable as an electrical insulator material for use in systems with sodium and sodium-containing alloys, the development of insulators for systems containing lithium and its alloys has proven to be more difficult.

The results of static immersion tests to determine the resistance of various insulating materials to molten lithium at 375°C are shown in Table V-8. In these experiments, the sample (about 0.32 by 0.32 by 2.5 cm) is sealed in a stainless steel capsule (~2.5-cm dia by 6.25 cm long) with an appropriate amount of lithium. The capsule is then held at an elevated temperature for the desired time.

In general, the data in Table V-8 indicate that high-purity grades of ThO_2, BN, AlN, Y_2O_3, BeO, and single-crystal MgO possess sufficient corrosion resistance to be utilized in most experiments with lithium up to 375°C. On the other hand, impure grades of the above materials, MgO, ZrO_2, Al_2O_3 (including single crystal), and SiO_2 (Pyrex and quartz) are not resistant to molten lithium at 375°C.

b. Corrosion by Molten Li-P_4S_{10} Mixtures

The corrosion resistance of various materials to molten Li-P_4S_{10} mixtures at 375°C was measured in both static immersion and corrosion agitator experiments. In the latter type of experiment, a paddle made of the test material is rotated slowly (1 rpm) in the cathode mixture. The results of these experiments are summarized in Fig. V-27. Several materials—namely, Hastelloy C, molybdenum, Durimet 20, Hastelloy B, tantalum, Inconel 718, niobium, and Uniloy—demonstrated corrosion rates of less than 5 mils/yr (0.12 mm/yr) and should be usable with Li-P_4S_{10} mixtures. Both niobium and molybdenum have been utilized in laboratory electrochemical cells, and corrosion caused no significant interference with their operation.

TABLE V-8. Corrosion of Test Materials by Molten Lithium at 375°C

Material	No. of Tests	Test Duration (hr)	Observed Corrosion Rate (mils/yr)	Remarks
ThO_2	4	234–1056	<1	
BN	7	64–1130	3–130	Low corrosion rates obtained with high purity BN.
AlN	1	1006	2	
Y_2O_3[a]	4	64–1051	0–3	
BeO	2	529, 1006	20–500	
MgO[b]	2	162, 983	19	
MgO	2	219, 602	High	Binder attacked.
ZrO_2	1	528	High	Sample destroyed.
Al_2O_3[b]	1	528	High	Sample destroyed.
SiO_2	Several	12–300	High	

[a] Air-fired at 1000°C; vacuum-fired at 1800°C.
[b] Single crystal.

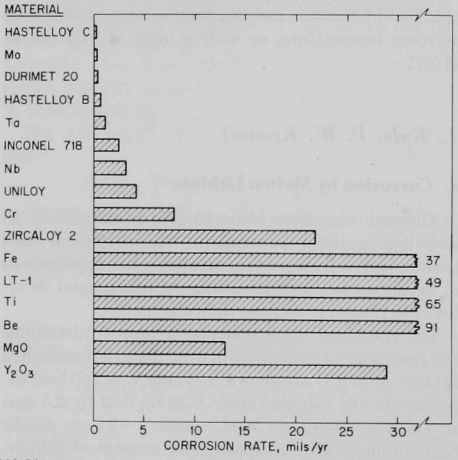

308-2196

FIG. V-27. Corrosion of Test Materials by Li-P_4S_{10} Mixtures (temperature: 375°C; lithium concentration: 5–20 at. %; test duration: 50–350 hr).

TABLE V-9. Corrosion of Test Materials by Molten Li-Se and Li-Te-Se Mixtures at 375°C for 50–350 Hr

Material	Observed Corrosion Rates (mils/yr)		
	10 at. % Li-90 at. % Se	20 at. % Li-80 at. % Se	10 at. % Li-10 at. % Te-80 at. % Se
Beryllium	1.3	15	98
Niobium	19	—	23
Nb-1% Zr	—	23	—
Chromium	—	—	28
Tungsten	21	—	—
Iron	170	—	—
304 SS	<70	117	—
Vanadium	—	1100	—
Tantalum	—	2200	—
Gold	—	34,000	—

c. Corrosion by Molten Li-Se and Li-Se-Te Mixtures

The use of molten selenium and lithium-selenium mixtures creates problems in the selection of corrosion-resistant containment materials. Selenium containment in metals is particularly difficult because selenides of most common metals are formed upon direct contact of the two elements at temperatures below 1000°C.

Several corrosion tests (static immersion and corrosion agitator) were conducted to determine the corrosion resistance of various materials to molten Li-Se and Li-Te-Se mixtures at 375°C. The Li-Te-Se system is of interest because the addition of tellurium to the selenium increases the electrical conductivity of the mixture, which is important in cell applications. The results of these tests are shown in Table V-9. Of the materials tested in the Li-Se mixtures, only beryllium, niobium, niobium-1% zirconium alloy, chromium, and tungsten possess sufficient corrosion resistance to be usable for cell applications. Niobium is resistant to Li-Te-Se mixtures but beryllium is not. Other selenium corrosion data are presented in Section V.D.2.d of this report.

D. BATTERY DEVELOPMENT (*E. J. Cairns*)

1. High-Specific-Energy Lithium/Selenium Batteries for Implantation[75]

The Chemical Engineering Division has undertaken work for the Artificial Heart Program of the National Heart and Lung Institute (NHLI) to develop an implantable battery that would deliver 10 W of power and store 120 W-hr of energy. The proposed battery is to be composed of four lithium/selenium cells having paste electrolytes of $LiAlO_2$ compacted with the eutectic salt of LiF-LiCl-LiI. The program has the following objectives:

1) to carry out design, fabrication, and electrical performance evaluations of the pertinent characteristics of cells 7.5 cm in diameter;

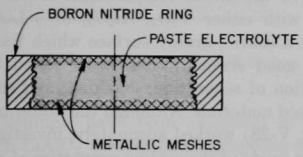

308-2197

FIG. V-28. Modified Paste Electrolyte Disk and Insulator (2.5 cm diameter).

2) to develop sealing and insulating materials that are stable during long-term battery operation under implantable conditions;

3) to design, fabricate, and test three first-generation batteries of implantable-sized and sealed configuration *in vitro* at 37°C.

a. Studies of Lithium/Selenium Single Cells

(1) Cells with Ceramic Ring Insulators (*H. Shimotake, J. C. Cassulo*)

Performance data at 375°C have been obtained for a lithium/selenium cell having a 2.5-cm dia paste electrolyte disk incorporating a boron nitride insulator. Figure V-28 shows the paste electrolyte disk used in this cell. The inner periphery of the boron nitride ring was threaded to form a well-bonded surface between the ring and the paste.

The cell assembly is shown in Fig. V-29. It consists of (1) an anode cup containing type 302 stainless steel Feltmetal (Huyck Metal Co.) wetted with lithium, (2) a cathode cup containing layers of niobium expanded mesh (0.023-cm die size, 57% porosity) wetted with selenium, and (3) a paste electrolyte disk having a composition of 60 wt % LiF-LiCl-LiI eutectic and 40 wt % $LiAlO_2$ filler.

The performance of the cell at 375°C is summarized in Table V-10. During the 26-hr experiment, the cell was charged and discharged 15 times; current densities during charging ranged from 0.25 to 1 A/cm^2. The cell resistance was high; however, no short-circuits were observed, indicating that the boron nitride ring

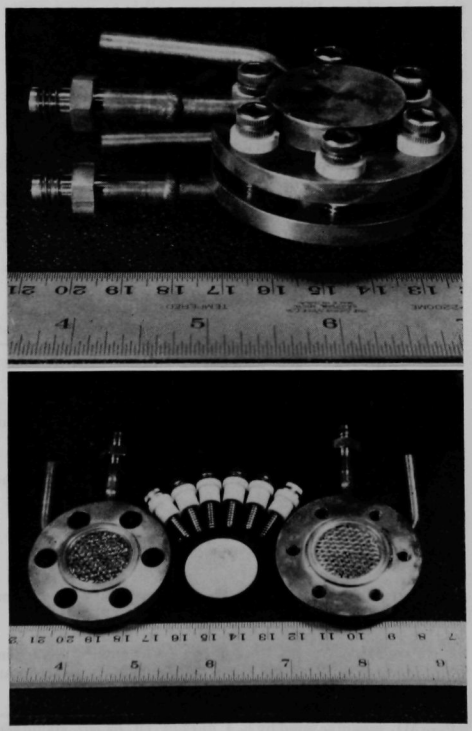

308-964

FIG. V-29. A 2.5-cm Diameter Lithium/Selenium Cell.

[75] This work is sponsored by the Artificial Heart Program, National Heart and Lung Institute.

TABLE V-10. SUMMARY OF PERFORMANCE DATA FOR LITHIUM/SELENIUM CELL WITH BORON NITRIDE RING/PASTE ELECTROLYTE DISK

Open-Circuit Voltage (V)	Short-Circuit Current Density (A/cm^2)	Diffusion Overvoltage[a] (V)	Resistance Overvoltage[a] (V)	Resistivity Ratio[b]
2.11	1.6	0.39	1.16	11.1

[a] At 0.26 A/cm^2 after 0.022 A-hr/cm^2 discharge. Diffusion overvoltage = open-circuit voltage − IR-free voltage. Resistance overvoltage = IR-free voltage − terminal voltage.
[b] Resistivity of the paste disk divided by the resistivity of the pure fused-salt electrolyte.

was successful in preventing the deposition of lithium in the gasket area.

(2) Cells with Polymer-Containing Insulators (*A. A. Chilenskas*)

An alternative to using a ceramic ring as an insulator and seal in a lithium/selenium cell is to use a composite material consisting of a high-temperature-resistant polymer mixed with an inert filler such as $LiAlO_2$ which can be cast in place. A cell design incorporating this concept is shown in Fig. V-30. Since the inner anode cup is electrically isolated from the outer cup by the insulation, the cell can be hermetically sealed by potting, brazing, or welding. Components for several cells based upon this design have been fabricated and will be tested for sealing and insulating capability. If warranted, electrical performance and corrosion resistance under operating conditions will be evaluated.

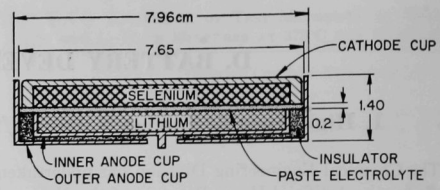

308-2198
FIG. V-30. Test Cell Utilizing a Laminated Anode Cup.

b. Studies of Sealing Methods (*A. A. Chilenskas, F. L. Ferry*)

As discussed above, boron nitride has proved to be a suitable material for sealing the anode compartment-paste interface in a lithium/chalcogen paste electrolyte cell so that lithium would not be deposited in the gasketing area of the anode compartment during the charging operation. In preliminary studies, the gasketing area of the anode compartment had been flame-sprayed with either Y_2O_3, Al_2O_3, or γ-$LiAlO_2$;[76] all three left a coarse, grainy surface which was not suitable for good sealing. These cells failed through a combination of separation, cracking, and corrosion of the sprayed materials. Although the boron nitride ring seal (Fig. V-28) worked adequately, investigations are also being made of the sealing properties of some polymeric materials, including polyimides, with the aim of reducing the cell weight and simplifying fabrication.

A polyimide (Pyre ML, manufactured by E. I. duPont), and a silicone resin (DC 63-502, manufactured

[76] Experiments conducted by E. C. Gay under AEC-sponsored work.

TABLE V-11. PREPARATION AND TESTING OF COMPOSITE SEALS AND INSULATORS

Binder[a]	Wt Ratio $LiAlO_2$/Binder	Cure	Results
Pyre ML	11[b]	4 hr at ~80°C in vacuum, 16 hr at ~150°C in air	Composite porous and easily crushed.
Pyre ML	22[b]	4 hr at ~80°C in vacuum, 16 hr at ~150°C in air	Not as porous as above, not as easily crushed.
DC-63-502	2	18 hr at ~142°C in air, ~4 hr at 225°C in air	Good bonding to SS shim stock. Hard and tough; sawed readily, difficult to crush.
Pyre ML	2.5[b]	2 hr at 80°C in vacuum, 16 hr at 225°C in air	Strong bond to SS shim stock. Porous structure, easily cut, easily crushed.
Pyre ML	2.5[b]	4 hr at 80°C in vacuum, 2 hr at 150°C in air, 16 hr at 225°C in air	Strongly bonded to SS anode cup. Some swelling during cure. Strong and resistant to crushing. Easily sawed and filed.

[a] Pyre ML, manufactured by E. I. duPont; DC-63-502, manufactured by Dow Corning.
[b] Assuming that the solvent is completely removed from the composite after curing.

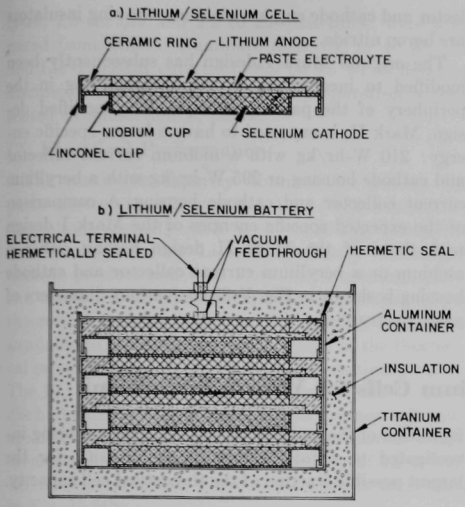

308-2199

FIG. V-31. Proposed NHLI Lithium/Selenium Battery (Mark I Design).

by Dow Corning), have been examined as possible binders with $LiAlO_2$ filler to form composite materials which possess both sealing and insulating properties. The initial results, which are summarized in Table V-11, indicate that structurally sound and adherent composites can be produced with both types of resins.

TABLE V-12. Characteristics of Proposed NHLI Lithium/Selenium Battery (Mark I Design)

Diameter of paste electrolyte:	8.3 cm
Active electrode area per cell:	38.7 cm²
Thickness of paste electrolyte:	0.2 cm
Thickness of selenium (without current collector):	0.3 cm
Total cathode thickness:	0.65 cm
Thickness of lithium and anode current collector:	0.35 cm
Diameter of cell:	9.4 cm
Thickness of cell:	1.36 cm
Number of cells:	4
Overall diameter of battery (with 1-cm thick insulation):	11.5 cm
Height of battery (with insulation):	7.5 cm
Volume of battery (with insulation):	781 cm²
Weight of battery:	1.09 kg
Specific energy of battery:	110 W-hr/kg
Operating temperature:	375°C
Open-circuit voltage (average):	2.0 V/cell, 8.0 V total
Operating voltage (average):	1.9 V/cell, 7.6 V total
Operating current:	1.32 A
Operating current density:	0.034 A/cm²
Short-circuit current density:	2.0 A/cm²

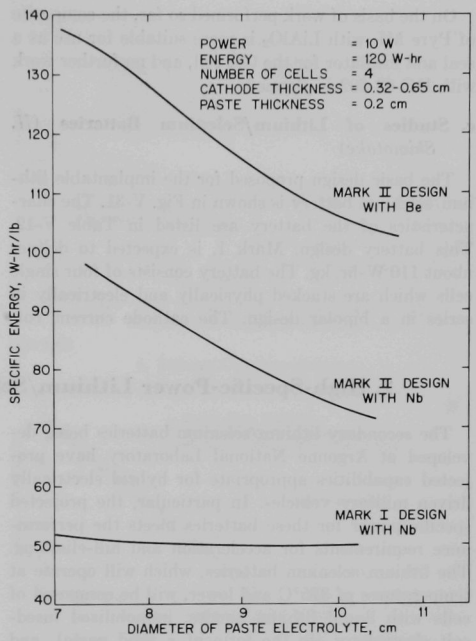

308-2200

FIG. V-32. Specific Energy Analysis of Proposed NHLI Batteries.

A composite of $LiAlO_2$ and Pyre ML was tested as an insulator in an anode cup of the design shown in Fig. V-30. The cup was thermally cycled from room temperature to 370°C under helium atmosphere; no cracking or separation of the composite from the walls of the cup occurred. Because the composite used in this cell design will be in contact with a paste electrolyte containing the molten LiF-LiCl-LiI eutectic, the corrosion resistance of the $LiAlO_2$ and Pyre ML composite towards the molten salt was also tested. After an exposure of 24 hr at 370°C under helium, attack of this composite was moderate and probably at an acceptable level.

DC 63-502, both as the pure resin and as a composite with $LiAlO_2$, was applied to two metal disks which were then joined and cured. Good bonding was achieved, but gas-tight seals were not obtained. In a corrosion test, a composite of DC 63-502 and $LiAlO_2$ was severely attacked by the molten LiF-LiCl-LiI eutectic after 24-hr exposure at 375°C under helium.

On the basis of work performed so far, the composite of Pyre ML with $LiAlO_2$ is more suitable for use as a seal and insulator for the test cell, and no further work with DC 63-502 is planned.

c. Studies of Lithium/Selenium Batteries (*H. Shimotake*)

The basic design proposed for the implantable lithium/selenium battery is shown in Fig. V-31. The characteristics of the battery are listed in Table V-12. This battery design, Mark I, is expected to deliver about 110 W-hr/kg. The battery consists of four single cells which are stacked physically and electrically in series in a bipolar design. The cathode current collector and cathode cup are niobium; the ring insulators are boron nitride.

The original Mark I design has subsequently been modified to incorporate a boron nitride ring in the periphery of the paste electrolyte. The modified design, Mark II, is expected to have a larger specific energy: 210 W-hr/kg with a niobium current collector and cathode housing or 295 W-hr/kg with a beryllium current collector and cathode housing. A comparison of the expected specific energies of the Mark I design with those of the Mark II design having either a niobium or a beryllium current collector and cathode housing is shown in Fig. V-32 for various diameters of paste electrolyte.

2. High-Specific-Power Lithium/Selenium Cells for Vehicle Propulsion[77]

The secondary lithium/selenium batteries being developed at Argonne National Laboratory have projected capabilities appropriate for hybrid electrically driven military vehicles. In particular, the projected specific power for these batteries meets the performance requirements for acceleration and hill-climbing. The lithium/selenium batteries, which will operate at temperatures of 375°C and lower, will be composed of cells with liquid lithium anodes, immobilized fused-salt electrolytes (in the form of a rigid paste), and liquid selenium cathodes. Typical peak power densities are 1 to 3 W/cm^2, which correspond to an estimated 440 W/kg for optimized multikilowatt batteries. Earlier work[5] on small (3.8 cm^2) laboratory-scale lithium/selenium cells resulted in the development of a cell having a peak power density of 2.7 W/cm^2, a cell life of at least 200 hr, and a cycle life of more than 50 charge-discharge cycles. The objective of the present program is to develop scaled-up cells (30–100 cm^2) having the same power-density capabilities as small cells and having long lives (1000–2000 hr and 1000–2000 charge-discharge cycles).

a. Studies of Scaled-up Lithium/Selenium Cells (*E. C. Gay, J. E. Kincinas*)

The cell scale-up program is concerned with (1) the development of large-area (~50 to 100 cm^2) lithium/selenium cells employing paste electrolytes and (2) the optimization of current collection at the selenium electrode. Cell performance is evaluated in terms of current density-voltage characteristics and voltage-time (capacity measurement) behavior as functions of cell structure and number of charge-discharge cycles. The porosity, pore-size distribution, and structural configuration of the cathode current collector are being investigated to obtain a high power density for the largest possible fraction of the theoretical cell capacity.

(1) Cell Components

An assembled paste electrolyte cell of 7.5-cm diameter, which was used for electrical performance measurements, is shown in Fig. V-33. In the cell, a boron nitride ring insulated the anode from the cathode compartment and also served as the anode housing. The anode consisted of stainless steel Feltmetal (type 302 SS, 1.6 mm thick, 90% porosity; or type 430 SS, 6.4 mm thick, 87% porosity) that had been soaked with lithium at 550°C. The cathode consisted of niobium expanded mesh, 72% porosity (0.078-cm die size) or 63% porosity (0.23-cm die size), wetted with selenium at 300°C. Prior to wetting, sheets of the niobium mesh had been welded together and then welded to the inner surface of the niobium cathode cup. The paste electro-

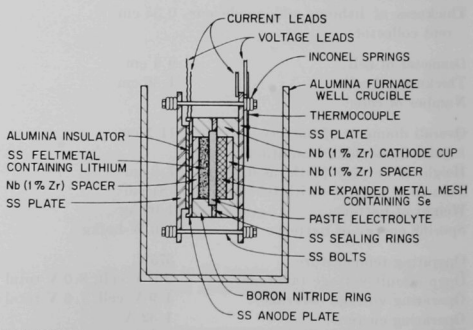

308-2201

FIG. V-33. Lithium/Selenium Cell with 7.5-cm Diameter Paste Electrolyte.

[77] This work is sponsored by the U.S. Army Mobility Equipment Research and Development Center, Ft. Belvoir, Virginia.

lytes, 7.5-cm dia and 2.2 to 2.8 mm thick, were prepared from lithium aluminate filler (50 or 40 wt %) and LiF-LiCl-LiI eutectic (50 or 60 wt %). A detailed discussion of the paste electrolyte preparation is presented in subsection b, below.

(2) Electrical Performance

The maximum capacity obtained for 7.5-cm dia paste-electrolyte cells was 10.1 A-hr (0.32 A-hr/cm^2); the voltage-capacity curve is shown in Fig. V-34a. On the assumption that Li_2Se is the fully discharged cathode product and with 7.6% excess selenium present, the 10.1 A-hr capacity corresponds to 60.5% of the theoretical capacity based on the quantity of lithium available to form product and to 50.0% of the theoretical capacity based on the quantity of selenium present. The 10.1 A-hr capacity was measured at 405°C, 1.5 A discharge current for 6.75 hr, and an average cell voltage of 1.3 V. During short-time voltage-current measurements, a short-circuit current density of 1.3 A/cm^2 (41 A) was obtained. These measurements are shown in Fig. V-34b.

The maximum short-circuit current density obtained from a 7.5-cm dia paste electrolyte cell was 3.8 A/cm^2 (120 A). This cell was also discharged at constant current densities of 0.31 A/cm^2 (9.7 A) and 0.49 A/cm^2 (15.6 A). The average cell voltages during these discharges were 1.75 and 1.54 V, respectively. These results are shown in Fig. V-35.

The major problem areas encountered during the initial performance tests for 7.5-cm dia paste electrolyte cells were:

1) The need to enhance wetting of the paste electrolyte by lithium in the anode. Lack of wetting in some cells has resulted in high internal resistance and correspondingly poor electrical performance.

2) The need to identify the major factors contributing to good electrical performance of the cells so that reproducible, optimum performance can be maintained for long periods of time. A major effort in the experimental program is directed toward varying cell parameters with the air of isolating the factors that contribute to optimum capacity density and provide high-power-density capabilities.

3) The need to improve current collection at the selenium electrode.

b. Studies of Paste Electrolytes for Lithium/Selenium Cells

An important area of investigation of lithium/selenium cells is the development of large-area (30 to 100 cm^2) paste electrolytes of maximum strength, minimum weight, and minimum electrolytic resistivity to serve as separators between the lithium anode and selenium cathode. The strength of the paste electrolyte

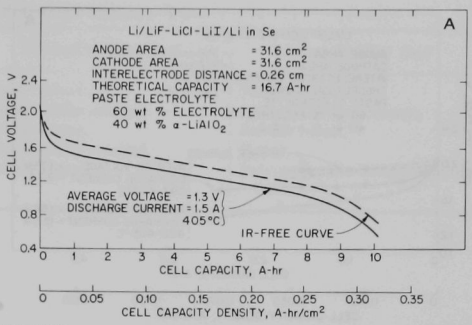

308-2202

a. Voltage-Capacity Curves.

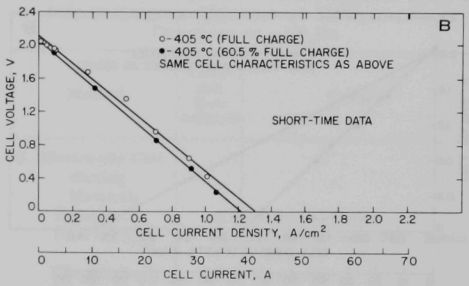

308-2203

b. Voltage-Current Characteristics.

FIG. V-34. Performance Curves for Lithium/Selenium Cell showing Maximum Capacity Density.

is increased by increasing the ceramic filler content, whereas the resistivity is decreased by increasing the fused-salt content. The objective, therefore, is to prepare a paste electrolyte with the maximum fused-salt content consistent with good strength.

(1) Physicochemical Properties of Paste Electrolytes (*L. E. Trevorrow, J. G. Riha*)

Studies aimed at developing paste electrolyte disks possessing an optimum combination of conductivity, strength, and wettability by molten lithium have begun. The initial experiments involved (1) pressing paste disks (13-mm, 2–3 mm thickness) from mixtures of LiF-LiCl-LiI eutectic and lithium aluminate and (2) investigating their resistances and wettability by molten lithium.

Since good wetting of the paste electrolyte by lithium is essential for valid resistance measurements, wetting experiments were conducted first. Wettability of the paste disks by molten lithium has been assessed by visual observation of the adherence of the lithium to paste surfaces. Paste surfaces exposed to molten lith-

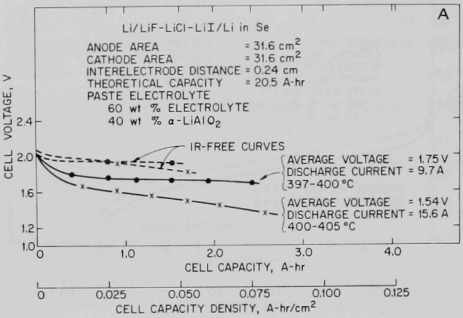

308-2204

a. Voltage-Capacity Curves.

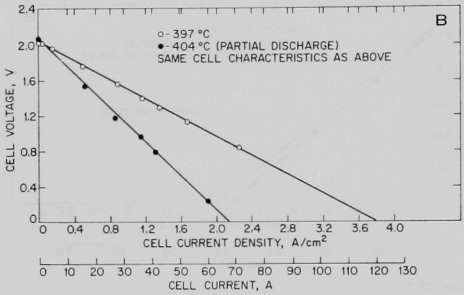

308-2205

b. Voltage-Current Characteristics (short-time data).

FIG. V-35. Performance Curves for Lithium/Selenium Cell showing Maximum Short-Circuit Current Density.

ium at 400 to 500°C became darkened and showed small areas of adhering lithium that increased in size with exposure time. Paste surfaces became pitted at these temperatures, possibly as a result of dissolution of salt in molten lithium. Additional wetting experiments showed that paste disks could be completely covered with an adherent coating of lithium by first exposing the disks to lithium vapor ($\sim 10^{-2}$ mm) at 530°C for about 16 hr, and then contacting them with molten lithium (previously saturated with LiF-LiCl-LiI eutectic) at 350 to 360°C. Further tests are needed to determine whether these are optimum conditions for wetting the paste electrolyte.

Resistances of the paste disks are currently being tested by dc measurements of the voltage across the disk and the current through the disk.

(2) Fabrication of Larger-Diameter Paste Electrolyte Disks (*E. C. Gay, J. E. Kincinas*)

Scaling-up the 2.5-cm dia lithium/chalcogen secondary cells requires the development of techniques for preparing paste electrolyte disks of 7.5-cm and larger diameters. Consequently, 7.5-cm dia paste electrolyte disks are being prepared under various pressing conditions to determine the effect of pressing force, temperature, and specific surface area of the ceramic filler material on the disk density. (Densities of approximately 99% of the theoretical value are desirable.) In recent tests, the LiF-LiCl-LiI eutectic was mixed with the filler under an inert atmosphere, the mixture pressed at temperatures from 25 to 275°C using a press of 5.9×10^4-kg capacity, and the density of the disk was then measured.

TABLE V-13. Densities of 7.5-cm Diameter Paste Electrolyte Disks

Electrolyte[a] Content (wt %)	Filler	Filler Surface Area (m²/g)	Filler Density[b] (g/cm³)	Pressing[c] Temperature (°C)	Pressing Time (min)	Paste Electrolyte Density (g/cm³)	Percent of Theoretical Density
50	α-$LiAlO_2$	34.8	3.83	~250	15	3.26	89
60	α-$LiAlO_2$	35.8	3.88	25	15	2.80	77
60	α-$LiAlO_2$	35.8	3.88	25	15	2.75	76
60	α-$LiAlO_2$	35.8	3.88	25	15	2.95	81
60	α-$LiAlO_2$	46.3	3.28	165	15	2.39	70
60	γ-$LiAlO_2$		2.89	260	15	3.27	99
60	γ-$LiAlO_2$		2.89	275	15	2.97	90
60	γ-$LiAlO_2$		2.89	270	15	3.26	99
60	γ-$LiAlO_2$		2.89	25	60	2.55	77
60	α-$LiAlO_2$	46.3	3.28	170	15	2.86	84
60	α-$LiAlO_2$	46.3	3.28	209	15	3.17	93
60	α-$LiAlO_2$	46.3	3.28	188	60	3.17	93
60	α-$LiAlO_2$	46.3	3.28	188	60	3.14	92
60	α-$LiAlO_2$	46.3	3.28	153	60	2.90	85

[a] LiF-LiCl-LiI eutectic, 3.50-g/cm³ density.
[b] The differences in the filler densities are a result of the varying quantities of α-$LiAlO_2$ and γ-$LiAlO_2$ in the mixtures.
[c] All disks were pressed with a force of 5.7×10^4 kg under vacuum.

TABLE V-14. Results of Polymeric Sealant Tests

Material	Type	Thermal Stability Test[a]	Lithium Stability Test[b]
Pyre ML[c]	Polyimide resin	Sample intact.	Sample intact.
DC-R-7521[d]	Silicone resin	Sample badly cracked.	Little additional attack.
XR-6-3502[d]	Silicone resin	Sample intact.	Sample intact.
GE-SR-82[e]	Silicone resin	Sample badly cracked.	Failed.
CHR Temp-R-Tape[f]	Polyimide film; silicone polymer adhesive	Sample intact.	Polyimide resin intact; adhesive failed.

[a] Temperature, 375°C; duration, 137 hr.
[b] Temperature, 190°C; duration, 102–119 hr.
[c] Product of E. I. duPont de Nemours and Co., Inc.
[d] Product of Dow-Corning Corp.
[e] Product of General Electric Corp.
[f] Product of Connecticut Hard Rubber Co., Inc.

Table V-13 shows the pressing conditions and measured densities for 7.5-cm dia paste electrolyte disks. Paste electrolytes were prepared with densities from 77 to 99% of the theoretical values. Although the optimum pressing conditions have not yet been determined, these data show that high-density paste electrolytes can be prepared from both α-$LiAlO_2$ and γ-$LiAlO_2$. Hot pressing under vacuum appears to be necessary for high density in the present pressing apparatus.

c. Sealants and Insulators for Lithium/Selenium Cells (*M. L. Kyle, P. W. Krause*)

Hermetically sealed cells and batteries may require sealants stable to lithium, selenium, and lithium-selenium alloys at 300 to 375°C. Several high-temperature polymers are being evaluated for use as sealants.

The polymers were tested both for their thermal stability at a temperature of 375°C and for their resistance to molten lithium at 190°C. The tests were run sequentially, with the polymer being cured according to the manufacturer's suggested procedure, then tested for thermal stability in a helium atmosphere for 137 hr at 375°C, and finally tested for resistance to molten lithium for 102 to 119 hr at 190°C. The exposure conditions were chosen so that the edge of a thin (~0.025-cm) polymer film was exposed to both helium and lithium. This type of exposure is considered to be typical of the conditions expected in actual service when the polymer would be used mostly as an adhesive. The results of these tests are shown in Table V-14.

These preliminary tests did not provide sufficient data to draw any general conclusions about the utility of polymers as insulators and sealants for a lithium/selenium cell or battery. The tests do, however, indicate that at least limited high-temperature stability and lithium resistance may be obtainable from polymers, and that more extensive testing under simulated cell environments is desirable.

TABLE V-15. Corrosion of Test Materials by 20 at. % Lithium-Selenium Mixtures at 375°C for Test Durations of ~300 Hr

Material	Corrosion Rate (mils/yr)	Remarks
A. Electrically Conducting Materials		
Niobium	3.0	Slight dissolution.
Nb-1 wt % Zr	4.3	Nonconductive film formation.
Chromium	7.1	Dissolution.
Haynes 25[a]	23	Thin nonconductive surface film.
Uniloy (50 wt % Cr-49 wt % Ni-1 wt % Ti)	79	Nonconductive film formation.
440 SS	270	Uniform dissolution.
Molybdenum	>330	Sample destroyed.
Hastelloy C	390	
Titanium	570	
405 SS	650	
Zircaloy-2	>1800	
B. Electrically Insulating Materials		
MgO[b]	26	Apparent Li reduction.
Y_2O_3	71	Reaction layer present.
BN[c]	<75	Resistant to attack.

[a] Product of Union Carbide Corp. Composition: 20 wt % Cr, 15 wt % W, 10 wt % Ni, 3 wt % Fe, 1 wt % Mn, 1 wt % Si, 0.10 wt % C, balance Co.
[b] Single crystal.
[c] Tested in pure selenium.

d. Corrosion by Lithium-Selenium Mixtures (*M. L. Kyle, P. W. Krause*)

The corrosion resistance of various materials to lithium-selenium mixtures at 375°C is being deter-

mined to identify suitable materials for use in lithium/selenium cells. Some preliminary data on lithium-selenium corrosion were presented in Section V.C.3 of this report. Table V-15 presents the results of more extensive static-immersion and corrosion-agitator tests.

The niobium, niobium-1% zirconium, and chromium data confirm the results of the preliminary tests (see Section V.C.3) and demonstrate that these materials, along with beryllium and tungsten (tested only in preliminary tests; longer term tests in progress), are suitable electrically conducting containment materials for lithium-selenium mixtures. The corrosion rates for niobium, niobium-1% zirconium, and chromium are, in general, lower than those measured in the preliminary tests because the present tests for these materials were longer, and linear extrapolation of the data resulted in lower average rates. Of the other electrically conducting materials tested only Haynes 25 appears suitable for containment of lithium/selenium mixtures. Two materials, Haynes 25 and the Nb-1% Zr alloy, formed non-electrically conducting surface films of unidentified composition; this may limit their application to those cell components not requiring good electrical conductivity.

Of the ceramic (insulating) materials tested, boron nitride is the most resistant to lithium-selenium mixtures, and it is being used in scale-up studies of preliminary cells.

3. Lithium/Sulfur Cells for Vehicle Propulsion[78]

Battery-powered electric vehicles should significantly reduce the amount of air pollution caused by combustion-engine exhaust gases. However, available bateries do not have sufficient energy storage capacity per unit weight and consequently are heavy, bulky, and too costly for consumer acceptance. Several recent studies[79, 80] have made it clear that a major improvement in specific energy (W-hr/kg) without sacrifice of peak specific power (W/kg) is necessary before electric passenger vehicles become technically attractive. For an electric passenger vehicle to have a range approaching 200 miles and an acceptable acceleration capability, the battery must have a specific energy of at least 200 W-hr/kg and a maximum specific power of at least 200 W/kg. To be economically feasible for passenger vehicles, the battery should have a cost of less than about $2/kg.[80]

The ultimate objective of the present experimental program is to provide the technology necessary to construct a multikilowatt secondary battery able to meet the above requirements. The short-term objectives are to investigate the performance characteristics of some promising lithium/chalcogen cells, to provide a cell structure compatible with vehicle applications, and to identify suitable materials of construction. The program is beginning with the study of lithium/sulfur cells having both liquid and paste electrolytes. The laboratory work has centered around the study of small-scale lithium/sulfur cells (0.7 to 4 cm^2 electrodes) and the achievement of high power densities (>5 W/cm^2 with liquid electrolytes) and high capacity densities (>0.3 A-hr/cm^2 with liquid electrolytes).

a. Investigation of Small-Scale Lithium/Sulfur-Cells (*H. Shimotake, J. C. Cassulo*)

(1) Cells with Liquid Electrolytes

Electrochemical cells with liquid electrolytes may not be suitable for vehicular application; however, small-scale experiments with such cells are valuable in the exploratory stages of our work. Liquid-electrolyte cells of two different designs have been operated: (1) cells in which the cathode and anode were held vertically in the electrolyte, and (2) cells in which the electrodes were held horizontally. Tests on these cells are described below.

Vertical cell. An experimental vertical lithium/sulfur cell has been operated at temperatures from 340 to 380°C under a helium atmosphere. The electrolyte was the molten LiF-LiCl-LiI eutectic (mp, 341°C). Both the cathode and anode compartments were made of type 304 stainless steel and had electrode areas of 3.8 cm^2 and depths of 1.25 cm. Pieces of stainless steel Feltmetal (90% porosity), soaked with either sulfur or lithium, were placed in the appropriate electrode holders; average amounts of reactants held in the Feltmetal pieces were 3.8 g sulfur and 3.6 g lithium, amounts which correspond to about 10 A-hr capacity. The interelectrode distance was varied, but for most of the experiments it was 1.0 cm.

As stated above, the cell was discharged and charged at temperatures from 340 to 380°C; the results for 350°C are shown in Fig. V-36. During the experiments,

[78] This work is sponsored by the National Air Pollution Control Administration of CPE Health Service, U.S. Department of Health, Education and Welfare.

[79] Report of the Panel on Electrically Powered Vehicles, "The Automobile and Air Pollution: A Program for Progress," U.S. Dept. of Commerce (October 1967).

[80] J. H. B. George, L. J. Stratton, R. G. Acton, "Prospects for Electric Vehicles. A Study of Low Pollution-Potential Vehicles—Electric," A. D. Little Report to U.S. Dept. of Health, Education and Welfare, NAPCA (May 1968).

some of the sulfur separated from the cathode, floated to the surface of the liquid electrolyte, and reacted with lithium in the anode. The products of the chemical reaction formed a bridge between the two electrodes, causing a short circuit. The voltage-current density curve for this cell shows that high performance can be expected if the loss of sulfur from the cathode can be prevented.

Horizontal cell. In experiments with the horizontal lithium/sulfur cell (similar to the one shown in Fig. V-21 and described in Section V.C.1.b. of this report), we have been attempting to reduce ohmic and diffusion overvoltages by seeking the optimum cathode current collector configuration. Seven cathode current collectors made of stainless steel Feltmetal having various porosities and pore sizes were evaluated in Li/LiF-LiCl-LiI/S cells at 375°C. Because of the limited corrosion resistance of stainless steel to sulfur, data were gathered within 2 hr after the start of the experiments. The physical characteristics and capacities of the cells are listed in Table V-16.

The results of this series of performance tests show that the capacity density of the lithium/sulfur cell, when operated under similar charge and discharge conditions, is related to the porosity of the cathode current collector. The following empirical expression, derived to aid in cell design, relates the capacity density to the porosity of the cathode current collector:

$$C = 0.26\ f^2 \qquad (12)$$

where C = capacity density, A-hr/cm^2, and f = void fraction or fractional porosity. Equation 12 is based on the best data taken at 1.4 A/cm^2 discharge at 375°C

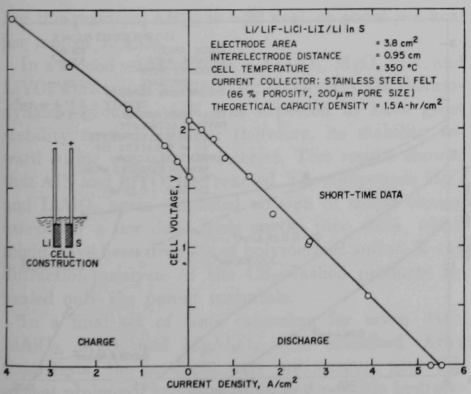

308-2206

FIG. V-36. Voltage-Current Characteristics of a Lithium/Sulfur Cell.

TABLE V-16. Characteristics of Cathode Structures and Cell Performance

Cell system	Li/LiF-LiCl-LiI/S
Anode area	2.6 cm²
Cathode area	0.7 cm²
Interelectrode distance	0.3 cm
Typical cell temperature	375°C

Cathode			Theoretical Capacity[a] (A-hr)	Capacity (A-hr)	Overvoltages[b]		
Material	Porosity (%)	Pore Size (μm)			η_r (V)	η_d (V)	η (V)
430 SS	80	240	0.910	0.12	0.48	0.50	0.98
430 SS	60	100	0.657	0.067	0.75	0.60	1.35
302 SS	40	19	0.437	0.030	1.0	0.90	1.9
302 SS	70	19	0.767	0.067	0.46	0.45	0.91
302 SS	60	19	0.657	0.042	0.75	0.80	1.55
302 SS	80	29	0.910	0.18	0.38	0.40	0.78
430 SS	80	240	0.910	0.14	0.48	0.65	1.13

[a] Based on the conversion of total sulfur charge into Li_2S. No consideration was made for evaporation losses.

[b] These overvoltages were calculated from IR-free voltages of the cells running at 1.4 A/cm² discharge after 0.047 A-hr/cm² operation. η_r = resistance overvoltage = IR-free voltage − terminal voltage. η_d = diffusion overvoltage = open circuit voltage − IR-free voltage. η = total overvoltage = $\eta_r + \eta_d$.

and is limited to porosity values ranging from 0.4 to 0.8. The equation indicates that the capacity density is highly sensitive to the porosity of the cathode current collector. A comparison between the experimental data and the values calculated from Eq. 12 is shown in Fig. V-37.

Several horizontal cells were operated at 290°C with an electrolyte of the LiCl-LiI-KI eutectic (mp, 265°C) to obtain performance data at a lower temperature than is possible with the LiF-LiCl-LiI eutectic electrolyte. In these cells, the lithium, which was held in the stainless steel Feltmetal anode current collector, was gradually displaced by the electrolyte, which eventually caused a short circuit. Moreover, the alumina cloth separator was not wetted by the LiCl-LiI-KI eutectic, although it was readily wetted by the LiF-LiCl-LiI eutectic.[81] Because of these problems, operation of the cells with LiCl-LiI-KI electrolyte was not stable. The highest short-circuit current density achieved for this cell was 2 A/cm^2.

Further investigations of liquid-electrolyte lithium/sulfur cells will be concerned primarily with the effects of different cathode current-collector configurations upon the current density and capacity density of the cells. Investigations will also be conducted on lower-melting electrolytes (e.g., LiBr-RbBr; mp, 259°C) and on additives to increase the electronic conductivity of sulfur.

[81] The separator prevents contact between the electrodes.

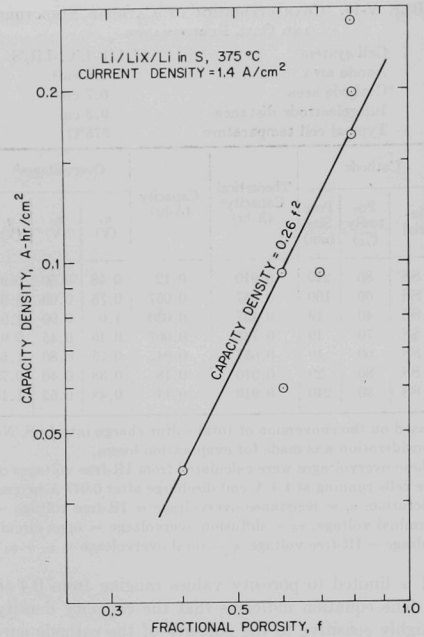

308-2207

FIG. V-37. Relationship between Porosity of Cathode Current Collector and Capacity Density for a Lithium/Sulfur Cell.

(2) Cells with Paste Electrolytes

Cells with liquid electrolytes may not be practical in vehicle applications where moderate motion could result in a short circuit. In this work, the electrolyte has been immobilized as a rigid paste by combining the fused salt with a finely divided inert ceramic filler, such as $LiAlO_2$. However, the performance of a cell with a paste electrolyte is reduced because the filler material increases the internal resistance of the cell.

To achieve the highest possible performance with a lithium/sulfur paste electrolyte cell, it is essential that the paste be well wetted by both electrode materials. Various methods of accomplishing this have been investigated. One of the methods has been to imbed metallic meshes in the two flat surfaces of the paste disks. Two paste disks have been pressed with a stainless steel mesh imbedded on one side and a niobium mesh on the other. The two pastes were made under a pressing force of 1.27×10^4 kg after adding more LiF to immobilize the LiF-LiCl-LiI eutectic (40 wt % LiF-60 wt % electrolyte). The strength of the bonded disks was sufficient for use in operating lithium/sulfur cells; the results are shown in Fig. V-38. Short-circuit current densities of 0.9 A/cm² and capacity densities of up to 0.05 A-hr/cm² were obtained. It appears that this method of pressing metallic mesh into the paste surface reduces the cell resistance. The pastes showed deformation, but the color remained white-to-gray after about 24 hr of operation. The lithium electrode showed good adhesion to the paste, the stainless steel mesh remaining well imbedded in the paste; however, the sulfur electrode, consisting of four niobium mesh layers, was dry, perhaps due to evaporation of the sulfur. Work will continue on the development of lithium/sulfur paste-electrolyte cells, with emphasis on current collector–paste electrolyte combinations that result in lower internal cell resistance and increased capacity densities.

b. Fillers for Paste Electrolytes for Lithium/Sulfur Cells (*A. K. Fischer, F. L. Ferry*)

Research on paste electrolyte fillers for the lithium/sulfur cell has centered on the synthesis of the materials $LiYO_2$ and $MgAl_2O_4$, and on the stability testing in molten sulfur of γ-$LiAlO_2$, AlN, $LiYO_2$, MgO, ThO_2, $MgAl_2O_4$, and CaO.

The compound $LiYO_2$ was prepared according to the reaction

$$Li_2CO_3 + Y_2O_3 \rightarrow 2LiYO_2 + CO_2$$

by heating the reactants at 800°C for one day. The product, after being washed with water, was obtained in greater than 90% yield. X-ray diffraction analysis showed that the product was $LiYO_2$ with only a minor amount of Y_2O_3 present.

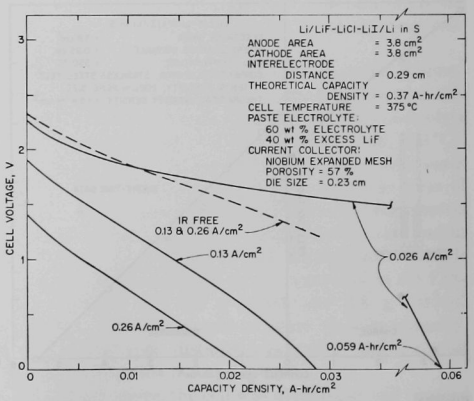

308-2208

FIG. V-38. Voltage-Capacity Curves for Li/S Cell.

The spinel, $MgAl_2O_4$, was prepared by the reaction

$$MgCl_2 \cdot 6H_2O + Li_2CO_3 + Al_2O_3 \rightarrow MgAl_2O_4 + 6H_2O + CO_2 + 2LiCl$$

The powdered reactants, mixed and compressed into a pellet, were heated at 900°C for three days. The product was washed free of carbonate, analyzed by X-ray diffraction, and found to contain $MgAl_2O_4$ as the major component. One weak line in the X-ray diffraction pattern could not be assigned to $MgAl_2O_4$.

A number of sulfur stability tests have been conducted. The general procedure was to mix each test material, as a powder, with sulfur and to hold the mixture at 375°C in a helium atmosphere for several days. These samples were then examined and analyzed.

In one series, γ-$LiAlO_2$, CaO, ThO_2, and MgO were tested for five days. At the end of this time, the ThO_2 had obviously reacted. Also, CaO reacted, although this might have been expected since the following reaction is known to occur at calcining temperatures:

$$4CaO + 4S \rightarrow 3CaS + CaSO_4$$

The compounds, γ-$LiAlO_2$ and MgO, were apparently unattacked, except for slight signs of darkening in the MgO. The samples were washed with CS_2 to remove sulfur and then analyzed by X-ray diffraction. In the MgO sample, no reaction products (such as MgS or $MgSO_4$) were found, but in the analysis of the $LiAlO_2$ sample, Li_2S was given as a possible, very minor constituent. A reaction between $LiAlO_2$ and sulfur may be possible:

$$5LiAlO_2 + 4S \rightarrow Li_2SO_4 + 2Al_2O_3 + \tfrac{3}{2}Li_2S + \tfrac{1}{2}Al_2S_3$$

For this reaction, ΔH°_{298} is -22 kcal, or about -4 kcal per mol of $LiAlO_2$.

In a second series of tests, γ-$LiAlO_2$, MgO, AlN, and $LiYO_2$ were tested at 375°C for seven days. On thermodynamic grounds, AlN was expected to have great stability toward lithium; therefore, its stability toward sulfur was also of interest. Test results showed that AlN and $LiYO_2$ had reacted. The compounds MgO and $LiAlO_2$ again exhibited no sign of major change except for a few dark spots on the tube walls, which might have been droplets of polymerized sulfur. X-ray diffraction analysis of the CS_2-washed products revealed only the parent materials.

In a final set of tests extending for seven days, $LiAlO_2$, MgO, and $MgAl_2O_4$ were examined. After these tests, the products were not washed with CS_2 so that prolonged exposure to air and possible hydrolysis of any reaction products would be avoided. X-ray diffraction analysis revealed no reaction products.

These results suggest that γ-$LiAlO_2$, MgO, and $MgAl_2O_4$ are reasonable candidates for fillers as far as sulfur stability is concerned. Lithium aluminate was included in all the tests because this filler has shown a high degree of stability so far. Nevertheless, it is still possible that, with enough time, $LiAlO_2$ might react with sulfur according to the reaction given above. Since prolonged exposure would occur in a practical lithium/sulfur battery, much longer stability tests will be needed, perhaps as long as six months in duration.

c. Corrosion by Sulfur-Containing Mixtures (*M. L. Kyle, P. W. Krause*)

The corrosion resistance of various materials to conditions that would be encountered in the anode and cathode compartments of lithium/sulfur cells is being determined to identify suitable materials of construction. Screening tests of 100- to 300-hr duration are performed to select promising materials. In more extensive evaluations, the promising materials are examined initially in longer-term corrosion tests, and ultimately as prototype cell parts.

Two classes of materials resistant to lithium-sulfur mixtures at temperatures near 375°C are needed. Firstly, a corrosion-resistant material possessing good electrical conductivity is required to serve as the cathode current collector and probably as the cathode housing. Secondly, a corrosion-resistant material that is electrically insulating is required to prevent short-circuit contact between the anode and cathode housings. At the present time, corrosion of electrically conducting materials by lithium is not being systematically investigated because small-scale cell studies have indicated that austenitic stainless steels possess adequate corrosion resistance for use in the present cell program.

The two types of corrosion tests that are being performed, static immersion and corrosion agitator tests, are described in Section V.C.3 of this report. After a sample has been exposed in either type of corrosion test, adhering cathode material is removed with water or carbon disulfide. The weight loss of the specimen is measured and the resulting value is converted to an annual corrosion rate, which is reported in mils per year penetration. For samples that lose weight, extrapolation is based on an assumed linear rate. For samples that gain weight because of film formation, extrapolation is based on an assumed parabolic rate. The exposed samples are examined metallographically to determine corrosion effects not apparent from simple weight-change considerations. All metal samples are also tested for electrical conductivity after exposure, since some sulfide films tend to be electrically insulat-

TABLE V-17. CORROSION OF MATERIALS BY LITHIUM-SULFUR MIXTURES AT 375°C

Material[a]	Lithium Concentration[b] (at. %)	Exposure Time (hr)	Corrosion Rate[c] (mils/yr)	Remarks
A. Electrically Conductive Materials				
Chromium	20	100	0.0	No detectable corrosion.
Chromium*	20	328	+6.6	Conductive surface film.
Molybdenum	10	100	0.1	No detectable corrosion.
Inconel 702*	20	311	0.9	Thin nonconductive surface film.
LT-1	10	101	1.0	Slight Al_2O_3 reduction.
Sandvik 2RK65*	20	311	1.3	Conductive surface film.
205 SS*	20	309	2.0	Conductive surface film.
Zircaloy-2	10	101	2.1	Slight dissolution.
Zircaloy-2	20	136	+0.2	Dissolution; surface film.
Worthite*	20	311	+2.6	Conductive surface film.
347 SS*	20	311	3.4	Conductive surface film.
Niobium*	20	306	3.7	
Sandvik 2RN65*	20	311	4.0	Conductive surface film.
Inconel 718	10	100	+4.5	Nonconductive surface film.
Sandvik 2RE10*	20	311	4.7	Conductive surface film.
Durimet 20	10	100	+9.3	Nonconductive surface film.
Tantalum	10	101	22	Dissolution.
Iron	10	100	93	Dissolution.
Nickel	10	100	71	Dissolution.
Beryllium*	20	233	22	Sample pitted.
Hastelloy B	20	309	76	Dissolution.
B. Electrically Insulating Materials				
Boron Nitride	0	101	<23	No detectable attack.
Yttria*	20	311	1.3	
Magnesia*	20	304	44	Single crystal sample.

All runs were corrosion agitator tests except those marked with an asterisk, which were static immersion tests.
[a] Balance sulfur.
[b] "+" sign indicates film formation resulting in weight gain of specimen.
[c]

ing. The results of tests conducted to date are presented in Table V-17.

Of the electrically conductive materials tested, molybdenum, chromium, Zircaloy-2, and Inconel 702 are the most corrosion resistant. Molybdenum evidenced virtually no corrosion. Chromium was unattacked in a corrosion agitator experiment, but was covered with a thin conductive film after a static immersion test; this difference may be due to the more dynamic conditions of the agitator test. Similarly, Zircaloy-2 showed little attack (2 mils/yr) in a corrosion agitator test. In a second test, low corrosion rates were also observed, but the sample was covered with a thin, nonconductive surface film. The reason for this difference in results between the two tests is, as yet, unexplained. Inconel 702 was only slightly attacked but a similar nonconductive surface film formed on the specimen surface. LT-1, a high-chromium cermet with Al_2O_3, was only slightly attacked by reduction of the Al_2O_3 content by lithium. These data also confirm the good corrosion resistance of chromium that was previously observed. A variety of austenitic stainless steels and high-temperature nickel-base alloys evidenced moderate corrosion rates of 4 to 10 mils/yr. The mechanism for corrosion protection was usually through the formation of thin surface films; some of these were electrically conductive whereas others were insulating. The compositions of these films have not been determined, but an effort will be made to determine their nature because alloys of these types appear promising.

Of the electrically insulating materials tested, boron nitride and yttria appear to be the most resistant and will be used in initial cell tests. Single-crystal magnesia is not resistant to the lithium-sulfur system.

4. Performance Comparison

To understand the capabilities of the various cells studied, including those previously reported (see ANL-7575, p. 157), the performance data must be placed in perspective. A comparison of the voltage-current density characteristics for the cells with liquid electrolytes is shown in Fig. V-39. For purposes of the comparison, the original data for the Li/P_4S_{10} and Li/P_4S_3 cells were adjusted (as indicated by the dashed lines) to correspond to a smaller interelectrode distance. The average interelectrode distance for the cells of Fig. V-39 was 0.4 cm, and the active electrode area varied from 0.7 to 10 cm^2. A similar comparison of voltage-current density characteristics is shown in Fig. V-40 for cells with paste electrolytes. Data are given for a scaled-up, 7.5-cm dia lithium/selenium cell as well as for 2.5-cm dia cells. Table V-18 lists the best capacity densities obtained for both the liquid- and paste-electrolyte cells; the best cell performance is achieved in cells having high capacity densities at high current densities. No data are given for the lithium/phosphorus cell, which has not performed well enough to be of further interest.

The performance data shown in Fig. V-40 and Table V-18 were used, together with a battery design similar to that shown above in Fig. V-31, to calculate the expected performance for fully engineered (lightweight) batteries with paste electrolytes. These calculated values (based on a 30-min rate for specific power and a 2-hr rate for specific energy) are shown in Table V-19 for lithium/tellurium, lithium/selenium, and lithium/sulfur batteries. The expected performance for a lithium/(selenium + tellurium) battery would be similar to that for the lithium/selenium battery; likewise, the expected performance for a lithium/P_4S_{10} battery would be almost the same as that for the lithium/sulfur battery. The calculations indicate that both specific power and specific energy increase as the equivalent weight of the cathode material decreases,

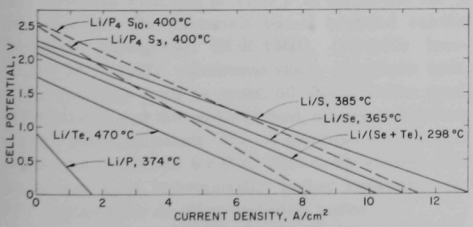

308-2209

FIG. V-39. Comparison of the Voltage-Current Density Characteristics of Cells with Liquid Electrolytes.

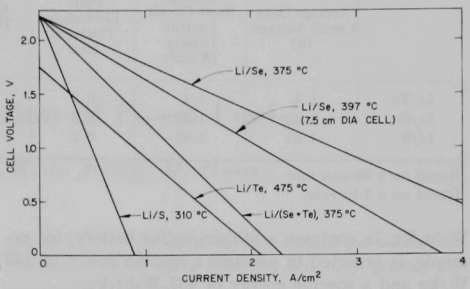

308-2210

FIG. V-40. Comparison of the Voltage-Current Density Characteristics for Cells with Paste Electrolytes (all cells 2.5 cm in diameter except as indicated).

TABLE V-18. Summary of Capacity Densities Achieved for Lithium/Chalcogen Cells

Cell	Type of Electrolyte[a]	Temperature (°C)	Capacity Density (A-hr/cm^2)
Li/LiF-LiCl-LiI/Te	L	470	0.125 at 2 A/cm^2
	P (2.5)	475	—
Li/LiF-LiCl-LiI/Se	L	365	0.52 at 2 A/cm^2
	P (2.5)	375	0.202 at 0.26 A/cm^2
	P (7.5)	397	0.32 at 0.5 A/cm^2
Li/LiCl-LiI-KI/Se + Te	L	298	0.52 at 0.13 A/cm^2
Li/LiF-LiCl-LiF/Se + Te	P (2.5)	375	0.274 at 0.26 A/cm^2
Li/LiF-LiCl-LiI/S	L	385	0.38 at 2.8 A/cm^2
$Li/LiBr-RbBr/P_4S_{10}$	L	400	0.05 at 0.6 A/cm^2
$Li/LiBr-RbBr/P_4S_3$	L	400	0.04 at 0.58 A/cm^2

[a] L indicates liquid-electrolyte cells ranging in active electrode area from 0.7 to 10 cm^2. P (2.5) indicates a 2.5-cm dia paste-electrolyte cell. P (7.5) indicates a 7.5-cm dia paste-electrolyte cell.

i.e., the lithium/sulfur battery would show the best performance of the three. From an economic standpoint, only batteries using small amounts of the relatively costly selenium and tellurium are practical.

The advantages of the lithium/chalcogen batteries can be seen by a comparison of their expected performance characteristics (see Table V-19) with the performance characteristics of conventional batteries. On the same rate basis (a 30-min rate for specific power and a 2-hr rate for specific energy), a Cd/Ni_2O_3 battery has a specific power of 70 W/kg and a specific energy of 35 W-hr/kg; a Pb/PbO_2 battery has a specific power of 50 W/kg and a specific energy of 30

TABLE V-19. SPECIFIC POWER AND SPECIFIC ENERGY CALCULATED FOR LITHIUM/CHALCOGEN BATTERIES

	Average Open Circuit Voltage (V)	Average Short-Circuit Current Density (A/cm^2)	Paste Electrolyte Thickness (cm)	Cathode Thickness (cm)	Cathode Cup Material	Anode Cup Material	Specific Power[a] (W/kg)	Specific Energy[b] (W-hr/kg)
Li/Te	1.4	1.4	0.2	0.5	W	Be	95	115
Li/Se	1.85	1.85	0.2	0.5	Be	Be	254	313
Li/S	1.85	1.85	0.2	0.5	Mg (or Be)	Be	342	437

[a] Based on a 30-min rate.
[b] Based on a 2-hr rate.

W-hr/kg. In contrast, a lithium/sulfur battery, for example, is expected to produce a specific power of 342 W/kg and a specific energy of 437 W-hr/kg.

Some of the applications that could be considered for a practical lithium/chalcogen battery include power for spacecraft, military communications, materials-handling vehicles, military vehicles, heart pumps, boats and submarines, remote locations, buses and trucks, urban automobiles, and off-peak energy storage for central stations.

VI

Fluidized-Bed Combustion of Fossil Fuels[1]

(*A. A. Jonke, E. L. Carls, R. L. Jarry, M. Haas*)

A major source of atmospheric pollutants is coal combustion in central power stations and industrial steam boilers. Fluidized-bed combustion of coal is being investigated because it appears to offer a means for effectively reducing the emission of pollutants while having other potential advantages over conventional combustion methods.

The concept involves feeding powdered fuel and an additive (such as limestone) that will react with SO_2 into a hot fluidized bed of solids. The solids consist of small particles of noncombustible material, such as ash, held in a dense suspension by a stream of air passing upward through them. As the fuel burns in the bed, the SO_2 produced by the sulfur in the coal reacts with the additive. The heat generated is transferred to boiler tubes immersed in the fluidized bed. The excellent heat-transfer characteristics of fluidized beds may make possible smaller combustors and thus result in lower capital and operating costs than those of conventional units. In addition, the efficient gas-solids contacting provided by a fluidized bed may greatly decrease SO_2 emission.

Combustion of coal and oil in fluidized beds has been explored by a number of organizations in this country and abroad. Intensive investigation is now under way in England and in the United States. Most of the U.S. work, including the ANL program, is sponsored by the National Air Pollution Control Administration (NAPCA) of the U.S. Department of Health, Education, and Welfare.

The program at ANL,[2] which emphasizes the pollution abatement aspect of fluidized-bed combustion, consists of three major parts: laboratory-scale supporting investigations, bench-scale experimentation, and evaluations.

[1] A summary of this section is given on pages 14 to 15.

[2] A. A. Jonke, E. L. Carls, R. L. Jarry, M. Haas, W. A. Murphy, C. B. Schoffstoll, "Reduction of Atmospheric Pollution by the Application of Fluidized-Bed Combustion, Annual Report, July 1968–July 1969," ANL/ES-CEN-1001 (1969).

A. LABORATORY-SCALE INVESTIGATIONS

After completion of a literature survey, laboratory-scale fixed-bed experiments were conducted on potential reactants with SO_2 at 1700°F in an air-0.5 vol % SO_2 mixture. The materials tested included calcitic limestone (designated BCR-1360), dolomitic limestone (BCR-1337), calcareous shale, phosphate rock, waste products such as spent oil shale, brown mud, and red mud, and the oxides of lead, manganese, nickel, copper, zinc, and cobalt. The off-gas from the reaction vessel was monitored for SO_2. This study showed that limestones have substantially higher capacities for SO_2 capture than do other materials tested.

An empirical model was developed (1) to estimate the reduction in SO_2 emission attainable with a fluidized-bed system and (2) to ascertain the effects of varying fluidized-bed operating parameters. The reaction rate data used were derived from kinetic data generated by NAPCA on limestones BCR-1337 and BCR-1360. The model quantified the relationships between the extent that SO_2 emission would be reduced and the operating parameters of a fluidized-bed system. A computer program was written to perform the calculations. The model predicts that SO_2 emissions would be decreased by decreasing the additive particle size and superficial gas velocity and by increasing the bed height.

B. BENCH-SCALE EXPERIMENTATION

A 6-in. dia bench-scale fluidized-bed combustor (Fig. VI-1) was constructed. Initially, exploratory bench-scale experiments were performed that aided in the selection of operating conditions. Next, a systematic set of bench-scale experiments were performed in which the emission of SO_2 was studied under conditions applicable to conceptual designs of both utility-sized power-generating stations and industrial steam boilers. An objective of the bench-scale experimental work is to determine the conditions necessary to achieve a high degree of SO_2 removal from the flue gas and efficient utilization of the limestone or other additive material.

The major results of the bench-scale experiments, which were all conducted at a combustion temperature of 1600°F and a superficial gas velocity of 3 ft/sec, are as follows:

1) The emission of SO_2 with limestone additive was 29 to 87% of the SO_2 concentration without additive, depending on the type, particle size, and quantity of limestone added.

2) The most favorable result thus far (87% reduction in the emission of SO_2) was obtained when a calcitic limestone (BCR-1359) of 25-μm average particle size was added at 2.2 times the stoichiometric requirement.

3) For any particular type of limestone additive, greater SO_2 removal was generally noted for finer-particle-sized material than for coarse particle size.

308-1674B

FIG. VI-1. Fluidized-Bed Bench-Scale Combustor and Associated Equipment.

4) From the experimental results, it appears that the calcitic limestone BCR-1360 is more reactive with SO_2 than either the calcitic limestone BCR-1359 or the dolomitic limestone BCR-1337 of the same particle size.

5) The time elapsed from the start of additive feeding to the achievement of a constant SO_2 level in the flue gas ranged from less than one hour to several hours, depending on the particle size of the additive.

6) The maximum utilization of CaO achieved during the experiments was 38%.

7) Partially reacted additive that accumulated in the fluidized bed contributed little to the overall SO_2 absorption, indicating that the CaO particles absorb SO_2 to a negligible extent after about 30% of the CaO is converted to $CaSO_4$.

8) The observed reductions in SO_2 emission are less than predicted by the ANL empirical model (90%, discussed in ANL-7550, pp. 98–99), presumably because the kinetic data upon which the model is based do not reflect the reactivity of material calcined and sulfated in a fluidized-bed coal combustor.

9) The combustion efficiency of a fluidized-bed system, expressed as the percentage of carbon completely burned, was determined to be 96.7 and 97.1% for two experiments. The principal loss of unburned carbon during these experiments was that associated with the solids elutriated from the fluidized bed (average carbon content, 15 wt %) and was about 3% of the carbon input associated with the coal feed. Recycle of elutriated solids would be expected to reduce the overall carbon losses from the system. The carbon monoxide and hydrocarbon contents of the flue gas were 75–400 ppm and 2–20 ppm, respectively, corresponding to a maximum loss of 0.26% of the input carbon. Solids withdrawn to maintain a constant bed level had a carbon concentration of only 0.01 to 0.1 wt %, and their total carbon content was 0.001 to 0.04% of the input carbon.

10) Analysis of solids elutriated during an experiment that employed a 25-μm particle-size additive indicated that the fines residence time in the fluidized bed was sufficient for about 80% of the additive to be calcined before it was elutriated.

11) Solids elutriation rates determined during periods of no additive feeding indicate that virtually all of the ash associated with the coal used in these experiments was elutriated. Other solids elutriated were $CaSO_4$, unreacted CaO, and uncalcined $CaCO_3$. Comparison of elutriation rates for experiments using different additives suggests that there was less decrepitation of additive material BCR-1359 than of BCR-1337 or BCR-1360.

12) The average particle size of elutriated solids was about 90 μm during periods of no additive feeding and decreased to about 60 μm during an experiment in which 25-μm additive was being added to the fluidized bed. The efficiencies of the two cyclones for separation of solids ranged from 86 to 90% of total solids for the primary cyclone and from 97 to 99% for the combined cyclones.

13) Bench-scale experiments conducted at 1600°F with argon substituted for nitrogen established that nitrogen compounds contained in coal are the source of NO_x compounds in the flue gas.

14) A reduction of 30–40% in nitric oxide emission in the flue gas was noted when limestone additive (BCR-1359) was introduced into the fluidized-bed combustor. This reduction (concomitant with the reduction in SO_2 concentration) could be due to catalysis or other enhancement of reactions to form NO_2, or decompose NO, or react NO with CaO or $CaSO_4$.

At the request of NAPCA, members of the ANL fluidized-bed combustion group accompanied NAPCA personnel and others to England for a review of British work on fluidized-bed combustion of fossil fuels. The results of this survey have been published.[3]

[3] "Review of British Program on Fluidized Bed Combustion; Report of U.S. Team Visit to England, February 17–28, 1969," ANL/ES-CEN-1000 (1969).

ARGONNE NATIONAL LAB WEST
3 4444 00007889 9